UMONS
University of Mons

Faculté
des Sciences

C M N

A joint experimental-modelling study of the structure and properties of functional monolayers for the control of organic crystal growth

Dissertation présentée en vue de l'obtention du grade académique de
Proefschrift voorgelegd tot het behalen van de graad van

Doctor of Science

Yansong Hao

Members of the jury:

Prof. Roberto Lazzaroni (promoter)

Prof. Sandra Van Aert (promoter)

Prof. Pascal Damman

Prof. Roland Resel

Prof. Sara Bals

Prof. Steven De Feyter

Prof. Yves Henri Geerts

Universiteit Antwerpen

EMAT

University of Antwerp
EMAT | Electron Microscopy for Materials Science

Acknowledgements

First and foremost, I would like to thank Prof. Roberto Lazzaroni and Prof. Sandra Van Aert for sharing your knowledge and the patient guidance you have given in the last four years. The visit of COVID may change our lifestyles in an unexpected way but your encouragements and supports have never changed. I would like to show my sincere gratitude for that and this means a lot for me.

This joint PhD between UMONS and UAntwerpn gives me an opportunity to work in each community of Belgium, if we also consider those interesting meetings/seminars/discussions we had in Brussels. This is a fantastic experience which gave me a chance to work with different people who are always generous to share their knowledge and, of course, passionate about science. I would like to say, thank you, to David, Andrea, Pocket, Manoj, Sinan, Alex, Noopur, Chuping, Ece, Zezhong Annick as well as other group members from CMN and EMAT for those inspiring scientific discussions and also for being part of my PhD life.

Of course, to my families and friends, thank you all for your support. Without you, I could never reach the destination of this PhD. Especially, to my wife Weitong, thanks for your unconditional support and accompany. You are the pillars of my life.

There is no doubt that it is impossible to fit my memories and gratitude in this short page. I would like to thank all the other people who has helped me during this PhD journey. All of you are important memories for my life.

And last but not least, I would like to say, thank you, to the readers and especially to all the professors in the jury. I hope you enjoyed reading this dissertation and sharing the same passion for science as I do.

Contents

List of Figures

Abstract

Among all types of discovered crystals, those formed by organic molecules show the greatest diversity, which results from the intrinsic complexity of the organic molecules and the weak interactions between them. Even for a given compound, different crystal structures can exist. This feature is referred to as polymorphism in the modern crystallographic context and those different crystal forms are called polymorphs. In reality, the crystallization of organic molecules is often performed at the surface of a substrate, giving rise to heterogeneous crystallization. Except for the well-known catalyzing effects, the existence of substrates brings more possibilities to the polymorphic behaviors of organic molecules, promoting the formation of new polymorphs that are only stable in the vicinity of the substrates. For this reason, these new polymorphic forms are often described as substrate-induced polymorphs (SIPs). It is of great importance to understand the formation of SIPs for organic molecules as it has been reported that SIPs can show superior properties with respect to their bulk form counterparts.

Up to now, most studies focus on the identifying and characterizing the presence of SIPs, which relies mainly on X-ray diffraction techniques. However, a detailed explanation about the origin of SIPs is still missing. In this work, we have combined several powerful experimental characterization techniques, including X-ray diffraction, transmission electron microscopy (TEM) and scanning tunneling microscopy (STM) in order to reach an integrated view over the formation of SIPs. These experimental studies are strongly supported by computational chemistry simulations, such as density functional theory and molecular dynamics. A big advantage of using atomistic simulations is that it enables the possibility to predict *a priori* the crystal structures of SIPs and to establish *a posteriori* the general rules for the formation of SIPs.

In practice, this thesis employs state-of-art atomistic simulation approaches in order to bridge substrate-induced polymorphism with a conceptually-connected research area: the self-assembly of molecular networks (SAMNs), also called 2D crystallization. Unlike SIPs, which extend at least several molecular layers, SAMNs are composed of a single layer of molecules with ordered packing. Our simulations have enabled a more comprehensive understanding about the role of substrate during the formation of SIPs and we elucidate how the positional and orientational order of molecules propagates from the substrate to the upper 2D and even 3D crystal layers. In this way, a fundamental understanding of the substrate-induced crystallization is gained by connecting 2D and 3D crystallization using substrate-induced approaches.

Chapter 1.

Introduction

1.1. Substrate-induced polymorphism: an intriguing field in crystal engineering

Crystals are arrays of atoms, ions or molecules that are arranged in a periodic, three-dimensional fashion [1]. The existence of crystals is quite extensive in both nature and our society, from minerals which constitute rocks, gem stones to man-made products such as iron bars, pharmaceuticals and cooking salts. Among all types of crystals, those formed by organic molecules show the largest diversity of crystal structures. This is attributed to the intrinsic complexity of the organic molecules and the relatively weak interactions (van der Waals, hydrogen bonds) that exist between them in the solid state. As a result, the molecules of a given compound are likely to pack in many different ways, forming crystalline solids with very similar stability [2, 3]. In the modern crystallographic context, this feature is referred to as polymorphism, which represents the ability of a certain compound to crystallize into different forms [4]. These crystal forms are then called polymorphs. Despite decades of research, the crystallization of organic molecules remains mysterious in many aspects and studying their polymorphism is of prime importance as it is related to many physical properties of materials, such as solubility, mechanical and electronic properties [5-7], with major impact in different areas, e.g. pharmaceutics [8, 9], electronics [5, 10] and liquid crystalline materials [11].

In reality, crystallization often occurs from the surface of substrates, which gives rise to heterogeneous crystallization [12]. The substrates thus play a pivotal role during the crystallization process. A well-known aspect is that the substrates significantly lower the activation energy barriers for the nucleation and therefore accelerate the crystallization [13-15]. In addition to those well-documented catalytic properties, it is observed in recent studies that the substrates can affect the crystallization process in a different way by promoting the formation of new polymorphic forms or by stabilizing polymorphs that are not stable in bulk materials [16-18]. These new polymorphs stay stable only in the vicinity of the substrates and show different crystal structures from the bulk phases. Divergence from the bulk properties is therefore expected because of the determining effects of crystal structures on the material properties. Several terms have been used to describe those new polymorphs, such as substrate-mediated phases, thin film phases and substrate-induced polymorphs [5]. In this dissertation, we will use the term substrate-induced polymorphs (SIPs).

Earlier studies of SIPs mainly focused on organic semiconductor (OSC) materials. Several reasons

account for this preference. First, for the fabrication of organic electronic devices, molecules are always deposited onto a substrate in the form of thin films. Because charge injection and transport processes take place very close to interfaces in those materials, the crystal structures of those films and the possible formation of SIPs need to be determined explicitly in order to have a complete understanding about the performance of the devices. Second, the molecular structures of OSC compounds are relatively simple and rigid such that the intermolecular interaction pattern is expected to be less complex, making the analysis of their SIPs more straightforward. The best-known example for SIPs of OSC materials is pentacene [5, 19] with some of its SIPs even showing improved charge transport mobility as compared to the bulk forms [19, 20]. SIPs have also been observed in other OSC materials. Figure 1.1 collects molecules for which SIPs have been reported in previous studies. Nowadays, with a broader diversity of applications of OSC devices, it is thus of great value to have a comprehensive understanding about the substrate-induced polymorphism for this class of molecules.
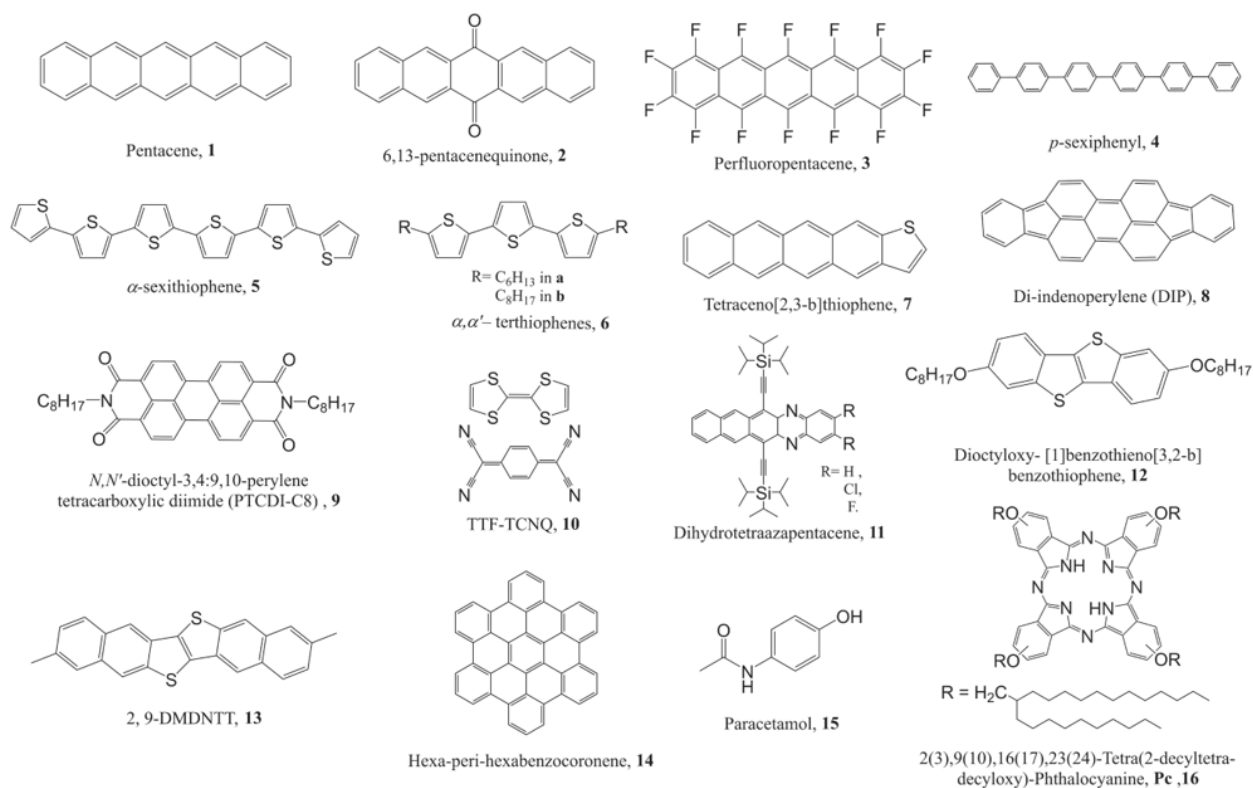
Figure 1.1 Examples of molecules for which SIPs have been observed experimentally [5]

Although most efforts were made to study the SIPs of OSC materials, it certainly does not mean that the SIPs exist only for this group of molecules. Recently, substrate-induced polymorphism

has become an increasingly important topic in the field of pharmaceutics. Metastable polymorphs of paracetamol [21, 22], with potentially better compression properties, were successfully stabilized through the on-surface crystallization. Three polymorphs of paracetamol are compared in Figure 1. 2. The herringbone packing of this molecule in the commercially-available form I leads to fewer slipping planes and therefore weaker plasticity, which is not ideal for the manufacture of paracetamol tablets where plastic deformations are needed.
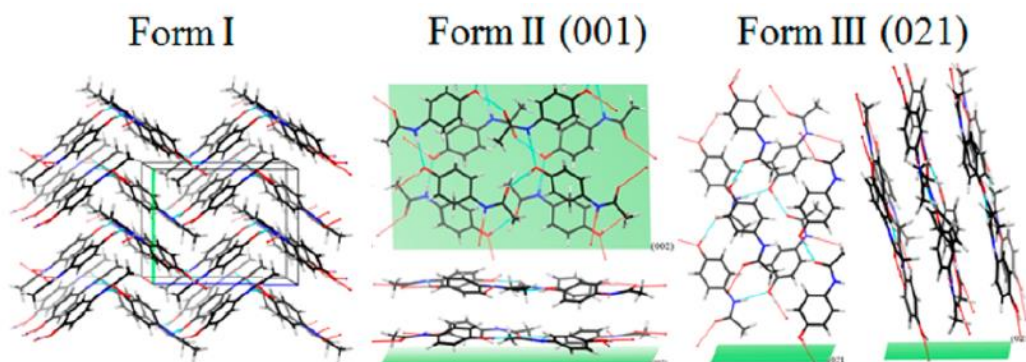
Figure 1. 2 Three polymorphs of paracetamol: (left) The most stable bulk polymorph. (center and right) Meta-stable polymorphs stabilized on the substrate with potentially improved compression properties [22].

Similar observations were also found for piracetam [23], where the selective control of polymorphs was achieved by employing silica substrates during the crystallization. A SIP of another pharmaceutical compound, phenytoin, has been reported to have an improved solubility compared with its bulk forms [24]. These examples demonstrate unequivocally the great benefits of understanding substrate-induced polymorphism in a pharmaceutical context since polymorphs of drug molecules with enhanced properties can be prepared in this manner. Another example showing the superior properties of SIPs is from deltamethrin, a widely-used contact insecticide. Its newly discovered SIP shows more efficient lethality against mosquitoes compared with the current available crystal form. This is considered as an enormous contribution to the control of malaria [25]. These observations of SIPs in different classes of organic molecules suggest that substrate-induced polymorphism is not restricted to a specific group of compounds but is rather a general phenomenon for organic compounds, which makes it interesting for a wide range of subjects in the scientific community.

To summarize, since the early studies of substrate-induced polymorphism in OSC materials, SIPs of versatile organic molecules have drawn increasing attention, given the tremendous importance

of polymorphism in physics, chemistry and pharmaceutical sciences. Meanwhile, experiments show that the formation of SIPs is highly sensitive to many factors, for example, the deposition condition and the nature of substrates. Such sensitivity makes it a very delicate task to reach a profound understanding about substrate-induced polymorphism. These challenges make substrate-induced polymorphism one of the most intriguing aspects in the field of crystal engineering.

1.2. From Self-Assembled Molecular Networks to Substrate-Induced Polymorphs

Another line of research, although conceptually connected to SIPs, is the self-assembled molecular networks (SAMNs) of organic molecules on substrates, also known as 2D crystallization. These two research areas are correlated because SAMNs can be seen as the thinnest possible SIPs, which is composed of a single layer of molecules adsorbed on surfaces. In contrast, SIPs typically extend vertically over at least several molecular layers. One common observation for SAMNs is that their molecular packing is often slightly or even dramatically different from that of bulk crystals [26]. Therefore, SAMNs may be considered as a potential starting point for the formation of new polymorphs. In other words, acting as the bridging layer between the substrate and the thin film crystals, the effects of molecular organization within SAMNs on the crystal growth that follows should not be neglected. Although extensive studies have been carried out in the field of SAMNs and SIPs respectively, the understanding and systematic approach to study the connection between them are lacking. The correlation between substrate, SAMNs and SIPs is still unclear.

1.3. The 2Dto3D project

This thesis is part of the 2Dto3D project, which is a multidisciplinary, multi-site project involving several laboratories from UMONS, UANTWERPEN, ULB, KU Leuven, TU Graz and the Max-Planck Institute for polymer Research (MPI). The general aim of this project is to gain a fundamental understanding of crystallization phenomena, by connecting 2D and 3D crystallization using substrate-directed approaches. This project covers all related aspects in order to develop a systematic approach to the investigation and structural characterization of the 2D to 3D growth of molecular crystalline films. The 2D to 3D crystallization of the synthesized molecules is carried out on conductive nanostructured carbon surfaces. It is expected that these surfaces provide ultimate control in directing the 2D and subsequent 3D crystallization process. These surfaces are also considered as excellent platforms to bring insights into the transition between 2D and 3D crystallization when combined with various structural characterization techniques.

Complementary to experimental characterizations, molecular modelling based on computational chemistry is employed in close interaction with all experimental work performed in this project. In this way, the project aims to elucidate how the positional and orientational order of molecules propagates from the substrate to the upper 2D or 3D crystal layers.

Different tasks of the project are organized among the partners as follows:

- Design and synthesis of molecular systems (ULB, MPI): Promising compounds for the 2Dto3D project are synthesized or purified, including several OSCs and pharmaceutical molecules.
- 2D crystallization and scanning probe microscopy (KUL): 2D crystallization of the selected compounds is performed on surfaces, with their structures being probed by various scanning microscopy techniques.
- Substrate-induced crystallization and thin film X-ray diffraction measurements (TU Graz): Thin films of organic molecules are produced and their crystal structures are solved using thin film X-ray diffraction techniques, from which new polymorphs can be discovered.
- Transmission electron microscopy (TEM) characterization (UANTWERPEN): Electron microscopy measurements are performed aiming to have a more integrated view over the crystal structures of SIPs. The use of TEM allows a direct observation of SIPs in real space at atomic-level resolution, which is an excellent complementary approach to the X-ray diffraction techniques that work only in reciprocal space.
- Molecular modelling of (supra)molecular systems (UMONS): Multiscale computational chemistry modelling is carried out to study the 2D to 3D crystallization process. This enables a better interpretation of the experimental results and brings deeper insights in the energetic aspects about the whole crystallization process. Furthermore, efforts are also made to predict the crystal structures of SIPs *a priori* using atomistic simulations.

1.4. Objectives and layout of the thesis

In the previous sections, a general introduction about the substrate-induced polymorphism of organic molecules is given. The importance to have a systematic investigation on this topic is related to the well-known correlation between crystal structures and material properties. The conceptual connection between SAMNs (2D crystallization) and SIPs has also been discussed. Taking these aspects into account, the scope of this thesis is set to marry these two concepts, which

are currently disconnected research areas and to gain more fundamental understanding about substrate-induced polymorphism. As a joint thesis between UMONS and UANTWERPEN, one major part of this work is the atomistic simulations of 2D and substrate-induced crystallization for selected organic molecules. The simulation results enable a more comprehensive understanding about the role of the substrate during crystallization. With this approach, the connection between two crystallization processes can be built successfully. More importantly, this simulation work also aims to predict crystal structures of SIPs without any prior experimental knowledge. We need to emphasize that these modelling activities interact regularly with experimental efforts undertaken by other partners in the 2Dto3D project consortium. Additionally, this study also covers radiation damage for beam-sensitive materials, including organic compounds. This is a long-standing topic in the TEM community since these materials are prone to be damaged by high-energy electrons used in the TEM. The characterization of organic crystals using TEM is therefore a challenging task. A quantitative approach is developed in our study to investigate radiation damage of organic crystals.

The dissertation is organized as follows:

In chapter 2 we give a more elaborate description about the chemistry lying behind the SAMNs and SIPs. The working principles of the experimental techniques that are used for the structural characterization of SAMNs and SIPs, including scanning tunneling microscopy (STM), grazing-incidence X-ray diffraction and TEM, are also explained.

Chapter 3 highlights the key role that computer simulations play within the current research community. Mostly, simulations are combined with experimental work and enable a solid elucidation of the experimental observations, promoting a more systematic understanding of materials that are being investigated. We present the main simulation techniques used in this work, namely Molecular Mechanics/Dynamics (MM/MD) and Density Functional Theory (DFT). First, we give a short review about the history of these simulation methods and their past use for the study of SAMNs and SIPs. After that, their principles and theoretical background are described in a more detailed way.

Chapter 4, 5 and 6 constitute the "Result and Discussion" part of this thesis.

In chapter 4, a joint STM/modelling approach is used to unravel the nature of the self-assemblies for a selected derivative of tetrathiafulvalene, a major OSC building block. Our study goes beyond

the traditional SAMNs which contain only a single layer of molecules adsorbed on surfaces. Instead, we focus on the multi-layer self-assemblies of this molecule. With the help of atomistic simulations, effects of substrates on the molecular adsorption conformation and long-range order of self-assemblies are understood in a detailed manner. This study is also considered as a steppingstone to move from the SAMNs (2D crystallization) towards the SIPs (3D thin film crystallization), which is the topic of chapter 5.

Chapter 5 aims to establish the connection between SAMNs and SIPs in a more explicit way. First, the formation and structural features of SAMNs are investigated for lead phthalocyanine (PbPc), which is another OSC compound. This study is further extended to explore the growth of PbPc thin crystalline films from the SAMNs using both molecular modelling and experimental characterization techniques. In this way, the first SIP of PbPc is successfully identified and the templating effects of the SAMNs on the subsequent growth of SIP are demonstrated.

Chapter 6 deals with radiation damage of TEM for beam sensitive materials. Using PbPc as an example, a quantitative approach is developed in this chapter which provides deeper insights about the radiation damage behavior of organic crystals in TEM. Furthermore, the methodology we developed also allows us to quantitatively compare the performance of different protection strategies. The framework built in this study is helpful for future applications of TEM in probing the structures of beam sensitive materials in general.

Finally, Chapter 7 summarizes the major findings of this thesis and proposes some prospects for further studies.

References

1.   Ashcroft, N.W. and N.D. Mermin, *Solid State Physics*. 1976, holt, rinehart and winston, new york London.

2.   Nyman, J. and G.M. Day, *Static and Lattice Vibrational Energy Differences between Polymorphs.* CrystEngComm, 2015. **17**: p. 5154-5165.

3.   Bernstein, J., *Polymorphism− a Perspective.* Cryst. Growth Des., 2011. **11**: p. 632-650.

4.   Nogueira, B.A., C. Castiglioni, and R. Fausto, *Color Polymorphism in Organic Crystals.* Communications Chemistry, 2020. **3**: p. 1-12.

5.   Jones, A.O., B. Chattopadhyay, Y.H. Geerts, and R. Resel, *Substrate-Induced and Thin-Film Phases: Polymorphism of Organic Materials on Surfaces.* Adv. Funct. Mater., 2016. **26**: p. 2233-2255.

6.   Hilfiker, R., *Polymorphism in the Pharmaceutical Industry*. Vol. 2. 2006: Wiley Online Library.

7.   Yoneya, M., M. Kawasaki, and M. Ando, *Are Pentacene Monolayer and Thin-Film Polymorphs Really Substrate-Induced? A Molecular Dynamics Simulation Study.* J. Phys. Chem. C, 2012. **116**: p. 791-795.

8.   Blagden, N., M. de Matas, P.T. Gavan, and P. York, *Crystal Engineering of Active Pharmaceutical Ingredients to Improve Solubility and Dissolution Rates.* Adv. Drug Delivery Rev., 2007. **59**: p. 617-630.

9.   Zhang, K., N. Fellah, A.G. Shtukenberg, X. Fu, C. Hu, and M.D. Ward, *Discovery of New Polymorphs of the Tuberculosis Drug Isoniazid.* CrystEngComm, 2020. **22**: p. 2705-2708.

10.   Yoshida, H., K. Inaba, and N. Sato, *X-Ray Diffraction Reciprocal Space Mapping Study of the Thin Film Phase of Pentacene.* Appl. Phys. Lett., 2007. **90**: p. 181930.

11.   Gbabode, G., N. Dumont, F. Quist, G. Schweicher, A. Moser, P. Viville, R. Lazzaroni, and Y.H. Geerts, *Substrate-Induced Crystal Plastic Phase of a Discotic Liquid Crystal.* Adv. Mater., 2012. **24**: p. 658-662.

12.   Mullin, J.W., *Crystallization*. 2001: Elsevier.

13.   Borisenko, E., *Crystallization and Materials Science of Modern Artificial and Natural Crystals*. 2012: BoD–Books on Demand.

14.   Kang, T., Y. You, and S. Jun, *Supercooling Preservation Technology in Food and Biological Samples: A Review Focused on Electric and Magnetic Field Applications.* Food science and biotechnology, 2020. **29**: p. 303-321.

15.   Yu, R., N. Lin, W. Yu, and X.Y. Liu, *Crystal Networks in Supramolecular Gels: Formation Kinetics and Mesoscopic Engineering Principles.* CrystEngComm, 2015. **17**: p. 7986-8010.

16.   Salzmann, I., D. Nabok, M. Oehzelt, S. Duhm, A. Moser, G. Heimel, P.

Puschnig, C. Ambrosch-Draxl, J.r.P. Rabe, and N. Koch, *Structure Solution of the 6, 13-Pentacenequinone Surface-Induced Polymorph by Combining X-Ray Diffraction Reciprocal-Space Mapping and Theoretical Structure Modeling.* Cryst. Growth Des., 2011. **11**: p. 600-606.

17. Schiefer, S., M. Huth, A. Dobrinevski, and B. Nickel, *Determination of the Crystal Structure of Substrate-Induced Pentacene Polymorphs in Fiber Structured Thin Films.* J. Am. Chem. Soc., 2007. **129**: p. 10316-10317.

18. Pithan, L., D. Nabok, C. Cocchi, P. Beyer, G. Duva, J. Simbrunner, J. Rawle, C. Nicklin, P. Schäfer, and C. Draxl, *Molecular Structure of the Substrate-Induced Thin-Film Phase of Tetracene.* J. Chem. Phys., 2018. **149**: p. 144701.

19. Dimitrakopoulos, C., A. Brown, and A. Pomp, *Molecular Beam Deposited Thin Films of Pentacene for Organic Field Effect Transistor Applications.* J. Appl. Phys., 1996. **80**: p. 2501-2508.

20. Bouchoms, I., W. Schoonveld, J. Vrijmoeth, and T. Klapwijk, *Morphology Identification of the Thin Film Phases of Vacuum Evaporated Pentacene on Sio2 Substrates.* Synth. Met., 1999. **104**: p. 175-178.

21. Yeager, J.D., K.J. Ramos, N.H. Mack, H.-L. Wang, and D.E. Hooks, *Transformation and Growth of Polymorphic Nuclei through Evaporative Deposition of Thin Films.* Crystal growth & design, 2012. **12**: p. 5513-5520.

22. Ehmann, H.M. and O. Werzer, *Surface Mediated Structures: Stabilization of Metastable Polymorphs on the Example of Paracetamol.* Cryst. Growth Des., 2014. **14**: p. 3680-3684.

23. Simões, R.G., I. Salzmann, R. Resel, C. Röthel, and Y.H. Geerts, *Stabilization of the Metastable Form I of Piracetam by Crystallization on Silicon Oxide Surfaces.* Cryst. Growth Des., 2018. **18**: p. 4123-4129.

24. Reischl, D., C. Röthel, P. Christian, E. Roblegg, H.M. Ehmann, I. Salzmann, and O. Werzer, *Surface-Induced Polymorphism as a Tool for Enhanced Dissolution: The Example of Phenytoin.* Crystal Growth & Design, 2015. **15**: p. 4687-4693.

25. Yang, J., B. Erriah, C.T. Hu, E. Reiter, X. Zhu, V. López-Mejías, I.P. Carmona-Sepúlveda, M.D. Ward, and B. Kahr, *A Deltamethrin Crystal Polymorph for More Effective Malaria Control.* Proc. Natl. Acad. Sci. U.S.A., 2020. **117**: p. 26633-26638.

26. Fu, C., H.-p. Lin, J.M. Macleod, A. Krayev, F. Rosei, and D.F. Perepichka, *Unravelling the Self-Assembly of Hydrogen Bonded Ndi Semiconductors in 2d and 3d.* Chem. Mater., 2016. **28**: p. 951-961.

Chapter 2

Self-Assembled Molecular Networks and Substrate-Induced Polymorphs of organic molecules

Following the general introduction to substrate-induced polymorphism of organic molecules in chapter 1, we discuss here, in a more comprehensive way, the chemistry fundamentals behind each aspect that are covered in this thesis. In the first part of this chapter, we give more detailed descriptions about the Self-Assembled Molecular Networks (SAMNs), in which 2D crystallization processes are at work, and Substrate-Induced Polymorphs (SIPs), in which crystal growth extends in the third dimension. The tools used for their structural characterization are presented in the second part of this chapter, which includes STM, thin film X-ray diffraction and TEM.

2.1. Chemistry fundamentals of Self-Assembled Molecular Networks, polymorph selections and Substrate-Induced Polymorphs

2.1.1. Self-Assembled Molecular Networks

Supramolecular chemistry, a subject aiming to understand the importance of non-covalent forces that hold molecules together in materials and their effects on material properties, is flourishing in recent years [1]. By assembling molecules into well-defined molecular adlayers on substrates, SAMNs represent a special topic in supramolecular chemistry. There are two typical environments for the preparation of SAMNs: in ultra-high vacuum (UHV) or at the solution/substrate interface. Similar to the traditional supramolecular chemistry studied in solution [2] or solid phases [3], SAMNs on solid substrates are also based on molecular recognition. Molecules recognize other molecules or ions via non-covalent intermolecular interactions, leading to the formation of ordered SAMNs on the substrates. Various interactions are responsible for such association of molecules, including hydrogen bonds [4-7], van der Waals (vdW) forces [8, 9], electrostatic [10, 11], π-π [12, 13] and dipolar [14, 15] interactions. Among them, hydrogen bonds and vdW forces are most often at work to govern the structures of SAMNs. Representative examples of self-assemblies controlled by these two interactions are shown in Figure 2. 1 and Figure 2. 2, respectively.
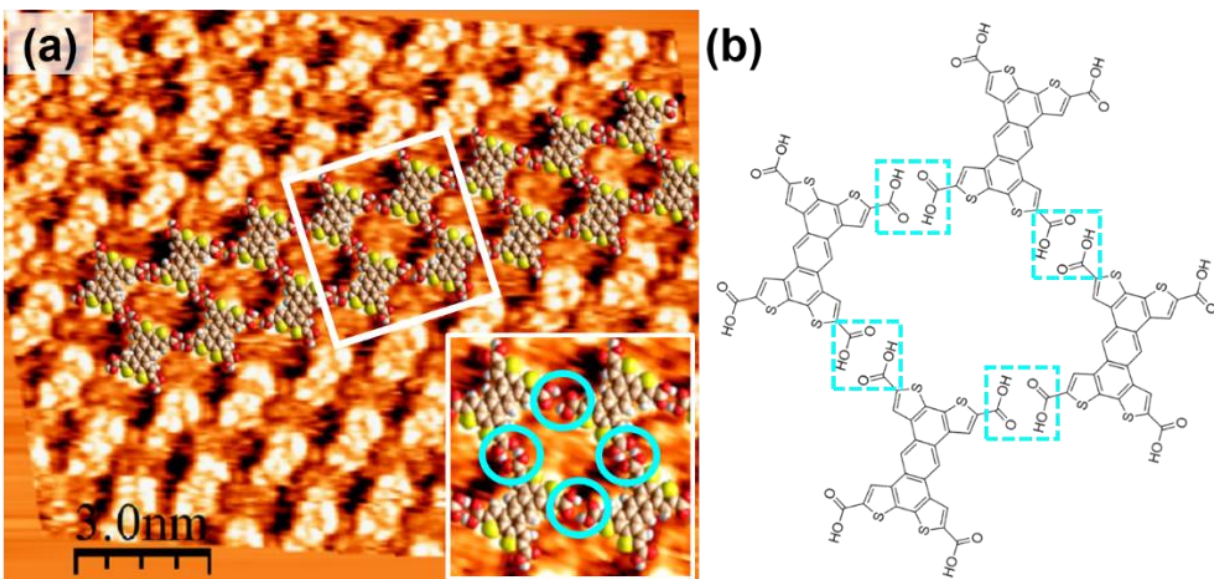
Figure 2. 1 (a) STM image of SAMNs of tetrathienoanthracene derivative (3-TTATA) and the inset shows the enlarged overlapping molecular model. (b) Molecular structures of 3-TTATA arranged in the same way as revealed in the STM image. Hydrogen bonds between carboxylic groups of neighboring molecules are highlighted [6].

Here, 3-TTATA molecules interact with their neighbors via the hydrogen bonds formed between the carboxylic groups (highlighted in both the inset of panel a and panel b). The large, defect-free and highly-ordered assembly indicates that the molecules are assembled in an energetically-favorable way. The collective strength from the hydrogen bonds is clearly sufficient to prevent such porous assembly from collapsing.
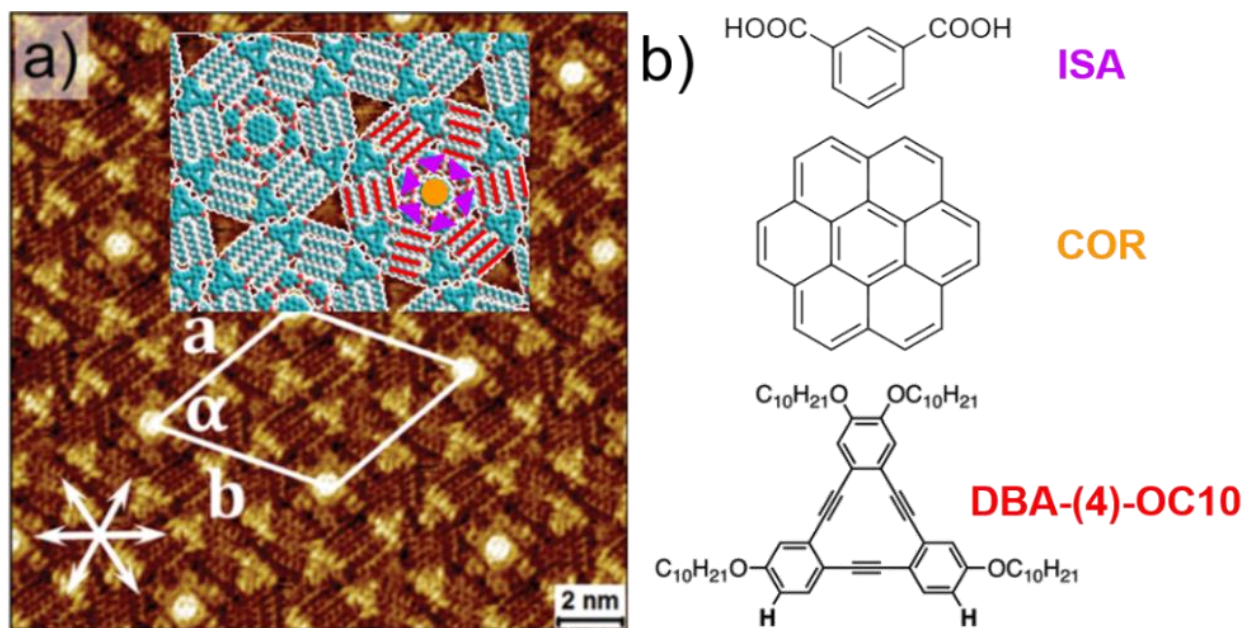
Figure 2. 2 (a) STM image of a multi-component SAMN constituted by coronene (COR), isophthalic acid (ISA) and a DBA derivative with four decyloxy chains (DBA-(4)-OC10). (b) Molecular structure of ISA, COR and the DBA derivative [16].

In Figure 2. 2 (a), the STM image is overlapped with a molecular model, where the ISA is shown by violet triangles, COR is represented by an orange disk and the decyloxy chains of DBA-(4)-OC10 are highlighted by the red lines. Clearly, the interdigitation of decyloxy chains, which relies on vdW forces, is a key ingredient to form this complex molecular assembly. The fact that this assembly extends more than tens of square nanometers and stays stable during the STM imaging demonstrates the ability of vdW forces to assemble molecules into supramolecular structures.

These non-covalent interactions are weaker than the covalent bonds, but as illustrated here, they can still be the driving force to construct large-scale SAMNs (up to thousands of square nanometers [17]) due to their high numbers and the consequent collective strength [1]. Meanwhile, the relative weakness and the diversity of these non-covalent interactions make it possible to manipulate the architecture of the SAMNs by varying the functional groups of molecules or the processing conditions, such as temperature [18, 19], the presence of electric field [20, 21] or the choice of solvent [22, 23] provided the SAMNs are formed at solution/substrate interfaces. Over the past couple of decades, SAMNs have been studied extensively and unprecedented control over their structures has been achieved [1, 24-28], which contributes enormously to the development of functional surfaces [29].

When studying SAMNs of organic molecules, the special role of solid substrates should be

15

emphasized. The presence of the substrate provides additional interfacial interactions, namely molecule-substrate and solvent-substrate (in case of SAMNs prepared at the solution/substrate interface) interactions that must be taken into account. Although this clearly increases the complexity for the investigation of SAMNs, it also offers another way to control the structure and properties of SAMNs: by altering the nature of the substrates [30, 31]. More importantly, with the integration of substrates, molecules are able to assemble themselves into a higher degree of coherence in terms of orientation and packing organization. This is of great value as it paves a possible way to integrate the SAMNs into real devices that rely on complex molecular architectures, ranging from thin-film field-effect transistors, sensors to molecular switches [32].

2.1.2. From polymorph selection to substrate-induced polymorphism

2.1.2.1. Role of thermodynamics and kinetics in polymorph selection: a short background

Similar to SAMNs, the traditional crystallization of organic molecules is also dominated by the molecular recognition via non-covalent intermolecular interactions (e.g. hydrogen bonds, van der waals, π-π stacking and electrostatic interactions) [33]. By maximizing these interactions and fulfilling close packing considerations [3], organic molecules get self-organized and pack into crystals. Owing to the inherent complexity of organic molecules, it is sometimes possible to satisfy the close packing considerations in multiple ways, while the favorable intra- and intermolecular interactions are maximized. This is one explanation accounting for the appearance of multiple polymorphs for a given organic compound. A simple way for the polymorph selection is based on their thermodynamic stability. At a given temperature T and constant pressure, the relative thermodynamic stability of different polymorphs can be evaluated by the difference of their Gibbs free energy G:

$$G = H - TS \tag{2.1}$$

where H represents the enthalpy term, which is related to the intermolecular interactions and associated lattice energy and the entropy term S is related to the disorder and lattice vibrations of the system. The crystallization of organic molecules can be classified into two types of polymorphic systems:

1) Monotropic systems, where a single polymorph is always the most thermodynamically stable below the melting temperature.

2) Enantiotropic systems, in which the relative stability of different polymorphs is a function of temperature.

Figure 2. 3 is a schematic G - T diagram for a single component system that exists in both amorphous and crystalline states. Intersection points in this diagram represent the co-existence of different phases and the temperature where the phase transitions occur; for example, the intersection points at crystalline and liquid states correspond to the melting (crystallization) temperatures (e.g. $T_{m,c}$), while a solid-phase transition temperature is the crossing between two crystalline states (e.g. $T_{t, A-B}$). The monotropic and enantiotropic systems are also defined by this diagram. If the system only has two polymorphs: form A and C, then it is a monotropic system where one form is more stable than the other one within the whole temperature range below the melting points. The enantiotropic system is represented by a system that is capable to crystallize into forms A or B, as there is a solid-transition point below the melting temperature ($T_{t, A-B}$) where the relative stability of these two polymorphs gets reversed.
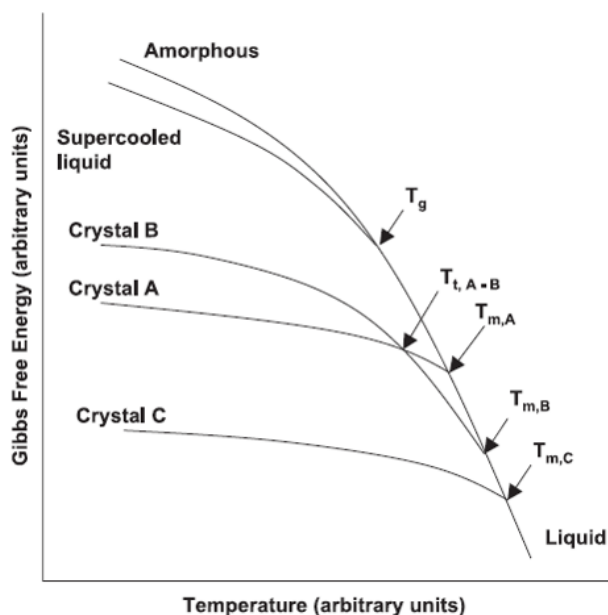
Figure 2. 3 Schematic G –T diagram for a fictitious single component system that consists of crystalline and amorphous phase transitions. Monotropic system (form A and C), enantiotropic system (form A and B) with transition temperature T_t, glass transition temperature T_g and melting points T_m are shown in the diagram [33].

This suggests a possible way for the polymorph selection in an enantiotropic system, which is done by simply controlling the temperature so that the desired polymorph exhibits better thermodynamic stability than others. However, the typical energy difference between different polymorphs for a

given compound is often less than 2 kJ/mol [34, 35], making it very difficult to separate different polymorphs based on their relative thermodynamic stabilities. Combined with the large diversity of polymorphs for organic molecules, it becomes a challenging task to have a successful polymorph selection with this methodology.

Besides thermodynamics, kinetics also plays a crucial role in determining which polymorph will form. Normal crystallization from solution follows the Ostwald's rule of stages [36]: during the crystallization, metastable forms could nucleate first, before transforming to more thermodynamically stable forms. Figure 2. 4 is a schematic Gibbs free energy-reaction progress diagram that explains the kinetic effects during the crystallization process.
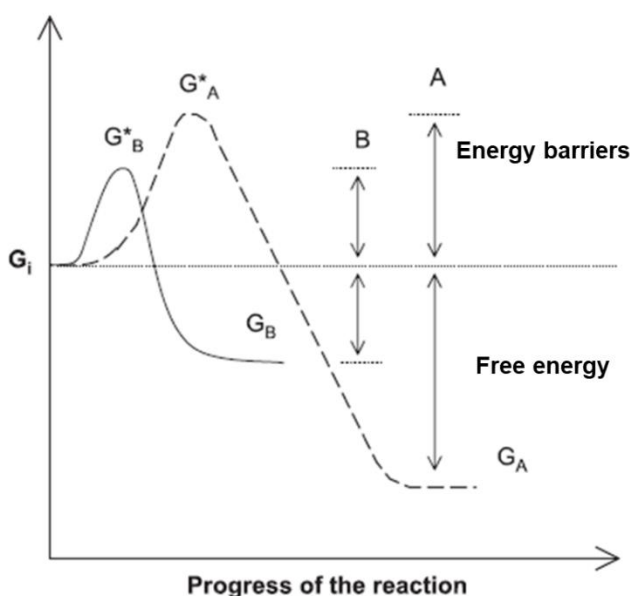
Figure 2. 4 Schematic diagram for a hypothetical crystallization process from the initial state G$_i$ to two polymorphs A or B. G$_A$ and G$_B$: free energy of the two polymorphic forms showing that form A is more stable. G_A^* and G_B^* activation energy barrier during the crystallization from the initial state to polymorph A and B [33].

The initial state G_i, typically a melt or solution for the crystallization, can transform into polymorph A or B. Form A shows a lower Gibbs free energy (G$_A$) and is therefore more stable than form B. For the transformation reaction from G_i to A or B, an energy barrier (G_A^* and G_B^*) resulting from, e.g. molecular diffusion, molecular re-orientation and molecular packing in the crystallization process, needs to be overcome. In this case, although form A has a better stability and transformation to form A experiences a larger decrease in free energy ($G_A - G_i$ larger than $G_B - G_i$), form B still nucleates at a faster rate and emerges first during the crystallization. The

18

reason behind this crystallization sequence is that, at an early stage, the nucleation rate is inversely correlated to the height of the energy barrier. Therefore, the less stable form B, with lower energy barrier, crystallizes first. The kinetics described here provides another possibility for the selective crystallization, where metastable polymorphs are trapped. This can be achieved by manipulating experimental parameters that affect the molecular recognition during the crystallization process, by which the activation energy barriers are tuned correspondingly. There have been experimental observations where the metastable polymorphs are stabilized successfully via this protocol, by employing different types of solvents [37] or using templating in solution [38].

2.1.2.2. Substrate-induced polymorphism: knowns and unknowns

As discussed in section 2.1.2.1, both thermodynamics and kinetics have significant impacts on the formation of different polymorphs. The polymorph selection is thus an intricate interplay between them. For most crystallizations that occur on a substrate, this process is further complicated as a result of additional effects from the substrate. Besides molecular recognition, interactions between (solvent) molecules and the substrate have to be taken into account as well. The influence of the substrate has been demonstrated by experimental observations of SIPs for a wide range of organic molecules (as mentioned in Chapter 1). Moreover, even for the same compound, it is possible to have different SIPs when the nature of the substrate changes. A typical example for this situation is the polymorphic behavior of pentacene, which shows different SIPs when deposited on graphene, metals [39-41], amorphous silica [42-44], NaCl [45] or polyimide nanogratings [46].
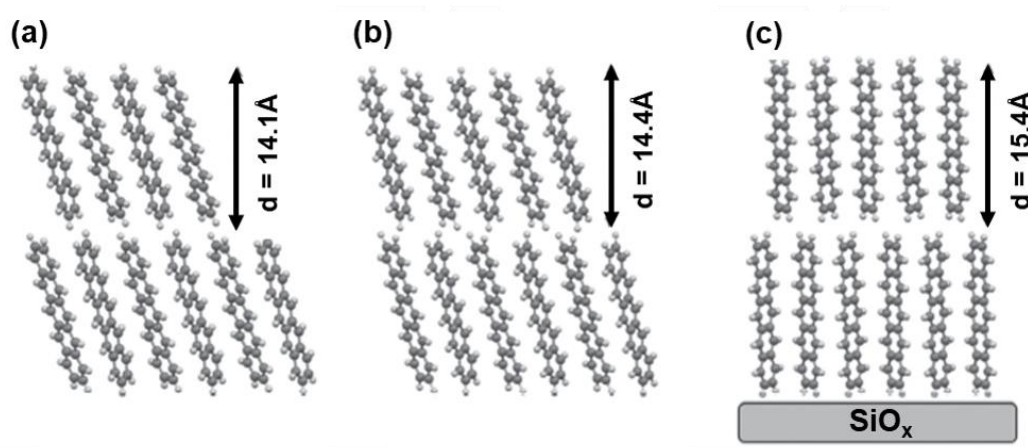
Figure 2. 5 Molecular model for two bulk phases of pentacene (a) and (b) with their molecular packing based on [47] and [48]; SIP of pentacene on the silica substrate (c). The models are oriented in a manner enabling a direct comparison of (001) d-spacings in different polymorphs [49].

The packing motifs of pentacene molecules in bulk phases and the SIP on the silica substrate are compared in Figure 2. 5. For pentacene, the (001) interplanar spacing has been used as the characteristic length to distinguish different polymorphs. Clearly, pentacene molecules adopt different orientations and larger (001) d-spacing in the SIP on the silica substrate. This interplanar distance also varies in other SIPs of pentacene, as summarized in Table 2. 1.

Table 2. 1 Comparison of (001) d-spacing for different SIPs of pentacene.

SIP of Pentacene	(001) d-spacing / Å
On silica [42]	15.4
On NaCl [45] and Kapton [50]	15.1
On polyimide nanogratings [46]	13.5

Pentacene is only one of the representative examples showing the intriguing substrate-induced polymorphic behaviors of organic molecules. As discussed above, SIPs have been observed experimentally for a large variety of materials, ranging from rigid core aromatics like pentacene, through pharmaceuticals, to flexible disordered liquid crystals [51]. However, most of those studies focus on identifying and characterizing the presence of SIPs without explaining their origins.

Based on these observations, different inferences have been proposed to explain the formation of SIPs. From the experimental perspective, one assumption is that the SIP formation is determined by the deposition method used for the thin film preparation, as, for instance, vapor deposition suppresses all contributions from the solvent molecules. Therefore, a significant difference in the structure of films is expected. Yet contradictory results are also reported where the same SIP was produced by both vapor deposition and solution casting techniques [52]. To clarify the role of the deposition technique in the formation of SIPs, a large amount of experimental work is needed since the deposition process is sensitive to numerous experimental parameters. This makes a systematic study on the effects of the deposition method hardly feasible in practice.

The origin of SIPs is also considered to be related with the wetting layer of molecules formed at the interface with the substrate. This is an interfacial molecular layer in direct contact with the substrate, on top of which subsequent molecular layers grow. An example of this wetting layer in thin films of DNTT is shown in Figure 2. 6.
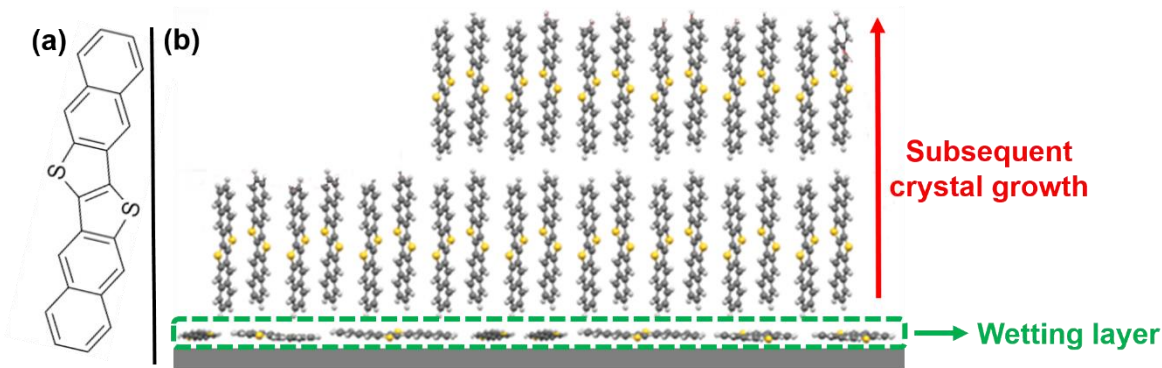
Figure 2. 6 (a) Molecular structure of DNTT. (b) Schematic molecular model showing the wetting layer in thin films of DNTT. In this case, subsequent crystal growth is not affected by the structure of the wetting layer. Panel b adapted from [53]

The existence of this wetting layer has been reported in thin films of different organic molecules, for example, 2,7-dioctyl-BTBT (C8-BTBT) [54], and α,α'-alkyl-disubstituted terthiophenes [52, 55] (see **6a** and **6b** in Figure 1.1). Interestingly, in the thin films of **6a**, a wetting layer is only found in regions where the SIP is present but not where the bulk forms are present. This clearly suggests a potential correlation between the wetting layer and formation of SIPs. Similarly, when deposited on the substrate, the growth mode of C_{60} differs depending on whether the molecules are deposited directly onto the substrate or onto a C_{60} layer [56]. Here, the first layer of C_{60} molecules can be seen as the "wetting layer" and governs the subsequent growth of the film.

Following these observations, efforts have been made to bridge the origin of SIPs and the underneath wetting layer (monolayer) whose structure highly depends on the substrate. The crucial role of the monolayer structure in the formation of SIPs has been highlighted for different organic molecules [55, 57, 58]. Nevertheless, this is not a generally applicable rule as, for some organic molecules, the correspondence between the formation of SIPs and structural features of the monolayer underneath does not exist [53]. In spite of the discrepancy in determining the connection between SIPs and monolayers, those experimental studies are still of great value as they provide a very promising background to understand the origin of SIPs.

Traditionally, the crystal structures of SIPs are determined by X-ray diffraction techniques, which enables accurate measurements of their crystallographic parameters. However, these diffraction measurements are not able to give a precise description of the molecular orientation or molecular ordering within the monolayer, due to the minute amount of materials present and the associated weak signals. Because of this limitation, the molecular orientation in the underneath wetting layer

21

(monolayer) was often merely inferred qualitatively to be flat-lying (parallel to the substrate) or upright-standing (perpendicular to the substrate) in previous X-ray diffraction studies on SIPs [58-60]. This uncertainty makes it difficult to draw solid conclusions about the role of the monolayer in the formation of SIPs. Moreover, even though effects from the monolayer structure on the formation of SIPs can be observed experimentally, the detailed interaction mechanism between the bottom monolayer and the molecular layers grown on top is still not clear, for example, how the monolayer is directing the subsequent crystal growth. This type of information is inaccessible to any individual experimental characterization techniques. To overcome these impediments and make a step further towards understanding the origin of SIPs, advanced surface characterization techniques (STM as discussed in section 2.2.1) and molecular modelling techniques have been integrated in this work as a complementary to traditional structural characterization techniques, such as X-ray diffraction and TEM. Through this combination, we hope to gain a systematic understanding about the formation of monolayer (2D crystallization) and the subsequent growth of SIPs extending in the third dimension.

2.2. Experimental characterization of Self-Assembled Molecular Networks and Substrate-Induced Polymorphs

In this section, we give a more thorough introduction to the experimental techniques that have been employed in this work to study the SAMNs and SIPs of organic molecules.

2.2.1. Working principles of Scanning Tunneling Microscopy

The rapid expansion of scientific research related to SAMNs has been strongly favored by the technological advancement in scanning probe microscopy, in particular STM which is one of the most used scanning probe techniques; it allows a direct observation of molecular structures adsorbed on conductive solid surfaces. The working principle of STM is depicted in Figure 2. 7 and discussed in the following paragraph.
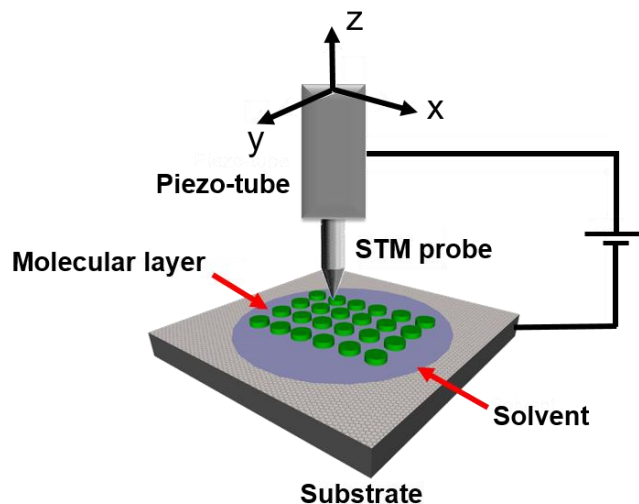
Figure 2. 7 Schematic representation of the working principle of STM at the solution/substrate interface

A sharp STM probe raster scans across the surface and a piezoelectric tube is used to guarantee the precise positioning of the probe with respect to the substrate. The typical working distance between the solid surfaces and the probe is only a few angstroms. Therefore, atomically-flat substrates are essential for using STM. When applying an external bias voltage V_{bias}, a tunneling current is generated between the probe and the surface, which is the output signal of the STM. Since the tunneling current varies exponentially with the tip-sample separation on the angstrom scale, the STM is a most accurate tool to map the surface topographic features. Moreover, this tunneling current gets modified by the nanoscale features underneath the probe, thus providing information about the surface-adsorbed molecular assemblies at each scanning point. There are two different working modes for the STM: constant current (CC) mode and constant height mode (CH). In CC mode, the z position of the probe is continuously adjusted so that a predefined tunneling current is maintained. In this mode, the STM image is generated by recording the change of the probe position along z direction during the scan. A topographic representation of the molecular assembly system is then formed. In contrast, the z position of the probe remains constant when operating in the CH mode. Images are formed by measuring the tunneling current at each scanning point. More detailed descriptions about the STM, such as the instrumentation and image processing can be found in [61].

Modern STM gives access to the analysis of SAMNs at sub-molecular level resolution and the images can be interpreted in terms of a direct visualization of molecular orbitals. Nowadays, it has become an irreplaceable tool for the structural characterization of SAMNs on surfaces. However,

one major limitation for STM is that it is very difficult to use it for the structural characterization of multilayer structures or thin films. In these circumstances, larger thickness forces the STM tip to be placed further away from the substrate during the scan in order to avoid potential disturbances to the multilayer structures. This leads to a drastic decrease of the tunneling current because of its exponential dependence on the tip-substrate distance. Such rapid decay can deteriorate the image resolution, therefore significantly complicating the interpretation of the experimental images [62-64]. Considering that SIPs generally extend at least several molecular layers from the substrate, STM is not the ideal tool to study their crystal structures. In this work, STM is mainly used to understand the structural features of SAMNs. Then, combined with X-ray diffraction, TEM, and atomistic modelling, a more comprehensive understanding is obtained about the formation of SIPs.

2.2.2. X-ray diffraction techniques for thin films

Experimentally, traditional X-ray diffraction methods, such as single-crystal X-ray diffraction and powder X-ray diffraction, are not applicable to determine the crystal structure of unknown SIPs since they exist only within thin films. When crystallized on substrates, organic molecules form thin films that contain numerous crystallites. These crystallites often share the same fiber axis normal to the substrate surface and have a common crystallographic plane parallel to the surface. In other words, the thin films are often highly-textured with a preferred orientation along the surface normal. The distribution of the azimuthal (in-plane) orientation for these crystallites is more complicated. Their in-plane orientations are completely random when an isotropic substrate is used [65]. When the crystallization is performed on anisotropic substrates, more complex texture behaviors are observed. In addition to the fiber texture along the surface normal, crystallites can also show extra in-plane preferred orientation, which is controlled by the anisotropic properties of the substrate. One typical example is the epitaxially-grown organic thin films whose preferred azimuthal orientation originates from the substrate underneath [66-68]. The crystal structure of these organic thin films can be determined by grazing-incidence X-ray diffraction (GIXD), which directly maps the reciprocal lattice of the crystallized thin films. However, it must be noted that the distribution of the reciprocal lattice points is highly associated with the presence of azimuthal orientation in the thin films.

Different types of reciprocal lattice point distributions are compared in Figure 2. 8. In the case of crystallites having random in-plane orientations, the reciprocal lattice points constitute continuous

concentric rings (Figure 2. 8(a)). Each ring corresponds to the same set of crystallographic planes that exist in all crystallites. The degeneration of reciprocal lattice points into continuous rings is due to the randomness of the crystallite orientation, which is similar to what happens in traditional polycrystalline diffraction. With the increase of in-plane alignment, the distribution of reciprocal points becomes non-uniform (Figure 2. 8(b)) and finally turns into individual reciprocal points (Figure 2. 8(c)). The understanding of these distributions is very important for the practical use of GIXD in real experiments, which will be discussed in the next section.
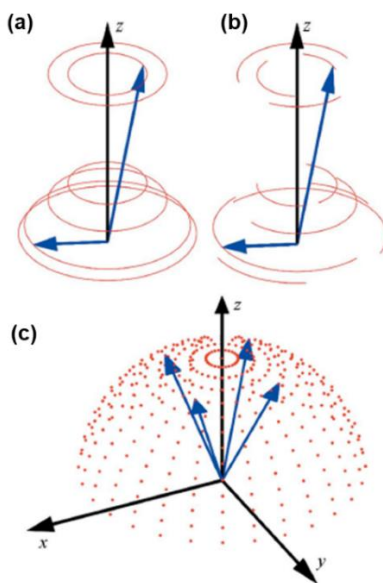
Figure 2. 8 Distribution of reciprocal lattice points for thin films with fiber-textured crystallites having (a) completely random in-plane orientation, (b) partial in-plane texture and (c) well-defined in-plane texture. Coordinates x, y, z are in the reciprocal space. Example reciprocal lattice vectors are represented by blue arrows. Adapted from [69].

Since the first development of GIXD in the 1970s [70], it has become almost a standard experimental tool to determine the crystal structure of organic thin films [71, 72]. The experimental geometry of GIXD is schematically illustrated in Figure 2. 9 (a).
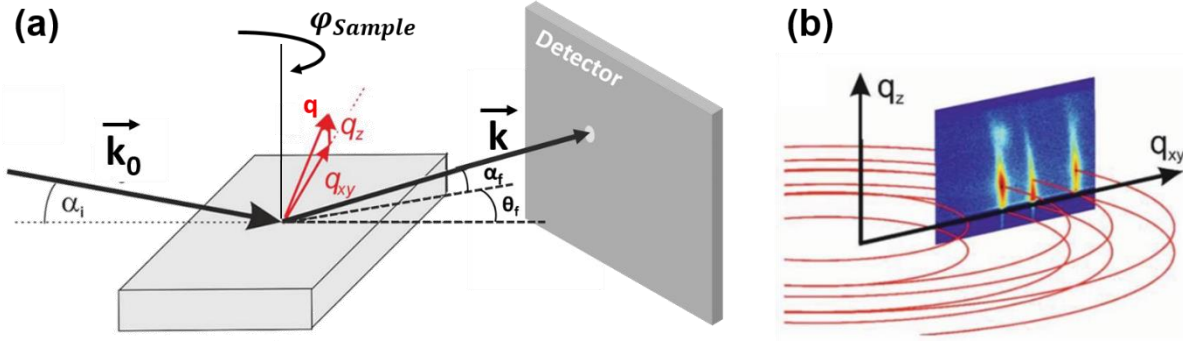
Figure 2. 9 (a) Geometry of GIXD experiments. (b) Example 2D reciprocal space map measured in GIXD experiments. Adapted from [73, 74].

Here, $\mathbf{k_0}$ represents the wavevector of the incident X-ray beam while $\mathbf{k}$ is the wavevector of the scattered beam. The scattering vector $\mathbf{q}$ is then defined as $\mathbf{q} = \mathbf{k_0} - \mathbf{k}$. Based on the Laue equation, diffraction only occurs when $\mathbf{q}$ is equal to a reciprocal lattice vector $\mathbf{g}$. For fiber-textured thin films (fiber axis normal to the surface) with random in-plane orientation, reciprocal lattice points of randomly-oriented thin film crystallites form continuous concentric rings (Figure 2. 8 (a)). Here, one static GIXD measurement at a single sample orientation, which is a section through the reciprocal space, is adequate to have all necessary diffraction information for structure analysis (Figure 2. 9 (b)). This section is equivalent to a 2D reciprocal map and often plotted as a function of q_{xy} and q_z which are the in-plane and out-of-plane components of the scattering vector $\mathbf{q}$. These components are calculated according to the diffraction geometry measured directly from the experiments, using the following equations [74]:

$$q_{xy} = \frac{2\pi}{\lambda_x}(cos^2\alpha_f + cos^2\alpha_i - 2cos\alpha_f cos\alpha_i cos\theta_f)^{1/2} \qquad (2.2)$$

$$q_z = \frac{2\pi}{\lambda_x}\left(\sin\alpha_f + \sin\alpha_i\right) \qquad (2.3)$$

with λ_x the wavelength of the X-ray beam, α_i and α_f the incident and exit angles of the incoming and scattered beam respectively (with respect to the surface of the substrate), while θ_f is the in-plane scattering angle. These equations enable a conversion from the detector space (real space) to the reciprocal space and all diffraction data are then represented by the reciprocal space coordinates. One obvious advantage for this conversion is that, for a given sample, GIXD measurements performed with different experimental setups become directly comparable, even with the absence of detailed knowledge for each experimental setup.

GIXD measurements for fiber-textured thin films comprising crystallites with preferred in-plane orientation are slightly more complicated. In this case, the reciprocal lattice points of crystallites do not form concentric rings, hence only one static GIXD measurement at a single sample orientation cannot provide all information needed for the analysis. This issue is solved by rotating the sample around the surface normal (φ_{sample} in Figure 2. 9 (a)) over 360° and GIXD patterns are recorded consecutively. Figure 2. 10 shows an example of two GIXD patterns that are taken at different φ_{sample} angles.
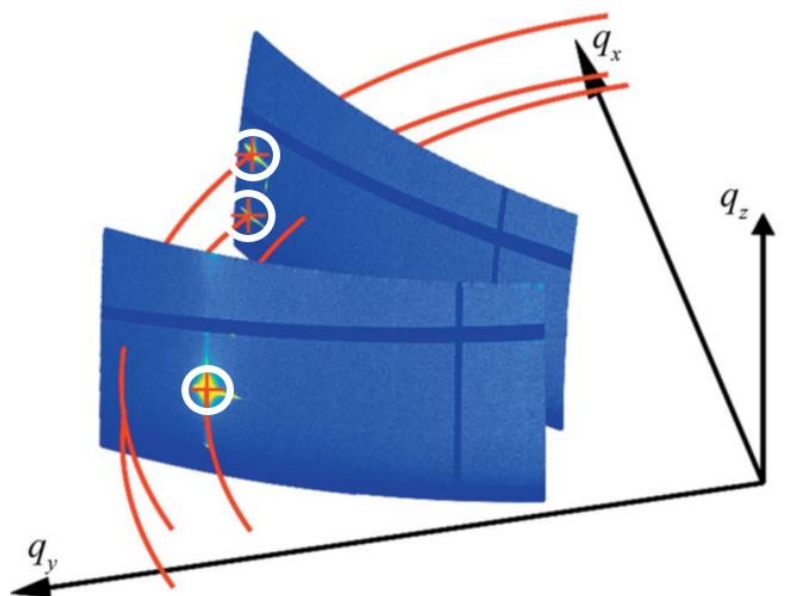
Figure 2. 10 Trajectory (red concentric lines) of reciprocal lattice points (highlighted by white circles) during the rotation of the sample around the surface normal. Two GIXD measurements at different φ_{sample} angles are also shown. Adapted from [69].

After acquisition of the GIXD measurements at all φ_{sample} angles, the full diffraction information is obtained by summing and averaging the recorded patterns. The intensity of each diffraction peak can then be extracted. After that, the peak positions and intensities are further compared to the expected values based on the theoretical crystal structures, through which the polymorph identification in organic thin films is achieved. More importantly, it is also possible to determine lattice parameters for unknown polymorphs via the indexation of the experimental GIXD pattern. This feature makes GIXD the most important and widely-used method to study substrate-induced polymorphism since the crystal structures of SIPs are often not known *a priori* and are different from the available bulk polymorphs. Indexing experimental GIXD patterns to solve lattice

parameters for unknown polymorphs is a very challenging mathematical task. Its details are not shown here but can be found in [69, 73, 75].

2.2.3. Transmission electron microscopy: a powerful complementary technique for structural characterization of SIPs in real space

GIXD can give an accurate solution for the lattice parameters of unknown SIPs because of its extraordinary resolution in reciprocal space. However, it has practically no resolution in real space and this prevents us to know how the organic molecules are packed in the determined lattice. The crystal structure solution for new SIPs of organic molecules cannot therefore depend solely on X-ray diffraction techniques. Additional real-space imaging techniques which enable direct observations of atomic arrangements within the crystal lattice are also needed. Modern TEM is a perfect tool for this purpose and has been employed as a powerful complementary technique to X-ray diffraction techniques in this project. A combination of these two techniques provides a possibility for full crystal structure solutions of previously-unknown SIPs.

2.2.3.1. Why do we need Transmission electron microscopy?

The typical size of the organic crystal lattice is often tens of Angstroms for large molecules. In order to directly visualize the atomic arrangements and thus have more explicit information about the molecular packing within the crystal lattice, a microscope with resolution down to nanometer level is required. The resolution of a microscope is defined as the minimum distance at which neighboring objects can still be resolved as separate entities. Based on Abbe's law, the resolution δ is limited by the wavelength of the radiation source through the following equation [76]:

$$\delta = \frac{0.61\lambda}{NA} \tag{2.4}$$

where λ is the wavelength of the radiation source, NA is the numerical aperture of the objective lens, which depends on the refractive index of the viewing medium and semi-angle of collection of the lens. In practice, the wavelength of visible light is between 400-700 nm, while the maximum value of NA is 0.95 for a dry lens and 1.4 for an oil immersion lens. The resolution of a visible-light microscope is then limited to approximately 300 nm, which is far beyond the size of organic crystal lattices. Therefore, other types of microscopes using different radiation sources must be considered.

This resolution limit is successfully overcome by employing TEM, where accelerated electrons are used as radiation source and deflected by electromagnetic lenses. It was shown by Louis de Broglie that the wavelength of electrons is related to their energy by:

$$\lambda = \frac{h}{\left(2m_0 E \left(1 + \frac{E}{2m_0 c^2}\right)\right)^{\frac{1}{2}}} \tag{2.5}$$

with h being Planck's constant, m_0 the rest mass of electrons, E the energy of electrons and c the speed of light. In TEM, the electrons are accelerated by a high acceleration voltage V and the corresponding energy is given by:

$$E = eV \tag{2.6}$$

The typical value for V used in a conventional TEM ranges from 60 to 300 kV. Based on equation 2.5, the corresponding wavelength of the electrons is only 2-4 pm. Compared with visible light, this is almost 100 000 times shorter and thus makes imaging at the atomic level possible. The practical resolution is, however, restricted by the aberrations of the electromagnetic lenses used in the electron microscope, which cannot be simply avoided by combining convex and concave lenses in a similar manner as in visible-light microscopes [77]. Two aberrations that show substantial effects on the TEM performance are the spherical and the chromatic aberration.

Spherical aberration is caused by different behaviors of the lens for the off-axis rays. Rays that are further from the optical axis of the lens are refracted stronger, which is illustrated in Figure 2. 11(a). The chromatic aberration is due to the fact that rays with different wavelengths are focused differently by the lens. An example is given in Figure 2. 11(b). As a result of these aberrations, a point in the original object is imaged as a disk of finite size. Nowadays, it is possible to correct the spherical aberrations by using multipole magnetic poles (e.g. quadrupoles, hexapoles or octupoles.), while the chromatic aberration can also be partially removed using a monochromator. In this way, state-of-art aberration-corrected TEM reaches a resolution which enables a direct observation of atomic arrangements of SIPs [78].
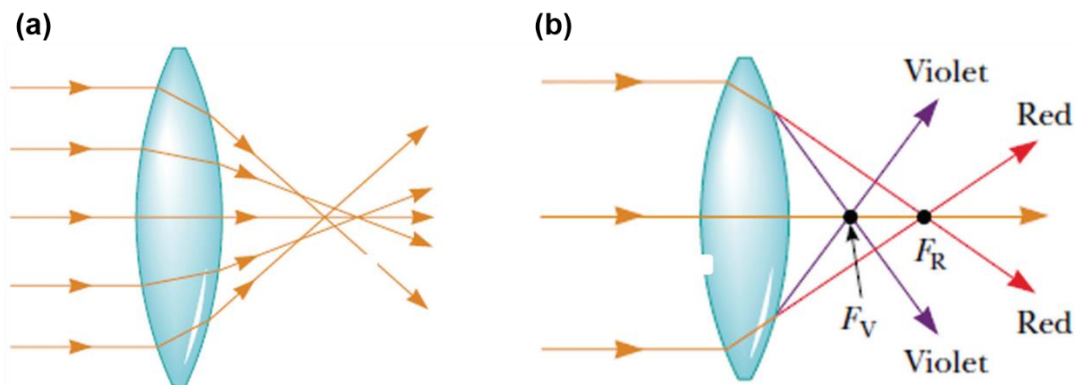
Figure 2. 11 Schematic illustrations of lens aberrations which occur in both light and electromagnetic lenses: (a) Spherical aberration. (b) Chromatic aberrations: violet rays with shorter wavelength are refracted more than red rays. F_V and F_R are the focus points for violet and red rays, respectively. Adapted from [79].

2.2.3.2. Interactions between electrons and sample

Various signals are generated from the interactions between the electrons and the sample. Electrons are low-mass, negatively-charged particles. When interacting with the sample, they can be deflected easily while passing through the negative electron cloud or approaching the positive nucleus of atoms. These deflections are caused by Coulomb interactions and electrons are scattered elastically without energy loss.

Incident electrons undergo a small angular deviation when they interact with the electron cloud of the sample atoms. Stronger scattering of electrons, with larger scattering angles, occurs as the electrons get closer to the nucleus of the atoms. Depending on the shape of the incident electron beam (parallel or convergent) and the selective collection of scattered electrons, different TEM imaging modes are available. For instance, electrons scattered at low angles (typically smaller than 10 mrad) are collected to form bright-field TEM images or diffraction patterns. Electrons with larger scattering angles (> 50 mrad) are used for high-angle annular dark-field imaging in the scanning transmission electron microscope (HAADF STEM) [76]. These two types of imaging modes are mainly used in the current work and discussed further in the following sections.

In addition to the elastic scattering of electrons, inelastic scattering can also occur when the incoming electrons interact with the sample. In this case, the energy of the incoming electrons is transferred to the atoms of the sample, generating other signals, such as X-rays, secondary electrons, phonons or Auger electrons. These signals are collected by specific TEM detectors and are very useful for the chemical analysis of the sample.

2.2.3.3. Conventional TEM: the instrument

To show the three major parts of the TEM, we consider a conventional TEM, where a parallel electron beam is used for imaging. This consists of the illumination system, the objective lens/stage and the imaging system. A much-simplified schematic build-up of a TEM is shown in Figure 2. 12.
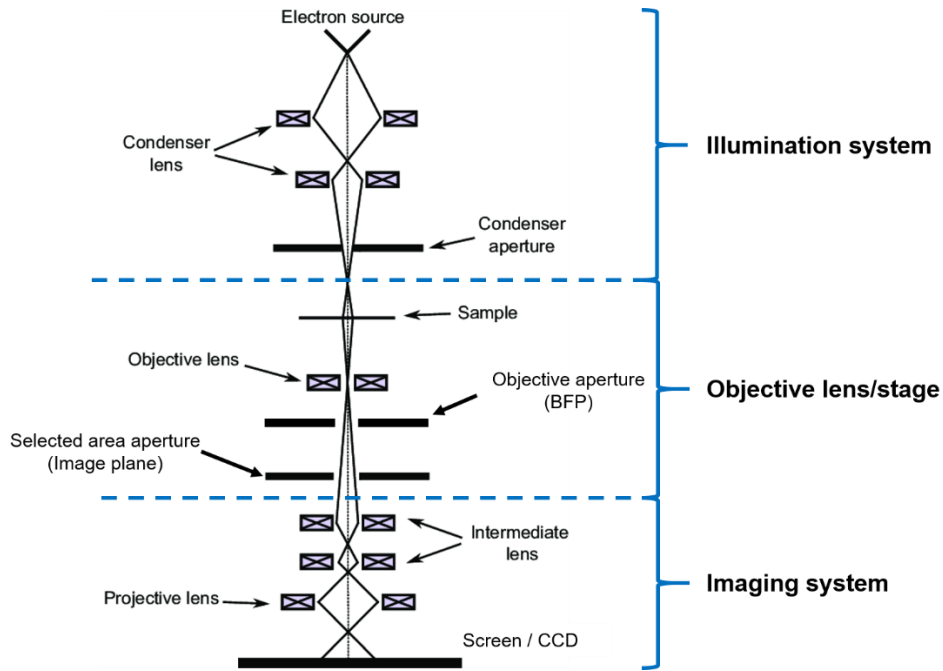
Figure 2. 12 Schematic build-up for a conventional TEM using a parallel electron beam. Note that this is a very simplified figure showing the most important parts of a TEM. In reality, more magnetic lenses, coils are used to guarantee the image quality. Adapted from [80].

In the illumination system, a thermionic gun or field emission gun is used to generate an electron beam. The latter is more widely-used since it gives more monochromatic electrons. The illumination system also contains several condenser lenses to focus electrons onto the sample. An additional condenser aperture can be inserted to filter out the high-angle electrons thus reducing the spherical aberration. Through the control of the condenser lens system, a parallel or convergent electron beam can be used for imaging. Finally, the beam tilt, the shift coil together with the scanning and stigmator coils complete the whole illumination system.

The objective lens/stage system is the heart of the TEM where all electron-sample interactions take place. The sample is mounted inside a holder and irradiated by the incident electron beam. After the interaction, electrons emerging from the sample are dispersed by the objective lens to form the

31

diffraction pattern at its back-focal plane (BFP). At this plane, it is possible to apply an objective aperture to reduce the lens aberrations and select diffraction spots depending on desired imaging mode (bright or dark field imaging). Another aperture, the selected area aperture, is placed at the image plane of the objective lens. By inserting this aperture, information (*e.g.* a diffraction pattern) from a specific-selected region of the sample can be extracted. To summarize, the most valuable information about the sample is extracted by the objective lens of the TEM. Electrons coming out from the sample are focused at its BFP to form the diffraction pattern. After that, a magnified image is formed as the electrons pass toward the image plane of the objective lens.

The last part of the TEM, *i.e.*, the imaging system, is composed of an intermediate lens and projector lenses, which are used to finally form a further magnified image of the sample in either real space or reciprocal space (diffraction pattern). The former is obtained when the image plane of the objective lens is placed at the object plane of the intermediate lens while the diffraction pattern is recorded if the BFP of the objective lens is located at the object plane of the intermediate lens. A fluorescent screen or a charged-couple device (CCD) are then used to record the acquired images.

2.2.3.4. Scanning transmission electron microscope (STEM): the instrument

In addition to the conventional TEM where a parallel electron beam is used, STEM employs a highly-convergent electron beam (a fine electron probe) for the imaging. Figure 2. 13 shows a simplified schematic illustration of the STEM.
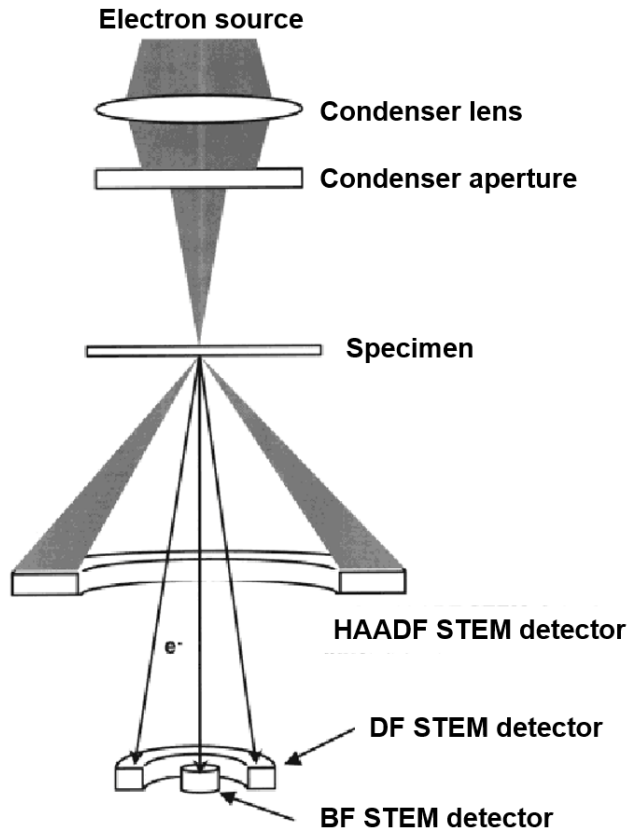
Figure 2. 13 Simplified schematic illustration of the STEM configuration. Adapted from [81].

During the measurement, the probe scans across the sample in a raster manner (the scan coil for moving the probe beam is omitted in Figure 2. 13). A STEM image is here generated pixel by pixel. For each pixel, corresponding to a specific probe position, the intensity is determined by the number of electrons scattered to the target detectors. In STEM, detectors are designed with different inner and outer angles so that electrons scattered into different angles can be selectively collected depending on the purpose of the experiments. Three types of annular detectors are shown in Figure 2. 13: the bright field (BF) detector, the annular dark-field (ADF) detector and the high-angle annular dark-field (HAADF) detector, which typically collects electrons with scattering angles smaller than 10 mrad, from 10 to 50 mrad and larger than 50 mrad, respectively. For the HAADF regime, Bragg-scattered electrons are not collected [76] because of their small scattering angles and in this way the diffraction contrast is minimized. The scattering in this regime is dominated by the Rutherford scattering [76]. As a result, the HAADF images exhibit Z-contrast as the intensity here is proportional to Z^n, where Z is the atomic number of the elements inside the sample and n is close to 2 [82, 83]. This feature provides a direct way to distinguish different

elements from the HAADF STEM images and therefore provides more information about the chemical composition of the sample.

Taking advantages of these features, HAADF STEM imaging has been used successfully in recent years to perform elemental analysis at atomic resolution level [84-87], in addition to traditional applications where the goal is to show the structure at interfaces between regions with different Z. An example of this compositional analysis is shown in Figure 2. 14. Here, HAADF STEM is used to image a multilayer structure of $La_{0.7}Sr_{0.3}MnO_3$(LSMO) - $SrTiO_3$(STO). Atomic columns with different intensities can be directly located and distinguished from the experimental HAADF image (panel a). Based on a quantitative analysis of the images using statistical parameter estimation, it is possible to assign atomic column types in the bulk region of LSMO and STO, respectively (panel b). The composition of columns at the interface (represented by 'X' in the legend) could be determined by quantitatively interpreting the scattered intensities of the atomic columns [85].
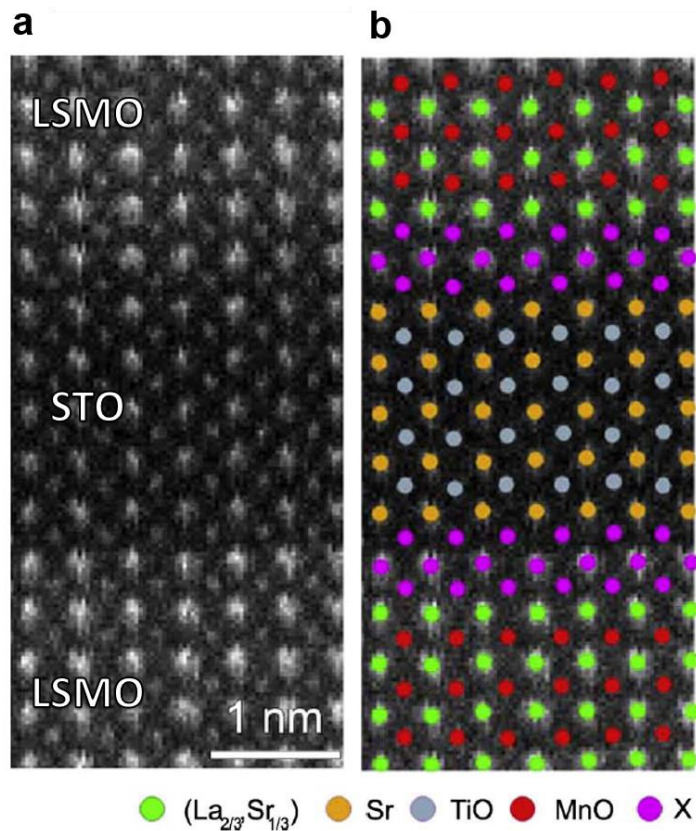
Figure 2. 14 (a) HADF STEM image of the La_{0.7}Sr_{0.3}MnO_3-SrTiO_3 multilayer structure along the [001] zone axis. (b) Overlay showing the estimated atomic column positions and the corresponding atomic column types. Adapted from [85]

Nevertheless, beam damage resulting from the bombardment of high-energy electrons on the crystals is a practical obstacle for using TEM to determine the crystal structures of organic crystals (for both bulk phases or SIPs). Organic crystals are formed by non-covalent interactions between molecules and this makes them particularly prone to be damaged in the TEM. In this thesis, the beam damage of organic crystals in TEM is studied in a quantitative way, which is discussed more detailed in Chapter 6.

To conclude, in this chapter we briefly reviewed the chemistry fundamentals behind the SAMNs and SIPs of organic molecules and the working principles of their associated experimental characterization techniques, from STM for the SAMNs to GIXD and TEM for SIPs. Previous experimental studies on SAMNs and SIPs have generated a solid knowledge basis. However, in order to bridge these two research areas and to further understand the formation of SIPs of organic molecules, not only these characterization techniques need to be combined, but atomistic modelling must also be involved since it can provide information that is not accessible from the experimental work. In the next chapter, we introduce the two main computational-chemistry based modelling approaches that have been used in this work.

References

1. Mali, K.S., N. Pearce, S. De Feyter, and N.R. Champness, *Frontiers of Supramolecular Chemistry at Solid Surfaces.* Chem. Soc. Rev., 2017. **46**: p. 2520-2542.
2. Jonathan W. Steed, J.L.A., *Supramolecular Chemistry*, p. i-xxxi.
3. Desiraju, G.R., *Crystal Engineering: From Molecule to Crystal.* J. Am. Chem. Soc., 2013. **135**: p. 9952-9967.
4. Ivasenko, O. and D.F. Perepichka, *Mastering Fundamentals of Supramolecular Design with Carboxylic Acids. Common Lessons from X-Ray Crystallography and Scanning Tunneling Microscopy.* Chem. Soc. Rev., 2011. **40**: p. 191-206.
5. MacLeod, J.M., Z. Ben Chaouch, D.F. Perepichka, and F. Rosei, *Two-Dimensional Self-Assembly of a Symmetry-Reduced Tricarboxylic Acid.* Langmuir, 2013. **29**: p. 7318-7324.
6. Fu, C., F. Rosei, and D.F. Perepichka, *2d Self-Assembly of Fused Oligothiophenes: Molecular Control of Morphology.* ACS nano, 2012. **6**: p. 7973-7980.
7. Nath, K.G., O. Ivasenko, J.M. MacLeod, J.A. Miwa, J.D. Wuest, A. Nanci, D.F. Perepichka, and F. Rosei, *Crystal Engineering in Two Dimensions: An Approach to Molecular Nanopatterning.* The Journal of Physical Chemistry C, 2007. **111**: p. 16996-17007.
8. Hentschke, R., B.L. Schürmann, and J.P. Rabe, *Molecular Dynamics Simulations of Ordered Alkane Chains Physisorbed on Graphite.* The Journal of chemical physics, 1992. **96**: p. 6213-6221.
9. Afsharimani, N., A. Minoia, C.d. Volcke, M. Surin, R. Lazzaroni, J.-Y. Balandier, C. Niebel, Y.H. Geerts, and B. Nysten, *Self-Assembly of Alkyl-Substituted Oligothiophenes on Mos2: A Joint Experimental/Theoretical Study.* The Journal of Physical Chemistry C, 2013. **117**: p. 21743-21751.
10. S. Klymchenko, A., S. Furukawa, M.V.d. Auweraer, K. Müllen, and S. De Feyter, *Directing the Assembly of Charged Organic Molecules by a Hydrophilic− Hydrophobic Nanostructured Monolayer at Electrified Interfaces.* Nano Lett., 2008. **8**: p. 1163-1168.
11. Lei, S.-B., K. Deng, Y.-L. Yang, Q.-D. Zeng, C. Wang, and J.-Z. Jiang, *Electric Driven Molecular Switching of Asymmetric Tris (Phthalocyaninato) Lutetium Triple-Decker Complex at the Liquid/Solid Interface.* Nano Lett., 2008. **8**: p. 1836-1843.
12. Piot, L., C. Marie, X. Feng, K. Müllen, and D. Fichou, *Hierarchical Self-Assembly of Edge-on Nanocolumnar Superstructures of Large Disc-Like Molecules.* Adv. Mater., 2008. **20**: p. 3854-3858.

13. Cristadoro, A., G. Lieser, H.J. Räder, and K. Müllen, *Field-Force Alignment of Disc-Type Π Systems.* Chemphyschem, 2007. **8**: p. 586-591.

14. Tong, W., Y. Wei, K.W. Armbrust, and M.B. Zimmt, *Dipolar Side Chain Control of Monolayer Morphology: Symmetrically Substituted 1, 5-(Mono- and Diether) Anthracenes at the Solution− Hopg Interface.* Langmuir, 2009. **25**: p. 2913-2923.

15. Wei, Y., W. Tong, C. Wise, X. Wei, K. Armbrust, and M. Zimmt, *Dipolar Control of Monolayer Morphology: Spontaneous Sam Patterning.* J. Am. Chem. Soc., 2006. **128**: p. 13362-13363.

16. Velpula, G., T. Takeda, J. Adisoejoso, K. Inukai, K. Tahara, K.S. Mali, Y. Tobe, and S. De Feyter, *On the Formation of Concentric 2d Multicomponent Assemblies at the Solution–Solid Interface.* Chem. Commun., 2017. **53**: p. 1108-1111.

17. Hao, Y., G. Velpula, M. Kaltenegger, W.R. Bodlos, F. Vibert, K.S. Mali, S. De Feyter, R. Resel, Y.H. Geerts, S. Van Aert, D. Beljonne and R. Lazzaroni, *From 2d to 3d: Bridging Self-Assembled Monolayers to a Substrate-Induced Polymorph in a Molecular Semiconductor.* Chem. Mater., 2022, 34(5), 2238-2248

18. Blunt, M.O., J. Adisoejoso, K. Tahara, K. Katayama, M. Van der Auweraer, Y. Tobe, and S. De Feyter, *Temperature-Induced Structural Phase Transitions in a Two-Dimensional Self-Assembled Network.* J. Am. Chem. Soc., 2013. **135**: p. 12068-12075.

19. Gutzler, R., C. Fu, A. Dadvand, Y. Hua, J.M. MacLeod, F. Rosei, and D.F. Perepichka, *Halogen Bonds in 2d Supramolecular Self-Assembly of Organic Semiconductors.* Nanoscale, 2012. **4**: p. 5965-5971.

20. Mali, K.S., D. Wu, X. Feng, K. Müllen, M. Van der Auweraer, and S. De Feyter, *Scanning Tunneling Microscopy-Induced Reversible Phase Transformation in the Two-Dimensional Crystal of a Positively Charged Discotic Polycyclic Aromatic Hydrocarbon.* J. Am. Chem. Soc., 2011. **133**: p. 5686-5688.

21. Lee, S.-L., Y. Fang, G. Velpula, F.P. Cometto, M. Lingenfelder, K. Müllen, K.S. Mali, and S. De Feyter, *Reversible Local and Global Switching in Multicomponent Supramolecular Networks: Controlled Guest Release and Capture at the Solution/Solid Interface.* ACS nano, 2015. **9**: p. 11608-11617.

22. Takami, T., U. Mazur, and K. Hipps, *Solvent-Induced Variations in Surface Structure of a 2, 9, 16, 23-Tetra-Tert-Butyl-Phthalocyanine on Graphite.* The Journal of Physical Chemistry C, 2009. **113**: p. 17479-17483.

23. Sirtl, T., W. Song, G. Eder, S. Neogi, M. Schmittel, W.M. Heckl, and M. Lackinger, *Solvent-Dependent Stabilization of Metastable Monolayer Polymorphs at the Liquid–Solid Interface.* ACS nano, 2013. **7**: p. 6711-6718.

24. Adisoejoso, J., K. Tahara, S. Okuhata, S. Lei, Y. Tobe, and S. De Feyter, *Two-Dimensional Crystal Engineering: A Four-Component Architecture at a Liquid–Solid Interface.* Angew. Chem. Int. Ed., 2009. **48**: p. 7353-7357.

25. Tahara, K., S. Furukawa, H. Uji-i, T. Uchino, T. Ichikawa, J. Zhang, W. Mamdouh, M. Sonoda, F.C. De Schryver, and S. De Feyter, *Two-Dimensional Porous Molecular Networks of Dehydrobenzo [12] Annulene Derivatives Via Alkyl Chain Interdigitation.* J. Am. Chem. Soc., 2006. **128**: p. 16613-16625.

26. Elemans, J.A., S. Lei, and S. De Feyter, *Molecular and Supramolecular Networks on Surfaces: From Two-Dimensional Crystal Engineering to Reactivity.* Angew. Chem. Int. Ed., 2009. **48**: p. 7298-7332.

27. Kim, M.K., Y. Xue, T. Pašková, and M.B. Zimmt, *Monolayer Patterning Using Ketone Dipoles.* Phys. Chem. Chem. Phys., 2013. **15**: p. 12466-12474.

28. Steeno, R., A. Minoia, M.C. Gimenez-Lopez, M.O. Blunt, N.R. Champness, R. Lazzaroni, K.S. Mali, and S. De Feyter, *Molecular Dopant Determines the Structure of a Physisorbed Self-Assembled Molecular Network.* Chem. Commun., 2021. **57**: p. 1454-1457.

29. Mali, K.S., J. Adisoejoso, E. Ghijsens, I. De Cat, and S. De Feyter, *Exploring the Complexity of Supramolecular Interactions for Patterning at the Liquid–Solid Interface.* Acc. Chem. Res., 2012. **45**: p. 1309-1320.

30. MacLeod, J., J. Lipton-Duffin, D. Cui, S. De Feyter, and F. Rosei, *Substrate Effects in the Supramolecular Assembly of 1, 3, 5-Benzene Tricarboxylic Acid on Graphite and Graphene.* Langmuir, 2015. **31**: p. 7016-7024.

31. Balandina, T., K. Tahara, N. Sändig, M.O. Blunt, J. Adisoejoso, S. Lei, F. Zerbetto, Y. Tobe, and S. De Feyter, *Role of Substrate in Directing the Self-Assembly of Multicomponent Supramolecular Networks at the Liquid–Solid Interface.* ACS nano, 2012. **6**: p. 8381-8389.

32. Goronzy, D.P., M. Ebrahimi, F. Rosei, Arramel, Y. Fang, S. De Feyter, S.L. Tait, C. Wang, P.H. Beton, and A.T. Wee, *Supramolecular Assemblies on Surfaces: Nanopatterning, Functionality, and Reactivity.* ACS nano, 2018. **12**: p. 7445-7481.

33. Rodríguez-Spong, B., C.P. Price, A. Jayasankar, A.J. Matzger, and N.r. Rodríguez-Hornedo, *General Principles of Pharmaceutical Solid Polymorphism: A Supramolecular Perspective.* Adv. Drug Delivery Rev., 2004. **56**: p. 241-274.

34. Bernstein, J., *Polymorphism− a Perspective.* Cryst. Growth Des., 2011. **11**: p. 632-650.

35. Nyman, J. and G.M. Day, *Static and Lattice Vibrational Energy Differences between Polymorphs.* CrystEngComm, 2015. **17**: p. 5154-5165.

36. Ostwald, W., *Studien Über Die Bildung Und Umwandlung Fester Körper.* Z. Phys. Chem., 1897. **22**: p. 289-330.

37. Threlfall, T., *Crystallisation of Polymorphs: Thermodynamic Insight into the Role of Solvent.* Organic Process Research & Development, 2000. **4**: p. 384-390.

38. Thomas, L.H., C. Wales, L. Zhao, and C.C. Wilson, *Paracetamol Form Ii: An Elusive Polymorph through Facile Multicomponent Crystallization Routes.* Crystal growth & design, 2011. **11**: p. 1450-1452.

39. Koch, N., A. Gerlach, S. Duhm, H. Glowatzki, G. Heimel, A. Vollmer, Y. Sakamoto, T. Suzuki, J. Zegenhagen, J.P. Rabe, et al., *Adsorption-Induced Intramolecular Dipole: Correlating Molecular Conformation and Interface Electronic Structure.* J. Am. Chem. Soc., 2008. **130**: p. 7300-7304.

40. Lee, W.H., J. Park, S.H. Sim, S. Lim, K.S. Kim, B.H. Hong, and K. Cho, *Surface-Directed Molecular Assembly of Pentacene on Monolayer Graphene for High-Performance Organic Transistors.* J. Am. Chem. Soc., 2011. **133**: p. 4447-4454.

41. Käfer, D., L. Ruppel, and G. Witte, *Growth of Pentacene on Clean and Modified Gold Surfaces.* Phys. Rev. B, 2007. **75**: p. 085309.

42. Dimitrakopoulos, C., A. Brown, and A. Pomp, *Molecular Beam Deposited Thin Films of Pentacene for Organic Field Effect Transistor Applications.* J. Appl. Phys., 1996. **80**: p. 2501-2508.

43. Minakata, T., I. Nagoya, and M. Ozaki, *Highly Ordered and Conducting Thin Film of Pentacene Doped with Iodine Vapor.* J. Appl. Phys., 1991. **69**: p. 7354-7356.

44. Schiefer, S., M. Huth, A. Dobrinevski, and B. Nickel, *Determination of the Crystal Structure of Substrate-Induced Pentacene Polymorphs in Fiber Structured Thin Films.* J. Am. Chem. Soc., 2007. **129**: p. 10316-10317.

45. Wu, J. and J. Spence, *Electron Diffraction of Thin-Film Pentacene.* J. Appl. Crystallogr., 2004. **37**: p. 78-81.

46. Chou, W.-Y., M.-H. Chang, H.-L. Cheng, Y.-C. Lee, C.-C. Chang, and H.-S. Sheu, *New Pentacene Crystalline Phase Induced by Nanoimprinted Polyimide Gratings.* J. Phys. Chem. C, 2012. **116**: p. 8619-8626.

47. Holmes, D., S. Kumaraswamy, A.J. Matzger, and K.P.C. Vollhardt, *On the Nature of Nonplanarity in the [N] Phenylenes.* Chemistry–A European Journal, 1999. **5**: p. 3399-3412.

48. Campbell, R., J.M. Robertson, and J. Trotter, *The Crystal Structure of Hexacene, and a Revision of the Crystallographic Data for Tetracene.* Acta Crystallogr., 1962. **15**: p. 289-290.

49. Jones, A.O., B. Chattopadhyay, Y.H. Geerts, and R. Resel, *Substrate-Induced and Thin-Film Phases: Polymorphism of Organic Materials on Surfaces.* Adv. Funct. Mater., 2016. **26**: p. 2233-2255.

50. Mattheus, C.C., A.B. Dros, J. Baas, G.T. Oostergetel, A. Meetsma, J.L. de

Boer, and T.T. Palstra, *Identification of Polymorphs of Pentacene.* Synth. Met., 2003. **138**: p. 475-481.

51. Gbabode, G., N. Dumont, F. Quist, G. Schweicher, A. Moser, P. Viville, R. Lazzaroni, and Y.H. Geerts, *Substrate-Induced Crystal Plastic Phase of a Discotic Liquid Crystal.* Adv. Mater., 2012. **24**: p. 658-662.

52. Wedl, B., R. Resel, G. Leising, B. Kunert, I. Salzmann, M. Oehzelt, N. Koch, A. Vollmer, S. Duhm, and O. Werzer, *Crystallisation Kinetics in Thin Films of Dihexyl-Terthiophene: The Appearance of Polymorphic Phases.* RSC Adv., 2012. **2**: p. 4404-4414.

53. Jung, M.-C., M.R. Leyden, G.O. Nikiforov, M.V. Lee, H.-K. Lee, T.J. Shin, K. Takimiya, and Y. Qi, *Flat-Lying Semiconductor–Insulator Interfacial Layer in Dntt Thin Films.* ACS Appl. Mater. Interfaces, 2015. **7**: p. 1833-1840.

54. He, D., Y. Zhang, Q. Wu, R. Xu, H. Nan, J. Liu, J. Yao, Z. Wang, S. Yuan, and Y. Li, *Two-Dimensional Quasi-Freestanding Molecular Crystals for High-Performance Organic Field-Effect Transistors.* Nature Communications, 2014. **5**: p. 1-7.

55. Lercher, C., C. Röthel, O.M. Roscioni, Y.H. Geerts, Q. Shen, C. Teichert, R. Fischer, G. Leising, M. Sferrazza, and G. Gbabode, *Polymorphism of Dioctyl-Terthiophene within Thin Films: The Role of the First Monolayer.* Chem. Phys. Lett., 2015. **630**: p. 12-17.

56. Liu, H. and P. Reinke, *C 60 Thin Film Growth on Graphite: Coexistence of Spherical and Fractal-Dendritic Islands.* The Journal of chemical physics, 2006. **124**: p. 164707.

57. Mannsfeld, S.C., A. Virkar, C. Reese, M.F. Toney, and Z. Bao, *Precise Structure of Pentacene Monolayers on Amorphous Silicon Oxide and Relation to Charge Transport.* Adv. Mater., 2009. **21**: p. 2294-2298.

58. Loi, M.A., E. Da Como, F. Dinelli, M. Murgia, R. Zamboni, F. Biscarini, and M. Muccini, *Supramolecular Organization in Ultra-Thin Films of A-Sexithiophene on Silicon Dioxide.* Nature materials, 2005. **4**: p. 81-85.

59. Spreitzer, H., B. Kaufmann, C. Ruzié, C. Röthel, T. Arnold, Y.H. Geerts, C. Teichert, R. Resel, and A.O. Jones, *Alkyl Chain Assisted Thin Film Growth of 2, 7-Dioctyloxy-Benzothienobenzothiophene.* Journal of Materials Chemistry C, 2019. **7**: p. 8477-8484.

60. Kowarik, S., A. Gerlach, S. Sellner, F. Schreiber, L. Cavalcanti, and O. Konovalov, *Real-Time Observation of Structural and Orientational Transitions During Growth of Organic Thin Films.* Phys. Rev. Lett., 2006. **96**: p. 125504.

61. Morris, M.D., *Microscopic and Spectroscopic Imaging of the Chemical State.* 1993: CRC Press.

62. Ciesielski, A., A. Cadeddu, C.-A. Palma, A. Gorczyński, V. Patroniak, M. Cecchini, and P. Samorì, *Self-Templating 2d Supramolecular Networks: A New Avenue to Reach Control over a Bilayer Formation.* Nanoscale, 2011. **3**: p. 4125-4129.

63. Elemans, J.A., S.J. Wezenberg, M.J. Coenen, E.C. Escudero-Adan, J. Benet-Buchholz, D. den Boer, S. Speller, A.W. Kleij, and S. De Feyter, *Axial Ligand Control over Monolayer and Bilayer Formation of Metal-Salophens at the Liquid–Solid Interface.* Chem. Commun., 2010. **46**: p. 2548-2550.

64. Blunt, M.O., J.C. Russell, M.d.C. Gimenez-Lopez, N. Taleb, X. Lin, M. Schröder, N.R. Champness, and P.H. Beton, *Guest-Induced Growth of a Surface-Based Supramolecular Bilayer.* Nat. Chem., 2011. **3**: p. 74-78.

65. Witte, G. and C. Wöll, *Growth of Aromatic Molecules on Solid Substrates for Applications in Organic Electronics.* J. Mater. Res., 2004. **19**: p. 1889-1916.

66. Simbrunner, C., D. Nabok, G. Hernandez-Sosa, M. Oehzelt, T. Djuric, R. Resel, L. Romaner, P. Puschnig, C. Ambrosch-Draxl, and I. Salzmann, *Epitaxy of Rodlike Organic Molecules on Sheet Silicates□ a Growth Model Based on Experiments and Simulations.* J. Am. Chem. Soc., 2011. **133**: p. 3056-3062.

67. Haber, T., A. Andreev, A. Thierry, H. Sitter, M. Oehzelt, and R. Resel, *Para-Sexiphenyl Thin Films on Kcl (1 0 0) Surfaces: Growth Morphologies and Their Individual Epitaxial Order.* J. Cryst. Growth, 2005. **284**: p. 209-220.

68. Müllegger, S., I. Salzmann, R. Resel, and A. Winkler, *Epitaxial Growth of Quaterphenyl Thin Films on Gold (111).* Appl. Phys. Lett., 2003. **83**: p. 4536-4538.

69. Schrode, B., S. Pachmajer, M. Dohr, C. Röthel, J. Domke, T. Fritz, R. Resel, and O. Werzer, *Gidvis: A Comprehensive Software Tool for Geometry-Independent Grazing-Incidence X-Ray Diffraction Data Analysis and Pole-Figure Calculations.* J. Appl. Crystallogr., 2019. **52**: p. 683-689.

70. Marra, W., P. Eisenberger, and A. Cho, *X-Ray Total-External-Reflection–Bragg Diffraction: A Structural Study of the Gaas-Al Interface.* J. Appl. Phys., 1979. **50**: p. 6927-6933.

71. Robinson, I. and D. Tweet, *Surface X-Ray Diffraction.* Rep. Prog. Phys., 1992. **55**: p. 599.

72. Schreiber, F., *Organic Molecular Beam Deposition: Growth Studies Beyond the First Monolayer.* physica status solidi (a), 2004. **201**: p. 1037-1054.

73. Simbrunner, J., C. Simbrunner, B. Schrode, C. Röthel, N. Bedoya-Martinez, I. Salzmann, and R. Resel, *Indexing of Grazing-Incidence X-Ray Diffraction Patterns: The Case of Fibre-Textured Thin Films.* Acta Crystallogr., Sect. A: Found. Adv., 2018. **74**: p. 373-387.

74. Simbrunner, J., S. Hofer, B. Schrode, Y. Garmshausen, S. Hecht, R. Resel,

and I. Salzmann, *Indexing Grazing-Incidence X-Ray Diffraction Patterns of Thin Films: Lattices of Higher Symmetry.* J. Appl. Crystallogr., 2019. **52**: p. 428-439.

75. Simbrunner, J., B. Schrode, J. Domke, T. Fritz, I. Salzmann, and R. Resel, *An Efficient Method for Indexing Grazing-Incidence X-Ray Diffraction Data of Epitaxially Grown Thin Films.* Acta Crystallogr., Sect. A: Found. Adv., 2020. **76**: p. 345-357.

76. Williams, D.B. and C.B. Carter, *Transmission Electron Microscopy a Textbook for Materials Science* 2009: Springer.

77. Scherzer, O., *Über Einige Fehler Von Elektronenlinsen.* Z. Phys., 1936. **101**: p. 593-603.

78. Erni, R., M.D. Rossell, C. Kisielowski, and U. Dahmen, *Atomic-Resolution Imaging with a Sub-50-Pm Electron Probe.* Phys. Rev. Lett., 2009. **102**: p. 096101.

79. Serway, R.A. and J.W. Jewett, *Physics for Scientists and Engineers.* 2018: Cengage learning.

80. Marturi, N., *Vison and Visual Servoing for Nanomanipulation and Nanocharacterization Using Scanning Electron Microscope.* 2013, Besançon.

81. Utsunomiya, S. and R.C. Ewing, *Application of High-Angle Annular Dark Field Scanning Transmission Electron Microscopy, Scanning Transmission Electron Microscopy-Energy Dispersive X-Ray Spectrometry, and Energy-Filtered Transmission Electron Microscopy to the Characterization of Nanoparticles in the Environment.* Environ. Sci. Technol., 2003. **37**: p. 786-791.

82. Pennycook, S. and D. Jesson, *High-Resolution Z-Contrast Imaging of Crystals.* Ultramicroscopy, 1991. **37**: p. 14-38.

83. Close, R., Z. Chen, N. Shibata, and S. Findlay, *Towards Quantitative, Atomic-Resolution Reconstruction of the Electrostatic Potential Via Differential Phase Contrast Using Electrons.* Ultramicroscopy, 2015. **159**: p. 124-137.

84. Martinez, G., A. Rosenauer, A. De Backer, J. Verbeeck, and S. Van Aert, *Quantitative Composition Determination at the Atomic Level Using Model-Based High-Angle Annular Dark Field Scanning Transmission Electron Microscopy.* Ultramicroscopy, 2014. **137**: p. 12-19.

85. Van Aert, S., J. Verbeeck, R. Erni, S. Bals, M. Luysberg, D. Van Dyck, and G. Van Tendeloo, *Quantitative Atomic Resolution Mapping Using High-Angle Annular Dark Field Scanning Transmission Electron Microscopy.* Ultramicroscopy, 2009. **109**: p. 1236-1244.

86. Kotaka, Y., *Direct Visualization Method of the Atomic Structure of Light and Heavy Atoms with Double-Detector C S-Corrected Scanning Transmission Electron Microscopy.* Appl. Phys. Lett., 2012. **101**: p. 133107.

87. Das, S., A. Rata, I. Maznichenko, S. Agrestini, E. Pippel, N. Gauquelin, J. Verbeeck, K. Chen, S. Valvidares, and H.B. Vasili, *Low-Field Switching of Noncollinear Spin Texture at L a 0.7 S R 0.3 Mn O 3− Srru O 3 Interfaces.* Phys. Rev. B, 2019. **99**: p. 024416.

Chapter 3

Modelling Self-Assembled Molecular Networks and Substrate-Induced Polymorphs of organic molecules

One major part of the work in this thesis focuses on the computational-chemistry based atomistic modelling of the Self-Assembled Molecular Networks (SAMNs) and Substrate-Induced Polymorphs (SIPs). Despite the fact that various experimental techniques, such as STM, GIXD and (S)TEM, have made enormous contributions in understanding the crystallization of organic molecules from 2D to 3D, atomistic modelling still plays an indispensable role in the studies of SAMNs and SIPs. Some important aspects of the formation and stability of those assemblies are not covered in pure experimental investigations but can be studied efficiently by modelling, such as the detailed description of the molecular structures and intermolecular interactions in both SAMNs and SIPs. More importantly, atomistic modelling actually opens new prospects in this field, e.g. the possibility to predict *a priori* the crystal structure of SIPs and to establish *a posteriori* the general rules for the formation of SIPs and its connection to the SAMNs. These insights are crucial in order to reach a fundamental understanding of the 2D to 3D crystallization.

Atomistic simulations for exploring the properties of condensed matter date back to 1950's. At that time, Monte Carlo (MC) and molecular dynamics (MD) simulations were first used by Metropolis et al. [1] and Alder et al. [2]. Since then, with the fast developments in hardware and software engineering, atomistic modelling has become much less time-consuming and more cost-efficient. This boosts the application of atomistic modelling in various scientific fields where it is employed as a tool for the analysis, interpretation or even prediction of experimental results, especially when the material behavior is too complicated for the empirical analytical models [3]. In computational-chemistry based molecular mechanics and dynamics (MM/MD) simulations, intermolecular interactions are described in an explicit way and the nature of the materials are investigated at the atomistic level. This paves a new path to understand the macroscopic experimental observations from the experimentally invisible microscopic molecular behavior. Practically, the abundant availability of reliable softwares to perform MM/MD simulations (e.g. NAMD [4], LAMMPS [5], Gromacs [6], Amber [7], etc.), together with auxiliary programs for visualizing and processing their outputs, have made MD simulations a routine protocol in research and interact closely with all kinds of experimental efforts.

MM/MD simulations have proved to be very efficient to study the SAMNs of organic molecules [8-11] because they provide efficient and accurate descriptions for the energetic features of the assembly process and they have the capacity to handle large-size systems (up to tens of thousands atoms). This is particularly suitable for the physisorbed SAMNs studied in this work. Physisorption

means that the molecules do not form any chemical bond with the substrate during the assembling process. Instead they interact with the substrate through weaker van der Waals (vdW) and electrostatic interactions. The SAMNs are then formed by the mutual recognition between numerous molecules on the surface. Up to now, MM/MD simulations are often used to acquire more insight about the structural features of the SAMNs that are probed by STM. Models for SAMNs are built and compared with experiments in terms of lattice parameters, molecular conformations and molecular packing motifs [8, 12-14]. These extra insights allow to have an integrated view over the whole assembly process and in turn contribute to purposeful design of SAMNs in experiments. For SIPs, MM/MD simulations play an important role in finding their complete crystal structure solutions. As discussed in chapter 2, the lattice parameters of SIPs can be accurately determined by indexing their GIXD patterns. However, it is not possible to know how molecules are packed within the lattice from the GIXD experiments due to the lack of resolution in the real space. This issue is solved by using MM/MD simulations to model the intermolecular interactions within the lattice, from which the correct molecular packing is determined. Such a protocol has been successfully implemented to determine the crystal structures of SIPs for different organic molecules [15, 16].

The accuracy of MM/MD simulations is highly dependent on the parameters used for describing the intra- and intermolecular interactions. These parameters typically come from *ab-initio* atomistic simulations, which are based on the quantum mechanical formalism, or the fitting of experimental data. In many studies, *ab-initio* calculations are even used to optimize the interaction parameters of the MM/MD simulations such that the desired properties can be successfully reproduced [17-21]. Although the *ab-initio* formalism is not a practically feasible way to investigate the structural features of SAMNs as it is limited to small-size systems (up to a couple of hundreds of atoms), it certainly does not mean that *ab-initio* calculations should be neglected. Actually, they can provide extra information for a more comprehensive interpretation of the experimental data. For instance, the surface electronic density obtained from the *ab-initio* calculations can be directly related to the contrast of experimental STM images. Such a correlation has been exploited in various SAMNs studies [22-25].

For the simulation work in this thesis, both MM/MD and *ab-initio* calculations are performed. All MM/MD calculations are carried out in the Forcite module of the BIOVIA Materials Studio 2018 package [26]. Materials Studio is a multifunctional modelling platform that combines structure

building, visualization and a large set of tools for output analysis; while *ab-initio* calculations are carried out in the density functional theory (DFT) formalism using different available DFT codes. In the next section, we first introduce the principles of MM/MD simulations and emphasize the core notion in these simulations, namely the force field. The principle of DFT calculations and associated key concepts are detailed in the subsequent section.

3.1. Molecular Mechanics and Molecular Dynamics simulations

3.1.1. The force field

The performance of MM and MD simulations is completely dependent on the accuracy of the description of the intra- and intermolecular interactions. The description of these interactions, which is the core of MM/MD simulations, is based on the force field. In MM/MD simulations, molecules are treated as collections of hard balls (atoms) held together by springs (chemical bonds). The potential energy of a system is then evaluated by a combination of several analytical bonded and non-bonded terms, which account for the intra- and intermolecular interactions, respectively. Bonded terms are used to describe energy changes associated with the deformation of bonds, such as bending, stretching, inversion or rotation around bonds, while non-bonded terms define energy changes that are not related to the chemical bonds but to other long-range interactions, for example, the vdW, electrostatic or hydrogen bonding interactions. The force field is actually a combination of these analytical terms and a set of parameters entering into these terms, devoted for specific applications.

Over the past decades, many force fields have been developed for MM/MD simulations with different levels of accuracy and complexity: the first-generation force fields e.g. CHARMM [27] and AMBER [7]; the more advanced, highly-parameterized force fields such as PCFF [28] and COMPASS [29] etc. Different force fields have different functional terms as well as associated parameters. Therefore, the applicability of force fields over the periodic table is variable: some force fields are only accurate for a narrow range of elements while others can provide acceptable accuracy for most of the elements. A general analytical expression for a force field is given by:

$$E_{tot} = E_{bonded} + E_{non-bonded} = \left[E_{Stretching} + E_{Bending} + E_{Torsion} + E_{Inversion} \right] +$$

$$\left[E_{vdW} + E_{Electrostatic} + E_{Hydrogen-bonding} \right] \tag{3. 1}$$

Four types of bond deformation included in the bonded terms are schematically shown in Figure 3. 1.
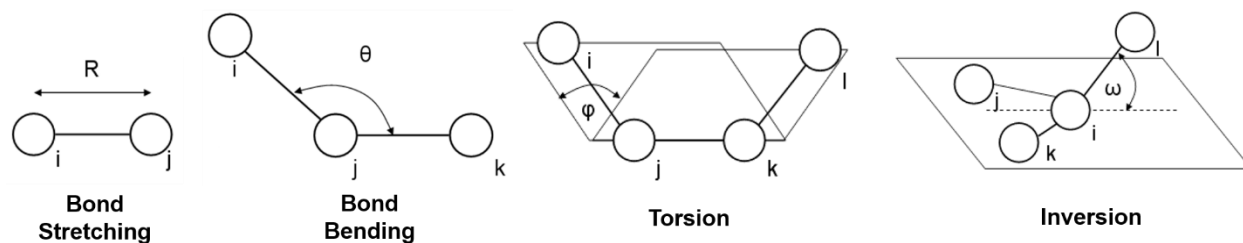
Figure 3. 1 Bond deformations in the force field related to the intramolecular energy. All angles (θ, φ, ω) are measured in radians.

In this work, we perform MM/MD simulations using the Dreiding [30] and Universal [31] force fields that are implemented in Materials Studio. Both have been used widely for modelling the crystal packing and self-assembly of organic molecules [32-36].

For the Dreiding force field, the analytical expressions for the bonded terms are defined as follows [26]:

- The harmonic bond stretching potential ($E_{Stretching}$):

$$E_{Stretching} = \frac{K_0}{2}(R - R_0)^2 \tag{3. 2}$$

  where R is the inter-atomic distance, R_0 is the equilibrium bond length and K_0 is the associated force constant of the harmonic potential.

- The harmonic bending potential ($E_{bending}$) between bond *ji* and *jk* (j, i and k are atomic indices as illustrated in the Figure 3. 1)

$$E_{Bending} = \frac{K_0}{2}(\theta - \theta_0)^2 \tag{3. 3}$$

  where θ is the interatomic angle, θ_0 is the equilibrium angle and K_0 is the force constant for the bond bending potential.

- The torsion interaction for bonds *ij* and *kl* connected by a common bond *jk* is defined in a Cosine-Fourier expansion form:

$$E_{Torsion} = \frac{1}{2}\sum_j B_j(1 - d_j cos[n_j\varphi]) \tag{3. 4}$$

  where B_j is the rotation barrier, φ is the dihedral torsion angle, while d_j and n_j are associated parameters for the Fourier series.

48

- The Umbrella potential for the inversion term:

$$E_{Inversion} = \frac{C}{2}(\cos\omega - \cos\omega_0)^2 \tag{3.5}$$

where C is the force constant and ω_0 is the equilibrium angle between the *il* bond and its projection on the *ijk* plane (see Figure 3. 1).

The Universal force field employs the same expression for the bond stretching, torsion and inversion potential. For the bond bending potential, the expression is adapted to:

$$E_{Bending} = \frac{K_0}{2}(\frac{[\cos\theta - \cos\theta_0]^2}{[\sin\theta_0]^2}) \tag{3.6}$$

Similar to the Dreiding force field, K_0 is the force constant, θ is the interatomic angle and θ_0 represents the equilibrium angle.

For non-bonded terms, both Dreiding and Universal force fields employ the 12-6 Lennard-Jones (LJ) potential [37] for the interatomic vdW interactions, whose analytical form is given by:

$$E_{vdW} = D_0\left[\left(\frac{R_0}{R}\right)^{12} - 2\left(\frac{R_0}{R}\right)^6\right] \tag{3.7}$$

Here, R is the interatomic distance, R_0 is the equilibrium distance and D_0 corresponds to the equilibrium well depth.

The expression for the electrostatic interactions in the Dreiding and Universal force fields are defined by classical Coloumbic terms (equation 3.8 and 3.9 respectively)

$$E_{Electrostatic}^{Dreiding} = C\frac{q_iq_jR_0}{\varepsilon R^2} \tag{3.8}$$

$$E_{Electrostatic}^{Universal} = C\frac{q_iq_j}{\varepsilon R} \tag{3.9}$$

In these expressions, C is a constant for the unit conversion, q_i and q_j are the atomic charges in electron units, R is the interatomic distance (in Angstrom), ε is the dielectric constant and R_0 is fixed to 1Å. In our forcefield simulations, the atomic charges are adapted from the ESP (electrostatic potential derived) charges calculated at the DFT level. Within DFT calculations, the ESP charges are generated by condensing the electron density and nuclear charges into partial atomic charges that reproduce the quantum-calculated electrostatic potential around the molecules. This scheme is widely used and considered as an optimal way to handle the interatomic

electrostatic interactions [38, 39]. Compared with vdW interactions described by the LJ potential, the calculation of electrostatic interactions is more expensive as it decays in a much slower way with respect to the interatomic distances. In other words, electrostatic interaction shows a long-range character and still contributes significantly to the potential energy even at large separations of atoms. A traditional way to handle the computational cost of these two non-bonded interactions is to set a cut-off distance above which the interatomic vdW and electrostatic interactions are not considered. However, for calculations performed using periodic boundary conditions (more details given in section 3.1.3.3. Periodic boundary conditions) or where the electrostatic interaction is significant, the use of a cut-off distance can lead to computational errors [40] and artificial fluctuations of electrostatic energy. To overcome this limitation, the Ewald summation method [41] has been used for the vdW and electrostatic interactions in all our force field simulations, which can make the convergence of their associated energies more efficient.

A unique advantage for the Dreiding force field is that the hydrogen-bonding interaction is described by a separate term in an explicit way:

$$E_{Hydrogen-bonding} = D_0 [5 \left(\frac{R_0}{R}\right)^{12} - 6(\frac{R_0}{R})^{10}] cos\,^4 \varphi \qquad (3.\,10)$$

This expression has a similar form as the vdW potential. The directionality of the hydrogen bonds is considered by the extra Cosine term. D_0, R_0 and R have the same physical meaning as in equation 3.7 while φ is the bond angle between the hydrogen donor, the hydrogen atom and the hydrogen acceptor.

3.1.2. Molecular Mechanics calculations

Force fields provide us a way to evaluate the potential energy of a system as a function of its geometry (atomic positions). This is then exploited in the molecular mechanics calculations in order to optimize the geometry of a desired system. Through the energy, the forces exerted on atoms are determined by:

$$f_i = - \frac{\partial U}{\partial r_i} \qquad (3.\,11)$$

where U is the potential energy and r_i represents the atomic positions. In a classical molecular mechanics calculation, an optimized geometry is then found as the potential energy minimum nearest to the initial structure on the basis of minimizing the atomic forces. As an example, the

geometry optimization of a H_2O molecule with respect to the length of one O-H bond is illustrated in Figure 3. 2. Here, one O-H bond is stretched on purpose from the equilibrium distance in the initial structure g1. During the optimization process, the bond length is adapted iteratively until the structure reaches the potential energy minimum located at g2.
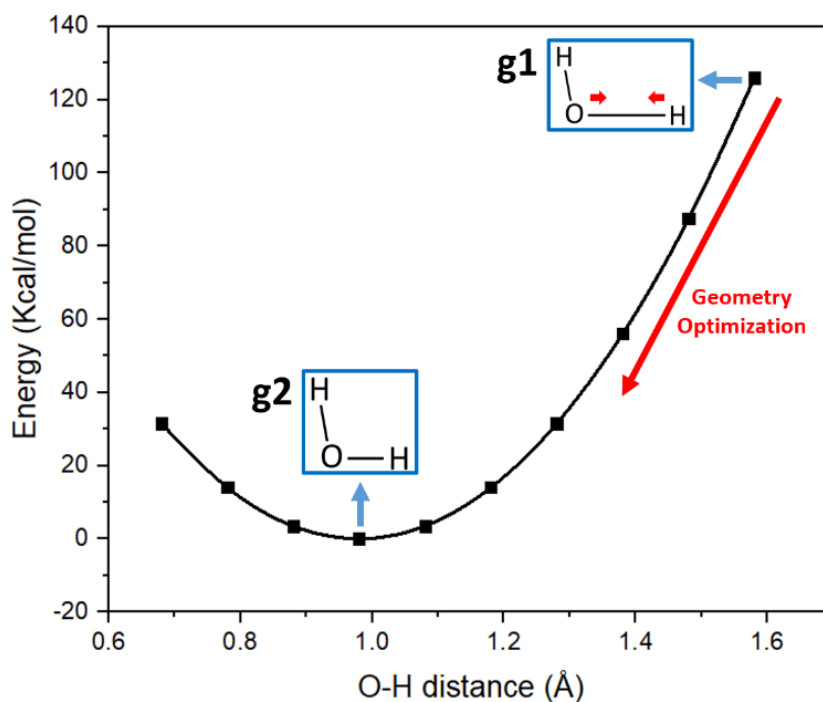
Figure 3. 2 Example of a geometry optimization procedure: the H_2O molecule with a stretched O-H bond (g1) is optimized to the equilibrium structure g2 located at a potential energy valley.

3.1.3. Molecular Dynamics (MD) simulations

3.1.3.1. General principles

One limitation for the MM simulations is that they only bring structures to the nearest local potential minimum from the initial structure. Once a local minimum is detected, the simulation stops. However, this becomes less accurate when the optimized structure of a complex system with many local potential minima needs to be determined. In other words, MM simulations are prone to be trapped in the local potential energy valleys. This is not the case for the MD simulations which allow the exploration of multiple potential energy valleys and generate different possible structures. In a MD simulation, the trajectories and velocities of individual atoms are calculated by iteratively applying classical Newtonian mechanics motion equations:

$$f_i = -\frac{\partial U}{\partial r_i}$$

$$-\frac{\partial U}{\partial r_i} = m_i \frac{\partial^2 r_i}{\partial t^2} \tag{3.12}$$

where U is the potential energy, r_i and f_i are the coordinates of and force exerted on the atom i. With given initial coordinates (normally from a database or previous MM simulations), the atomic forces and associated acceleration are calculated from the potential energy U. The initial velocities of atoms are generated from a temperature-dependent Gaussian distribution. Combining the initial coordinates, atomic forces (acceleration) and initial velocities, atomic trajectories can be calculated as a function of time. Practically, this is done by iterative integration of the equations of motion over a small time step Δt. There are many algorithms for this integration; the Verlet algorithm [42] is the most widely used and is also employed in the MD simulations performed in this work. The atomic coordinates, accelerations and velocities after a time step Δt from the moment t are calculated as follows:

$$\boldsymbol{r}(t + \Delta t) = \boldsymbol{r}(t) + \Delta t \boldsymbol{v}(t) + \frac{\Delta t^2 \boldsymbol{a}(t)}{2} \tag{3.13}$$

$$\boldsymbol{a}(t + \Delta t) = \frac{f(t+\Delta t)}{m} \tag{3.14}$$

$$\boldsymbol{v}(t + \Delta t) = \boldsymbol{v}(t) + \frac{1}{2}\Delta t[\boldsymbol{a}(t) + \boldsymbol{a}(t + \Delta t)] \tag{3.15}$$

This procedure is iterated until the MD simulations run over the desired time span from which we get the trajectories of the atomic system.

3.1.3.2. Statistical ensembles

The equations of motion implemented in the Verlet algorithm provide a way to calculate the atomic trajectories using MD simulations. However, in order to mimic a realistic environment as much as possible, external conditions of the MD simulations, for example the pressure and temperature, have to be controlled. This is achieved by using different types of statistical ensembles such as NVT, NPT, NVE, where different physical quantities are held constant. In the microcanonical ensemble (NVE), the number of particles N, volume V and the total energy of the system E are constant. NVT (canonical) and NPT (isobaric) ensembles share some common features. First, the

number of particles N is fixed. Then both NVT and NPT ensemble allow the system to exchange thermal energy with an external thermal source (called thermostat in MD simulations) so the temperature T is kept constant during the simulations. The difference is that in NVT ensemble, the volume V of the system is kept constant, while in the NPT ensemble, the volume is allowed to change but the pressure of the system is controlled at a constant value by coupling the system to a pressure bath (barostat). Because of this feature, the NPT ensemble enables the system to converge to a well-defined density value.

The MD simulations carried out in this work are performed in the NVT or NPT ensemble. For the NVT ensemble, the Nose-Hoover-Langevin (NHL) thermostat [43] is used as it allows a more efficient convergence to the required temperature. The pressure control in NPT simulations is achieved by the Parrinello-Rahman barostat [44, 45]. In this case, both the volume and shape of the simulation cell are allowed to change. Compared with other barostats, such as the Andersen [46] and Berendsen [47] barostat where only the volume is allowed to change, the Parrinello-Rahman barostat introduces a more natural relaxation of the molecular systems without any geometry constrains.

3.1.3.3. Periodic boundary conditions

All MD simulations performed in this work employ periodic boundary conditions (PBC). The PBC approach is an infinite replication of the simulation cell in all Cartesian directions, along which the atoms get translated. All periodic lattices have identical motifs; for every particle leaving the main simulation cell, an identical particle enters from the opposite side of the simulation cell. One big advantage of using PBC in the simulations is that the edge effects such as the presence of vacuum or a solid wall are avoided [48], making simulations of periodic crystal systems more realistic. This is also very useful and efficient for the simulations of molecular adsorption (e.g. SAMNs on surfaces) as the infinite surface can be represented by a much smaller but periodic simulation cell, which clearly decreases the total computational cost. Note that in that case, the simulation box comprises a vacuum or solvent slab above the molecular adsorbate to better represent the real situation, which also avoids the artificial interactions between the surfaces in the periodic cells. In our MM/MD simulations, the geometry of the substrate is frozen as the physisorption of molecules is not expected to affect the substrate structure.

Figure 3. 3 shows an example of the use of PBC in modelling the adsorption of PbPc molecules on the graphite surface. Here, each periodic simulation cell is bounded by the white square and molecules in each cell move in exactly the same way. In such manner, the molecules can be seen as moving on an infinite surface but for the simulation, just one cell is already enough.
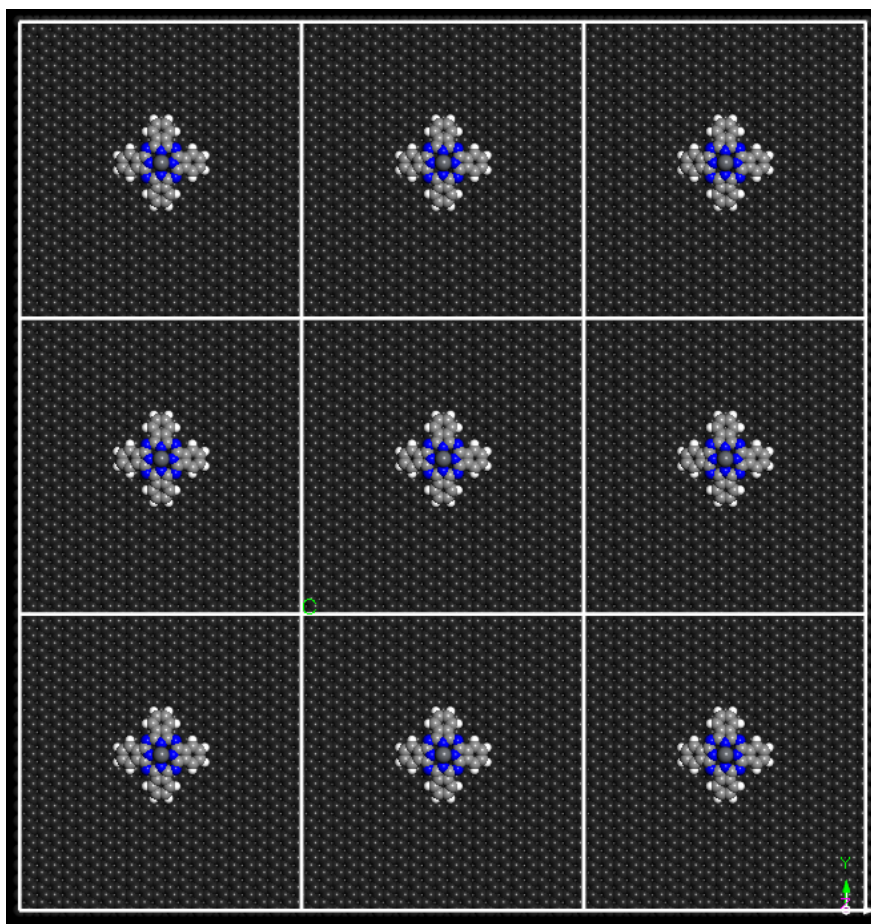
Figure 3. 3 Modelling the adsorption of a lead-phthalocyanine molecule on the graphite surface with PBC. Only 9 periodic cells are shown but the system actually extends to infinity.

3.2. Density functional theory (DFT)

The MM and MD simulations are efficient approaches to study the structural and energetic features of the SAMNs and SIPs for organic molecules. However, as discussed above, the accuracy of these simulations is completely dependent on the parameters employed by the force field to describe the intra- and intermolecular interactions. One classical way to generate these parameters is to perform *ab-initio* calculations based on the quantum mechanical formalism on small model systems.

Besides, the explicit description of the electronic structure in the *ab-initio* calculations provides extra valuable information that is not accessible through the MM/MD simulations, e.g. the electronic densities and orbitals, which are extremely useful as they can be compared directly to the experimental STM images. These advantages make the combination of *ab-initio* and MM/MD simulations a robust strategy to perform computational studies on the 2D to 3D crystallization of organic molecules. In this work, all *ab-initio* calculations are carried out within the DFT framework and the principles of DFT calculations are detailed in the following sections.

3.2.1. Schrödinger equations

The core equation we need to solve for the description of the electronic states of a system is the Schrödinger equation:

$$\widehat{H}\Psi(\boldsymbol{r}_1, \dots \boldsymbol{r}_n, \boldsymbol{R}_1, \dots \boldsymbol{R}_N) = E\Psi(\boldsymbol{r}_1, \dots \boldsymbol{r}_n, \boldsymbol{R}_1, \dots \boldsymbol{R}_N) \tag{3.16}$$

where Ψ is the full wavefunction of the system, which depends on the positions of n electrons and N atomic nuclei. $\widehat{H}$ is the Hamiltonian operator written in atomic units as:

$$\widehat{H} = -\sum_{i=1}^{n}\frac{1}{2}\nabla_i^2 - \sum_{I=1}^{N}\frac{1}{2M_I}\nabla_I^2 - \sum_{i,I}\frac{Z_I}{|\boldsymbol{r}_i-\boldsymbol{R}_I|} + \sum_{i<j}\frac{1}{|\boldsymbol{r}_i-\boldsymbol{r}_j|} + \sum_{I<J}\frac{Z_IZ_J}{|\boldsymbol{R}_I-\boldsymbol{R}_J|} \tag{3.17}$$

In this Hamiltonian operator, the first two terms represent the kinetic energy of the electrons and atomic nuclei, respectively. The third, fourth and fifth term corresponds to the electron-nuclear, electron-electron and nuclei-nuclei interaction potential, respectively. However, with this form of Hamiltonian operator, it is too complicated to solve the wavefunction from equation 3.16. The first approximation used for the simplification is the famous Born-Oppenheimer approximation [49]. It is based on the fact that the atomic nuclei are much heavier than the electrons, which makes it reasonable to decouple the movements of the electrons from the nuclei and suppose the electrons move near nuclei located at fixed positions. This simplification is important in two aspects: the kinetic operator for the atomic nuclei in equation 3. 17 can be neglected and the nuclear-nuclear interaction potential (last term in equation 3. 17) is reduced to a constant. In this way, the total Hamiltonian is simplified to the electronic Hamiltonian, which depends only on the positions of the electrons:

$$\widehat{H_{elec}} = \underbrace{-\sum_{i=1}^{n}\frac{1}{2}\nabla_i^2}_{\widehat{T}} \underbrace{-\sum_{i,I}\frac{Z_I}{|r_i - R_I|}}_{\widehat{V_{ext}}} + \underbrace{\sum_{i<j}\frac{1}{|r_i - r_j|}}_{\widehat{U}}$$

(3. 18)

The electronic wavefunctions are then to be solved from the following equation:

$$\widehat{H_{elec}}\varphi(r,\underline{R}) = E_{elec}\varphi(r,\underline{R})$$

(3. 19)

where $\underline{R}$ represents the given positions of the atomic nuclei.

For a set of atomic nuclei at given positions, the electron configuration with the lowest energy is defined as the ground state of the electrons. Finding the ground state of the electrons is a key task in *ab-initio* calculations as it is directly related to many molecular and materials properties, such as the density of states, the spatial and energetic distribution of the molecular orbitals and the chemical reactivity. In practice, the positions of the atomic nuclei under which the ground state of the electrons is to be determined, can be acquired using different ways, for instance, a previously-run MM/MD simulation, a crystal structure database or an iterative adaption of the starting geometry until certain convergence criteria are satisfied. The last approach is similar to the geometry optimization performed using MM.

3.2.2. Electron Density

In the previous section, we gave a short introduction to the Schrödinger equation from which the electron wavefunction of a system can be solved. There are several circumstances where the Schrödinger equation can be solved exactly, such as the particle in a box or harmonic oscillator [50]. However, the scenario we are interested in, where multiple electrons interact with multiple atomic nuclei, is much more complicated. A complete Schrödinger equation in this case is a combination of eq 3.18 and 3.19:

$$\left[-\sum_{i=1}^{n}\frac{1}{2}\nabla_i^2 - \sum_{i,I}\frac{Z_I}{|r_i - R_I|} + \sum_{i<j}\frac{1}{|r_i - r_j|}\right]\varphi(r_1, \dots r_n) = E\varphi(r_1, \dots r_n)$$

(3. 20)

In the first term on the left side of the equation, we have operators for the kinetic energy of the electrons, the electron-nuclei interaction potential and the interaction potential between electrons, respectively. The full wavefunction φ is a function of the spatial coordinates of each electron and

E is the ground state energy of the system. The full electron wavefunction φ can be approximated as a product of individual electron wavefunctions as:

$$\varphi = \varphi_1(\boldsymbol{r})\varphi_2(\boldsymbol{r}), \dots, \varphi_n(\boldsymbol{r}) \tag{3.21}$$

and this form of approximation is known as the Hartree product. In real systems (e.g. molecules or crystals), the number of electrons is considerably large. For each electron, its individual wavefunction is a 3-dimensional function and this makes the dimension of the full electron wavefunction equal to *3n.* Taking a single H_2O molecule as an example, its full wavefunction is a 30-dimensional function (3 dimensions for each of the 10 electrons). Such high dimension makes it impossible to find a full wavefunction solution to the Schrödinger equation directly.

Another hindrance to solve the Schrödinger equation comes from the electron-electron interaction potential in the Hamiltonian (see eq. 3.20). The form of this contribution means that each individual electron wavefunction $\varphi_i(r)$ can only be found with simultaneous considerations of the individual electron wavefunctions for all other electrons. From this perspective, the Schrödinger equation is a typical many-body problem that cannot be solved exactly.

We have seen that finding a full wavefunction solution directly to the Schrödinger equation is an untractable task. One thing to notice is that the electron wavefunctions are not measurable observables. Instead, what can be measured is the probability of *n* electrons existing at a specific set of coordinates, $\boldsymbol{r}_1, \boldsymbol{r}_2, \dots \boldsymbol{r}_n$. This probability is directly related to the electron wavefunctions, which equals to $\varphi^*(\boldsymbol{r}_1, \boldsymbol{r}_2, \dots \boldsymbol{r}_n)\varphi(\boldsymbol{r}_1, \boldsymbol{r}_2, \dots \boldsymbol{r}_n)$ with the asterisk representing a complex conjugate. Moreover, the electrons are not distinguishable, meaning the actual quantity of interest is the probability that *n* electrons (in any order) have coordinates $\boldsymbol{r}_1, \boldsymbol{r}_2, \dots \boldsymbol{r}_n$. A quantity closely related to this is the density of electrons at a particular position ρ(r), which can be written as a function of individual electron wavefunctions:

$$\rho(\mathbf{r}) = \sum_i \varphi_i^*(\boldsymbol{r})\varphi_i(\boldsymbol{r}) \tag{3.22}$$

and the probability P of finding an arbitrary electron at position **r** is simply equal to:

$$P = \rho(\mathbf{r})d\boldsymbol{r} \tag{3.23}$$

In equation 3. 22, the summation goes over all individual electron wavefunctions occupied by the electrons. Each term inside the summation represents the probability to find an electron in wavefunction φ_i located at the position **r**. The concept of electron density is the core of DFT as it

illustrates that the electron density $\rho(\mathbf{r})$, which is a function of only three variables (x, y, and z), contains valuable information that is related to the full wavefunction solution of the Schrödinger equation, which is a function of *3n* coordinates. In the next section, we will discuss two of the most important theorems that connect the electron density to the problem of finding a solution for the Schrödinger equation and build the fundamentals for the practical use of DFT.

3.2.3. Hohenberg-Kohn theorems

In mid-1960s, Hohenberg and Kohn put forward two essential theorems [51] that actually formulate the practical use of the electron density theory. The first theorem is expressed as follows:

The electron density uniquely determines the Hamiltonian operator and consequently the wavefunctions and all electronic properties of the system.

The importance of this theorem lies in the fact that it provides a new way to solve the Schrödinger equation by finding a solution as a function of electron density, which is a function of three spatial coordinates, instead of a function with *3n* variables. The second Hohenberg-Kohn theorem makes a step further and defines an important property of the functional:

The electron density that minimizes the energy of the overall functional is the density corresponding to the solution of the Schrödinger equation and to the ground state of the system.

From the first theorem, we know that all properties of the system can be described as a functional of the electron density and it confirms the existence of an electron-density functional that can be used to solve the Schrödinger equation while the second theorem gives a clear answer to the question "which electron density are we looking for?".

Practically, it is possible to write the total electronic energy associated with the electronic Hamiltonian (eq. 3. 18) as a functional of the electron density:

$$\mathrm{E}(\rho) = T[\rho(\boldsymbol{r})] + U[\rho(\boldsymbol{r})] + \int v_{ext}(\boldsymbol{r})\rho(\boldsymbol{r})d\boldsymbol{r} \qquad (3.24)$$

The terms on the right side are the electron kinetic energies, the Coulomb interactions between pairs of electrons and the Coulomb interactions between the electrons and the nuclei, respectively. Nevertheless, a practical problem when using this equation is that there is no available analytical expression to describe the kinetic energy of many electrons interacting with each other. This issue

is overcome by Kohn and Sham in 1960s and their solution is detailed in the following paragraph.

3.2.4. Kohn-Sham equations

As discussed above, the Hohenberg-Kohn theorems build an explicit correlation between the electron density and the solution to the Schrödinger equation of many-electron systems. After that, Kohn and Sham [52] proposed a mathematically feasible way to find the correct electron density that corresponds to the ground state of the system. In this approach, the real system with n interacting electrons is simplified to an imaginary system with n independent electrons. The full wavefunction of the ground state of the system is then described as the Slater determinant made of $n/2$ spatial orbitals (according to Pauli principle, each spatial orbital can accommodate two electrons with opposite spins) of the individual electrons.

This simplification allows to build a set of Schrödinger equations in which each equation describes a single electron. This set of equations is called Kohn-Sham equations and every equation has the following form:

$$\left[-\frac{\hbar^2}{2m}\nabla_i^2 + V_{ext}(\boldsymbol{r}) + e^2 \int \frac{\rho(r')}{|r-r'|}dr' + V_{xc}(\boldsymbol{r})\right]\varphi_i = \epsilon_i\varphi_i \qquad (3.25)$$

On the left side of the equation, there are three types of potentials, V_{ext}, $e^2 \int \frac{\rho(r')}{|r-r'|}d\boldsymbol{r}'$ and V_{xc}. The first potential represents the interaction between the electrons and the atomic nuclei. The second is called the Hartree potential, which describes the Coulomb potential between electrons, and the last term, named exchange-correlation potential, is used to cover all differences between the real interacting system and the fictitious non-interacting system.

The solutions of the Kohn-Sham equations φ_i are then used to calculate the electron density ρ of the original "true" system via equation 3. 22. However, it must be noticed here that the potentials used to solve the Kohn-Sham equations, like the Hartree potential and the exchange-correlation potential, actually depend on the electron density ρ, therefore also on the φ_i which are actually the unknown solutions of the Kohn-Sham equations. Accordingly, the Kohn-Sham equations have to be solved in an iterative manner, as shown in Figure 3. 4. Such iterative methodology to find the solution of the Kohn-Sham equations is also called the self-consistent field (SCF) method. The SCF procedure starts from defining an initial, trial electron density, $\rho_{in}(\mathbf{r})$. The effective potential

$V_{eff}(\boldsymbol{r})$ is then calculated based on that initial electron density and this enables to solve the Kohn-Sham equations, obtaining the eigenvalues ϵ_i and wavefunctions φ_i. Following this, the updated electron density $\rho_{out}(\mathbf{r})$ is calculated. The termination of the SCF procedure is based on the comparison between the input and updated electron density. Once the difference between these two densities is smaller than a pre-defined convergence criterion, the SCF calculation is stopped and the electron density at current SCF cycle is exported. The calculated electron density together with the wavefunctions obtained from the Kohn-Sham equations can be then used to calculate other properties of interest.
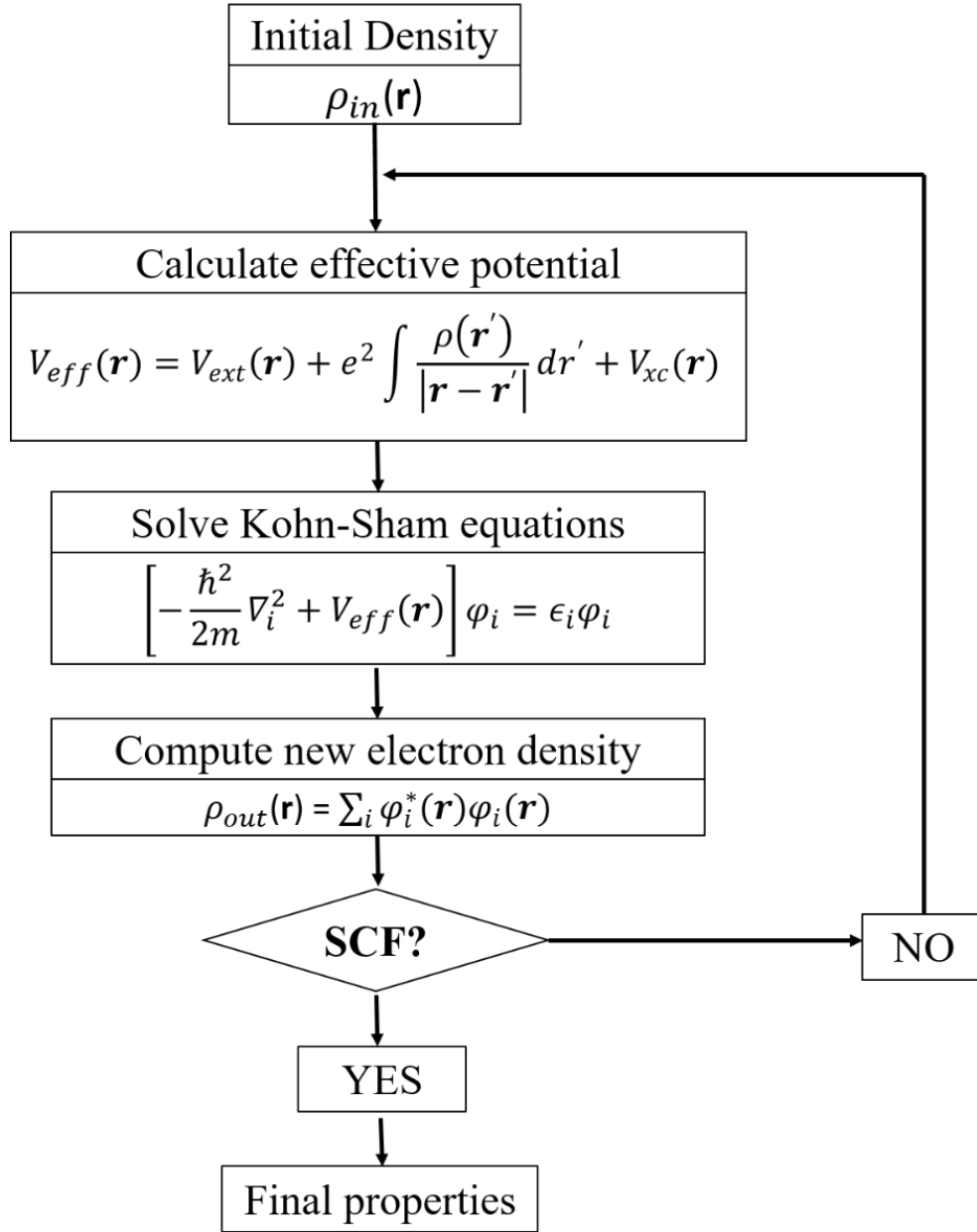
Figure 3. 4 Flow chart of SCF method used for solving the Kohn-Sham equations.

3.2.5. Exchange-correlation functionals

One critical point to solve the Kohn-Sham equations is that the exchange-correlation potential $V_{xc}(r)$ has to be specified. This is not an easy task since, in most cases, the true form of the exchange-correlation potential is actually not known. The only situation where the exchange-correlation potential can be derived explicitly is for the uniform electron gas (UEG) [52]. In that

case, the electron density is constant in space:

$$\rho(\boldsymbol{r}) = constant \tag{3.26}$$

This situation does not seem very useful because the electron density in any real molecule/material is certainly non-uniform. However, the UEG model provides a practical way to solve the Kohn-Sham equations. This is done by setting the exchange-correlation potential at each position to be the known exchange-correlation potential of the UEG with the same electron density observed at that position:

$$V_{xc}(\boldsymbol{r}) = V_{xc}^{UEG}[\rho(\boldsymbol{r})] \tag{3.27}$$

Here, only the local electron density is used to approximate the exchange-correlation functional employed in the Kohn-Sham equations; therefore it is named as the *local density approximation* (LDA). That approximation enables to build Kohn-Sham equations completely and then find a solution to the Schrödinger equation.

The LDA is not the only approximation that has been used to estimate the true form of the exchange-correlation functional. Another representative class of the approximation beyond LDA is the *generalized gradient approximation* (GGA), where information from both the local electron density and the local gradient of the electron density are used. Mathematically, it can be written as:

$$V_{xc}^{GGA}(\boldsymbol{r}) = V_{xc}[\rho(\boldsymbol{r}), \nabla\rho(\boldsymbol{r})] \tag{3.28}$$

Compared with LDA, the formulation of GGA is richer because there exist several ways to include the information from the gradient of the electron density. Two of the most representative GGA functionals are the Perdew-Wang functional (PW91) [53] and the Perdew-Burke-Ernzerhof functional (PBE) [54]. In addition to the GGA functionals in which additional information from the gradient of the electron density is considered, more sophisticated functionals have been developed, using extra physical information related to the electron density, for example, the Meta-GGA [55-57] where the second order derivative of the electron density is also involved.

3.2.6. The nuts and bolts of the DFT

Up to now, we have discussed how DFT simplifies the long-standing problem of solving the Schrödinger equation for a many-electron system. In practice, there are other important concepts that need to be understood to perform the DFT calculations.

3.2.6.1 Basis sets

One important aspect to consider in any DFT calculation is which type of basis set is employed. The basis set is a set of mathematical functions used to represent the electron wavefunctions obtained from the Schrödinger equation. Generally speaking, current DFT simulation packages employ either spatially-localized functions or spatially-extended functions as the basis set, depending on the system of interest being isolated molecules or periodic crystals. For isolated molecules, their wavefunctions or electron densities decay to zero far from the molecule. This makes them very suitable to be described by spatially-localized functions. A schematic example of using spatially-localized functions as the basis set of wavefunctions is shown in Figure 3. 5.
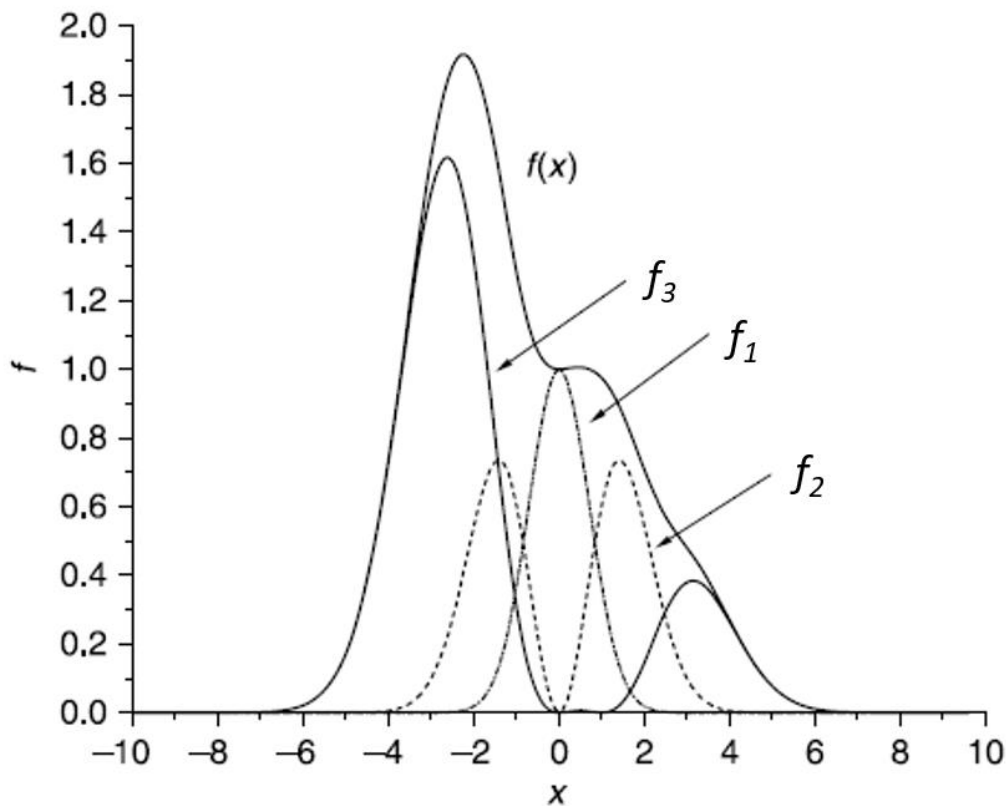
Figure 3. 5 Schematic diagram illustrating the usage of spatially-localized functions as the basis set, adapted from [50].

where $f_1(x) = \exp(-x^2)$

$$f_2(x) = x^2 \exp(-x^2/2)$$

$$f_3(x) = \frac{1}{10} x^2 (1-x)^2 \exp\left(-\frac{x^2}{4}\right)$$

$$f(x) = f_1(x) + f_2(x) + f_3(x)$$

In this example, f_1, f_2, and f_3 are typical spatially-localized functions whose value rapidly approaches zero at large values of $|x|$. The idea behind this example is to show that the overall function $f(x)$ can be defined by a combination of multiple independent functions with different spatial extension, symmetry and other features. Here, we can say that f_1, f_2, and f_3 form a basis set of the overall function $f(x)$. Similarly, the electron wavefunctions in the DFT calculations are also represented by a set of pre-defined functions that constitute the basis set. These electron wavefunctions are then combined to build the wavefunctions of the whole system, *i.e.* the molecule.

It is also possible to define the basis set by a set of spatially-extended functions, which is more suitable and convenient for the study of bulk materials, such as the crystals or surfaces where the wavefunction is periodic and extends infinitely in space. One schematic example to show this idea is depicted in Figure 3.6.
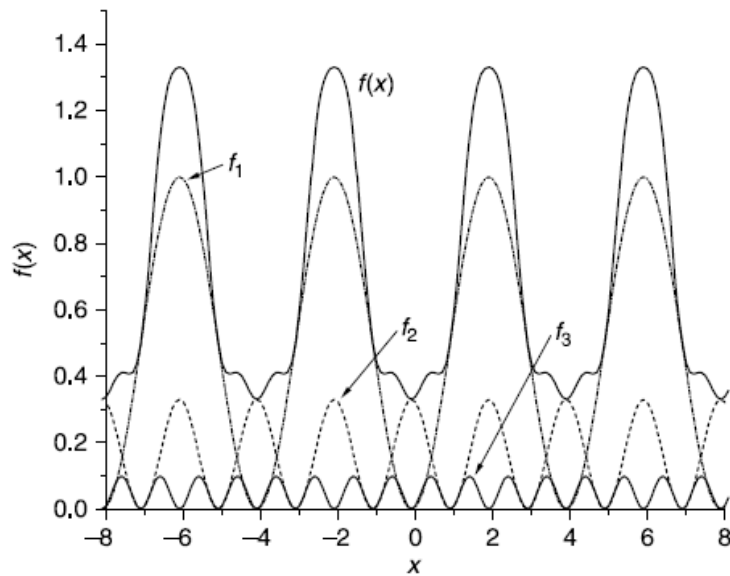
Figure 3. 6 Schematic diagram illustrating the usage of spatially-extended functions as the basis set, adapted from [50].

where $f_1(x) = sin^2(\frac{\pi x}{4})$

$\quad\quad f_2(x) = \frac{1}{3}cos^2(\frac{\pi x}{2})$

$\quad\quad f_3(x) = \frac{1}{10}sin^2(\pi x)$

$\quad\quad f(x) = f_1(x) + f_2(x) + f_3(x)$

The overall function is periodic where:

$$f(x + 4n) = f(x)$$

with n an integer. Again, the overall function $f(x)$ is represented by three basis set functions with different shapes and periodicities.

In both cases, more individual functions can be added to the basis set, which makes the description of the wavefunction as accurate as possible. A larger basis set with more individual functions, however, inevitably increases the computational cost of the DFT calculations. Therefore, it is always more efficient to select a basis set that has a good compromise between the computational cost and accuracy.

3.2.6.2 Pseudopotentials

For atoms with many electrons or large molecules, the DFT calculations require a very large number of basis functions to describe their wavefunctions with good accuracy. This problem is partly solved by introducing pseudopotentials that reduce the number of electrons considered in the calculations. In general, the electrons of atoms are divided into core electrons and valence electrons. The core electrons are closer and strongly bound to the nucleus; therefore they contribute only marginally to the interactions between atoms. In contrast, the valence electrons are responsible for many properties of the system, for example, the breaking and formation of chemical bonds between atoms. The prototype of the pseudopotential, namely the frozen core approximation [58-61], is based on this difference. In this approximation, only the valence electrons are treated explicitly in the calculations while the nucleus and core electrons are frozen and considered as a *pseudo-ion*. This approximation is further extended by the concept of pseudopotential, in which the frozen core is replaced by an effective ionic potential. In this way, the number of electrons that need to be taken into account in the calculations is decreased dramatically, enabling a much more efficient treatment for larger systems.

3.2.7. DFT and STM image simulations

One of the major applications of the DFT calculations in this thesis is to simulate the STM images of molecules adsorbed on graphite and compare them to the experimental data. This enables a more comprehensive understanding of the experimental images and the structural features of the SAMNs. The STM image simulations are performed at the DFT level using the SIESTA software package [62] where a meaningful mapping between the experimental settings (e.g. bias voltage V_{bias}) and the computational parameters is available. More specifically, the simulated STM images are generated based on the Tersoff-Hamann approximation [63]. We have focused on simulating images at negative sample bias (tunneling electrons flow from the substrate/adsorbate to the tip of STM) since the corresponding experimental images are acquired under the same condition. In the Tersoff-Hamann approximation, an explicit computational description is given to the tunneling current I_c, which is the measured quantity in a real STM:

$$I_c = C \int_{E_f+eU}^{E_f} \rho(\boldsymbol{r}, E) dE \tag{3. 29}$$

Here, C is a prefactor depending on the characteristics of the tip, E_f is the Fermi energy of the sample, and $\rho(\boldsymbol{r}, E)$ is the local density of electronic states of energy E. This equation shows that the tunneling current I_c in STM is proportional to the integrated local density of states (iLDOS). An alternative way to write this equation is using the Kohn-Sham individual electron wavefunctions:

$$I_c = C \sum_{i=1}^{n} |\varphi_i(\boldsymbol{r}_0)|^2 \tag{3. 30}$$

where $\varphi_i(\boldsymbol{r}_0)$ is an electron wavefunction with energy ϵ_i at the position of the STM tip $\boldsymbol{r}_0$. The number of wavefunctions involved in the summation, n, is dependent on the condition $\epsilon_i - E_f \leq eV_{bias}$. In this way, by using the Tersoff-Hamann approximation, the experimental bias voltage V_{bias} is directly linked to the eigenvalues of the electron wavefunctions calculated from the DFT simulations and determines the energetic range of the wavefunctions that contribute to the STM images [24]. This demonstrates a way to connect the experimental STM image with the wavefunctions of the substrate-SAMNs supersystem that describe the electronic states of the substrate and molecular adsorbates. It is these features that make STM image simulation a valuable tool to have deeper insights about the structure and electronic properties of SAMNs on substrates.

In this chapter, we reviewed two types of computational-chemistry simulation methodologies that

are employed in the work of this thesis: force field simulations and DFT calculations. Both play a very significant role in understanding the assembly of organic molecules from 2D to 3D from the following perspectives: i) covering aspects that are not accessible by the experimental investigations; ii) providing valuable information that helps us to gain a deep insight about the experimental results and iii) guiding experimental work *a priori* based on the output of the modelling. In the following "result and discussion" chapters of this thesis, we show how these advantages are exploited in studying SAMNs and SIPs of several types of organic molecules.

References

1. Metropolis, N., A.W. Rosenbluth, M.N. Rosenbluth, A.H. Teller, and E. Teller, *Equation of State Calculations by Fast Computing Machines.* The journal of chemical physics, 1953. **21**: p. 1087-1092.

2. Alder, B.J. and T.E. Wainwright, *Phase Transition for a Hard Sphere System.* The Journal of chemical physics, 1957. **27**: p. 1208-1209.

3. González, M., *Force Fields and Molecular Dynamics Simulations.* École thématique de la Société Française de la Neutronique, 2011. **12**: p. 169-200.

4. Phillips, J.C., R. Braun, W. Wang, J. Gumbart, E. Tajkhorshid, E. Villa, C. Chipot, R.D. Skeel, L. Kale, and K. Schulten, *Scalable Molecular Dynamics with Namd.* J. Comput. Chem., 2005. **26**: p. 1781-1802.

5. Thompson, A.P., H.M. Aktulga, R. Berger, D.S. Bolintineanu, W.M. Brown, P.S. Crozier, P.J. in't Veld, A. Kohlmeyer, S.G. Moore, and T.D. Nguyen, *Lammps-a Flexible Simulation Tool for Particle-Based Materials Modeling at the Atomic, Meso, and Continuum Scales.* Comput. Phys. Commun., 2022. **271**: p. 108171.

6. Van Der Spoel, D., E. Lindahl, B. Hess, G. Groenhof, A.E. Mark, and H.J. Berendsen, *Gromacs: Fast, Flexible, and Free.* J. Comput. Chem., 2005. **26**: p. 1701-1718.

7. Case, D.A., T.E. Cheatham III, T. Darden, H. Gohlke, R. Luo, K.M. Merz Jr, A. Onufriev, C. Simmerling, B. Wang, and R.J. Woods, *The Amber Biomolecular Simulation Programs.* J. Comput. Chem., 2005. **26**: p. 1668-1688.

8. Steeno, R., A. Minoia, M.C. Gimenez-Lopez, M.O. Blunt, N.R. Champness, R. Lazzaroni, K.S. Mali, and S. De Feyter, *Molecular Dopant Determines the Structure of a Physisorbed Self-Assembled Molecular Network.* Chem. Commun., 2021. **57**: p. 1454-1457.

9. Bragança, A.M., A. Minoia, R. Steeno, J. Seibel, B.E. Hirsch, L. Verstraete, O. Ivasenko, K. Müllen, K.S. Mali, and R. Lazzaroni, *Detection and Stabilization of a Previously Unknown Two-Dimensional (Pseudo) Polymorph Using Lateral Nanoconfinement.* J. Am. Chem. Soc., 2021. **143**: p. 11080-11087.

10. Steeno, R., A. Minoia, R. Lazzaroni, K.S. Mali, and S. De Feyter, *Host–Guest Chemistry under Confinement: Peeking at Early Self-Assembly Events.* Chem. Commun., 2022. **58**: p. 3138-3141.

11. Martsinovich, N. and A. Troisi, *Modeling the Self-Assembly of Benzenedicarboxylic Acids Using Monte Carlo and Molecular Dynamics Simulations.* The Journal of Physical Chemistry C, 2010. **114**: p. 4376-4388.

12. Minoia, A., Z. Guo, H. Xu, S. George, A.P. Schenning, S. De Feyter, and R.

Lazzaroni, *Assessing the Role of Chirality in the Formation of Rosette-Like Supramolecular Assemblies on Surfaces.* Chem. Commun., 2011. **47**: p. 10924-10926.

13. Minoia, A., I. Destoop, E. Ghijsens, S. De Feyter, K. Tahara, Y. Tobe, and R. Lazzaroni, *Design of Efficient Sergeant Molecules for Chiral Induction in Nano-Porous Supramolecular Assemblies.* RSC Adv., 2015. **5**: p. 6642-6646.

14. Afsharimani, N., A. Minoia, C.d. Volcke, M. Surin, R. Lazzaroni, J.-Y. Balandier, C. Niebel, Y.H. Geerts, and B. Nysten, *Self-Assembly of Alkyl-Substituted Oligothiophenes on Mos2: A Joint Experimental/Theoretical Study.* The Journal of Physical Chemistry C, 2013. **117**: p. 21743-21751.

15. Truger, M., O.M. Roscioni, C. Röthel, D. Kriegner, C. Simbrunner, R. Ahmed, E.D. Głowacki, J. Simbrunner, I. Salzmann, and A.M. Coclite, *Surface-Induced Phase of Tyrian Purple (6, 6'-Dibromoindigo): Thin Film Formation and Stability.* Crystal growth & design, 2016. **16**: p. 3647-3655.

16. Jones, A.O., C. Röthel, R. Lassnig, O. Bedoya-Martínez, P. Christian, I. Salzmann, B. Kunert, A. Winkler, and R. Resel, *Solution of an Elusive Pigment Crystal Structure from a Thin Film: A Combined X-Ray Diffraction and Computational Study.* CrystEngComm, 2017. **19**: p. 1902-1911.

17. Saiev, S., L. Bonnaud, L. Dumas, T. Zhang, P. Dubois, D. Beljonne, and R. Lazzaroni, *Do Carbon Nanotubes Improve the Thermomechanical Properties of Benzoxazine Thermosets?* ACS Appl. Mater. Interfaces, 2018. **10**: p. 26669-26677.

18. Hoyas, S., V. Lemaur, Q. Duez, F. Saintmont, E. Halin, J. De Winter, P. Gerbaux, and J. Cornil, *Pepdroid: Development of a Generic Dreiding-Based Force Field for the Assessment of Peptoid Secondary Structures.* Advanced Theory and Simulations, 2018. **1**: p. 1800089.

19. Shao, C., Y. Jin, K. Pipe, M. Shtein, and J. Kieffer, *Simulation of Crystalline and Amorphous Copper Phthalocyanine: Force Field Development and Analysis of Thermal Transport Mechanisms.* The Journal of Physical Chemistry C, 2014. **118**: p. 9861-9870.

20. Kaledin, A.L., A.C. Van Duin, C.L. Hill, and D.G. Musaev, *Parameterization of Reactive Force Field: Dynamics of the [Nb6o19h X](8–X)–Lindqvist Polyoxoanion in Bulk Water.* The Journal of Physical Chemistry A, 2013. **117**: p. 6967-6974.

21. Huang, L. and B. Roux, *Automated Force Field Parameterization for Nonpolarizable and Polarizable Atomic Models Based on Ab Initio Target Data.* J. Chem. Theory Comput., 2013. **9**: p. 3543-3556.

22. Reynaerts, R., A. Minoia, S.M. Gali, L. Daukiya, N. Van Velthoven, D. De Vos, R. Lazzaroni, K.S. Mali, and S. De Feyter, *Coplanar Versus Noncoplanar Carboxyl Groups: The Influence of Sterically Enforced*

Noncoplanarity on the 2d Mixing Behavior of Benzene Tricarboxylic Acids. J. Phys. Chem. C, 2020. **124**: p. 24874-24882.

23.   Bouatou, M., R. Harsh, F. Joucken, C. Chacon, V. Repain, A. Bellec, Y. Girard, S. Rousset, R. Sporken, and F. Gao, *Intraconfigurational Transition Due to Surface-Induced Symmetry Breaking in Noncovalently Bonded Molecules.* The Journal of Physical Chemistry Letters, 2020. **11**: p. 9329-9335.

24.   Sanz-Matías, A., O. Ivasenko, Y. Fang, S. De Feyter, K. Tahara, Y. Tobe, and J.N. Harvey, *Computational Insight into the Origin of Unexpected Contrast in Chiral Markers as Revealed by Stm.* Nanoscale, 2018. **10**: p. 1680-1694.

25.   Jarvinen, P., S.K. Hamalainen, M. Ijas, A. Harju, and P. Liljeroth, *Self-Assembly and Orbital Imaging of Metal Phthalocyanines on a Graphene Model Surface.* The Journal of Physical Chemistry C, 2014. **118**: p. 13320-13325.

26.   *Biovia, Dassault Systèmes, Biovia Materials Studio, 2018, San Diego: Dassault Systèmes, 2018.*

27.   Brooks, B.R., C.L. Brooks III, A.D. Mackerell Jr, L. Nilsson, R.J. Petrella, B. Roux, Y. Won, G. Archontis, C. Bartels, and S. Boresch, *Charmm: The Biomolecular Simulation Program.* J. Comput. Chem., 2009. **30**: p. 1545-1614.

28.   Sun, H., S.J. Mumby, J.R. Maple, and A.T. Hagler, *An Ab Initio Cff93 All-Atom Force Field for Polycarbonates.* J. Am. Chem. Soc., 1994. **116**: p. 2978-2987.

29.   Sun, H., *Compass: An Ab Initio Force-Field Optimized for Condensed-Phase Applications Overview with Details on Alkane and Benzene Compounds.* The Journal of Physical Chemistry B, 1998. **102**: p. 7338-7364.

30.   Mayo, S.L., B.D. Olafson, and W.A. Goddard, *Dreiding: A Generic Force Field for Molecular Simulations.* J. Phys. Chem., 1990. **94**: p. 8897-8909.

31.   Casewit, C., K. Colwell, and A. Rappe, *Application of a Universal Force Field to Organic Molecules.* J. Am. Chem. Soc., 1992. **114**: p. 10035-10046.

32.   Svard, M. and Å.C. Rasmuson, *Force Fields and Point Charges for Crystal Structure Modeling.* Ind. Eng. Chem. Res., 2009. **48**: p. 2899-2912.

33.   Panina, N., F. Leusen, F. Janssen, P. Verwer, H. Meekes, E. Vlieg, and G. Deroover, *Crystal Structure Prediction of Organic Pigments: Quinacridone as an Example.* J. Appl. Crystallogr., 2007. **40**: p. 105-114.

34.   Guo, Z., I. De Cat, B. Van Averbeke, J. Lin, G. Wang, H. Xu, R. Lazzaroni, D. Beljonne, A.P. Schenning, and S. De Feyter, *Affecting Surface Chirality Via Multicomponent Adsorption of Chiral and Achiral Molecules.* Chem. Commun., 2014. **50**: p. 11903-11906.

35.   Abdel-Mottaleb, M.M., E. Gomar-Nadal, M. Surin, H. Uji-i, W. Mamdouh, J.

Veciana, V. Lemaur, C. Rovira, J. Cornil, and R. Lazzaroni, *Self-Assembly of Tetrathiafulvalene Derivatives at a Liquid/Solid Interface—Compositional and Constitutional Influence on Supramolecular Ordering.* J. Mater. Chem., 2005. **15**: p. 4601-4615.

36. Leclere, P., M. Surin, P. Viville, R. Lazzaroni, A. Kilbinger, O. Henze, W. Feast, M. Cavallini, F. Biscarini, and A. Schenning, *About Oligothiophene Self-Assembly: From Aggregation in Solution to Solid-State Nanostructures.* Chem. Mater., 2004. **16**: p. 4452-4466.

37. Jones, J.E., *On the Determination of Molecular Fields.—Ii. From the Equation of State of a Gas.* Proceedings of the Royal Society of London. Series A, Containing Papers of a Mathematical and Physical Character, 1924. **106**: p. 463-477.

38. Campañá, C., B. Mussard, and T.K. Woo, *Electrostatic Potential Derived Atomic Charges for Periodic Systems Using a Modified Error Functional.* J. Chem. Theory Comput., 2009. **5**: p. 2866-2878.

39. Dupradeau, F.-Y., A. Pigache, T. Zaffran, C. Savineau, R. Lelong, N. Grivel, D. Lelong, W. Rosanski, and P. Cieplak, *The Red. Tools: Advances in Resp and Esp Charge Derivation and Force Field Library Building.* Phys. Chem. Chem. Phys., 2010. **12**: p. 7821-7839.

40. Joseph, S. and N. Aluru, *Hierarchical Multiscale Simulation of Electrokinetic Transport in Silica Nanochannels at the Point of Zero Charge.* Langmuir, 2006. **22**: p. 9041-9051.

41. Karasawa, N. and W.A. Goddard III, *Force Fields, Structures, and Properties of Poly (Vinylidene Fluoride) Crystals.* Macromolecules, 2002. **25**: p. 7268-7281.

42. Verlet, L., *Computer" Experiments" on Classical Fluids. I. Thermodynamical Properties of Lennard-Jones Molecules.* Phys. Rev., 1967. **159**: p. 98.

43. Samoletov, A.A., C.P. Dettmann, and M.A. Chaplain, *Thermostats for "Slow" Configurational Modes.* J. Stat. Phys., 2007. **128**: p. 1321-1336.

44. Parrinello, M. and A. Rahman, *Polymorphic Transitions in Alkali Halides, a Molecular Dynamics Study.* Le Journal De Physique Colloques, 1981. **42**: p. C6-511-C516-515.

45. Parrinello, M. and A. Rahman, *Strain Fluctuations and Elastic Constants.* The Journal of Chemical Physics, 1982. **76**: p. 2662-2666.

46. Andersen, H.C., *Molecular Dynamics Simulations at Constant Pressure and/or Temperature.* The Journal of chemical physics, 1980. **72**: p. 2384-2393.

47. Berendsen, H.J., J.v. Postma, W.F. Van Gunsteren, A. DiNola, and J.R. Haak, *Molecular Dynamics with Coupling to an External Bath.* The Journal of chemical physics, 1984. **81**: p. 3684-3690.

48. Rapaport, D., *The Art of Molecular Dynamics Simulation (Cambridge Univ. Press, Cambridge.* 2004.

49. Born, M. and R. Oppenheimer, *Zur Quantentheorie Der Molekeln.* Annalen der physik, 1927. **389**: p. 457-484.

50. Sholl, D.S. and J.A. Steckel, *Density Functional Theory: A Practical Introduction*. 2011: John Wiley & Sons.

51. Hohenberg, P. and W. Kohn, *Inhomogeneous Electron Gas.* Phys. Rev., 1964. **136**: p. B864.

52. Kohn, W. and L.J. Sham, *Self-Consistent Equations Including Exchange and Correlation Effects.* Phys. Rev., 1965. **140**: p. A1133.

53. Perdew, J.P., P. Ziesche, and H. Eschrig, *Electronic Structure of Solids' 91*. 1991, Akademie Verlag, Berlin.

54. Perdew, J.P., K. Burke, and M. Ernzerhof, *Generalized Gradient Approximation Made Simple.* Phys. Rev. Lett., 1996. **77**: p. 3865.

55. Kurth, S., J.P. Perdew, and P. Blaha, *Molecular and Solid-State Tests of Density Functional Approximations: Lsd, Ggas, and Meta-Ggas.* Int. J. Quantum Chem, 1999. **75**: p. 889-909.

56. Van Voorhis, T. and G.E. Scuseria, *A Novel Form for the Exchange-Correlation Energy Functional.* The Journal of chemical physics, 1998. **109**: p. 400-410.

57. Tao, J., J.P. Perdew, V.N. Staroverov, and G.E. Scuseria, *Climbing the Density Functional Ladder: Nonempirical Meta–Generalized Gradient Approximation Designed for Molecules and Solids.* Phys. Rev. Lett., 2003. **91**: p. 146401.

58. Baerends, E., D. Ellis, and P. Ros, *Self-Consistent Molecular Hartree—Fock—Slater Calculations I. The Computational Procedure.* Chem. Phys., 1973. **2**: p. 41-51.

59. Sachs, E.S., J. Hinze, and N.H. Sabelli, *Frozen Core Approximation, a Pseudopotential Method Tested on Six States of Nah.* The Journal of Chemical Physics, 1975. **62**: p. 3393-3398.

60. Matsuoka, O., *A Frozen-Core Approximation Using Reduced Core-Basis Functions.* The Journal of chemical physics, 1992. **96**: p. 6773-6777.

61. Pettersson, L. and U. Wahlgren, *An Investigation of Basis Sets and Basis Set Superposition Error in Transition Metals Using Frozen Core and Frozen Orbital Techniques.* Chem. Phys., 1982. **69**: p. 185-192.

62. Soler, J.M., E. Artacho, J.D. Gale, A. García, J. Junquera, P. Ordejón, and D. Sánchez-Portal, *The Siesta Method for Ab Initio Order-N Materials Simulation.* J. Phys.: Condens. Matter, 2002. **14**: p. 2745.

63. Tersoff, J. and D.R. Hamann, *Theory of the Scanning Tunneling Microscope.* Phys. Rev. B, 1985. **31**: p. 805.

Chapter 4

Unravelling the nature of peculiar molecular self-assemblies at the solid/liquid interface: A theoretical study on an alkylated tetrathiafulvalene derivative

As discussed in Chapter 2, the study of SAMNs of organic molecules on surfaces has flourished over the past decades and it is considered as one of the most important aspects of the supramolecular chemistry. In this chapter, we go beyond the traditional SAMNs which contain only a single layer of molecules adsorbed on surfaces. We investigate the multilayer self-assembly for a selected derivative of tetrathiafulvalene (TTF): tetrakis-octadecylthio-tetrathiafulvalene (TTF-(SC$_{18}$)$_4$, TODT-TTF, see Figure 4. 1) with a joint STM/molecular modeling approach. This molecule is an important building block for OSCs. The chapter begins with a general introduction over the TTF molecules and its derivatives. Following that is the description for the STM images of TODT-TTF self-assemblies, which shows many peculiar features. The rest of this chapter focuses on the modeling work we have performed in order to understand the self-assembly behaviors of the TODT-TTF molecule. Here, besides the fundamental interest of understanding the self-assembly of TTF derivatives, this study is also a steppingstone to move from SAMNs (2D crystallization) towards SIPs (thin film crystallization in 3D), which will be described in chapter 5.
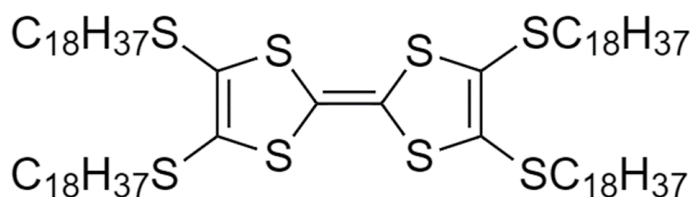
Figure 4. 1 Molecular structure of TODT-TTF

4.1. Tetrathiafulvalene derivatives: from self-assembled molecular networks to multilayer structures

As of the first synthesis in 1970s [1], the TTF molecule and its abundant derivatives (TTFs) have been studied extensively and considered as very attractive materials for molecular electronics [2-5]. For this reason, TTFs are active components in different applications, including the synthesis of metal-organic frameworks with improved catalytic properties [6] and the preparation of charge transfer complexes or superconducting salts [7-9]. Nowadays, TTFs are often synthesized in the form of crystalline thin films with a thickness ranging from the thinnest SAMNs to tens-of-nanometers, which are then incorporated in semi-conducting devices as active layers [10-14]. It is essential to understand and control the molecular packing of TTFs in the thin films because of its close relation with many key properties of the materials (e.g. charge mobility) that determine the

performance of the semi-conducting devices.

Many STM studies have been carried out on SAMNs of TTFs in order to determine their molecular-scale structures [9, 15-17]. The self-assembly behavior of TTFs is found to be governed by many factors, for example, the preparation methods (evaporation in UHV or deposition from solution in ambient conditions) [18], the type of solvents in case molecules self-assemble at the solution/substrate interfaces [19] and the type of functional groups on the TTF core [20]. A key motivation to study the self-assembly process of TTFs is that the molecular packing/crystal structure in the grown thin films can be potentially templated by the SAMNs, opening new opportunities in controlling the crystal structure of the thin films. Such correlation has been claimed by Fu et al., but only inferred from a simple structure comparison [21]. In practice, it remains challenging to understand the correlation between the SAMNs and thin films. A good starting point for this purpose is to investigate the multilayer molecular self-assemblies on surfaces, which can be considered as a bridging stage between the SAMNs and the thin films (and potentially the SIPs). The study on such multilayer self-assemblies can contribute to a better understanding over the 2D to 3D crystallization of the organic molecules.

Structural characterization of multilayer assemblies is however not straightforward. Both STM and X-ray diffraction techniques (working principles discussed in chapter 2) have their own bottlenecks. In STM, the scanning probe is normally only a few Angstroms from the surface. Therefore, it can easily disturb or even destroy the assembled multilayers. In addition, the contrast of STM images for multilayer assemblies is more complicated, hindering a straightforward interpretation of the recorded images. Despite these impediments, efforts were still made to understand the self-assembly behavior of organic molecules beyond the monolayers using STM. Several studies focused on the formation of bi-layer assemblies using host-guest chemistry [22-24]. Others have investigated the dependence of multi-layer assembly structures on the solution concentration [25], external electric field [23] and foreign molecules [26]. Nevertheless, all these studies suffer from poor STM image resolution due to the fragility of the self-assembled multilayers under the STM tip, making it difficult to understand the molecular adsorption conformations and organizations within the assembly. In parallel, thin film X-ray diffraction techniques face other challenges. For instance, due to the limited amount of material, the signal intensity collected in X-ray diffraction measurements can decrease significantly. This makes it difficult to determine the structure of multilayer self-assemblies by thin film X-ray diffraction. In

order to bridge this gap regarding the structural characterization of multilayer self-assemblies, we have chosen TODT-TTF as an example to study its self-assembly behavior for both monolayer and bi-layer. Self-assembled monolayers and bi-layers of TODT-TTF were prepared at the solution/HOPG interface. Then, *in-situ* STM was employed to probe the molecular organization within these assemblies. Images with sub-molecular level resolution were successfully acquired for both the monolayer and bi-layer assemblies. Combined with DFT and force field calculations, a comprehensive understanding of the molecular adsorption conformation and molecular packing of these assemblies is obtained. In this way, we gain an integrated view over the assembly behavior of TODT-TTF at the solution/HOPG interface. Despite the fact that structural features are only revealed up to the bi-layer assembly, this is already a step further to unravel the crystallization of organic molecules on surfaces from 2D to 3D and to understand the formation of SIPs. More importantly, our work proves the possibility of studying multilayer self-assembly using STM, which overcomes the traditional limitations in the STM community and paves a way to study more complicated assembly behavior of organic molecules on surfaces.

4.2. Experimental STM measurements on TODT-TTF layers

Figure 4. 2 shows the highly ordered self-assemblies of TODT-TTF that form at the 1-phenyloctane(1-PO)/HOPG interface (self-assemblies prepared by Catarina Delfino from KU Leuven, see Appendix 4.1 for more experimental details). These assemblies contain defect-free domains that extend over several hundred squared nanometers. Some peculiar features can be seen directly from these STM images:

- 1) Three different types of objects are observed: (i) single or (ii) double-blob objects in the monolayer assembly and (iii) uniform rectangular-shaped objects in the bi-layer assembly;
- 2) The long-range arrangement of molecules differs between the monolayer and bi-layer assembly, which is evidenced by their rather different lattice parameters. For the monolayer assembly, the lattice parameters are: a=22±2Å, b=38±2Å and α=73±4° while the lattice parameters of the bi-layer assembly are: a=19±1Å, b=29±1Å and α=75±5°.

As discussed in chapter 2, the contrast of STM images is directly related to the adsorption conformation of the molecules on the surfaces. It is therefore hypothesized that the TODT-TTF molecules display different conformations in the monolayer/bi-layer assembly, which can then lead to different packing motifs. These intriguing features clearly show the complexity of

the molecular self-assembly process on the surfaces and the interest of studying this process in order to understand the packing behavior of molecules and the origins of SIPs.
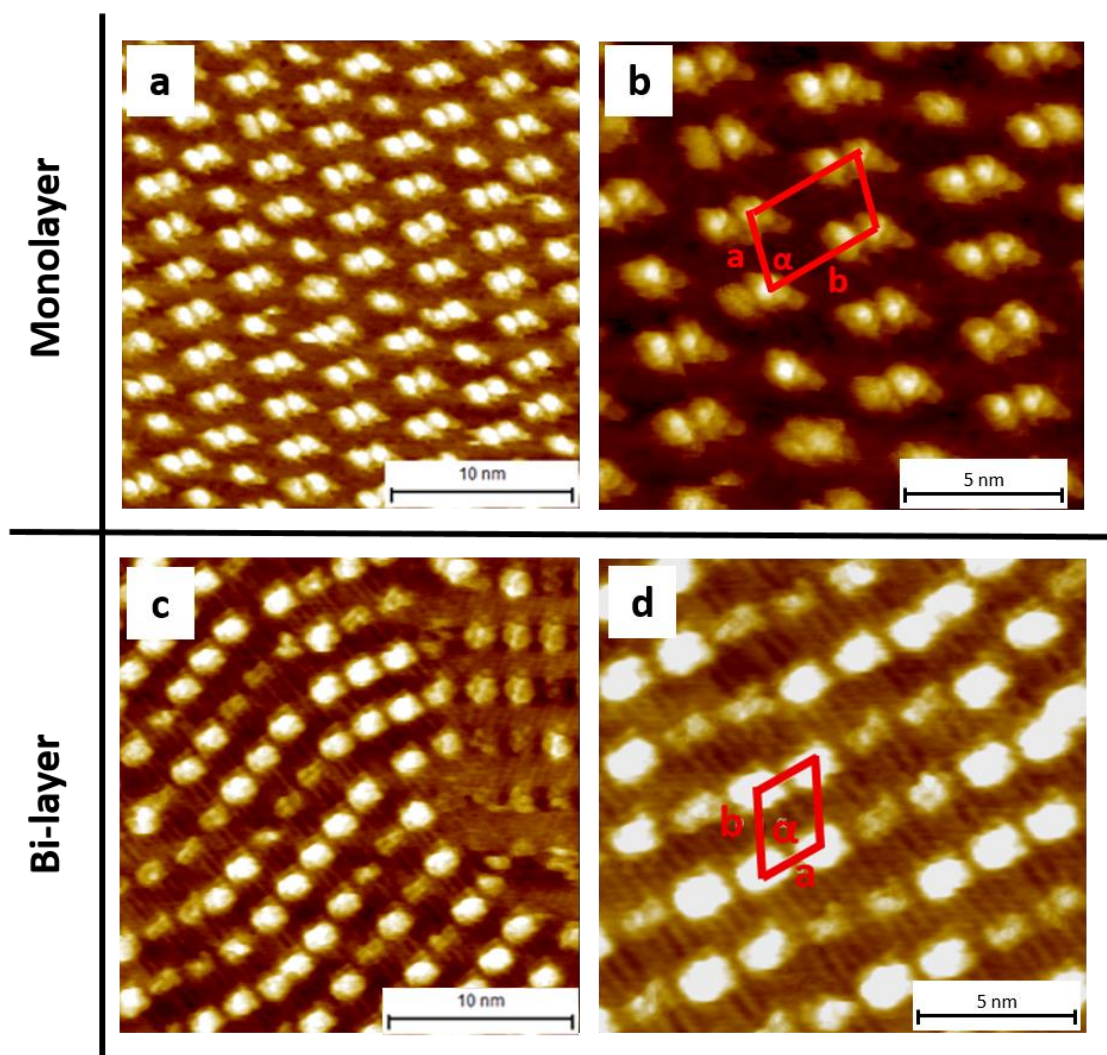
Figure 4. 2 STM images of TODT-TTF monolayer (a, b) and bi-layer (c, d) self-assembly at the 1-PO/HOPG interface. The unit cells are overlaid on the STM images. Imaging parameters: Iset = 0.05 nA − 0.09 nA, Vbias = -0.9V. Images obtained by Catarina Delfino from KU Leuven.

4.3. Force field optimization for the TODT-TTF molecule

In order to better understand the origin of different features observed in the monolayer/bi-layer assemblies and determine the adsorption conformation of TODT-TTF on the HOPG substrate, elaborate molecular modelling studies are performed, including force field calculations and STM image simulations on the basis of the DFT formalism. On the one hand, force field simulations allow a comparison of the energetic stabilities of different adsorption conformations. It also

enables us to investigate the packing motifs of the molecules by modelling the self-assembly directly, which is too time-consuming for the DFT calculations. On the other hand, the simulated STM images can be directly compared to their experimental counterparts, bringing us extra indications for the molecular adsorption conformations. As discussed in section 3.1, the reliability of force field simulations relies completely on the parameters used to describe the intra- and intermolecular interactions. In this section, we discuss how a suitable force field is selected and adjusted for the TODT-TTF.

In previous studies, F. Gao [27] and L. Wang [28] have reported that the simplest alkylated thiol-TTF molecule, tetrakis-methylthio-tetrathiafulvalene (TMT-TTF), shows a non-planar geometry with a boat-like shape. This has been verified in our own DFT calculations (See Figure 4. 3). Since the length of alkyl side chains is not expected to affect the geometry of the TTF core, the TODT-TTF molecule that is used in our experiments should keep the same boat-like shape.
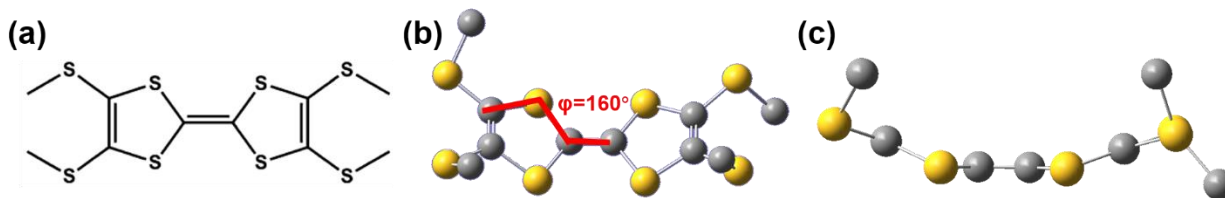
Figure 4. 3 (a) Molecular structure of TMT-TTF. (b, c) Top and side view of the DFT-optimized TMT-TTF molecule, with the non-planarity represented by the torsion angle φ. In total, there are four equivalent torsion angles across the TTF core. Only one is shown here for better visual clarity. DFT calculations performed with the Gaussian 16 package, using B3LYP exchange-correlation functional and the 6-31+G(d) basis set.

As a comparison, the geometry of TMT-TTF was also optimized by different force fields implemented in the BIOVIA Materials Studio software package. However, all of them predict the molecule to be completely planar. Such disagreement means that the force fields have to be modified before being used in the simulations of any alkylated thiol-TTF molecules. In this case, it is difficult to modify specific force field parameters directly to reproduce the correct molecular geometry since the non-planarity of TODT-TTF is not controlled by any individual potential. Instead, it is a result of several highly-coupled bending and torsion potentials across the TTF core (see the definition of force field potentials in section 3.1.1). Because of this situation, an alternative modification is used in all of the force field simulations: an additional restraint potential is applied on the torsion angle φ and its three equivalents. These restraints are harmonic potentials with the equilibrium angle at $\varphi_0 = 160°$ (value from the DFT-optimized structure) and a force constant of

$k_0 = 25$ kcal/mol/°. The functional form of these harmonic restraints are:

$$E_{restraint} = \frac{k_0}{2}(\varphi - \varphi_0)^2$$

In this way, an energy penalty is applied when the molecule planarizes and the molecular core is forced to preserve the boat-like shape as it is revealed by the DFT optimizations. However, it must be noted that using harmonic restraints on these torsions is only an empirical way to reproduce the correct molecular geometry. For this reason, more tests were performed to guarantee a suitable stiffness of these restraints.

These tests were done by modelling the adsorption of TMT-TTF on the HOPG substrate using the Universal force field [29, 30] with the above-mentioned harmonic restraint applied. This force field has been used to model a variety of TTFs in a previous study [20]. The alkylated thiol-TTFs with longer alkyl chains, e.g. the TODT-TTF studied in our experiments, are not used in these tests since we want to avoid any disturbances from the long alkyl chains on the adsorption conformations. In other words, before moving to more complex situations, it needs to be ensured that the core stiffness of the alkylated thiol-TTF can be correctly described by the force field. The comparison of the adsorption geometries is summarized in Figure 4. 4. Again, we use DFT-optimized structure as a reference for our force field simulations.
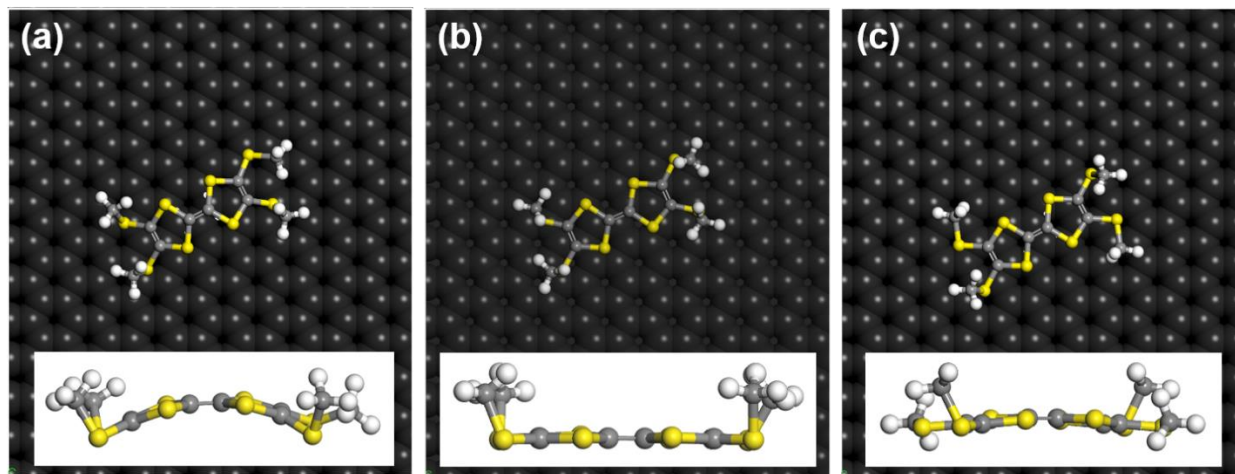
Figure 4. 4 Adsorption of TMT-TTF on the HOPG substrate: (a) Input structure. (b) DFT-optimized structure and (c) Force field optimized structure. DFT optimizations performed with the SIESTA software package. Atomic charges of TMT-TTF used in the force field simulations are adapted from the ESP charges calculated at the DFT level (Gaussian 16, B3LYP functional and the 6-31+G(d) basis set). HOPG substrate is shown underneath the adsorbed molecule.

Here, only the "core-up" ('capsized boat') conformation (see Figure 4. 4 (a)) is optimized since it

provides the best way to assess the rigidity of the restrained molecules. With the DFT formalism, the molecule readily gets planar when interacting with the HOPG surface (Figure 4. 4 (b)); this is also the case when the optimization is performed with the modified force field (Figure 4. 4 (c)). This comparison shows that, with a force constant of 25 kcal/mol/°, the planarization of the adsorbed TMT-TTF observed in the DFT-optimized structure is successfully reproduced by the force field simulations, confirming the reliable description of the molecular adsorption geometry by the modified force field. Stiffer restraints with higher force constant k_0 were also tested. However, the planarization of the adsorbed molecule is very limited in those cases, which indicates that too stiff restraints have been applied. Based on these results, the harmonic restraint described above ($\varphi_0 = 160°$, $k_0 = 25$ kcal/mol/°) is employed in all the following force field simulations where the Universal force field is used.

4.4 Modelling the adsorption conformation of TODT-TTF and STM image simulations

Our modelling studies start from the bi-layer assembly of TODT-TTF since it has very comparable lattice parameters and contrast to the STM data collected before [20]. STM images recorded in our experiments show uniform rectangular-shaped bright objects with periodic lamella strips perpendicular to them (see Figure 4. 2 (c, d)). Based on the previous study [20], it is hypothesized that the uniform rectangular-shaped object is from the core of the TODT-TTF while the periodic strips are attributed to the interdigitated alkyl chains perpendicular to the core. Figure 4. 5 (a) shows the adsorption of TODT-TTF on the HOPG substrate in this manner. After optimization, the core of the molecule clearly goes through planarization (see inset at the top-right corner of Figure 4. 5 (d)), which agrees with the structural model proposed before [20]. This geometry is then referred as the 'core-flat' conformation in the following text because of the planarized core. The simulated STM image for this 'core-flat' conformation is shown as another inset of Figure 4. 5 (d), enabling a more direct comparison to the experimental image. The core of TODT-TTF in the simulated STM image appears as a uniform rectangular-shaped object, which closely resembles

the experimental STM images of the bi-layer assembly.

Nevertheless, the STM data collected for the monolayer assembly of TODT-TTF (Figure 4. 2 (a, b)) look completely different. There, the STM images show a mixture of single and double-blob features. Such difference from the bi-layer assembly suggests the existence of different molecular adsorption conformations in the monolayer assembly. Due to the boat-like molecular core, there are two other possible ways for TODT-TTF molecules to be adsorbed on the surfaces, namely 'core-down' (sailing boat) and 'core-up' (capsized boat). These two conformations are shown in Figure 4. 5 (b) and (c), respectively. In this case, the long alkyl chains of TODT-TTF are expected to be paired into two groups. The arguments for this arrangement are:

-The interdigitated alkyl chains resolved in the STM images of the bi-layer assembly do not appear in the monolayer assembly (see Figure 4. 2), indicating the organization of alkyl chains is different.

- The unitcell of the monolayer assembly is larger than that of the bi-layer assembly. The long alkyl chains are therefore not supposed to desorb from the substrate since a denser assembly with smaller lattice parameters would be expected if desorption took place.

Taking these arguments into consideration, alkyl chain pairing is presumed as a reasonable organization for the alkyl chains adsorbed on the substrate. This hypothesis is further ascertained below by modelling the monolayer assembly of TODT-TTF.

Input structure | **Optimized structure**

(a) (d)

(b) (e)

(c) (f)
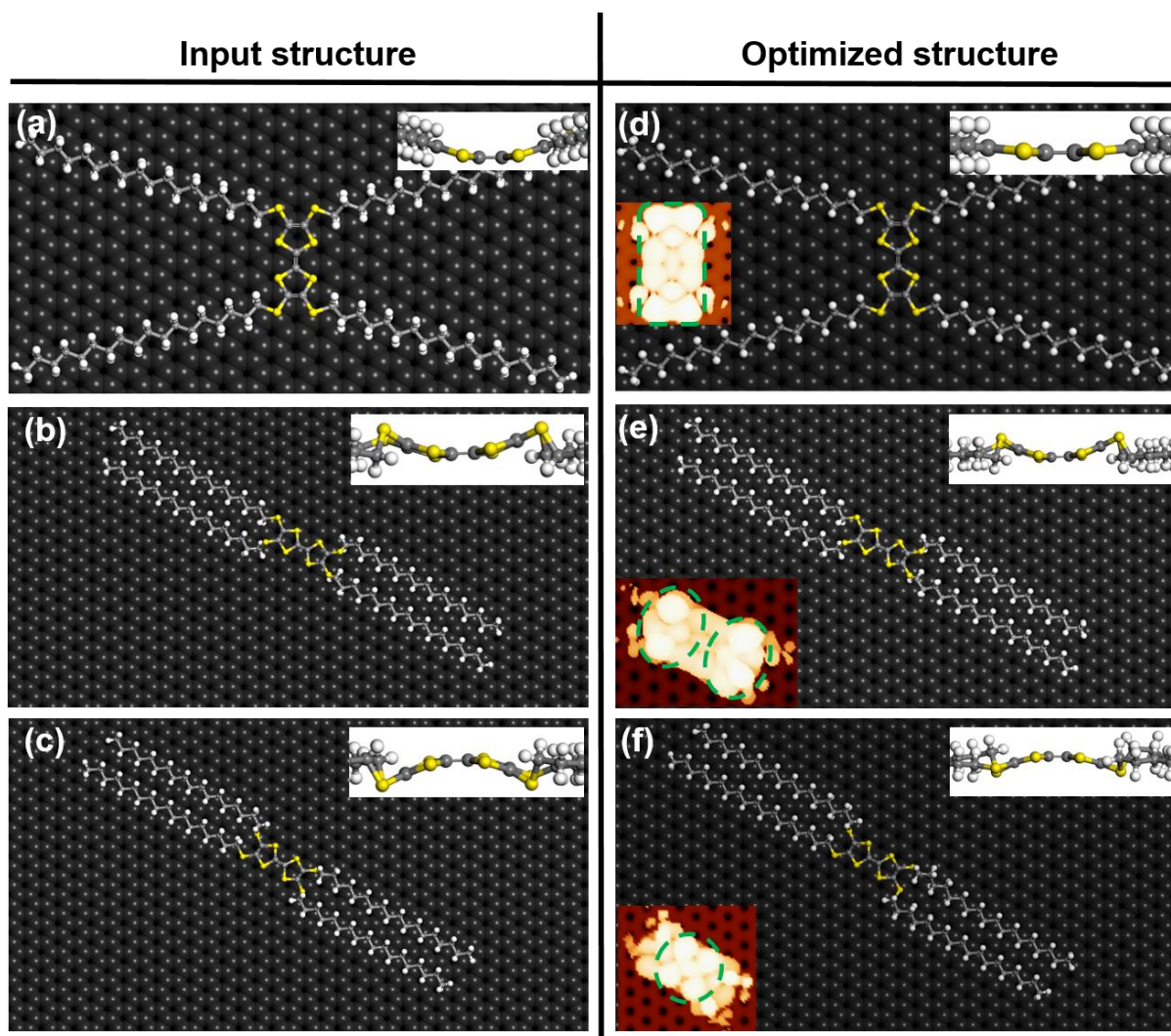
Figure 4. 5 Input and force field optimized structures for the core-flat (a,d), core-down (b,e) and core-up (c,f) conformation of TODT-TTF. Insets in the top-right corner are the side views of the molecular core in order to better distinguish different adsorption conformations. Simulated STM images for each conformation are shown as an inset in panels d, e and f. When simulating STM imags, the alkyl chains of the adsorbed TTF-$(SC_{18})_4$ molecule are chopped to six carbon atoms in order to reduce the computational cost. HOPG substrate is also shown underneath the adsorbed molecule.

Figure 4. 5 (e) and (f) show the corresponding force field optimized structure for the core-down and core-up conformation, where the boat-like core of the TODT-TTF are preserved in both conformations (see the inset at the top-right corner of Figure 4. 5 (e) and (f)). STM images were then simulated for these two conformations based on their optimized structures. For the core-down conformation, the simulated STM image shows an overall bright rectangular-shaped object corresponding to the core of the molecule. However, unlike the core-flat conformation where the contrast is almost uniform, stronger responses are present at the two ends of the rectangle

83

(highlighted by green-dash circles), corresponding to the protruding sulfur atoms at the edge of the molecular core in the core-down conformation. The appearance of this simulated STM image could then be correlated to the double-blob features in the experimental monolayer assembly. On the contrary, the simulated STM image for the core-up conformation shows different characteristics, with a stronger response at the center of the molecule (shown by the green-dashed circle in the inset of Figure 4. 5 (f)). This is explained by the adsorption geometry of the core-up conformation where the most central part of the molecular core stays at a higher elevation above the substrate. Such contrast could then be related to the single-blob objects observed in the experimental monolayer assemblies. However, it has to be noted that, compared with experimental STM images, the single/double-blob features are less pronounced in their simulated counterparts. A similar discrepancy between the local contrast in experimental/simulated STM images was also reported in a previous study [31]. A possible reason for this is that the response of the tip in the experimental constant-current mode of STM is simply represented by the cross-sections of the integrated local DOS in the simulations. Moreover, the electronic field generated between the STM tip and the surface resulting from the applied bias voltage, is not considered in the STM image simulations. In spite of these limitations, the most typical features in the experimental STM images are successfully reproduced by our simulations, which indicates a proper correspondence between the diverse objects (single/double-blob and uniform rectangle) observed in the experiments and three different adsorption conformations of the TODT-TTF molecule.

Another interesting feature of the experimental monolayer assembly is that the double-blob objects are much more frequent than the single-blob ones. These two types of features have been determined to originate from the TODT-TTF adsorbed either in the core-down (double-blob) or in the core-up (single-blob) conformation. The difference in their population at the surface can be explained by the difference in the energetic stability between them. For the force field-optimized structures (see Figure 4. 5 (e, f)), the potential energy for the core-down conformation is -141.8 kcal/mol, while it is only -125.3 kcal/mol for the core-up conformation, meaning that the former one is more energetically preferable, consistent with the higher frequency of the double-blob objects in the experimental monolayer assembly. Meanwhile, the optimized core-flat conformation (see Figure 4. 5 (d)) shows an intermediate stability with a potential energy of -136.0 kcal/mol. We believe that the core-down conformation gains such superior stability from the interactions involving the long paired alkyl chains. One may argue that the core-up conformation is the least

stable one although the alkyl chains are also paired there. This can be explained by the weaker vdW interactions of the alkyl chains with the substrate due to the less-ordered adsorption geometry: first, the core of the TODT-TTF does not adsorb in a favorable way on the substrate. There exists a stronger competition between the tendency to planarize the molecular core and to preserve the original boat-like shape. Second, the arrangement of the alkyl chains near the core of the molecule is also less ordered in the core-up adsorption compared with the other two conformations.

A final aspect, demonstrated from the experimental data and the molecular modeling, is that the arrangement of the alkyl chains plays a crucial role in determining the adsorption conformation of the TODT-TTF on the substrate. The core-flat conformation is only stable when the alkyl side chains are perpendicular to the molecular core, while the core-down and core-up conformations are preferred once the alkyl chains are paired. To validate this argument, the adsorption behavior of alkylated thiol-TTFs with shorter alkyl chains (TTF-$(SC_3)_4$) was studied in our force field simulations using the same settings as the TODT-TTF. Figure 4. 6 shows the optimized geometries of TTF-$(SC_3)_4$ when adsorbed on the HOPG substrate in core-flat, core-down and core-up conformation. Their input structures have the same geometry as the adsorption of TODT-TTF except that the alkyl side chains become shorter.
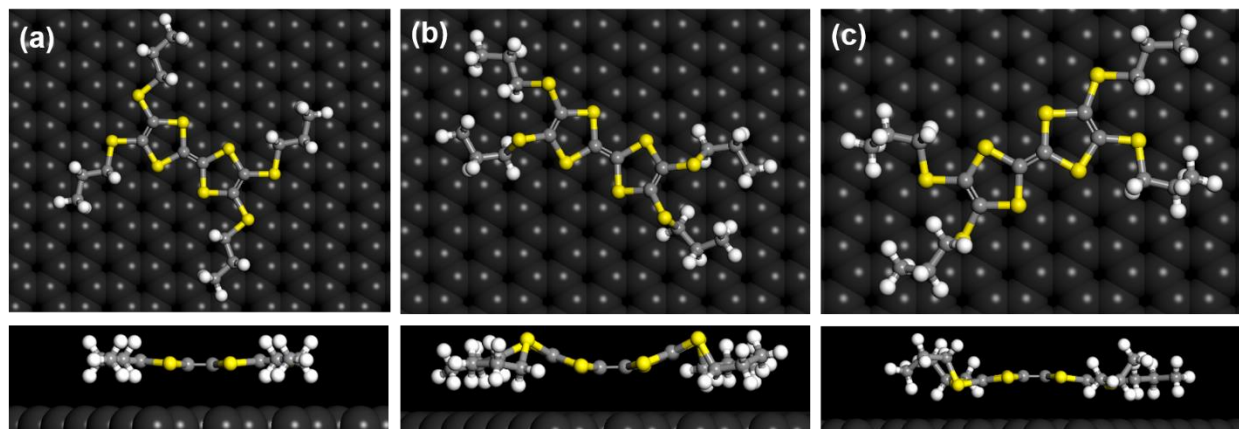
Figure 4. 6 Force field-optimized structures for the adsorption of TTF-$(SC_3)_4$ on the HOPG substrate in core-flat (a), core-down (b) and core-up (c) conformation. HOPG substrate is shown underneath the adsorbed molecule.

Here, the core-flat conformation shows the best energetic stability rather than the core-down conformation, as it is for TODT-TTF. The potential energy of the core-down and core-up

conformations is 24.3 kcal/mol and 27.4 kcal/mol higher, respectively. Using the same input structures, an identical stability ranking and similar geometries are also obtained from geometry optimization at the DFT level, which confirms the proper description of TTF-$(SC_3)_4$ adsorption by the force field. It should be noted that the alkyl side chains are still paired in the core-down and core-up conformations of TTF-$(SC_3)_4$ although a much weaker interaction is expected due to the shortened length. For this reason, a lower stability is gained from the alkyl chains for TTF-$(SC_3)_4$, making the relative energetic stability inversed between the core-flat and core-down conformation as compared to TODT-TTF. The core-up conformation still suffers from the less favored geometry and continues to be the least stable structure.

Following the optimization, 100ps-long MD simulations at 298K were performed on these optimized structures. At the end of the MD runs, both the core-down and core-up conformation convert to the core-flat conformation with opened alkyl chains (see Figure 4. 7).
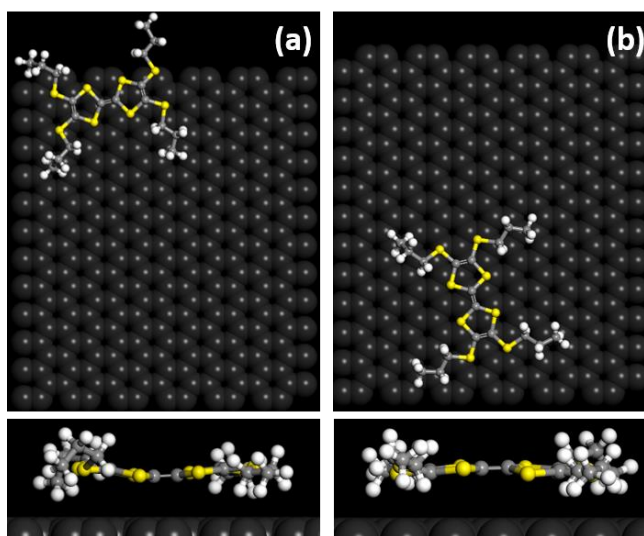
Figure 4. 7 Adsorption geometry at the end of MD simulations for the core-down (a) and core-up (b) conformations of TTF-$(SC_3)_4$. Top panel: top views showing the arrangement of the alkyl chains; Bottom panel: side views showing the geometry of the molecular core. HOPG substrate is shown underneath the adsorbed molecule.

However, such conversion between different adsorption conformations does not happen in the adsorption of TODT-TTF. Combining this structural conversion and the change of relative energetic stability among different adsorption conformations, we can thus conclude that the adsorption conformation of alkylated thiol-TTFs is very sensitive to the arrangements of the alkyl side chains. The initial boat-like-shaped molecular core is preserved during the adsorption only when the molecules have long and paired alkyl chains adsorbed on the substrates. These alkyl

chains interact strongly between themselves and with the HOPG substrate. They therefore act as anchors and hinder the planarization of the molecule. This is apparently not the case for the core-flat conformation where the alkyl chains are not paired and the planarization is easier to achieve. Such anchoring effects are also evidenced by the fact that, compared to TODT-TTF, the core-up conformation is readily planarized for TTF-$(SC_3)_4$ because of less impediments from the shorter alkyl chains.

The effects of the alkyl chains on the planarization of the alkylated thiol-TTFs are further investigated by modelling. The optimized geometry of TTF-$(SC_3)_4$, TTF-$(SC_6)_4$, and TTF-$(SC_{18})_4$ in the core-up conformation are shown in Figure 4. 8. As expected, the planarization is more evident in the molecule with the shorter alkyl chains.
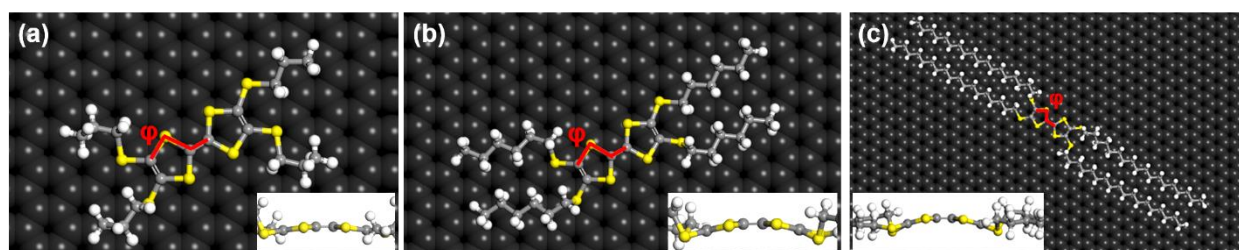
Figure 4. 8 Force field-optimized structure for TTF-$(SC_3)_4$ (a), TTF-$(SC_6)_4$ (b) and TTF-$(SC_{18})_4$ (c) in the core-up conformation. Insets are side views of the molecular core. The torsion angle φ associated with molecule planarization is also labelled. There are four equivalent torsion angles in the molecular core. Only one is shown here for better visual clarity. HOPG substrate is shown underneath the adsorbed molecule.

In order to examine the effects of the alkyl side chains in a more quantitative way, the torsion angle φ associated with this planarization is compared. There are four equivalent torsion angles in the molecular core but only one is shown in Figure 4. 8. The averaged value of φ is summarized in Table 4.1, which confirms a clear correspondence between the length of the alkyl side chains and the molecular planarization: the shorter the alkyl chains, the stronger the tendency for the molecule to be planarized upon adsorption.

Table 4. 1 Average value of φ for different alkylated thiol-TTFs adsorbed on the HOPG substrate in the core-up conformation.

TTF derivatives	TTF-$(SC_3)_4$	TTF-$(SC_6)_4$	TTF-$(SC_{18})_4$
Average value of φ / °	172.3	167.2	165.7

To conclude, with the help of molecular modelling, the peculiar contrast observed in the monolayer/bi-layer self-assemblies of TODT-TTF are successfully explained based on different adsorption conformations of the molecule: the uniform rectangular, double-blob and single-blob features are correlated to the core-flat, core-down and core-up conformation, respectively. These conformations originate from the boat-like-shaped molecular core of TODT-TTF, which was not reported in previous studies. Our modelling results also show that the adsorption conformation is controlled by the arrangement of the alkyl side chains on the HOPG substrate, emphasizing the vital role of substrate-adsorbate interactions in the 2D crystallization of organic molecules.

4.5. Modelling the long-range order in the self-assemblies of TODT-TTF

In parallel to STM image simulations, long-range arrangements of TODT-TTF in monolayer and bi-layer assemblies were also studied by molecular modelling (In collaboration with A. Minoia, UMONS). This enables us to ascertain the building blocks for the monolayer/bi-layer assemblies and understand better the packing behaviors of TODT-TTF on the surfaces. TODT-TTF molecules in a core-flat conformation are packed in the same way as the experimental bi-layer assembly, while the other two conformations are organized according to the experimental monolayer assembly. After geometry optimizations, the lattice parameters of the modelled assemblies are compared to the experimental values, which enables a further confirmation of the building blocks for different experimental assemblies.

Figure 4. 9 shows the optimized molecular model where TODT-TTF molecules in the core-flat conformation are packed in the same way as in the experimental bi-layer assembly. Such model including only one layer of molecules is sufficient to represent this packing since in the experimental bi-layer assembly, the molecules in the bottom and top layer share the same arrangement (see inset in Figure 4. 9).
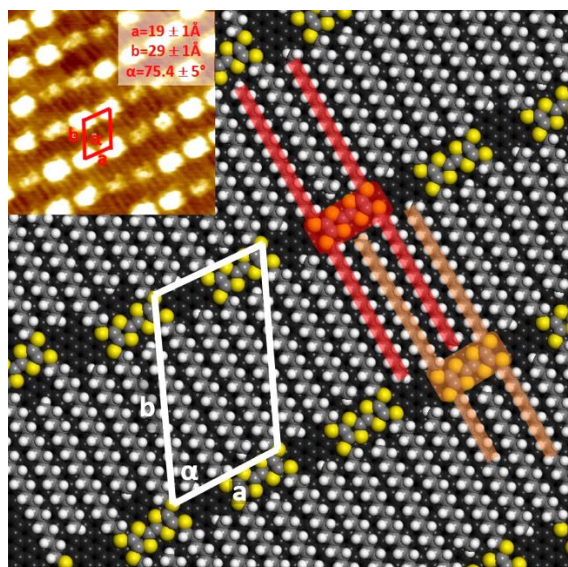
Figure 4. 9 Force field-optimized molecular model of core-flat TODT-TTF molecules that are packed in the same way as in the experimental bi-layer assembly. Inset is the STM image of experimental bi-layer assembly together with its unit cell and lattice parameters. HOPG substrate is shown underneath the adsorbed molecule.

In Figure 4. 9, two neighboring TODT-TTF molecules are colored in red and orange to highlight their interdigitated alkyl chains. Our model shows an excellent agreement with the experimental STM image where the interdigitation of the alkyl chains is illustrated by the thin lamellas between the bright rectangular objects (which are the cores of TODT-TTF molecules). As for the lattice parameters, the unit cell in the modelled self-assembly is shown by the white parallelogram in Figure 4. 9 with a = 18.1 Å, b = 31.4 Å and α = 68.2°, also matching with their experimental counterparts. These results indicate that the molecular arrangement within the bi-layer self-assembly is successfully reproduced by our modelling and it is determined that the bi-layer self-assembly is composed of TODT-TTF molecules in the core-flat conformation. This is in line with our STM image simulations which indicate the bright rectangular objects can be attributed to the TODT-TTF adsorbed on the substrate in a core-flat conformation.

The molecular packing of the monolayer assembly is studied in a similar way. First, a structural model (see Figure 4. 10 (a)) is built according to the experimental lattice parameters. Here, the building block is TODT-TTF in the core-down conformation. This is based on the STM image simulations that connect those dominating double-blob objects in the monolayer assembly to the TODT-TTF molecule adsorbed in this conformation.
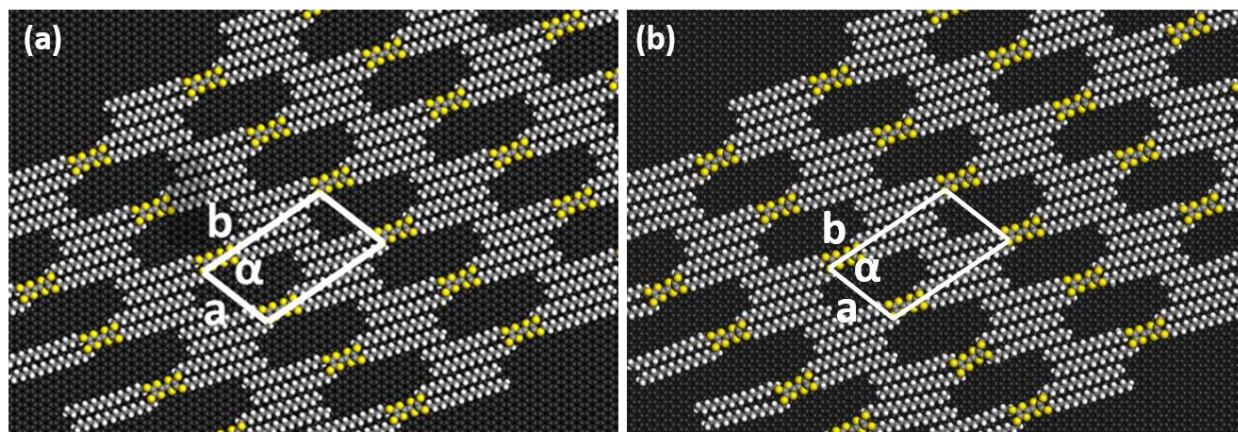
Figure 4. 10 Input (a) and force field-optimized (b) structure for the monolayer assemblies of TODT-TTF. The unit cell is overlaid on each model. For the input structure, the lattice parameters are kept the same as the experimental values, with a = 22 ± 2Å, b = 38 ± 2Å and α = 73 ± 4°. HOPG substrate is shown underneath the adsorbed molecule.

The force field-optimized structure is shown in Figure 4. 10 (b). It is clear that the overall molecular arrangement is well-preserved. A parallelogram-shaped unit cell is extracted from the monolayer model and its lattice parameters are very comparable to the experimental values: a = 21 Å, b = 37 Å and α = 71°. Such an excellent agreement regarding the lattice parameters provides a robust proof that the experimental monolayer assembly is formed by TODT-TTF molecule in the core-down conformation, again consistent with the STM image simulations.

However, one thing to be noted is that, compared with the molecular packing of the bi-layer assembly (see Figure 4. 9), the alkyl chains of TODT-TTF are only partly interdigitated in the monolayer assembly. This results in a loosely-packed structure with large void areas present between neighboring TODF-TTF molecules. In principle, such loose packing is energetically less-favored and rather fragile. Nevertheless, the monolayer assembly remains stable in the experiments, suggesting it gains extra stability from other aspects. One possible way is to have the solvent molecules co-adsorbed in the void areas between TOTD-TTF molecules. It has been reported by Ghosh S. *et al*. [32] that hydrogen-bond-like interactions can exist between –CH donors and sulfur acceptors. This type of interaction could take place upon co-adsorption of 1-phenyloctane (1-PO) solvent molecules within the monolayer assembly. As shown in Figure 4. 11 (a), pairs of 1-PO molecules can be co-adsorbed between the TODT-TTF molecules and one -CH group on the phenyl ring (red-colored) is positioned to interact with the sulfur atoms on the core of the neighboring TODT-TTF molecule. This co-assembly is then optimized, leading to the structure shown in Figure 4. 11 (b). The molecular arrangement in the monolayer assembly is not

disturbed by the solvent molecules and the lattice parameters are almost unchanged, with a = 22 Å, b = 37 Å and α = 73°. This confirms that the co-adsorption of 1-PO can certainly take place and could play a role in stabilizing the loosely-packed monolayer assembly.
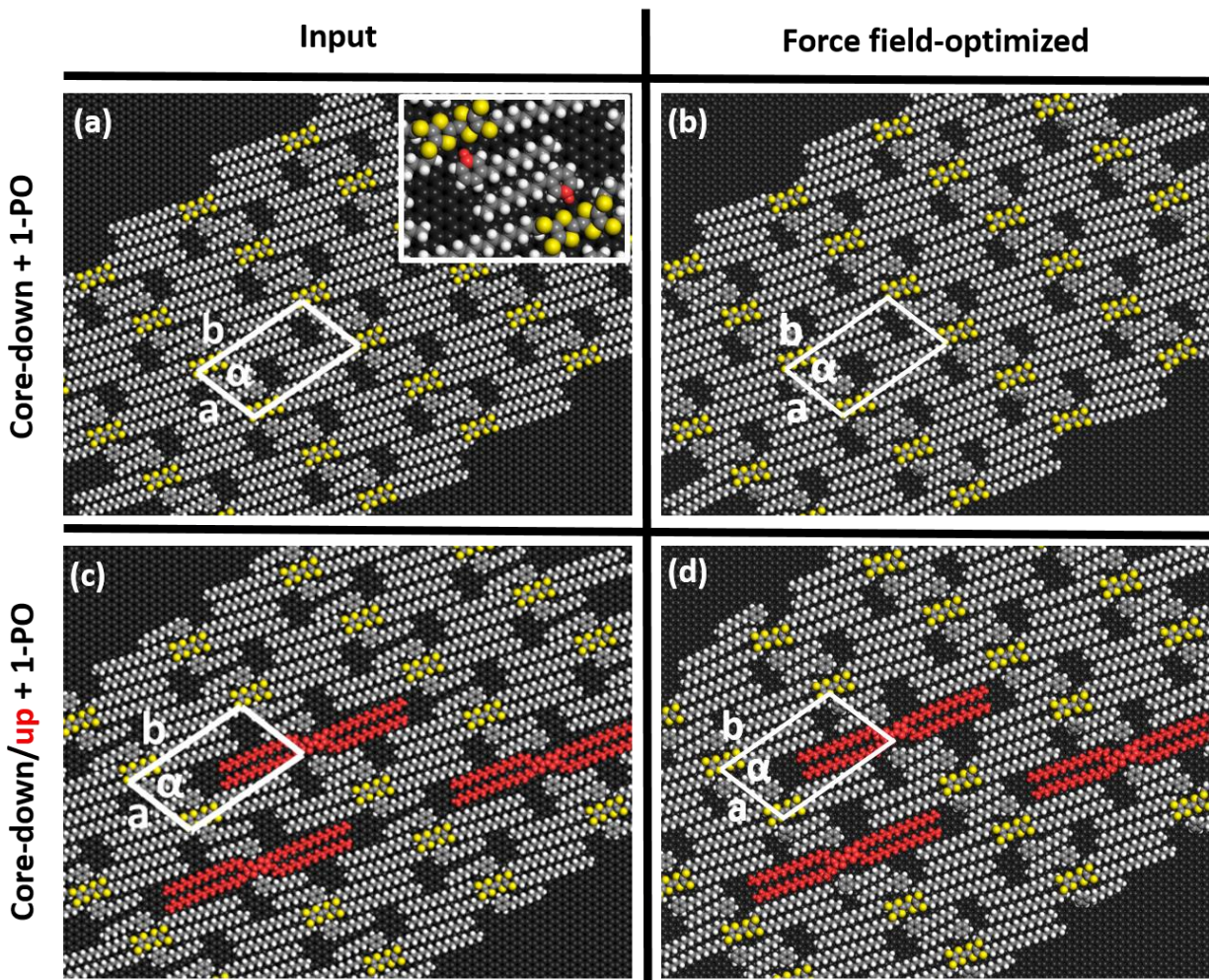
Figure 4. 11 Input and force field-optimized structures for the TODT-TTF/1-PO co-assemblies: TODT-TTF in the core-down conformation + 1-PO (a, b). TODT-TTF in the core-down/up conformation +1-PO (c, d). Inset in panel a gives a better view of the molecular arrangement that favors the potential C-H ··· S interactions. TODT-TTF molecules in the core-up conformation are red-colored in panel c and d. HOPG substrate is shown underneath the adsorbed molecule.

Since single-blob objects also appear in the experimental STM images of the monolayer assembly and their origin has been ascribed to TODT-TTF molecules adsorbed in the core-up conformation, three molecules in the co-assembly are randomly picked and switched from the core-down to core-up conformation (red-colored in Figure 4. 11 (c)). After optimization, the overall structure (Figure 4. 11(d)) stays similar to both the original co-assembly and the modeled assembly that includes only TODT-TTF (Figure 4. 10 (b)). The lattice parameters of these assemblies are then compared

and summarized in Table 4. 2. Their consistency confirms the excellent structural compatibility between TODT-TTF adsorbed in core-down and core-up conformation, and therefore also the feasibility to form monolayer assemblies mixing these two conformations.

Table 4. 2 Lattice parameters of the experimental and modeled monolayer assemblies

Lattice parameter	a (Å)	b (Å)	A (°)
Experimental monolayer assembly	22 ± 2	38 ± 2	72.5 ± 4
Modelled monolayer assembly (only TODT-TTF)	21	37	71
Modelled monolayer co-assembly (core-down + 1-PO)	22	37	73
Modelled monolayer co-assembly (core-down/up + 1-PO)	22	37	73

4.6. Conclusions

To summarize, the multiscale molecular modelling work we have performed provides very strong and consistent indications on the molecular-scale structure of the monolayer/bi-layer assemblies observed experimentally. Force field simulations allow us to compare explicitly the energetic stabilities of different adsorption conformations and to model the packing of molecules in the monolayer/bi-layer assemblies. Combined with STM image simulations, it is concluded that the experimental monolayer assemblies are a mixture of TODT-TTF molecules adsorbed in the core-down and core-up conformations, while only the core-flat conformation is present in the bi-layer assemblies. Our study shows clearly the crucial role of the substrate in the 2D crystallization of organic molecules.

Appendix

Appendix 4.1 Experimental details for the preparation of TODT-TTF self-assembled molecular networks and STM measurements

A stock solution of tetrakis-octadecylthio-tetrathiafulvalene (TODT-TTF, $C_{TODT-TTF} = 7.5 \times 10^{-4}\ M$) was prepared by dissolving appropriate amounts of the compound in 1-phenyloctane(1-PO). The solvent 1-PO was purchased from Sigma-Aldrich (>99%) and used without further purification. The stock solution was diluted further with 1-PO to prepare a concentration series. The self-assemblies were then prepared by drop-casting a drop of solution onto a freshly cleaved surface of the highly oriented pyrolytic graphite (HOPG). Following that, all STM measurements were performed at room temperature (21–23°C), using a PicoSTM (Agilent) operating in constant-current mode with the tip immersed in the liquid. STM tips were prepared by mechanically cutting a Pt/Ir wire (80%/20%, diameter 0.2 mm). The images were corrected for drift via Scanning Probe Image Processor (SPIP) software using the recorded graphite images for calibration, which allows the unit cell determination. The unit cell parameters were determined by examining several images.

Appendix 4.2 Computational details of STM image simulations and geometry optimization in DFT.

DFT calculations were performed using the 4.1 version of the SIESTA package [33]. The exchange-correlation was described by the PBE functional [34] within the general gradient approximation. Valence electrons were described by a polarized double-zeta (DZP) basis set while the core electrons were treated by the Trouillier-Martins pseudopotentials [35]. A reasonable mesh cut-off of 250 Ry was utilized with a Monkhorst-Pack grid of $(1 \times 1 \times 1)$. A single point is sufficient for the sampling as the dimension of the smallest unit cell we used in the calculations is already large: around 25Å and 30Å in x and y direction respectively. Along Z direction, a distance of 60Å was used to avoid the artificial interactions due to periodic boundary conditions. Van der Waals interactions were considered in the calculations through the Grimme corrections.[36] For geometry optimizations, atomic positions of the adsorbed molecules were relaxed until the atomic forces are smaller than 0.04 eV/ Å. While, the simulated STM images were generated based on the force field-optimized geometries using the WSxM software [37].

References

1. Wudl, F., D. Wobschall, and E.J. Hufnagel, *Electrical Conductivity by the Bis (1, 3-Dithiole)-Bis (1, 3-Dithiolium) System.* J. Am. Chem. Soc., 1972. **94**: p. 670-672.

2. Nielsen, M.B., C. Lomholt, and J. Becher, *Tetrathiafulvalenes as Building Blocks in Supramolecular Chemistry Ii.* Chem. Soc. Rev., 2000. **29**: p. 153-164.

3. Li, H.-x., R.-h. Zheng, and Q. Shi, *Theoretical Study on Charge Carrier Mobilities of Tetrathiafulvalene Derivatives.* Phys. Chem. Chem. Phys., 2011. **13**: p. 5642-5650.

4. Rovira, C., *Bis (Ethylenethio) Tetrathiafulvalene (Bet-Ttf) and Related Dissymmetrical Electron Donors: From the Molecule to Functional Molecular Materials and Devices (Ofets).* Chem. Rev., 2004. **104**: p. 5289-5318.

5. Mas-Torrent, M., M. Durkut, P. Hadley, X. Ribas, and C. Rovira, *High Mobility of Dithiophene-Tetrathiafulvalene Single-Crystal Organic Field Effect Transistors.* J. Am. Chem. Soc., 2004. **126**: p. 984-985.

6. Souto, M., A. Santiago-Portillo, M. Palomino, I.J. Vitórica-Yrezábal, B.J. Vieira, J.C. Waerenborgh, S. Valencia, S. Navalón, F. Rey, and H. García, *A Highly Stable and Hierarchical Tetrathiafulvalene-Based Metal–Organic Framework with Improved Performance as a Solid Catalyst.* Chemical science, 2018. **9**: p. 2413-2418.

7. Gorgues, A., P. Hudhomme, and M. Sallé, *Highly Functionalized Tetrathiafulvalenes: Riding Along the Synthetic Trail from Electrophilic Alkynes.* Chem. Rev., 2004. **104**: p. 5151-5184.

8. Bendikov, M., F. Wudl, and D.F. Perepichka, *Tetrathiafulvalenes, Oligoacenenes, and Their Buckminsterfullerene Derivatives: The Brick and Mortar of Organic Electronics.* Chem. Rev., 2004. **104**: p. 4891-4946.

9. Zu, X., J. Li, Y. Qian, W. Duan, and Q. Zeng, *Progress in Self-Assembly of Ttf Derivatives at Hopg Interface.* New J. Chem., 2019. **43**: p. 1654-1662.

10. Gao, X., W. Qiu, Y. Liu, G. Yu, and D. Zhu, *Organic Field-Effect Transistors Based on Tetrathiafulvalene Derivatives.* Pure Appl. Chem., 2008. **80**: p. 2405-2423.

11. Yang, G., C.a. Di, G. Zhang, J. Zhang, J. Xiang, D. Zhang, and D. Zhu, *Highly Sensitive Chemical-Vapor Sensor Based on Thin-Film Organic Field-Effect Transistors with Benzothiadiazole-Fused-Tetrathiafulvalene.* Adv. Funct. Mater., 2013. **23**: p. 1671-1676.

12. Marszalek, T., A. Nosal, R. Pfattner, J. Jung, S. Kotarba, M. Mas-Torrent, B. Krause, J. Veciana, M. Gazicki-Lipman, and C. Crickert, *Role of Geometry,*

Substrate and Atmosphere on Performance of Ofets Based on Ttf Derivatives. Org. Electron., 2012. **13**: p. 121-128.

13.   Jiang, H., X. Yang, Z. Cui, Y. Liu, H. Li, W. Hu, and C. Kloc, *Adjusting Tetrathiafulvalene (Ttf) Functionality through Molecular Design for Organic Field-Effect Transistors.* CrystEngComm, 2014. **16**: p. 5968-5983.

14.   Mas-Torrent, M. and C. Rovira, *Tetrathiafulvalene Derivatives for Organic Field Effect Transistors.* J. Mater. Chem., 2006. **16**: p. 433-436.

15.   Cui, L., Y.-F. Geng, C.F. Leong, Q. Ma, D.M. D'Alessandro, K. Deng, Q.-D. Zeng, and J.-L. Zuo, *Synthesis, Properties and Surface Self-Assembly of a Pentanuclear Cluster Based on the New Π-Conjugated Ttf-Triazole Ligand.* Sci. Rep., 2016. **6**: p. 1-8.

16.   Xu, J., X. Xiao, K. Deng, and Q. Zeng, *Transformation of Self-Assembly of a Ttf Derivative at the 1-Phenyloctane/Hopg Interface Studied by Stm—from a Nanoporous Network to a Linear Structure.* Nanoscale, 2016. **8**: p. 1652-1657.

17.   Gao, F., X.-M. Zhang, L. Cui, K. Deng, Q.-D. Zeng, and J.-L. Zuo, *Tetrathiafulvalene-Supported Triple-Decker Phthalocyaninato Dysprosium (Iii) Complex: Synthesis, Properties and Surface Assembly.* Sci. Rep., 2014. **4**: p. 1-7.

18.   Nair, M.N., C. Mattioli, M. Cranney, J.-P. Malval, F.o. Vonau, D. Aubel, J.-L. Bubendorff, A. Gourdon, and L. Simon, *Stm Studies of Self-Assembled Tetrathiafulvalene (Ttf) Derivatives on Graphene: Influence of the Mode of Deposition.* The Journal of Physical Chemistry C, 2015. **119**: p. 9334-9341.

19.   Lee, S.-L., Y.-C. Chu, H.-J. Wu, and C.-h. Chen, *Template-Assisted Assembly: Scanning Tunneling Microscopy Study of Solvent-Dependent Adlattices of Alkyl-Derivatized Tetrathiafulvalene.* Langmuir, 2012. **28**: p. 382-388.

20.   Abdel-Mottaleb, M.M., E. Gomar-Nadal, M. Surin, H. Uji-i, W. Mamdouh, J. Veciana, V. Lemaur, C. Rovira, J. Cornil, and R. Lazzaroni, *Self-Assembly of Tetrathiafulvalene Derivatives at a Liquid/Solid Interface—Compositional and Constitutional Influence on Supramolecular Ordering.* J. Mater. Chem., 2005. **15**: p. 4601-4615.

21.   Fu, C., H.-p. Lin, J.M. Macleod, A. Krayev, F. Rosei, and D.F. Perepichka, *Unravelling the Self-Assembly of Hydrogen Bonded Ndi Semiconductors in 2d and 3d.* Chem. Mater., 2016. **28**: p. 951-961.

22.   Blunt, M.O., J.C. Russell, M. del Carmen Gimenez-Lopez, N. Taleb, X. Lin, M. Schröder, N.R. Champness, and P.H. Beton, *Guest-Induced Growth of a Surface-Based Supramolecular Bilayer.* Nat. Chem., 2011. **3**: p. 74-78.

23.   Zheng, Q.N., X.H. Liu, X.R. Liu, T. Chen, H.J. Yan, Y.W. Zhong, D. Wang, and L.J. Wan, *Bilayer Molecular Assembly at a Solid/Liquid Interface as*

Triggered by a Mild Electric Field. Angew. Chem., 2014. **126**: p. 13613-13617.

24. Korolkov, V.V., M. Baldoni, K. Watanabe, T. Taniguchi, E. Besley, and P.H. Beton, *Supramolecular Heterostructures Formed by Sequential Epitaxial Deposition of Two-Dimensional Hydrogen-Bonded Arrays.* Nat. Chem., 2017. **9**: p. 1191-1197.

25. Ciesielski, A., A. Cadeddu, C.-A. Palma, A. Gorczyński, V. Patroniak, M. Cecchini, and P. Samorì, *Self-Templating 2d Supramolecular Networks: A New Avenue to Reach Control over a Bilayer Formation.* Nanoscale, 2011. **3**: p. 4125-4129.

26. Elemans, J.A., S.J. Wezenberg, M.J. Coenen, E.C. Escudero-Adan, J. Benet-Buchholz, D. den Boer, S. Speller, A.W. Kleij, and S. De Feyter, *Axial Ligand Control over Monolayer and Bilayer Formation of Metal-Salophens at the Liquid–Solid Interface.* Chem. Commun., 2010. **46**: p. 2548-2550.

27. Gao, F., F.-F. Zhu, X.-Y. Wang, Y. Xu, X.-P. Wang, and J.-L. Zuo, *Stabilizing Radical Cation and Dication of a Tetrathiafulvalene Derivative by a Weakly Coordinating Anion.* Inorg. Chem., 2014. **53**: p. 5321-5327.

28. Wang, L., J.-P. Zhang, and B. Zhang, *4, 4', 5, 5'-Tetrakis (Methylsulfanyl) Tetrathiafulvalene.* Acta Crystallogr. Sect. Sect. E: Struct. Rep. Online, 2005. **61**: p. o65-o66.

29. Rappé, A.K., C.J. Casewit, K. Colwell, W.A. Goddard III, and W.M. Skiff, *Uff, a Full Periodic Table Force Field for Molecular Mechanics and Molecular Dynamics Simulations.* J. Am. Chem. Soc., 1992. **114**: p. 10024-10035.

30. Casewit, C., K. Colwell, and A. Rappe, *Application of a Universal Force Field to Organic Molecules.* J. Am. Chem. Soc., 1992. **114**: p. 10035-10046.

31. Reynaerts, R., A. Minoia, S.M. Gali, L. Daukiya, N. Van Velthoven, D. De Vos, R. Lazzaroni, K.S. Mali, and S. De Feyter, *Coplanar Versus Noncoplanar Carboxyl Groups: The Influence of Sterically Enforced Noncoplanarity on the 2d Mixing Behavior of Benzene Tricarboxylic Acids.* The Journal of Physical Chemistry C, 2020. **124**: p. 24874-24882.

32. Ghosh, S., P. Chopra, and S. Wategaonkar, *C–H⋯S Interaction Exhibits All the Characteristics of Conventional Hydrogen Bonds.* Phys. Chem. Chem. Phys., 2020. **22**: p. 17482-17493.

33. Soler, J.M., E. Artacho, J.D. Gale, A. García, J. Junquera, P. Ordejón, and D. Sánchez-Portal, *The Siesta Method for Ab Initio Order-N Materials Simulation.* J. Phys.: Condens. Matter, 2002. **14**: p. 2745.

34. Perdew, J.P., K. Burke, and M. Ernzerhof, *Generalized Gradient Approximation Made Simple.* Phys. Rev. Lett., 1996. **77**: p. 3865.

35. Troullier, N. and J.L. Martins, *Efficient Pseudopotentials for Plane-Wave*

Calculations. Phys. Rev. B, 1991. **43**: p. 1993.

36.   Grimme, S., *Semiempirical Gga-Type Density Functional Constructed with a Long-Range Dispersion Correction.* J. Comput. Chem., 2006. **27**: p. 1787-1799.

37.   Horcas, I., R. Fernández, J. Gomez-Rodriguez, J. Colchero, J. Gómez-Herrero, and A. Baro, *Wsxm: A Software for Scanning Probe Microscopy and a Tool for Nanotechnology.* Rev. Sci. Instrum., 2007. **78**: p. 013705.

Chapter 5

A bottom-up approach bridging self-assembled molecular networks and substrate-induced polymorphs for a prototypical organic semiconductor

In chapter 4, we have shown how molecular modelling can be used to understand the self-assembly of functional organic molecules on substrates. Deep insights are gained for both the adsorption conformation and long-range arrangement of TODT-TTF on the HOPG substrate. Unlike previous studies, our work is not limited to the formation and structure of the first adsorbed monolayer but extends to the bi-layer assembly. This can be considered as a stepping stone for exploring the growth of a SIP, which is composed of a larger number of molecular layers. Following this strategy, we move a step further in this chapter, to study the possible formation of a SIP for another organic semiconductor compound: lead phthalocyanine.

5.1. Lead phthalocyanine: a perfect candidate

In order to further understand the effects of the substrate on the formation of SIPs and to have a clearer picture about the connection between SAMNs and SIPs, we choose a compound from a prototypical class of organic semiconductors: lead phthalocyanine (PbPc, Figure 5. 1) and study the SAMNs it forms at the interface between the solution and the HOPG substrate. Going beyond the 2D crystallization process, crystal growth on top of the self-assembled network in the third dimension is further explored from both the modelling and experimental perspective, with the aim to understand the formation of possible SIPs for PbPc.
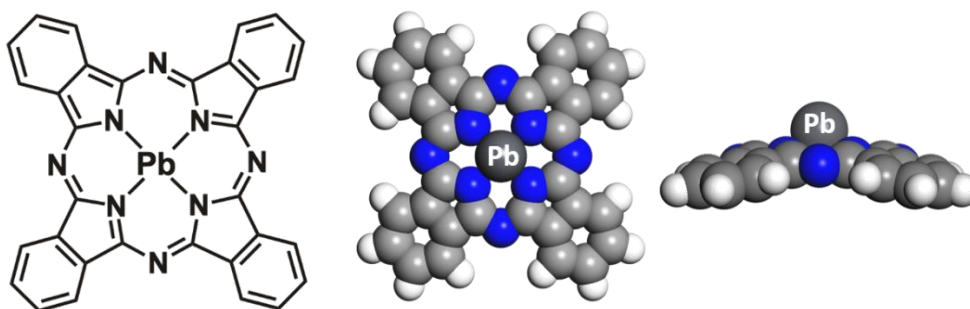
Figure 5. 1 Molecular structure and geometry of PbPc

PbPc has shown many interesting physical and chemical properties, such as high chemical and thermal stability [1], high coloring property and photoconductivity [2], along with promising electrical properties for use in sensors for hazardous gases [3-5]. Besides those electronic and optical properties, the structural features of PbPc are also interesting in the context of this work, since the molecule is highly symmetric but non-planar (C_{4v}), in contrast to many other metal

phthalocyanine molecules, *e.g.* completely planar FePc, CuPc and other transition metal phthalocyanines. The non-planarity of PbPc can lead to different molecular adsorption conformations when assembled on the substrate, which potentially directs the subsequent crystal growth in different manners. The peculiarity of this non-planar geometry and its effects on the organization of PbPc monolayer and multilayer structures are discussed below in a more detailed way.

Last but not least, PbPc is also of special interest for the joint modelling/experimental strategy that is followed in this work. Modelling-wise, the study of the electronic structure of metal phthalocyanine molecules, as investigated by quantum-chemical calculations, has been well established [1, 6-9]. This provides instructive background for our modelling work. From the experimental point of view, metal phthalocyanines are one of the workhorses of STM studies in the field of molecular self-assembly on surfaces [10-14]. However, those STM work focus more on the planar transition metal phthalocyanines, instead of non-planar metal phthalocyanines such as PbPc, which can have more intriguing assembly/crystallization behaviors on the surfaces. Another advantage of using PbPc is that, compared with pure organic compounds, it makes the TEM imaging a bit less challenging due to the presence of the heavy lead atom in the center of the molecule. Heavy atoms like Pb show a stronger scattering of the electrons and benefit especially the HADDF-STEM that we used for the imaging of PbPc crystals because of the Z-contrast in this imaging mode (where Z is the atomic number, more details in section 2.2.3.4).

SAMNs of PbPc were first reported as deposited by molecular beam epitaxy on an MoS_2 substrate. The STM data revealed three arrangements of the assembled PbPc molecules [15]. In a more recent study, PbPc monolayers were deposited onto epitaxial graphene on SiC and their internal organization was investigated by STM under ultra-high vacuum [16]. PbPc molecules were found to be packed into a long-range ordered self-assembly with a square 2D unit cell (Figure 5. 2).
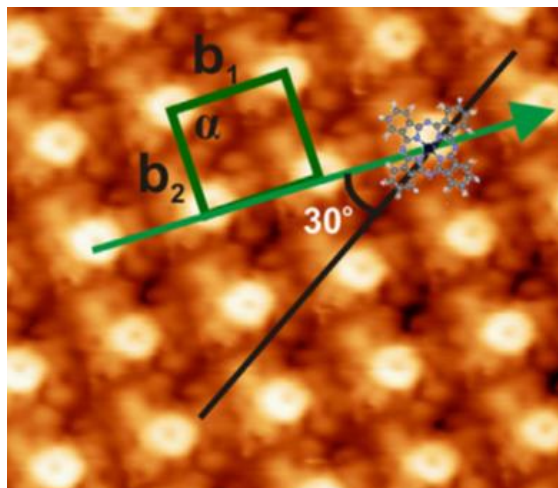
Figure 5. 2 STM image of PbPc self-assembly monolayer grown on graphene. The unit cell is highlighted by the green square. Adapted from [16]

One central question related to STM imaging of PbPc self-assembled monolayers is to determine the molecular adsorption conformation within the assembly. Due to the non-planarity of the PbPc molecule, different adsorption conformations are possible: in particular, the central Pb atom of the molecule can either point away from (Pb-up) or towards (Pb-down) the substrate (see section 5.3.2 below). Up to now, an unambiguous determination of the PbPc molecular adsorption conformation within its assemblies is still missing.

As for 3D crystals, two bulk polymorphs have been reported for PbPc: a monoclinic phase with *P2₁/c* space group [17] and a triclinic phase with *P-1* space group [18]. The crystal structures of these two bulk phases are shown in Figure 5. 3.
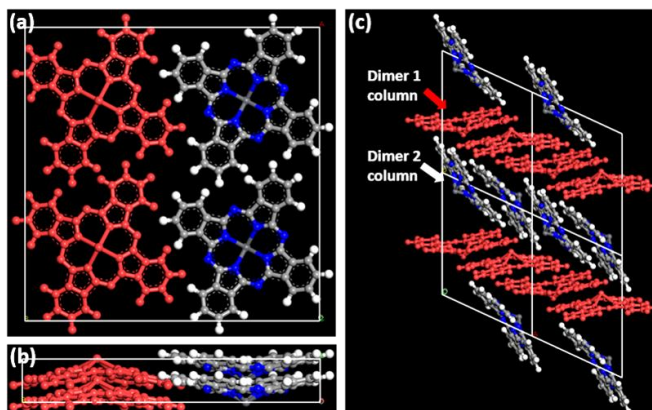
Figure 5. 3 Crystal structure of the bulk monoclinic phase of PbPc, viewing from the crystallographic c axis (a) and a axis (b). Crystal structure of the bulk triclinic phase of PbPc, viewing from the crystallographic c axis (c)

In the bulk monoclinic phase, PbPc molecules stack linearly and form molecular columns. The unit cell is composed of two pairs of columns with opposite molecular orientation, which are arranged in a square array. In Figure 5. 3(a), the pair of molecular columns with PbPc molecules pointing outwards is colored in red. A similar situation is also found in the bulk triclinic phase of PbPc. Its unit cell contains two types of PbPc dimers with different orientations. Those two types of dimers are colored differently in Figure 5. 3(c). Within each type of dimer, neighboring PbPc molecules face each other with their concave or convex side in an alternating manner. To the best of our knowledge, the question whether the SAMN of PbPc directs its crystal growth into the known bulk phases or unknown substrate-induced polymorphs within thin films has never been addressed. In other words, the state-of-art of PbPc studies in the field of SAMNs and SIPs make this molecule a perfect candidate to be investigated in the context of our 2Dto3D project.

In this work, PbPc self-assembly was studied at KU Leuven at the solution/HOPG interface, instead of common high-vacuum deposition conditions. With this approach, self-assembled monolayers form in the presence of the solution, which is closer to the equilibrium condition as compared to vacuum deposition. STM is employed *in-situ* to determine the structural organization of the assembly with a resolution down to the (sub)molecular level. The adsorption conformation of the PbPc molecules is then determined unequivocally by comparing simulated and experimental STM images. In parallel to the STM measurements, force field simulations are employed in order to have a better understanding about the molecular packing within the assembly. The crystal growth of the PbPc molecule, as templated by the self-assembled monolayer, is then modelled using force field simulations, considering successive adsorption of up to four molecular layers. Complementarily, PbPc thin films were prepared by physical vapor deposition (PVD) at TU Graz and their crystal structure is determined by TEM (UAntwerpen) and X-ray diffraction techniques (TU Graz). The modelled crystal structure is then compared with the results from the TEM and X-ray diffraction measurements in order to gain an integrated view over the 2D to 3D assembly of this molecular semiconductor.

5.2. Experimental Self-Assembled Molecular Networks of PbPc

Figure 5. 4 shows the highly-ordered self-assembled monolayers that PbPc forms upon physisorption at the heptanoic acid (HA)/HOPG interface (self-assemblies prepared by Gangamallaiah Velpula from KU Leuven, see Appendix 5.1. Experimental details for the preparation of PbPc self-assembled molecular networks and STM measurementsfor more experimental details). The monolayer consists of defect-free domains that extend over several thousand square nanometers. A close inspection of the STM images reveals that each molecular row consists of PbPc molecules closely packed along the row axis and each molecule appears as a collection of 16 bright dots (see the inset in panel (b), dots highlighted by the white dashed circles).
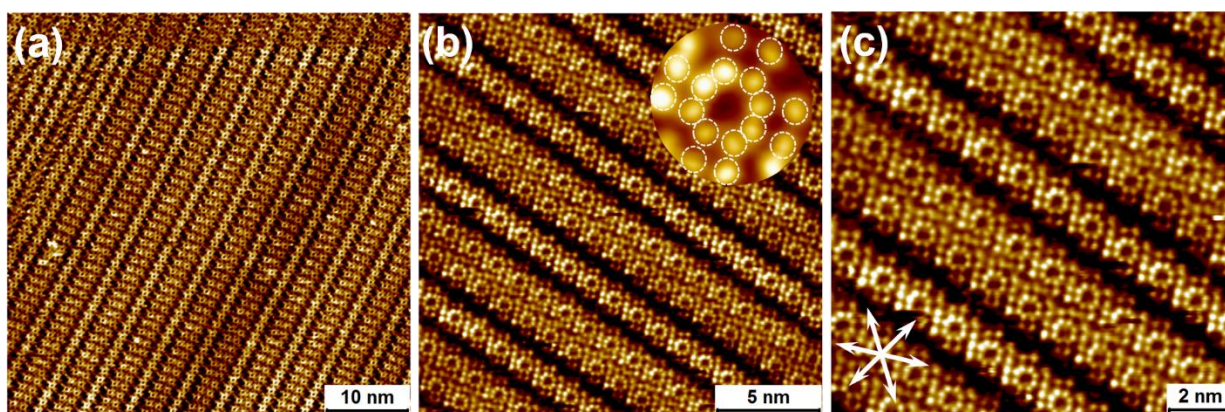
Figure 5. 4 STM images of PbPc self-assembly at the HA/HOPG interface. The graphite symmetry axes are shown in the lower left corner of panel c. Imaging parameters: I_{set} = 70 pA, V_{bias} = -1.29 V. STM images obtained by Gangamallaiah Velpula from KU Leuven.

The STM data presented in Figure 5. 4 are somewhat unusual. The first peculiar feature of the acquired STM data is the appearance of the individual PbPc molecules. Specifically, the center of the PbPc molecules, where the lead atom is located, appears as a depression. This is in contrast to the STM data obtained under UHV conditions where the Pb atom appears as a bright protrusion in the STM images (see Figure 5. 2. [16]). Furthermore, in self-assembled networks of alkyl-substituted lead pyrenocyanine formed at the solution-solid interface, the lead atom is observed as a bright protrusion as well [19]. However, a few molecules in the network of alkyl-substituted lead pyrenocyanine show a depression at their molecular center and this depression is ascribed to molecules adsorbed with a Pb-down adsorption conformation [19]. Those observations might be related to the prevalence of either the Pb-up or the Pb-down adsorption conformation, resulting from the large size of the central metal atom, which does not fit inside the isoindole cavity of the

103

phthalocyanine. Tin phthalocyanine behaves similarly: depending on the orientation of the metal center, the central cavity of the molecule adsorbed on metal surfaces appeared in the STM images either as a protrusion (Sn above the molecular plane, Sn-up) or as a depression (Sn below the molecular plane, Sn-down) [20].

5.3. Modelling Self-Assembled Molecular Networks of PbPc

In order to identify the factors contributing to the STM contrast of the PbPc molecules in the self-assembled network and to determine the adsorption conformation of PbPc on the graphite surface, detailed modelling studies are carried out. These studies include force field simulations and STM image simulations based on the DFT formalism. The former can determine the preferential adsorption conformation (Pb-up or Pb-down) from energetic criteria while the latter enables a direct comparison with the experimental STM images. As discussed in chapter 3.1, the reliability of force field simulations depends completely on the parameters used to describe the intra- and intermolecular interactions. In the first part of this section, we discuss how a suitable force field is selected and further parameterized for the PbPc molecule.

5.3.1. Force field parameterization for PbPc

To determine which force field is able to reproduce the basic properties of PbPc (e.g. molecular geometry and bulk crystal parameters) and therefore can be used in the simulations, the geometry of the PbPc molecule is first optimized by several Pb-included force fields available in the Materials Studio software package. The optimized structures are shown in Figure 5. 5. However, all of them show large discrepancy from the experimental molecular structure [17, 18]. The molecule suffers from a weakly-protruding Pb atom, abnormal Pb-N bond length and severe distortion in the universal-, pcff- and cvff-optimized structure, respectively. These abnormal molecular geometries indicate that some force field parameters are not appropriate and have to be adjusted before performing further simulations.
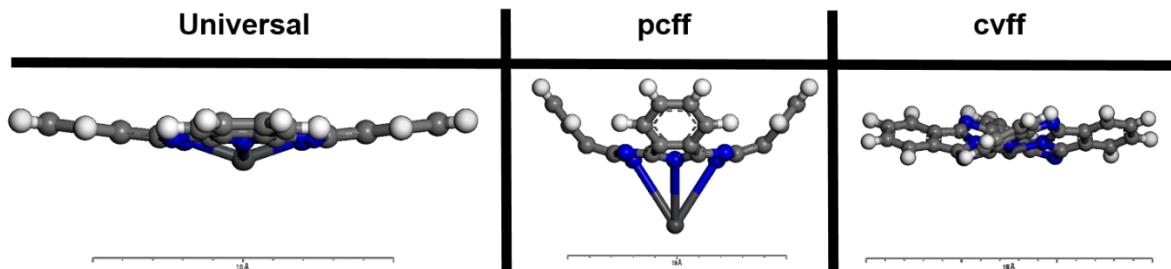
Figure 5. 5 Optimized molecular geometry using Pb included force fields: Universal, pcff and cvff

In order to minimize the workload for the force field modification, the geometry of the metal-free phthalocyanine molecule (H$_2$Pc) is first optimized by the three force fields tested above (Universal, pcff and cvff) as well as the Dreiding force field which has been widely used to model conjugated molecules [21-23]. The optimized structures are then compared to the known planar geometry of the H$_2$Pc molecule [24] and shown in Figure 5. 6.
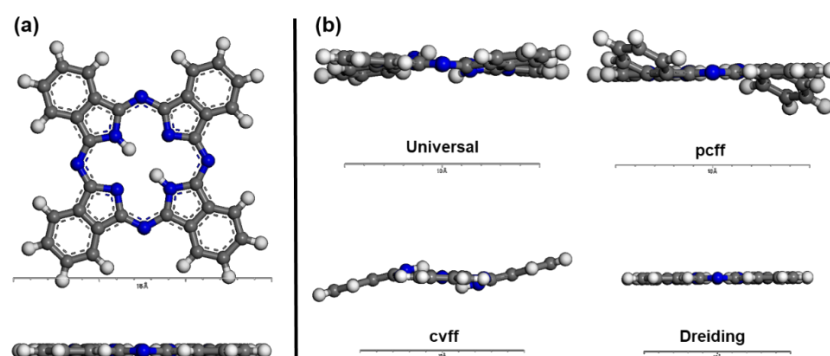
Figure 5. 6 (a) Molecular structure of H$_2$Pc, top and side view [24]. (b) Optimized molecular structure from Universal, pcff, cvff and Dreiding force fields. Only side views are shown in panel b, in order to examine how the different force fields reproduce the molecular planarity.

After optimization, the planar geometry of the H$_2$Pc molecule can be reproduced only by the Dreiding force field, which indicates its capability to accurately describe the global geometry of the phthalocyanine compounds. However, the Pb atom type is not defined in the original Dreiding force field. In order to perform simulations for the SAMNs and crystal growth of PbPc, a Pb-included Dreiding forcefield is developed in this work. With this approach, we avoid modifying force field parameters for the C, N and H atoms, which should have been done for the other three force fields.

Two sets of parameters need to be set in order to define the Pb atom type in the Dreiding forcefield. The first group of parameters defines the intramolecular properties. For PbPc, parameters need to

be defined for the description of Pb-N bond stretching, N-Pb-N bond bending and Pb-N-C bond bending (see Figure 5. 7).
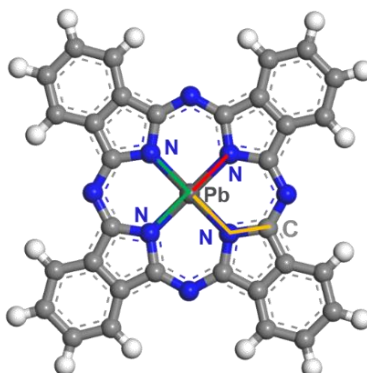
Figure 5. 7 Force field parameters to be defined for intramolecular interactions: Pb-N bond stretching (red), N-Pb-N bond bending (green) and Pb-N-C bond bending (orange).

As discussed in section 3.2, one way to generate force field parameters is to rely on *ab-initio* calculations. Here, the geometry of the PbPc molecule is optimized at the DFT level using the Gaussian 16 [25] software package. We use the M06-2X exchange-correlation functional [26] and the 6-311G(d) basis set [27] for the C, N and H atoms. As for the Pb atom, the LANL2DZ basis set and pseudopotential [28] are employed. These settings have proved to give an accurate description of the molecular geometry for PbPc [1]. This DFT-optimized structure is then used as a reference to define the force field parameters for the three intramolecular potentials related to the Pb atom.

Considering that these three potentials govern the inversion behavior of the Pb atom with respect to the molecular plane, the potential energy profile associated with this inversion is calculated at the DFT level. The force field parameters for those three potentials are then defined in order to match the DFT results. The inversion of the Pb atom and the associated energy profile are shown in Figure 5. 8.
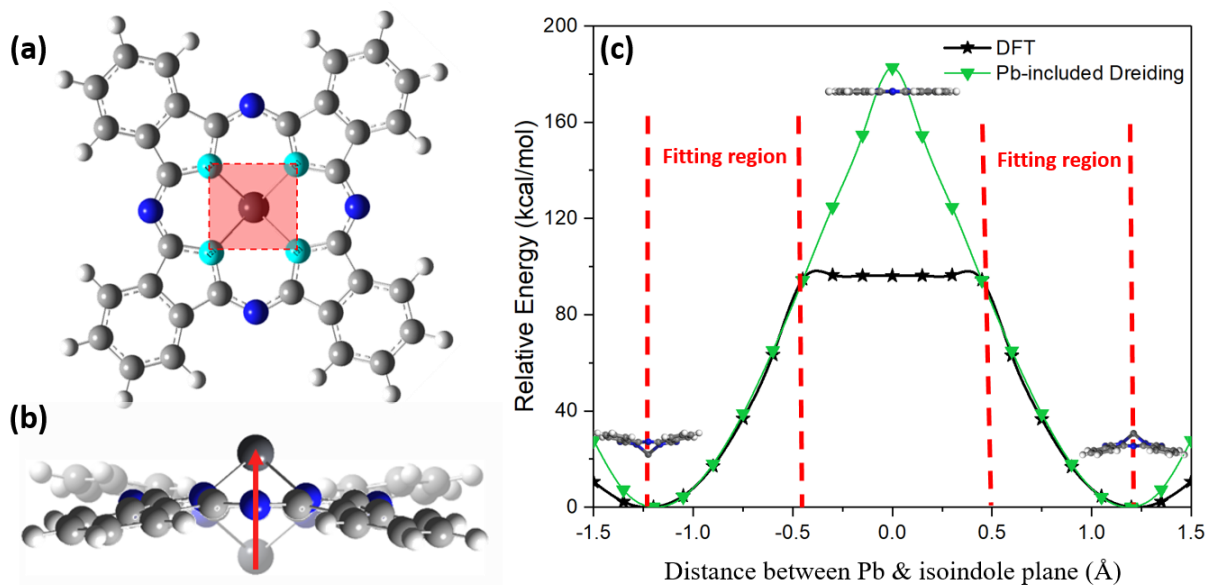
Figure 5. 8 (a) Schematic representation for the inversion of the Pb atom. The isoindole plane is highlighted by the red square in the top view of the molecule. In this case, the Pb atom is pushed from the downside to the upside of the molecule. (b) Energy profile associated with the Pb inversion, calculated with DFT and the developed Pb-included Dreiding force field.
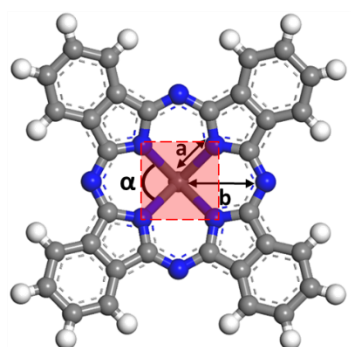
The details to calculate this potential energy profile are the following: In the DFT-optimized molecule, the four isoindole nitrogen atoms (highlighted in cyan in Figure 5. 8(a)) are fixed and form the isoindole plane (red-shaded square in Figure 5. 8 (a)). Then, the Pb atom is pushed across the isoindole plane from the bottom to the symmetric position on the other side (see Figure 5. 8 (b)) with a step distance of 0.15Å. After each step, the molecule gets optimized with the Pb atom being fixed at the current position. The relative energy with respect to the fully optimized molecule is then plotted as a function of the distance between the Pb atom and the isoindole plane (Figure 5. 8(c)). The energy penalty associated with this inversion is 96 kcal/mol, which agrees well with previous studies [29]. As for the force field parameters of the three potentials mentioned above, their values are determined on the basis of accurately reproducing the inversion energy profile calculated at the DFT level and summarized in Table 5. 1.

Table 5. 1 Values for three Pb-related potentials in the Pb-included Dreiding force field (the functional form of the bond stretching and bending potentials can be found in section 3.1.1)

Potential	Force constants	Equilibrium value
Pb-N bond stretching	358 (kcal/mol/Å^2)	2.3 Å
N-Pb-N bond bending	48 (kcal/mol/rad^2)	74°
Pb-N-C bond bending	103 (kcal/mol/rad^2)	123°

Using these parameters, the inversion energy profile calculated at the DFT level is well-reproduced by the force field calculations (see Figure 5. 8 (c)). Despite larger deviations when the Pb atom is located close to the isoindole plane, the energy profiles calculated with the two methods are in excellent agreement in the two regions close to the equilibrium positions. These fitting regions, which correspond to small molecular deformations, are the most relevant as the relatively weak non-bonded interactions that dominate in the physisorption of PbPc onto the HOPG substrate and in the PbPc crystals are not expected to change the molecular geometry to a large extent. In other words, the Pb atom is not likely to deviate far from its equilibrium position. Finally, the geometry of the PbPc molecule is optimized by our Pb-included Dreiding forcefield and the resulting structure shows very good agreement with its DFT-optimized counterpart. The results are summarized in Table 5. 2.

Table 5. 2 Comparison of several geometrical parameters between the DFT- and Pb-included Dreiding force field-optimized structures. Each parameter is shown schematically in the molecule left to the table. The isoindole plane is represented by a red-shaded square.

Parameter	By DFT	By Pb-included Dreiding forcefield
a / Å	2.33	2.29
b / Å	3.65	3.63
α / °	74.1	74.5
Distance between Pb and isoindole plane / Å	1.22	1.18

As for the parameters describing the intermolecular interactions, the vdW parameters for the Pb atom are adapted from the Universal force field: a 12-6 Lennard-Jones potential is used with D0 = 0.663 kcal/mol and R0 = 4.297 Å. The atomic charges describing the Coloumbic interactions in the force field simulations are adapted from the ESP charges calculated at the DFT level

(Gaussian 16, same exchange-correlation functional and basis set as for the geometry optimization).

The performance of our force field for describing the intermolecular interactions is then evaluated by MD simulations carried out on the two bulk phases of PbPc. To do that, 4x4x4 supercell models are built for those two phases (Figure 5. 9) and a 500ps-long MD simulation in the NPT ensemble is performed for each of them.
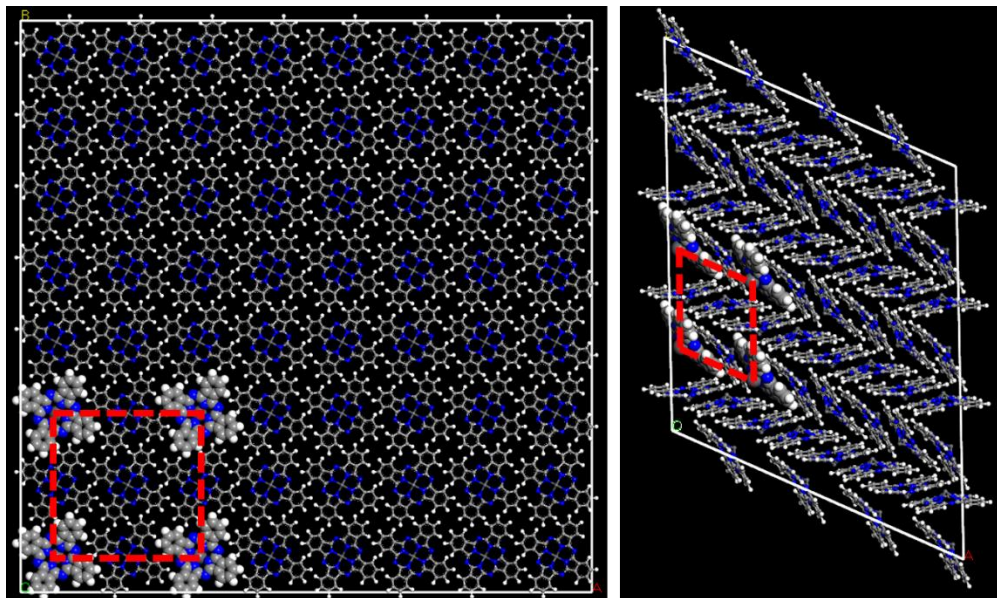
Figure 5. 9 Supercells of: monoclinic (left) and triclinic (right) PbPc crystalline structures, viewing along the direction of lattice vector c. A corresponding unit cell is highlighted in each supercell.

After the MD simulations reach the equilibrium stage, the unit cell parameters are averaged over the supercell. The values so obtained for these two phases are listed in Table 5. 3, together with the experimental data. Clearly, the experimental unit cell parameters for both phases are well-reproduced by the MD simulations using our newly-developed Pb-included Dreiding force field. Based on the excellent agreement with respect to both the DFT-optimized molecular structure and the experimental unit cell parameters, the excellent performance of this Pb-included Dreiding force field is confirmed and it is used further to model the SAMNs and crystal growth of PbPc.

Table 5. 3 (a) Unit cell parameters for the MD-calculated monoclinic (top) and triclinic (bottom) PbPc crystal structures, compared with the corresponding experimental values [17, 18].

(a) Monoclinic	Experiment	Pb-included Dreiding
a (Å)	25.48	24.85
b (Å)	25.48	24.56
c (Å)	3.73	3.96
α (deg)	90	89.99
β (deg)	90	89.99
γ (deg)	90	90.11

(b) Triclinic	Experiment	Pb-included Dreiding
a (Å)	13.15	13.28
b (Å)	16.06	16.24
c (Å)	12.37	12.50
α (deg)	94.67	94.49
β (deg)	95.13	95.30
γ (deg)	113.60	113.54

5.3.2. Adsorption conformation of single PbPc molecules and STM image simulations

The accurate description of the intra- and intermolecular interactions by the Pb-included Dreiding force field provides us a way to determine the preferred adsorption conformation for a PbPc molecule on the HOPG substrate. For this purpose, a single PbPc molecule is adsorbed in Pb-up (the lead atom points away from the substrate) or Pb-down (the lead atom points towards the substrate) conformation on the bilayer graphene that acts as a model substrate. Both structures are then optimized using force field calculations. The optimized structure for each conformation is shown in Figure 5. 10 (b) and (c) respectively. Their relative stability is then evaluated by comparing the adsorption energy, which is calculated by the following equation:

$$E_{adsorption} = E_{tot} - E_{mol} - E_{substrate}$$

where E_{tot} is the total potential energy of the optimized adsorption system, E_{mol} and $E_{substrate}$ are the potential energies for the isolated molecule and the substrate. The adsorption energy for the Pb-up conformation is found to be -76.8 kcal/mol while it is only -47.6 kcal/mol for the Pb-down conformation. The Pb-up conformation is clearly preferred since it maximizes the vdW interactions between the phthalocyanine ring of the PbPc molecule and the HOPG substrate. In contrast, in the Pb-down conformation, only a part of the phthalocyanine ring is in close contact with the substrate, leading to weaker vdW interactions.
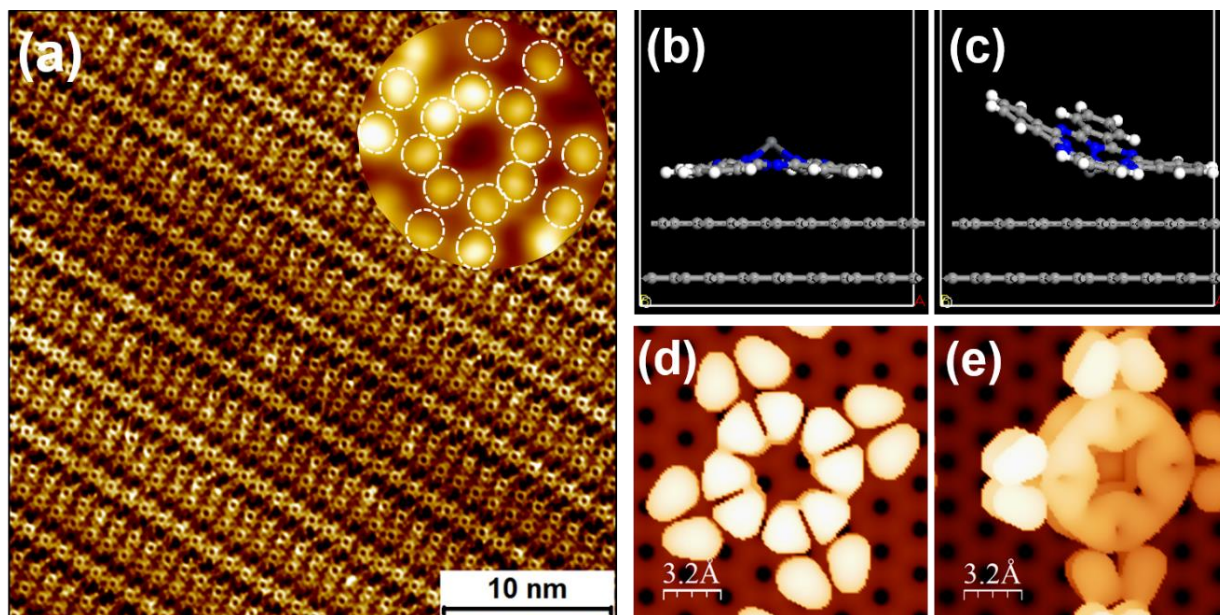
Figure 5. 10 (a) Self-assembly of PbPc at the HA/HOPG interface, with a zoomed image for a single PbPc molecule. Imaging parameters: I_{set} = 70 pA, V_{bias} = -1.29 V. Optimized atomistic models for Pb-up (b) and Pb-down (c) conformations and corresponding simulated STM images (d and e) at the experimental bias voltage, V= -1.29 V. Experimental STM image obtained by Gangamallaiah Velpula from KU Leuven.

The simulated STM images (see computational details in Appendix 5.2. Computational details of STM image simulations) for the Pb-up and the Pb-down adsorption conformation are shown in Figure 5. 10 (d) and (e), respectively. This enables a more direct comparison to the experimental image (see inset of Figure 5. 10 (a)) and determination of the molecular adsorption conformation within the experimental assembly. The simulated STM image for the Pb-up conformation is made up of 16 bright features, which is in line with the experimentally-obtained STM image. Most importantly, the center of the molecule (corresponding to the position of the lead atom) appears dark compared to the periphery of the molecule. In contrast, the simulated image for the Pb-down conformation has clearly different features: (i) a clear brightness gradient arises over the molecule where the upper-left part of the molecule is brighter than the lower-right part, which is attributed to the inclination of the PbPc molecule, and (ii) a non-zero response is also present at the molecular center. The simulated STM image of the Pb-down adsorption conformation clearly does not match with the experimental STM data.

While the experimental and simulated STM data obtained in this work agree closely, they differ from the experimental STM data reported recently by Nguyen *et al*. [16]. As depicted in Figure 5. 2, PbPc molecules appear with a bright central protrusion in their self-assembled network formed

on graphene on SiC under UHV conditions. In order to understand this difference, and to further ascertain the adsorption conformation of PbPc in our experiments, we simulated STM images at several bias voltages for the Pb-up configuration to cover the experimental conditions used in the work of Nguyen *et al.* and compared those data to the molecular frontier orbitals of PbPc. Note that the UHV-STM images were acquired at a bias voltage of -1.5V [16], whereas the STM data collected in the present experiments are recorded at a bias voltage of -1.29V.
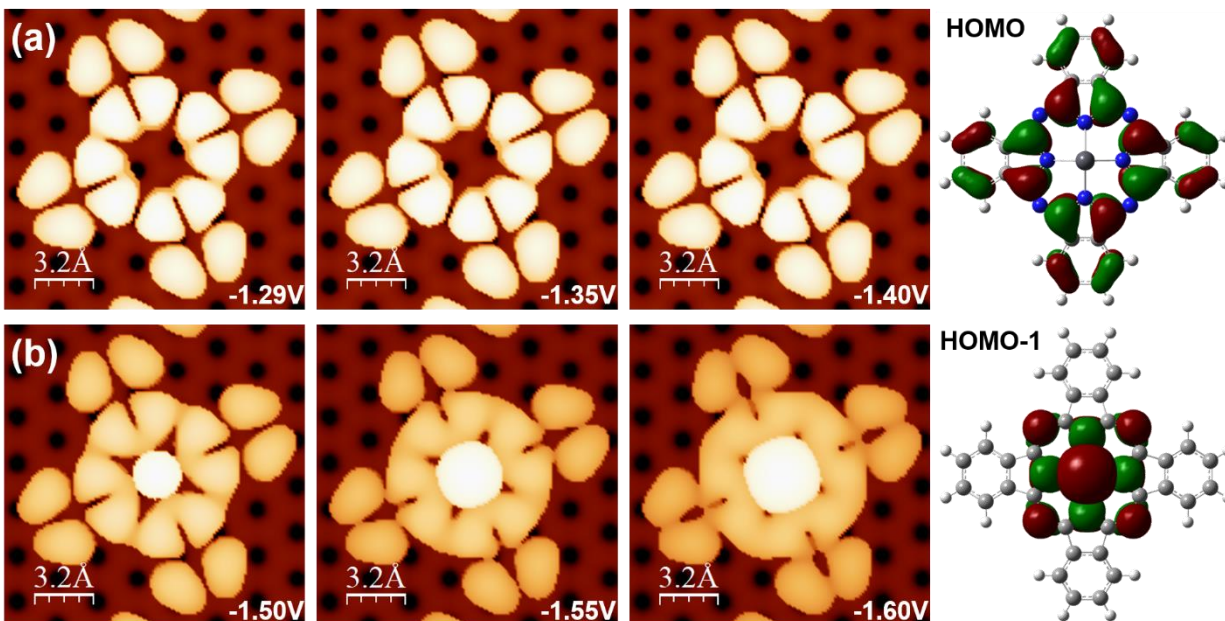
Figure 5. 11 Simulated STM images for the Pb-up conformation at different bias voltages, together with the HOMO and HOMO-1 orbitals of the PbPc molecule. The simulated STM images at the bias values used in this work and in ref [16] are shown in panel a and b, respectively.

Figure 5. 11 shows a series of simulated STM images at different bias voltages together with the frontier molecular orbitals of PbPc. Clearly, the patterns of the STM images are closely related to the shape of those orbitals. It can be noticed that at moderate bias voltage (i.e., -1.40V or a less negative value), only the HOMO orbital of PbPc contributes to the image. Since the HOMO has a node on the central atom, brightness at the molecular center is not expected, fully consistent with the aspect of the molecules in our experiments (see Figure 5. 10 (a)). Once the bias voltage is turned to more negative values (lower than -1.5V), additional contributions from the HOMO-1 orbital are present in the simulated image. In particular, the bright molecular center observed in Nguyen's experiments is reproduced by our simulations. Such a bright center is due to the contribution of the Pb atom, which is characteristic for the HOMO-1 orbital. We also find that the

intensities coming from the phthalocyanine ring are increasingly smeared out as the bias voltage becomes more negative. This is associated with the contributions in the HOMO-1 orbital from the four nitrogen atoms that connect the isoindole fragments of the molecule. More and more contributions from these nitrogen atoms are involved in the STM images as the bias voltage turns more negative. Combining the experimental data with all the simulated STM images, it is concluded that the PbPc molecules all have the "Pb-up" conformation in our experimental assembly, while the aspect of the molecular center is directly related to the shape of the molecular orbitals that are probed at a given bias voltage.

5.3.3. Long-range order in PbPc self-assembled molecular networks

Apart from the appearance of individual PbPc molecules in the experimental STM images, the second peculiar feature of the assembly lies in the arrangement of molecules perpendicular to the row direction. A small-scale STM image of the same domain as shown in Figure 5. 10 (a) is depicted in Figure 5. 12. It clearly shows that the assembly consists of alternating single and double rows of PbPc molecules separated by dark narrow gaps.
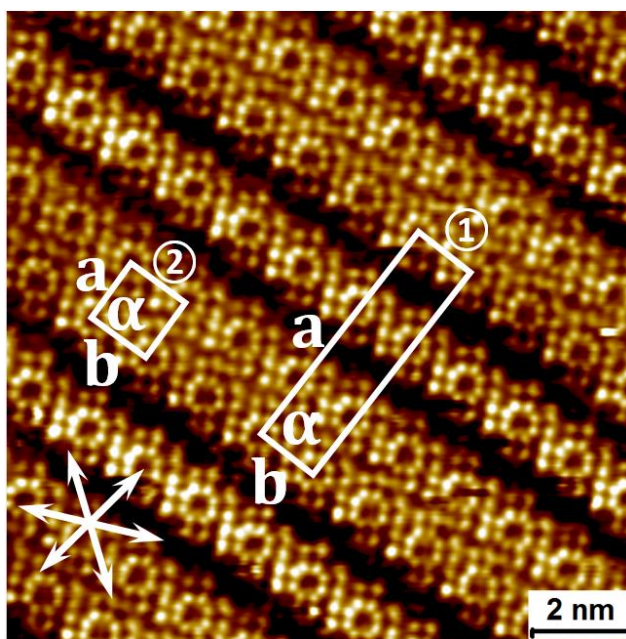
Figure 5. 12 Small-scale STM image with sub-molecular resolution. The graphite symmetry axes are shown in the lower left corner. The unit cells are overlaid on the STM image. Imaging parameters: Iset = 70 pA, Vbias = -1.29 V. Images obtained by Gangamallaiah Velpula from KU Leuven.

Within these rows, the relative orientation of molecules remains the same. Therefore, two sets of lattice parameters can be extracted from the images. The corresponding unit cells are also shown in Figure 5. 12: a rectangular one that encompasses the single row/double row alternation and a square one within the double rows. The lattice parameters for the rectangular unit cell are a=52±1Å, b=14±1Å and α=88±1°; the square unit cell has dimensions of a=b=14±1Å and α=88±1°.

Given that PbPc molecules do not possess any long peripheral alkyl groups, their conjugated cores are expected to form close-packed assemblies. In fact, when self-assembled under ultrahigh vacuum on the surface of graphene, PbPc indeed forms a close-packed SAMN without any gaps [16]. The formation of molecular rows separated by 'dark' narrow gaps thus appears to be specific to the solution/solid interface. Force field simulations are then employed to investigate the reasons for the formation of this particular molecular arrangement, based on the hypothesis that solvent co-adsorption may take place. The solvent used in the present experiments is heptanoic acid (HA). Co-adsorption of HA within molecular assemblies has been reported by Sirtl *et al*. [30]. In their work, the co-adsorption of the solvent molecules was inferred by comparing assemblies prepared in high-vacuum and at the solution/HOPG interface. Nevertheless, direct proof for the existence of co-adsorbed solvent molecules was not reported.

To understand the special molecular packing motif observed in our experiments, our modelling study starts from building several candidate assemblies including co-adsorbed solvent molecules that are packed differently; hereafter, these will be called 'co-assemblies'. Considering the structure of the HA molecule (see Figure 5. 13), two types of intermolecular interactions must be considered when investigating its packing within the self-assembly: the hydrogen bond between carboxylic groups and the vdW interactions between interdigitated alkyl chains.
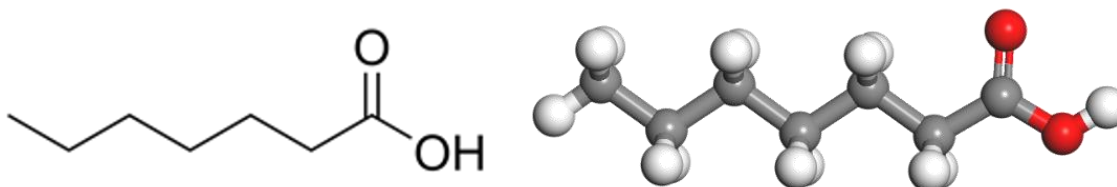
Figure 5. 13 Molecular structure and geometry of heptanoic acid

114

In the simulations, five PbPc assemblies with co-adsorbed solvent molecules are built in such a way that each co-assembly promotes one or both of those two interactions. Their unit cell parameters are kept the same as the experimental values (see Figure 5. 12). These co-assemblies are shown in Figure 5. 14. For a better visualization and easier comparison, the alkyl chains of some heptanoic acid molecules are highlighted by yellow sticks while the hydrogen bonds between neighboring molecules are circled in green.
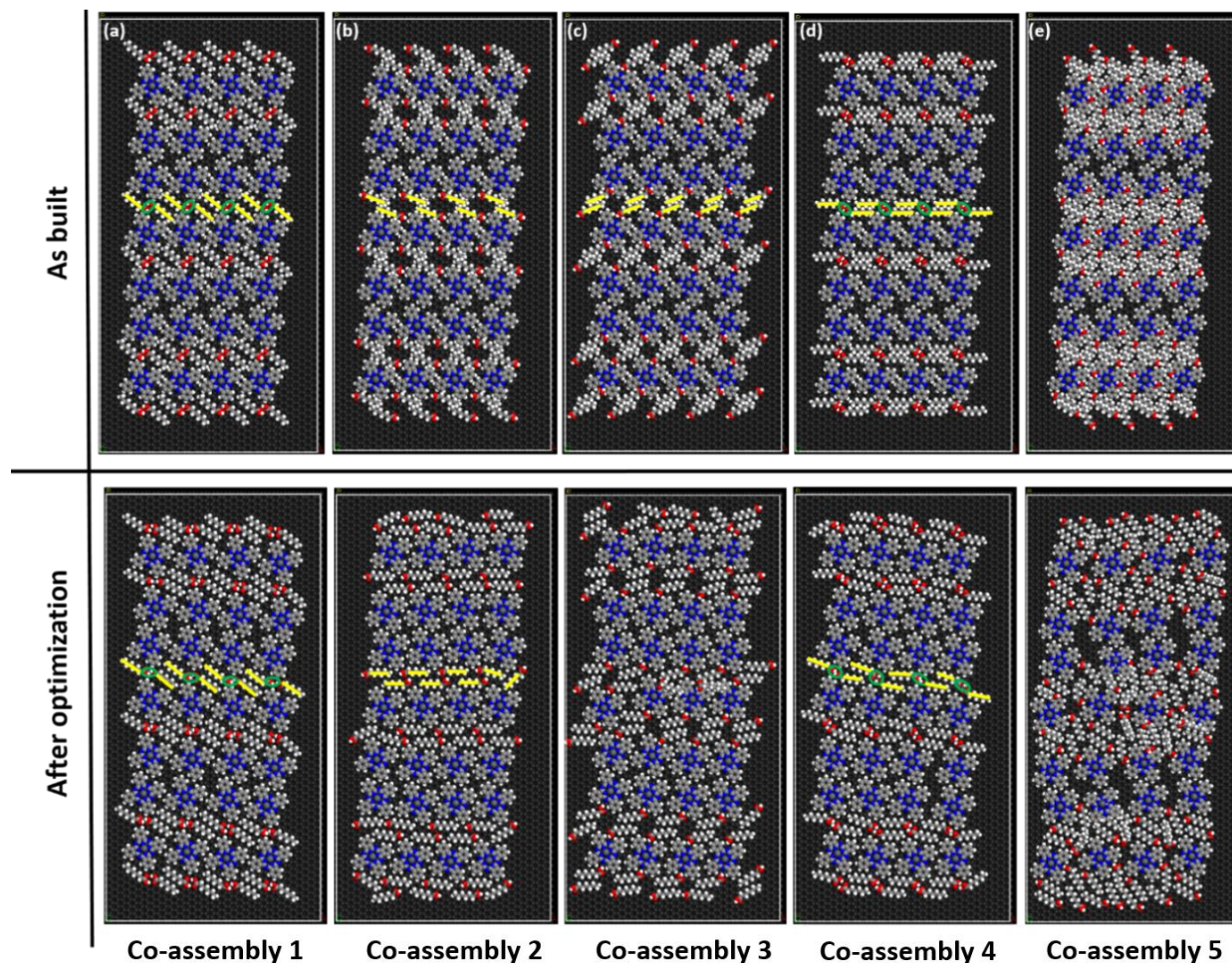
Figure 5. 14 Five candidate co-assemblies

HA molecules in co-assembly 1 interact solely through hydrogen bonds. In contrast, only vdW interactions between the interdigitated alkyl chains exist in co-assemblies 2 and 3. As for co-assembly 4, both interactions are present. In co-assembly 5, the largest possible number of HA molecules is filled into the void spaces between PbPc rows. However, it is difficult to distinguish a periodic pattern of hydrogen bonds or interdigitated alkyl chains in this packing. These five co-assemblies are then optimized in the force field simulations. After optimization, co-assemblies 3

and 5 turn into disordered systems, which is a sign of low structural stability. For co-assemblies 1, 2 and 4, the structural features are well-preserved in the optimized structures. However, the potential energy for co-assemblies 1 and 4 is significantly lower than that of co-assembly 2 (by 97 kcal/mol and 123 kcal/mol, respectively), i.e., these two co-assemblies are the most stable ones. This can be attributed to the fact that, after being optimized, solvent molecules in these two assemblies interact through both hydrogen bonds and vdW forces (see the highlighted yellow sticks and green circles), which is apparently not the case for co-assembly 2 where only vdW interactions exist between solvent molecules. In order to mimic the large-scale periodic self-assembly observed in the experiments and avoid boundary effects as much as possible, co-assemblies 1 and 4 are then expanded and further MM/MD simulations are carried out on them.

The input structures of the two expanded assemblies are shown in Figure 5. 15 (a) and (b), respectively. In the expanded co-assembly 1, solvent molecules are tilted and partly inserted into the PbPc rows while they are packed in a more parallel way to the PbPc rows in the expanded co-assembly 4. In both co-assemblies, we can define two types of unit cells, as in the experimental images (see Figure 5. 12): (1) the unit cell reflecting the 'single row-double row' alternation, and (2) the unit cell defining the arrangement of PbPc molecules within a double row.

Expanded co-assembly 1   **Expanded co-assembly 4**
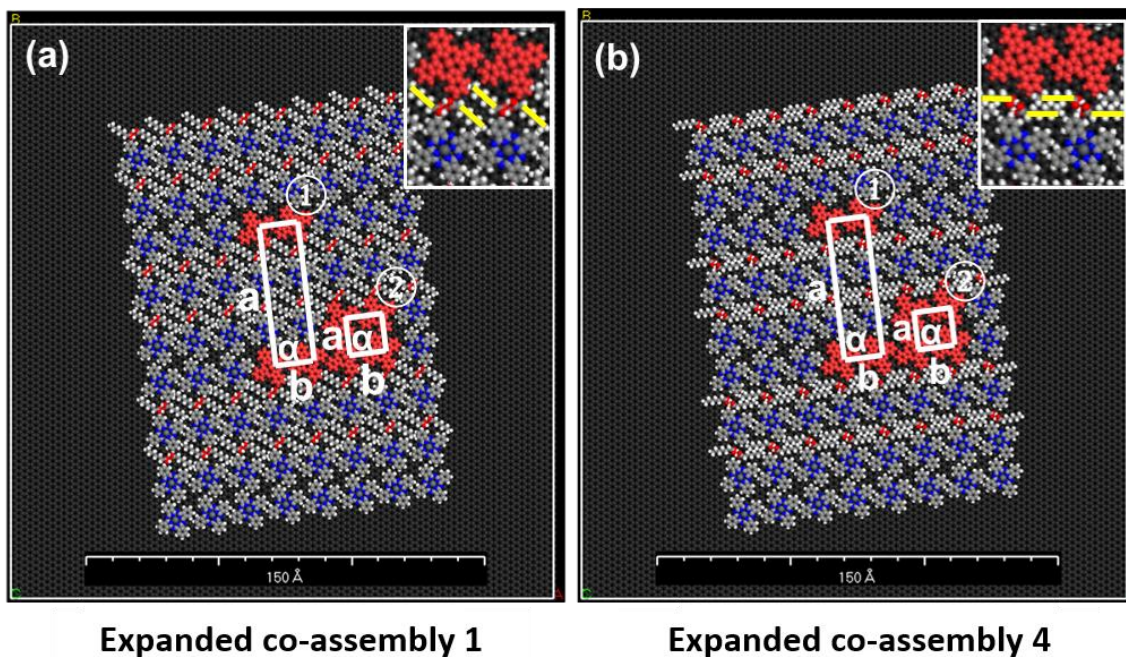
Figure 5. 15 Input structures for the expanded PbPc + HA co-assemblies overlaid with the two types of unit cell. Insets are the enlarged central part of the model where the tilted- and parallel-packed solvent molecules are represented by yellow sticks. The unit cell parameters have been set at the experimental values.

These structures are then optimized and further refined by quench MD simulations. The quench MD simulation is a protocol used to refine the geometry of the initially-optimized structures and avoid the structure being trapped in local minima. The principle of the quench MD scheme is shown in Figure 5. 16.
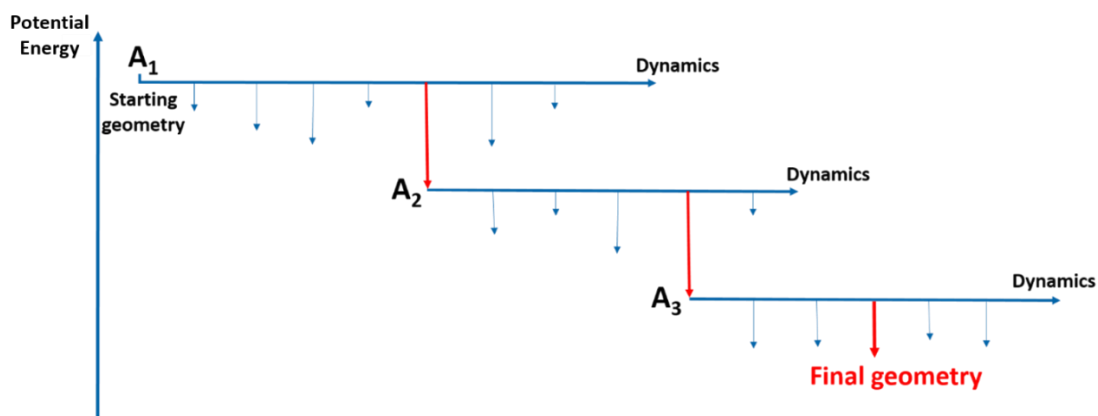
Figure 5. 16 Principle of the quench MD simulations

Compared to classical MD simulations, additional optimizations are performed periodically during each MD run; those optimization steps are represented by the vertical arrows in Figure 5. 16. The most stable structure from a given MD run, which is represented by the red arrow, is then used as the starting point for the next round of MD simulations. This process is iterated until all optimized structures from the same MD run have a very similar energy and the geometry of the most stable structures from neighboring MD runs do not show large deviations. In our case, the two optimized expanded co-assemblies are used as the starting point for the quench MD refinement. A 25ps-long MD simulation is performed at 50K for each of them. Every 0.25ps, the structure is fully optimized. Therefore 100 optimized structures are obtained from each MD run. A relatively low temperature is used because, although expanded, the model is still only a segment of the experimental assembly. The organization of the modelled co-assembly cannot be kept if a higher temperature is applied, because of growing disorder originating from the dynamics of the edges. Meanwhile, instead of trying to predict the assembly organization from scratch, we use this quench MD scheme for refining those initially-optimized co-assemblies whose structures are based on the experimental observations. Taking these into consideration, a higher temperature, which causes larger thermal disturbances to the co-assembly organizations, does not bring extra benefits and therefore is not necessary. The most stable structures for the two expanded co-assemblies from the quench MD refinement are depicted in Figure 5. 17.

117

Expanded co-assembly 1   **Expanded co-assembly 4**
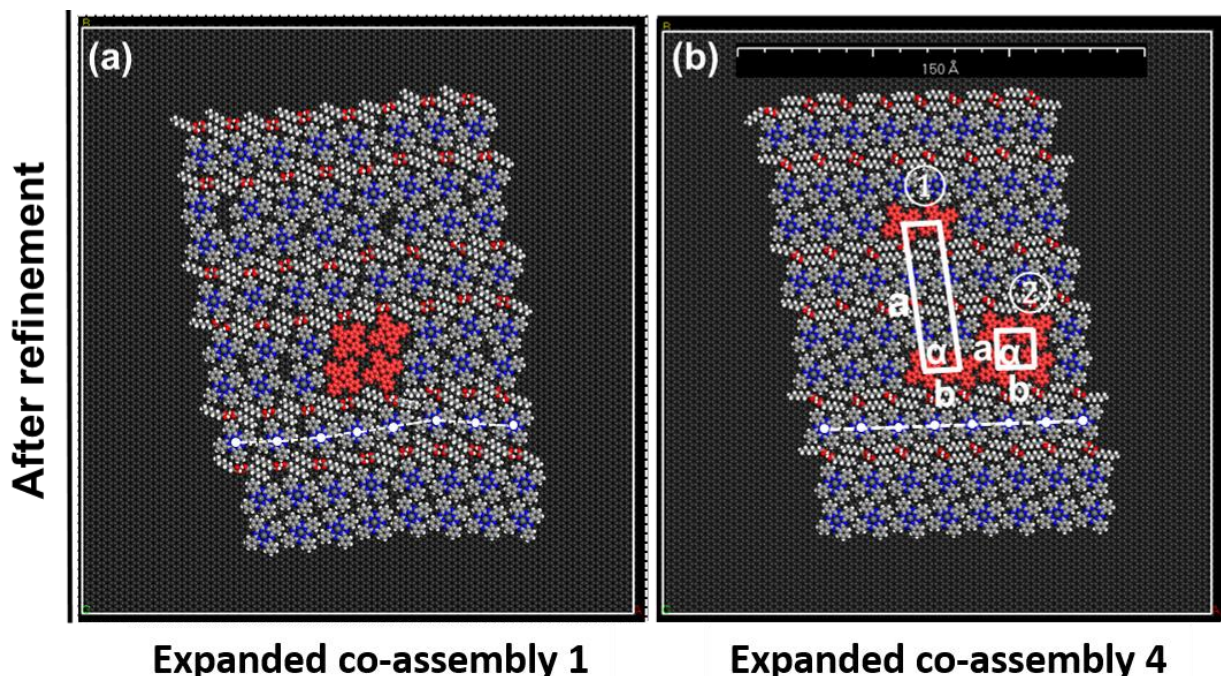
Figure 5. 17 The most stable structure from the quench MD refinement for each expanded co-assembly.

One big advantage of using force field simulations is that it enables us to compare the potential energy, and hence the structural stability, of different structures in an explicit way. After the refinement, we compare the potential energy (PE) of these two co-assemblies. The PE of each co-assembly is partitioned into three major contributions, namely: valence (VE), van der Waals (vdW) and Hydrogen-bonding (HB) energy, which are summarized in Table 5. 4.

Table 5. 4 Potential energy and its decomposition for the two expanded co-assemblies after refinement, together with their energy difference (in kcal/mol)

Structure	PE	VE	vdW	HB
Assembly 1	-27662.9	10377.0	-4922.5	-274.5
Assembly 4	-27767.8	10350.8	-4978.8	-301.9
Energy difference ($E_{assembly4}$-$E_{assembly1}$)	-104.9	-26.2	-56.3	-27.4

The data shows that co-assembly 1 is less stable than co-assembly 4 by about 105 kcal/mol. Such difference is explained by less favored intermolecular interactions in co-assembly 1, which is confirmed by less negative vdW and HB energies there. In addition, higher (i.e., more positive) VE energy in co-assembly 1 suggests that higher intramolecular strain exists in this co-assembly. In other words, molecules belonging to co-assembly 1 must experience some distortions to

118

maintain the structure. We hypothesize that the unfavorable energetics of co-assembly 1 are related to the less organized structure, which is evidenced by the geometry of the co-assembly shown in Figure 5. 17 (a). After being refined, solvent molecules in co-assembly 1 partly insert into the neighboring PbPc rows, leading to some disordering: (i) clear variations in the molecular orientations between neighboring PbPc molecules in the double row (four molecules with different orientations have been highlighted in red in Figure 5. 17 (a)); (ii) molecular misalignment is also manifest within the single row. Such misalignment is exemplified by the white dashed line in Figure 5. 17 (a). This line connects the Pb atoms of neighboring molecules and it clearly shows that, even in the same row, the PbPc molecules are not aligned with their neighbors. In contrast, supramolecular order is much better in the expanded co-assembly 4. For this reason, the expanded co-assembly 4 is selected and compared to the experimental structure (Figure 5. 18).
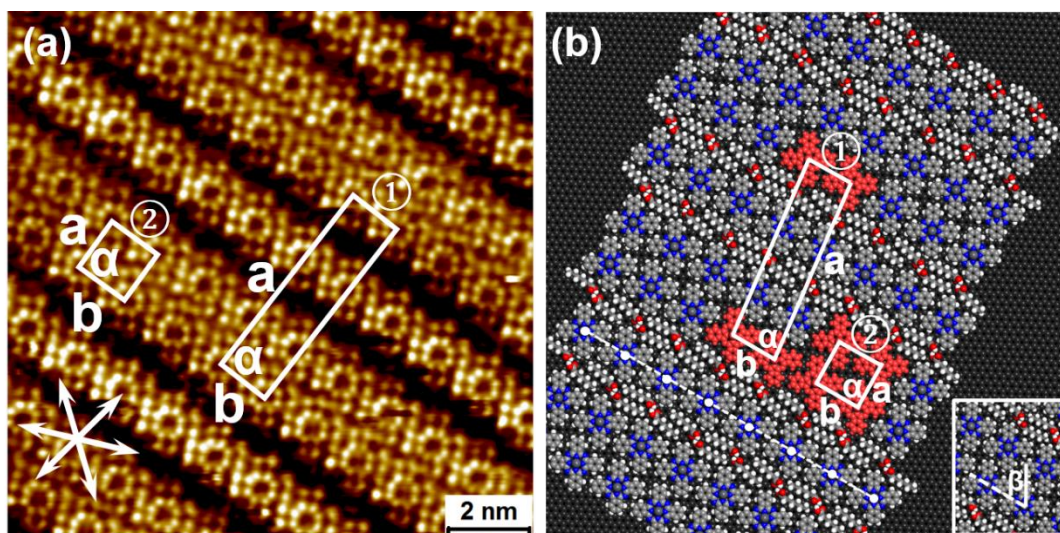
Figure 5. 18 (a) Small-scale STM image with sub-molecular resolution. The graphite symmetry axes are shown in the lower left corner. The unit cells are overlaid on the STM image. Imaging parameters: Iset = 70 pA, Vbias = -1.29 V. (b) Quench MD-refined atomistic model for the expanded co-assembly 4. Experimental STM image obtained by Gangamallaiah Velpula from KU Leuven.

In Figure 5. 18 (b), the solvent molecules between PbPc rows are paired by hydrogen bonds without disturbing the organization of the surrounding PbPc molecules. In addition, all PbPc molecules are oriented in the same way and they are perfectly aligned within the rows, explaining the more favorable energetic stability of this modelled co-assembly. Similar to the experiment, two types of unit cell are extracted and illustrated in the Figure 5. 18 (b). Unit cell 1 is almost rectangular with dimensions of a=55.3 Å, b=13.8 Å and α=83.0°, while molecules within the PbPc

double rows pack into a quasi-square unit cell, namely unit cell 2, with parameters a=b=13.8 Å, and $\alpha = 88.5°$. Inside each molecular row, the PbPc molecules are rotated with respect to the row axis by $\beta=62\pm0.6°$. The lattice parameters for the unit cells of the experimental and the modelled co-assemblies are compared in Table 5. 5.

Table 5. 5 Lattice parameters of the two unit cells in the experimental and modelled co-assemblies

	Unit cell 1		Unit cell 2	
	Experimental	**Modelled**	**Experimental**	**Modelled**
a / Å	52 ± 1	55.3	14 ± 1	13.8
b / Å	14 ± 1	13.8	14 ± 1	13.8
α / °	88 ± 1	83.0	88 ± 1	88.5
β / °	$61.5 \pm 1.7°$	$62.0 \pm 0.57°$	$61.5 \pm 1.7°$	$62.0 \pm 0.57°$

The lattice parameters of the experimental and simulated co-assemblies show an excellent agreement. The slight deviation found for unit cell 1 can be explained by the fact that mobile solvent molecules are included in this unit cell. As a comparison, unit cell 2 is constituted of PbPc molecules only and the lattice parameters of the modelled co-assembly agree even better with the experimental values. The calculated parameters for unit cell 2 also show an excellent agreement with the experimental measurements for PbPc assemblies formed in high vacuum [16]. Through these comparisons, a convincing match between the experimental and modelled assembly is found, which confirms the accurate description of the PbPc assembly by our model.

This model also includes the solvent co-adsorption, leading to the special alternating row arrangement observed in the experiments. The specific '*single row-double row*' organization is considered to stem from a possibly better registry between PbPc rows and the HOPG substrate when adsorbed in this periodicity. Although direct observation of solvent molecules by STM is always challenging because of their high mobility. In the present experiments, bright wavy stripes between PbPc molecular rows are imaged occasionally. One example is shown in Figure 5. 19 (a). In this STM image, bright wavy strips between PbPc rows are clearly observed, which is interpreted to be the co-adsorbed solvent molecules. One pair of bright spots that appear periodically along those wavy structures is labelled by a white rectangle. This can be linked to the hydrogen bonds between the paired solvent molecules as it is revealed by the atomistic model

shown in the panel (b). This agreement further confirms the success of the solvent co-adsorbed model we built in order to understand the experimental assembly behavior of PbPc molecules.
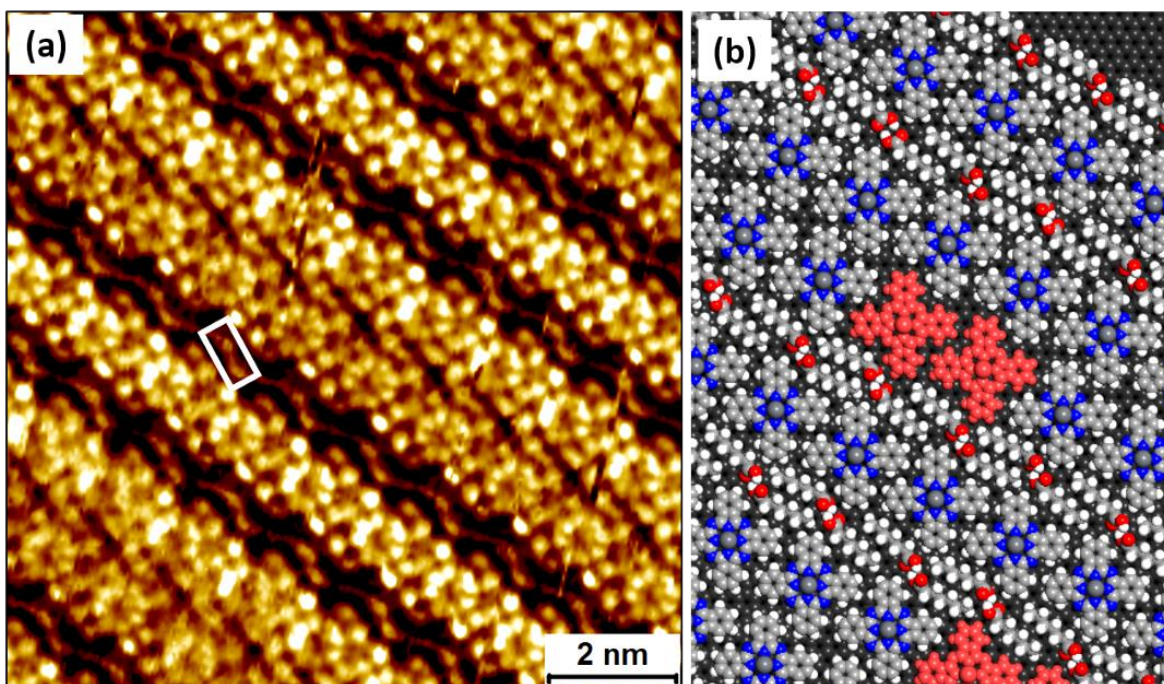
Figure 5. 19 (a) Experimental STM image that shows bright wavy stripes between PbPc molecular rows (b) Atomistic model of the HA/PbPc co-assembly, extracted from Figure 5. 18 (b), showing the arrangement of PbPc molecules together with the rows of hydrogen-bonded heptanoic acid molecules. Experimental STM images obtained by Gangamallaiah Velpula from KU Leuven.

The ability of solvent molecules to co-adsorb within the assembly network can in principle provide a possibility to control the width of the gap between PbPc rows, in other words, the assembly behavior of PbPc molecules. However, co-adsorption of solvent molecules is rather difficult to control and can hardly be used as a design strategy in real experiments. One typical way to modify the packing scheme of molecules at the solution/substrate interface is to use a different solvent in the same category (in our case, a carboxylic acid with different alkyl groups). In the current co-assemblies, however, HA molecules co-adsorb with their alkyl chains parallel to the PbPc rows. Therefore, the gap width between PbPc rows is not expected to change even if a solvent with longer alkyl chains is employed.

5.4. Crystal growth templated by the self-assembled molecular networks of PbPc

The specific alternating row arrangement observed in the PbPc monolayers formed at solution/substrate interface has been explained by the solvent co-adsorption. Nevertheless, in order

to investigate whether a thin film growing from a PbPc monolayer can generate the known bulk polymorphs or a substrate-induced polymorph of PbPc, we remove the solvent molecules and build compact PbPc multilayer assemblies. This choice is based on the fact that multilayer formation is rarely observed at the solution/substrate interface and is more relevant to deposition in dry conditions (e.g., by vacuum sublimation). Top and side view of the optimized atomistic model for the compact monolayer assembly are shown in Figure 5. 20 (a) and (b), respectively.
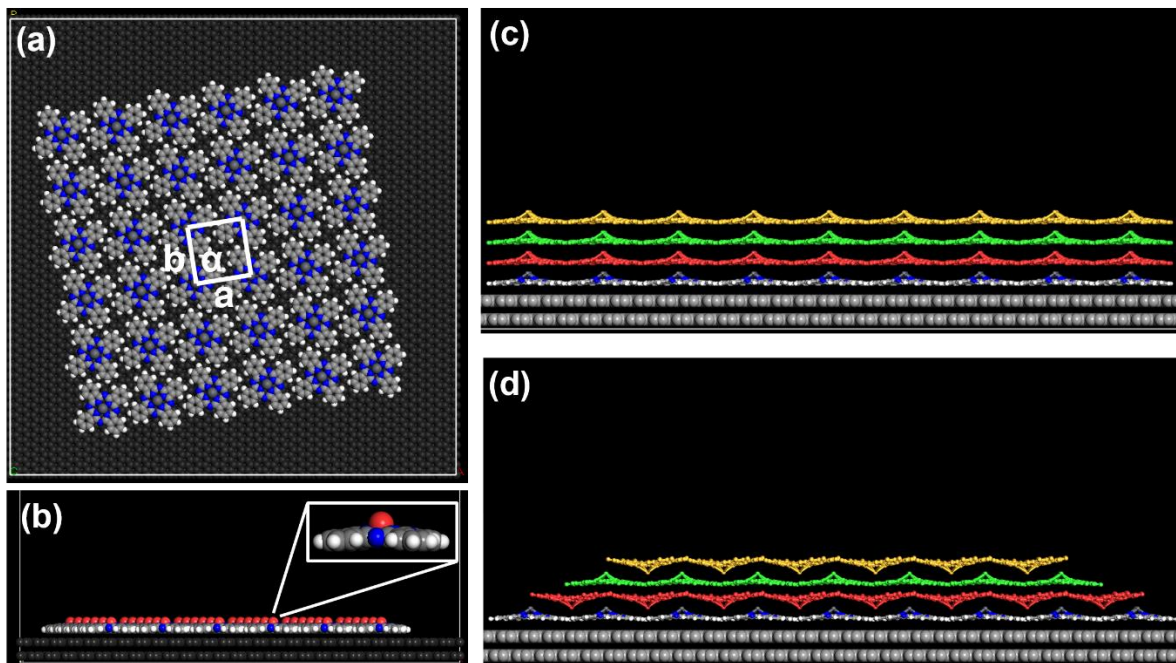
Figure 5. 20 (a) Top view of the optimized compact PbPc assembly. Unit cell parameters: a = b =13.7 Å, α = 90°. These parameters agree well with the PbPc assemblies deposited in high vacuum [16]. (b) Side view of the compact PbPc assembly after optimization, where all molecules are in Pb-up conformation, as shown in the inset. All Pb atoms are red-colored for better visualization. (c) Multilayer structures of PbPc grown from a compact assembly in columnar stacking. (d) Multilayer structures of PbPc grown from a compact assembly in alternating stacking. PbPc molecules in different layers are colored differently.

In this compact monolayer assembly, all PbPc molecules adsorb in the preferential Pb-up conformation. They stay on the same plane due to the geometric confinement exerted by the flat HOPG substrate. However, such organization is not present in either the bulk monoclinic or the triclinic phase of PbPc (see Figure 5. 3), which indicates the possibility to grow a substrate-induced polymorph of PbPc from this assembly, instead of generating the known bulk phases directly. The growth of a possible SIP is first studied in simulations, where it is modelled by successive adsorption of up to four molecular layers. Here, two possible growth modes are proposed:

122

columnar stacking (Figure 5. 20 (c)) and alternating stacking (Figure 5. 20 (d)). Columnar stacking is similar to the bulk monoclinic phase of PbPc, except that all PbPc molecules keep the same orientation. As for the alternating stacking, molecules in adjacent layers have different orientations and are packed alternatingly in either "face to face" (*e.g.,* between the 1st and 2nd layer) or "back to back" (e.g. between the 2nd and 3rd layer) arrangement. The existence of such alternating stacking is deduced from spectroscopic measurements on a PbPc bi-layer structure [31, 32], but no related information exists on thicker multilayer structures. To evaluate the structural rigidity and energetic stability of these two stacking organizations, MM and MD simulations are performed.

5.4.1. Molecular Mechanics simulations of PbPc grown in columnar stacking

The optimized columnar stacking of PbPc molecules is shown in Figure 5. 21. It can be seen from panel (a) that the upper layers (the 2nd, 3rd and 4th layer) of molecules shrink in the lateral direction after the optimization. This shrinkage is also visible in the side view of the optimized columnar stacking (panel (b)), where the boundary of the upper layers is highlighted by two white vertical bars. Furthermore, the zoomed-in image of the central region of this columnar-stacked multilayer (Figure 5. 21(c)) shows that molecular columns have different orientations. As an example, the misorientation among three molecular columns is illustrated by three arrows. The appearance of such disorder suggests that a long-range, periodic organization of PbPc molecules, i.e., crystalline structures, cannot be built on the basis of this columnar stacking.
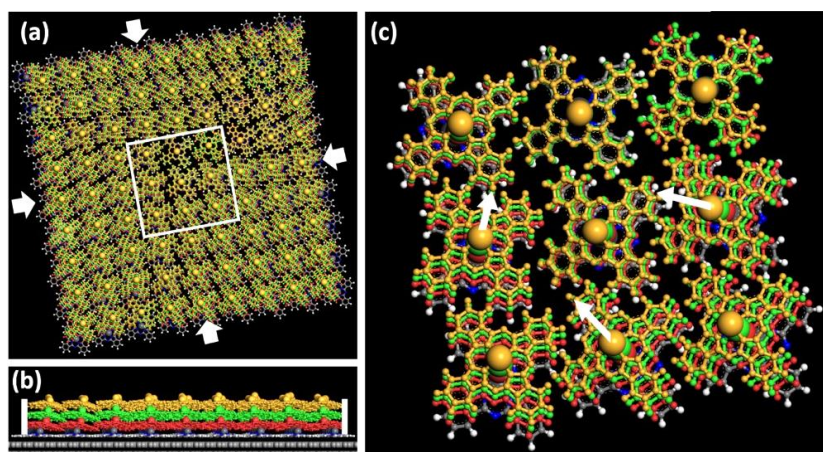
Figure 5. 21 Top view (a) and side view (b) of the optimized columnar-stacked PbPc multilayer. (c) Zoomed-in central region of this PbPc multilayer, corresponding to the white square in (a), which shows a more detailed molecular arrangement.

5.4.2. Molecular Mechanics and dynamics simulations of PbPc grown in alternating stacking

Following the same strategy, the PbPc multilayer structure in alternating stacking is also optimized using force field simulations. Unlike the columnar stacking, the alternating-stacked PbPc multilayer preserves a highly-ordered structure after the optimization. The optimized structure is therefore further refined by the quench MD scheme. The most stable structure from the quench MD refinement is shown in Figure 5. 22 (a) and (b). The geometry features in the input structure of the alternating stacking are well-retained, which already indicates a superior structural stability for PbPc molecules to be packed in this manner on top of its self-assembled monolayer.
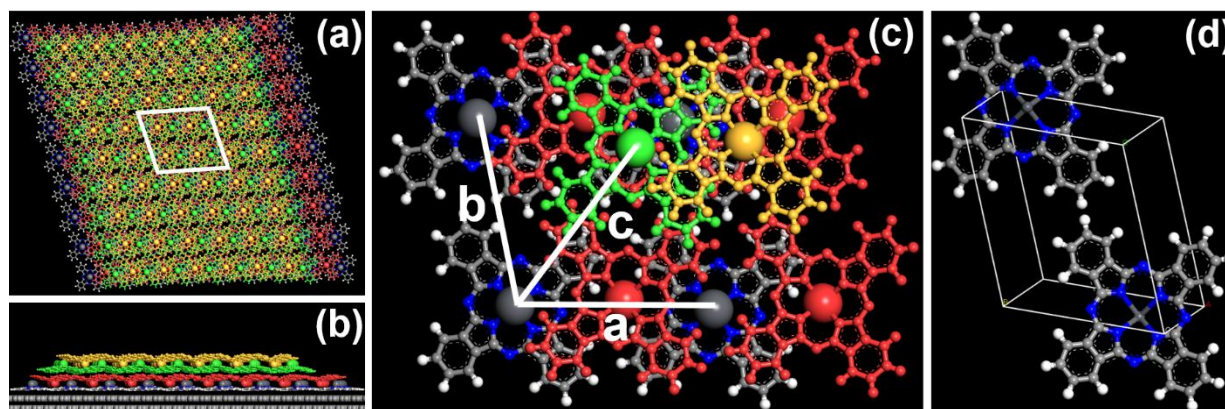
Figure 5. 22 Top view (a) and side view (b) of the refined alternating-stacked PbPc multilayer. (c) Zoomed image of the region corresponding to the white parallelogram in (a), which shows a more detailed molecular arrangement and three lattice parameters to define the SIP. (d) Unit cell of the proposed PbPc SIP after Niggli cell reduction.

To have a better understanding about the energetic features of the alternating stacking, the interaction energies between neighboring molecular layers are calculated based on the following equation:

$$E_{(i+1)th-ith} =$$

$$\frac{E_{total\ energy\ of\ adsorbed\ (i+1)\ layer} - E_{total\ energy\ of\ adsorbed\ i\ layer} - E_{energy\ of\ freestanding\ (i+1)th\ layer}}{N_{(i+1)th\ layer}}$$

The term on the left side is the interaction energy between neighboring layers. On the right side, three terms are in the numerator. They represent the total potential energy when *(i+1)* layer(s) of molecules adsorb on the substrate, the total potential energy when *i* layer(s) of molecules adsorb on the substrate and the potential energy of the freestanding *(i+1)th* molecular layer. This energy difference is then normalized to the number of molecules in the *(i+1)th* layer. The results are summarized in Table 5. 6.

Table 5. 6 Interaction energy (per molecule) between neighboring layers in the refined alternating stacking of PbPc.

	Interaction energy per molecule (Kcal/mol)
1st layer & HOPG	-72.9
2nd & 1st layer	-58.1
3rd & 2nd layer	-53.5
4th & 3rd layer	-58.6

The calculation shows the existence of a stronger interaction ($\simeq$ - 58 vs. $\simeq$ - 53 kcal/mol) between "face to face" stacked molecules. This provides a solid proof for the bi-layer growth mechanism assumed in previous experimental studies [32, 33], based on which the PbPc thin film grows per "face to face" stacked dimer and molecules have alternating orientations in adjacent layers. In all force field simulations performed for the alternating-stacked PbPc multilayers, the HOPG substrate is always included. Combined with its excellent structural rigidity and energetic stability, it is therefore reasonable to hypothesize that a PbPc SIP can possibly be derived from this alternating packing manner.

Figure 5. 22 (c) shows the enlarged central region of the alternating-stacked multilayer, corresponding to the white parallelogram in Figure 5. 22 (a). The color code for molecules belonging to different layers stays the same as above: molecules in the second, third and fourth layer are colored in red, green and orange, respectively. It is very clear that molecules in different layers have exactly the same orientation, which makes it feasible to define a unit cell for the possible SIP from this multilayer structure. Three lattice parameters a, b and c of the possible SIP are illustrated in Figure 5. 22 (c). The Niggli cell reduction [34] is performed to improve the highly-skewed unit cell that is extracted directly from the multilayer structure. This reduction provides a unique representation of the basis vectors for a given lattice. The reduced unit cell keeps the volume of the original cell but has the lowest sum of lattice vectors and its lattice angles are closer to 90 degrees. After reduction, a triclinic unit cell belonging to the P-1 space group is obtained for the predicted SIP (Figure 5. 22 (d)). There are two molecules within the unit cell and the lattice parameters are: $a = 7.70$ Å, $b = 12.23$ Å, $c = 13.30$ Å, $\alpha = 71.39°$, $\beta = 80.70°$ and $\gamma = 78.09°$. The density of this predicted SIP unit cell is 1.91 g/cm^3, which is only 1% and 2.5% lower than

the values for the bulk triclinic and monoclinic phases of PbPc, respectively. Such difference is quite reasonable when comparing the density of SIPs and bulk polymorphs for a given compound.

5.5. Experimental crystal structure determination of PbPc thin films

To validate the predicted SIP, PbPc thin films were prepared on TEM graphene grids via PVD (By Noopur Jain from EMAT, UANTWERPEN) with a thickness ranging from 5nm to 30nm. Their crystal structures were then investigated by STEM (See Appendix 5.3. Experimental details of the STEM measurementsfor more experimental details). One big advantage of using graphene grids is that they are chemically similar to the HOPG substrates used in the self-assembly experiments. Such similarity makes the crystallization of PbPc in 2D (SAMN) and 3D (thin films) more comparable, from which their connections can be studied reliably. Although the PbPc thin films are prepared in dry conditions instead of the solution environment as for the SAMNs, it is reasonable to hypothesize, based on the reported STM studies [16], that the first molecular layer in the thin films still adsorbs on the graphene grids in the Pb-up conformation, as in the self-assembly from solution and as determined from the modelling.
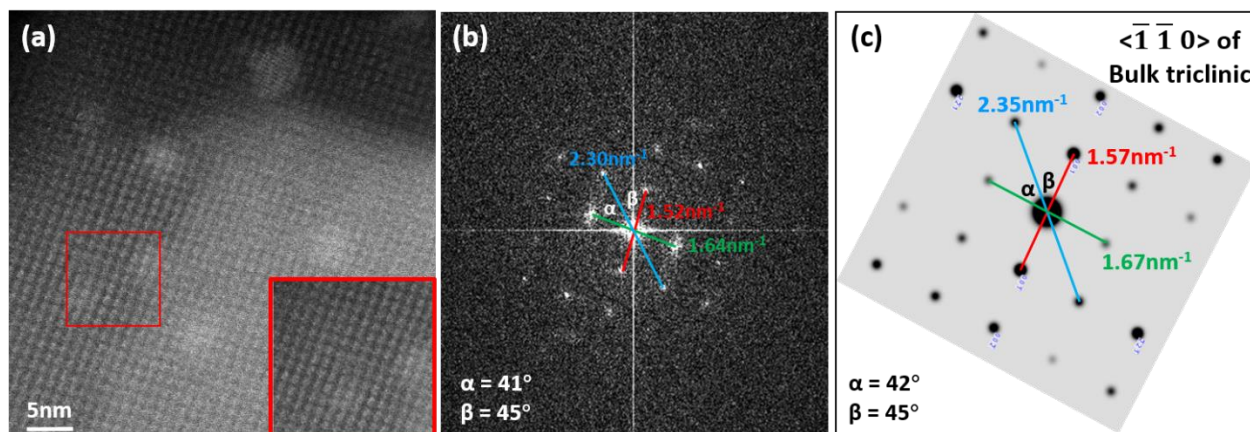
Figure 5. 23 (a) STEM image of the PbPc thin film deposited on the TEM graphene grids. (b) FFT pattern of the STEM image. (c) Simulated diffraction pattern from the <$\bar{1}\,\bar{1}$ 0> zone axis of bulk triclinic phase of PbPc. Simulated diffraction pattern generated by SingleCrystal™, CrystalMaker Software Ltd, Oxford, England. STEM image acquired by Noopur Jain from EMAT.

One representative STEM image of the prepared thin films is shown in Figure 5. 23(a). The signal-to-noise ratio of this image is not perfect, which is attributed to the low electron dose used during the acquisition of the image. Nevertheless, the low-dose imaging enables a better control of the

electron beam damage towards the PbPc crystals, enabling the periodic lattice to be distinguished from the image regardless of the noise. It must be emphasized that capturing such an image is very challenging since PbPc crystals are extremely sensitive to the high-energy electron beam used in the STEM. To determine the crystal phase within the thin films, the FFT pattern of this image (Figure 5. 23 (b)) is then indexed with respect to three polymorphs of PbPc: the two previously known bulk polymorphs and the SIP predicted from the modelling. The indexation is illustrated in the Figure 5. 23 (b), which is done by measuring distances of three Friedel diffraction pairs located closest to the center of the FFT pattern. The excellent agreement with respect to the theoretical diffraction pattern along the $<\bar{1}\,\bar{1}\,0>$ zone axis of the bulk triclinic polymorph (see Figure 5. 23(c)) evidences the existence of this polymorph within the thin films.

The FFT pattern is also compared with theoretical diffraction patterns of the predicted SIP along different zone axes; however, the agreement there is far from satisfactory. One hypothesis for the absence of the predicted SIP in the thin films is that, although chemically similar, the graphene grids still promote crystallization in different ways compared to the HOPG substrate used in the self-assembly experiments and modelled during the prediction of SIP. Therefore, in addition to the STEM analyses, specular X-ray diffraction and grazing incidence X-ray diffraction (GIXD) measurements were performed (By M. Kaltenegger et al, TU Graz) on PbPc thin films deposited on HOPG by PVD (see Appendix 5.4. Experimental details for thin film preparation and the X-ray diffraction measurements for experimental details); the typical thickness of those samples is in the 20-40 nm range. Specular X-ray diffraction measurements are first carried out to probe the out-of-plane periodicities of the thin films and the result is depicted in Figure 5. 24 (a)
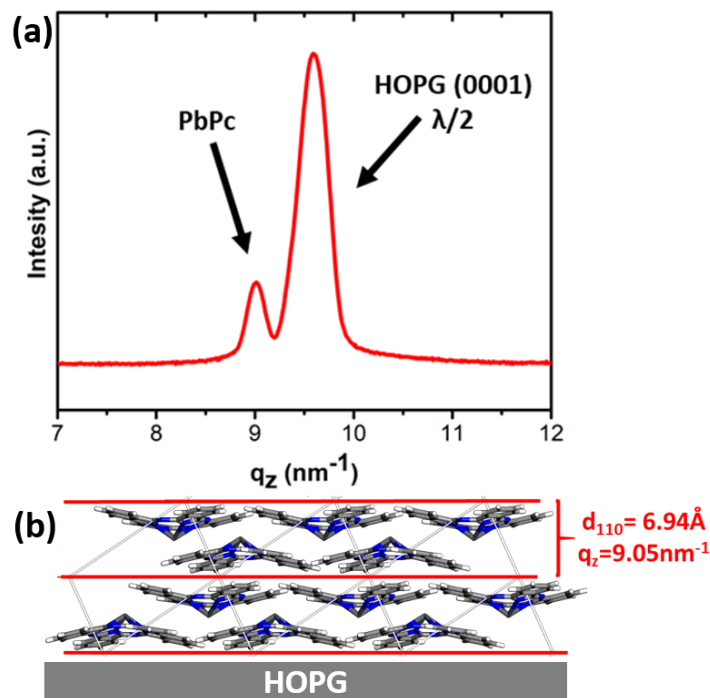
Figure 5. 24 (a) Specular X-ray diffraction pattern of a PbPc thin film with a thickness of ~40 nm. (b) Molecular model showing the simulated SIP in the orientation determined by the specular X-ray diffraction: the (110) plane of the simulated SIP is parallel to the substrate, with $d_{110} = 6.94$ Å and corresponding $q_z = 9.05 nm^{-1}$. XRD measurements performed by Martin Kaltenegger from TU Graz.

Diffraction peaks are found at $q_z = 9.01$ nm^{-1} and 9.48 nm^{-1}, which correspond to d-spacings of 6.97 Å and 6.63 Å, respectively. The d-spacing of the first peak is in an excellent agreement with the interplanar distance of the (110) planes ($d_{110} = 6.94$ Å) of the simulated SIP. The second peak at 9.48 nm^{-1} (6.63 Å) is related to the HOPG substrate. The preferred orientation of the crystallites within the experimental thin film can be accordingly determined: the (110) plane of the simulated SIP is parallel to the substrate. With this orientation, the C4 symmetry axis of the PbPc molecules is perpendicular to the substrate, as shown in Figure 5. 24 (b).

After the out-of-plane order of the thin films is determined by specular X-ray diffraction, the in-plane order is probed by the GIXD measurements (see Figure 5. 25). Strong and clear Bragg peaks in the pattern indicate a highly crystalline structure within the thin films. The pattern is then indexed with respect to the SIP predicted from molecular modelling. The indexation is based on the fact that the (110) plane of the predicted SIP is parallel to the substrate, as it is determined by specular X-ray diffraction measurements. The final result is shown in the right side of Figure 5. 25.
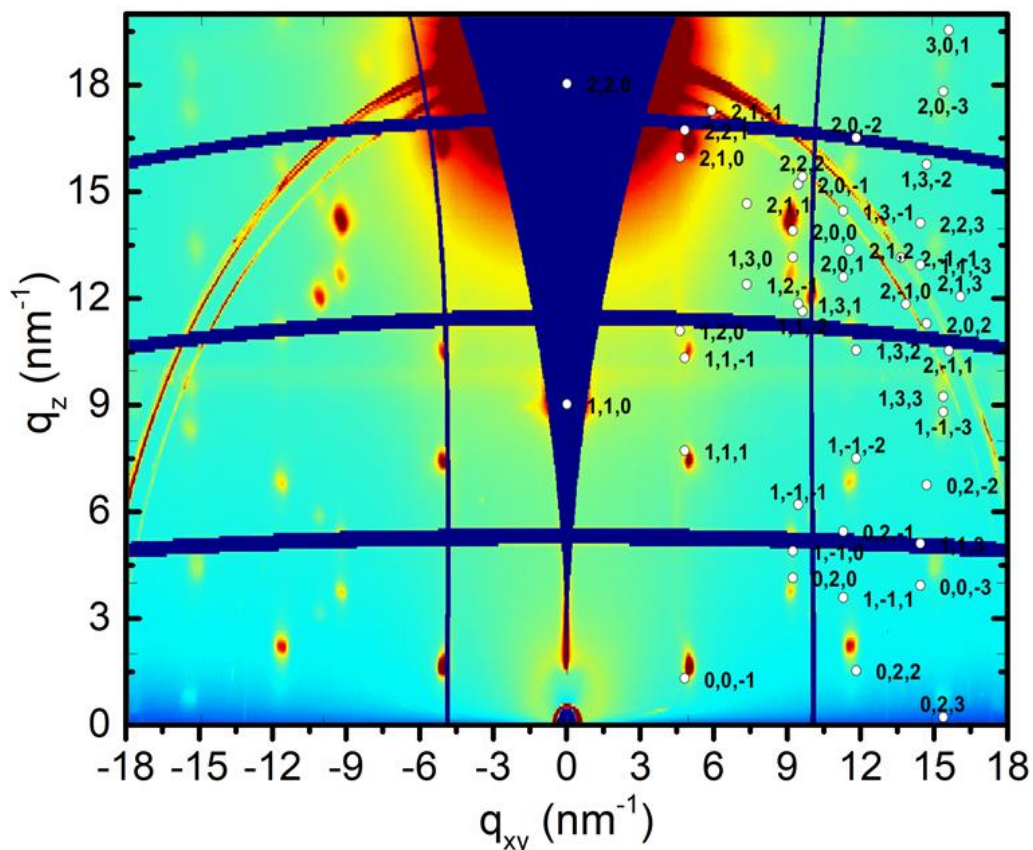
Figure 5. 25 Grazing incidence X-ray diffraction pattern of the PbPc thin film depicting both the raw pattern (left side) and the indexed pattern based on the predicted SIP from modelling (right side). XRD measurements and indexation performed by Martin Kaltenegger from TU Graz.

Here, the theoretical position of each peak based on the predicted SIP is represented by a white dot. Considering the fact that the SIP is predicted based only on the successive adsorption of molecules in the simulation without any experimental inputs, the overall agreement between experimental and theoretical peak positions is remarkable. In parallel, attempts were made to fit the experimental GIXD data with respect to the known bulk triclinic phase of PbPc. However, those fittings are far from satisfactory. This further indicates that a new SIP for PbPc has been identified from the molecular modelling and confirmed by the experimental thin film X-ray diffraction measurements. In spite of the very good overall agreement, some deviations between experimental and theoretical peak positions are still present in Figure 5. 25. To better understand such deviations, the unit cell parameters for PbPc crystals in the thin films are determined from the experimental pattern using the GIDInd software [35] and compared with the originally predicted SIP. The results are shown in Table 5. 7.

Table 5. 7 Unit cell parameters of the PbPc SIP determined from molecular modelling and experimental pattern. Experimental determination of unit cell parameters done by Martin Kaltenegger from TU Graz.

	Molecular model prediction	Experimental determination
a / Å	7.70	8.14
b / Å	13.23	12.86
c / Å	13.30	13.03
α / °	71.39	68.41
β / °	80.70	80.95
λ / °	78.09	81.21
V / Å³	*1250*	*1245.8*

The experimental pattern gives a very comparable unit cell with respect to that predicted by the molecular modelling. The energetic stabilities of these two unit cells are then evaluated by MM simulations. The lattice parameters of the originally predicted SIP unit cell are adapted to the values determined from the experimental pattern, while the molecular arrangement within the unit cell is kept the same. The geometry optimization calculations are performed on both the originally predicted unit cell and the one after the adaptation of lattice parameters. During the optimization, the unit cell parameters are held constant. The calculations show that the energy difference between these two unit cells is only 0.8 kcal/mol. In other words, these two unit cells are energetically equivalent. After the successful prediction of the lattice parameters by the molecular modelling is confirmed, the molecular arrangement within the predicted lattice is examined by comparing its associated squared structural factors to the experimental intensities. Figure 5. 26 shows the experimental GIXD map together with a calculated peak pattern based on the adapted SIP with its (110) plane parallel to the substrate.
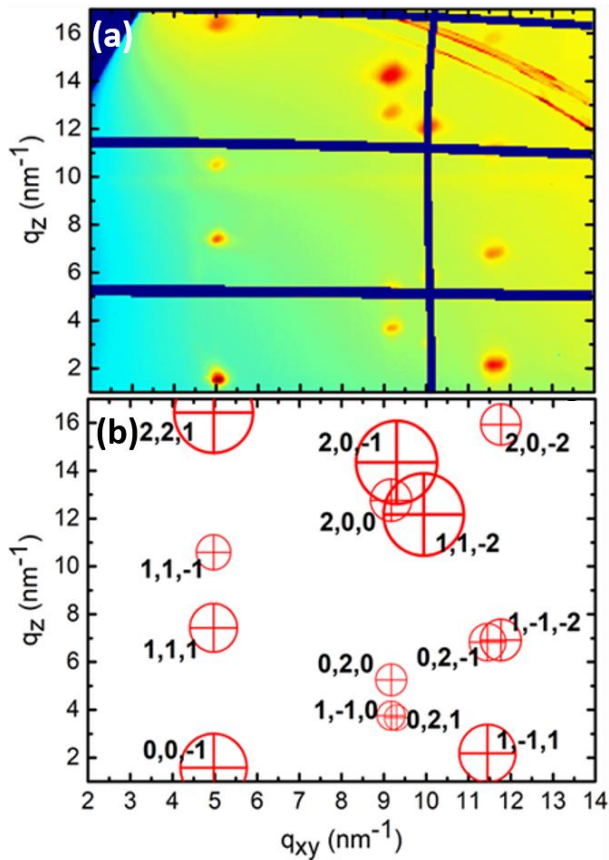
Figure 5. 26 (a) GIXD map of a 40 nm thick PbPc film on HOPG measured at an incidence angle of 0.5° and (b) Calculated peak positions (red crosses) and squared structure factors (red circles) of the adapted SIP in the 110 orientation. The size of the circles corresponds to the calculated intensities normalized to the highest value. XRD measurements and theoretical patterns by Martin Kaltenegger from TU Graz.

In panel (b), the theoretical peak positions are marked with red crosses while the squared structural factor of each peak is proportional to the area of the associated circle. We observe excellent matching with the experimental peak intensities. As the structural factors are directly related to the molecular arrangement within the crystal lattice, this demonstrates that the packing of PbPc molecules within the thin films is the same as in our predicted SIP unit cell. Based on the excellent agreements on both the peak positions and intensities, it can be concluded that the crystal structure of the PbPc thin films is successfully predicted by our molecular modelling studies, pointing to the existence of a previously unknown substrate-induced polymorph for PbPc. The crystal structure information file (cif) of this SIP has been uploaded into the Cambridge Structural Database under reference number 2121171.

The existence of a SIP in the PbPc thin films deposited on HOPG and its absence on the graphene

grids illustrates again that the crystallization of organic molecules in thin films is very sensitive to the nature of the substrate. A new attempt using a different protocol has thus been made to visualize the SIP with STEM. Here, the samples are prepared by scraping materials directly from PbPc thin films deposited on the HOPG substrates onto classical TEM carbon grids. A STEM image of these new samples is shown in Figure 5. 27.
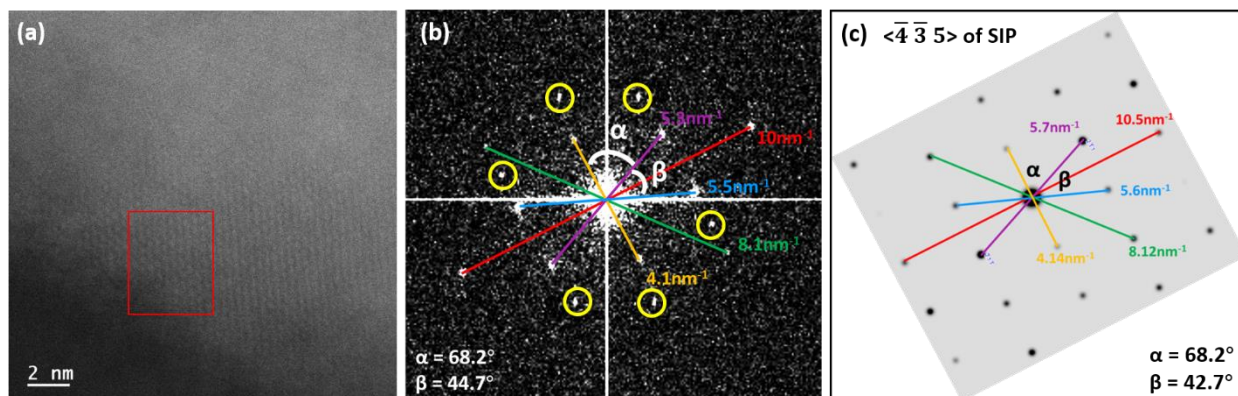
Figure 5. 27 (a) STEM image of PbPc crystallites scraped from thin films deposited on HOPG. (b) FFT pattern of the STEM image. (c) Simulated diffraction pattern from the $<\bar{4}\ \bar{3}\ 5>$ zone axis of the PbPc SIP. Simulated diffraction pattern generated by SingleCrystal™, CrystalMaker Software Ltd, Oxford, England. STEM image acquired by Noopur Jain from EMAT.

It can be noted that the resolution of this STEM image is further degraded, which originates from unavoidable crystallite agglomeration during the scraping process and the associated increase of sample thickness. Despite this, the periodic crystal lattice can still be distinguished in the relatively thin region of the image (highlighted by the red rectangle in Figure 5. 27 (a)). The FFT pattern of the image (Figure 5. 27 (b)) is then indexed with respect to the SIP using an in-house developed Matlab script, from which it can be concluded that the zone axis corresponds to the $<\bar{4}\ \bar{3}\ 5>$ of the SIP (see Figure 5. 27(c) for the theoretical diffraction pattern in this zone axis). Such a peculiar zone axis also indicates the agglomeration and re-orientation of crystallites during sample preparation. The extra paired spots in the FFT pattern (yellow-circled in Figure 5. 27 (b)) could potentially result from crystallites in different orientations present in thicker regions of the imaging area. This is verified by the FFT pattern of the thinner regions, which does not have those extra diffraction spots and shows better agreement with the theoretical diffraction pattern. This comparison is summarized in Figure 5. 28.
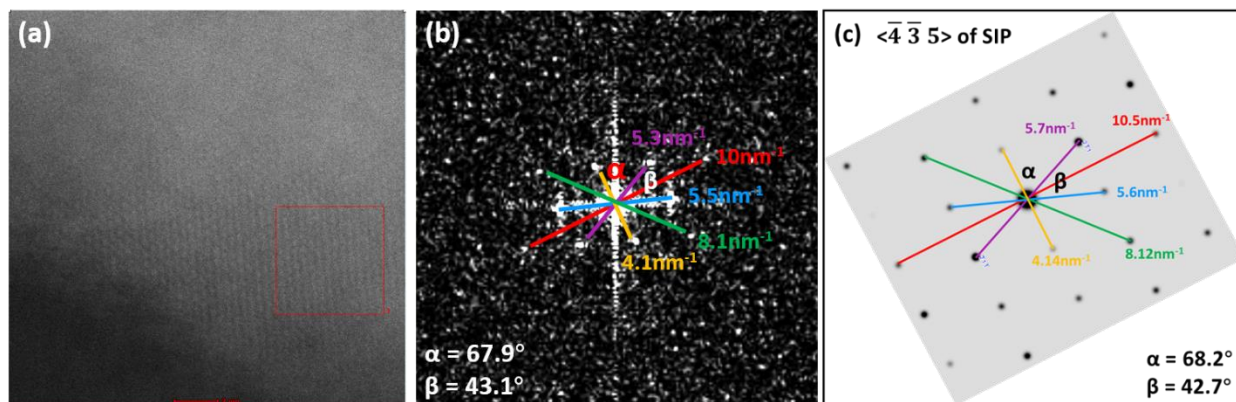
Figure 5. 28 (a) STEM image of the PbPc crystals scraped from thin films deposited on HOPG. (b) FFT pattern of the selected thinner area (red square in panel a) in the STEM image. (c) Simulated diffraction pattern from the <$\overline{4}\ \overline{3}$ 5> zone axis of PbPc SIP. Simulated diffraction pattern generated by SingleCrystal™, CrystalMaker Software Ltd, Oxford, England. STEM image acquired by Noopur Jain from EMAT.

To conclude, a previously-unknown SIP for PbPc is successfully predicted by our molecular modelling studies, which is verified by X-ray diffraction and STEM measurements. Both experiments confirm the existence of the predicted SIP in thin films that are prepared on the HOPG substrate. Although PbPc crystals (like many other organic crystals) suffer from considerable electron beam damage, a periodic crystal lattice is still distinguishable in the STEM images we acquired. This is a remarkable experimental achievement since, up to now, there are only very few (S)TEM works that focus on studying SIPs of organic molecules. Besides, the absence of SIP in the thin films deposited on the graphene grids shows again the decisive role of the substrate in governing the crystal structures of organic molecules, pointing to the huge potential for controlling crystal structures through modifying the nature of the substrate.

As from the early studies of substrate-induced polymorphism for organic molecules [36], the SIPs are only stable in the vicinity of the substrate. With the increase of the film thickness, a conversion between SIPs and the bulk polymorphs is expected to occur. For this to happen, a structural commensurability between SIPs and bulk polymorphs should exist. This potential correlation is also investigated by MM simulations in our studies. Considering the fact that the bulk monoclinic polymorph is never observed in our XRD and STEM experiments and its crystal structure is largely different from that of the SIP, we focus on the possibility for the bulk triclinic polymorph of PbPc to grow on top of a thin slab made up of the predicted SIP. The optimized geometry of this deposition is shown in Figure 5. 29 (a). After optimization, the molecular orientation and

arrangement are well-preserved in the deposited bulk triclinic polymorph, which is verified by comparing the original crystal lattice with that extracted from the deposited bulk polymorph (see Figure 5. 29 (b)). Such a good agreement between the two lattices indicates the excellent stability of this packing motif where the bulk triclinic phase of PbPc is grown on the SIP. In this way, the commensurability between that bulk polymorph and the SIP is confirmed.
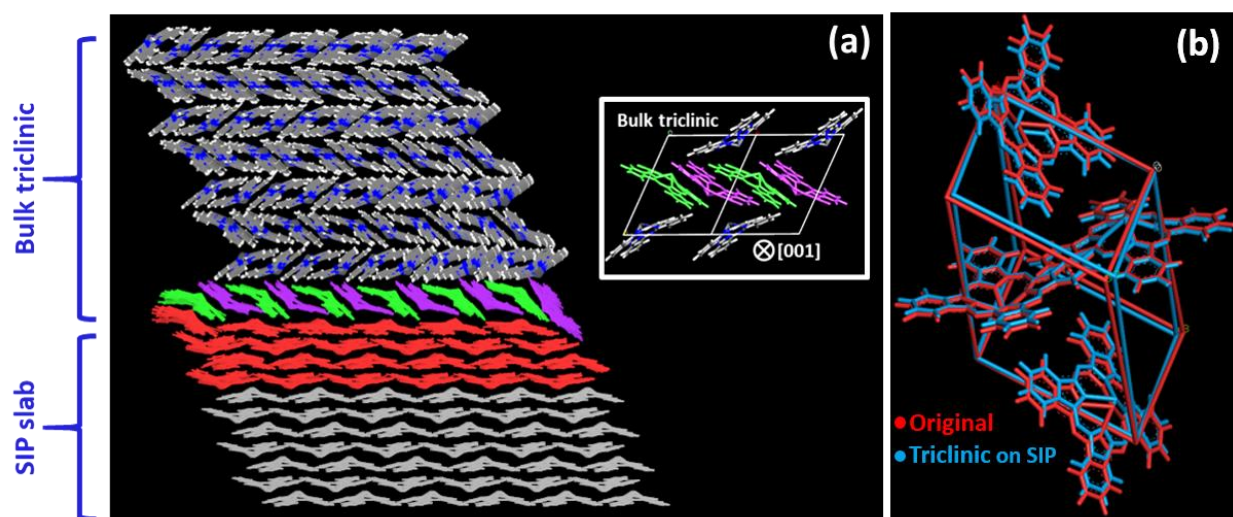
Figure 5. 29 (a) Optimized structure of bulk triclinic PbPc deposited on a SIP slab. The bottom layers of the SIP slab are frozen (gray molecules) during the optimization, while the molecules in the top layers of the SIP slab (colored in red) are free to adapt their geometries. The inset shows the orientation of the bulk triclinic polymorph when deposited on the SIP, where one row of molecules is colored alternatingly in green and violet for comparison to the interface layer in the deposited structure. (b) Comparison between the lattice of original bulk triclinic polymorph and that extracted from the deposited structure.

5.6. Conclusions

In summary, the formation, structure and stability of a substrate-induced polymorph in a prototypical molecular semiconductor, PbPc, was studied in detail. In classical Crystal Structure Prediction (CSP) calculations, the effects of the substrate are not considered, which makes it difficult to predict SIPs using CSP. Here we started from the substrate surface by investigating first the formation of SAMNs of PbPc at the solvent/graphite interface. The adsorption conformation of the PbPc molecules within the monolayer was ascertained by combining STM experiments, STM image simulations and atomistic MM/MD simulations. The non-planarity of the PbPc molecule appears as a major feature affecting the structural characteristics of the monolayer, which has the potential to direct the following crystal growth.

Our study was then extended to explore the structure of PbPc multilayers on the HOPG substrate, in order to mimic the growth of thin crystalline films. The growth of a new SIP for PbPc was successfully modelled by force field simulations, and the prediction of that SIP was proved to be successful when compared to the crystal structure of PVD-prepared thin films. To our knowledge, this is the first SIP identified for PbPc.

Appendix

Appendix 5.1. Experimental details for the preparation of PbPc self-assembled molecular networks and STM measurements

Stock solution of PbPc ($C_{PbPc} = 2.9 \times 10^{-4}$ M) was prepared by dissolving appropriate amounts of the compound in 1-heptanoic acid (HA). The stock solution was diluted further with HA to prepare a concentration series. All STM experiments were performed at room temperature (21-23°C) using a PicoSPM (Agilent) machine operating in constant-current mode with the tip immersed in the supernatant solution. STM tips were prepared by mechanically cutting a Pt/Ir wire (80%/20%, diameter 0.2 mm). Prior to imaging, a drop of solution was placed onto a freshly-cleaved surface of highly-oriented pyrolytic graphite (HOPG, grade ZYB, Advanced Ceramics Inc., Cleveland, USA). The experiments were repeated in 2-3 sessions using different tips to check for reproducibility and to avoid experimental artefacts, if any. For analysis purposes, recording of a monolayer image was followed by imaging the graphite substrate underneath under the same experimental conditions, except for increasing the current and lowering the bias. The images were corrected for drift with the Scanning Probe Image Processor (SPIP) software (Image Metrology ApS), using the recorded graphite images for calibration purposes, allowing a more accurate unit cell determination. The unit cell parameters were determined by examining at least 4 images and only the average values are reported. The images were Gaussian filtered. The imaging parameters are indicated in the figure caption: tunneling current (I_{set}), and sample bias (V_{bias}).

Appendix 5.2. Computational details of STM image simulations

To simulate STM images, density functional theory (DFT) calculations were carried out using the 4.1 version of the SIESTA code including periodic boundary conditions [37]. The exchange-correlation functional was described by the generalized gradient approximation (GGA) in the Perdew-Burke-Ernzerhof (PBE) form. A double-zeta polarized atomic basis set was used in the simulations to describe the valence electrons. The nuclei and core electrons were described by Troullier-Martins pseudopotentials [38]. A reasonable mesh cut-off of 250 Ry was utilized with a Monkhorst-Pack grid of ($1 \times 1 \times 1$). The Grimme correction was used to account for the van der Waals (vdW) interactions [39]. All SIESTA calculations were performed on the structures obtained from the force field calculations. In SIESTA, the local density of states (LDOS) were integrated over an energy window that is determined by the experimental bias voltage used for

recording the STM images. The simulated images were then generated from this LDOS based on the Tersoff-Hamann approximation by using the WSxM software [40].

Appendix 5.3. Experimental details of the STEM measurements

The HAADF-STEM images of PbPc crystals were obtained by using an aberration-corrected Thermo Fisher Scientific Titan microscope operating at 300 kV. A probe convergence semi-angle of 21 mrad and a beam current of 3 pA were used to collect the high-resolution images. The atomic columns with a bright contrast correspond to Pb in the crystal. The crystal structure is determined by the Fourier transform (FFT) of the obtained images.

Appendix 5.4. Experimental details for thin film preparation and the X-ray diffraction measurements

Highly-Oriented Pyrolytic Graphite (HOPG) monochromators were purchased from Momentive Performance Materials Quartz Inc. with a ZYB grade. This corresponds to X-ray mosaic spread of 0.5 to 1°. The dimensions of the HOPG substrates are 12x12x12 mm. Thin films of PbPc were prepared on HOPG via PVD. To clean the HOPG, sticking tape was dabbed on the surface and subsequently removed. The cleaned substrates were then transferred into the high-vacuum chamber of the PVD reactor. After reaching a high vacuum (low 10^{-6} mbar level), PbPc was sublimed from an effusion evaporator. The PbPc film growth was controlled via a microbalance.

Specular X-ray diffraction experiments on the samples were performed using an Empyrean reflectometer (Panalytical, the Netherlands) equipped with a copper sealed tube (wavelength of 0.15418 nm), a parallel mirror, beam masks, slits and a PixCel3D detector was used in scanning line (1D) mode. Grazing Incidence X-ray Diffraction (GIXD) experiments were performed at the Elettra Synchrotron in Trieste in order to study the crystal structures of the thin films. The wavelength on the beamline (XRD1) was set to 0.140 nm and the scattering intensities were collected via a 2M Pilatus detector. For better statistics, the sample was rotated during the measurement. Calibration was performed using LaB_6 standards. The GIDVis [41] software was used to analyze the collected data and the corresponding GIXD pattern was indexed with the GIDInd software [35]. During indexation, the lattice parameters were solved in a two-step procedure. In the first step, two Miller indices of the contact plane between the thin-film crystal and the substrate: *h* and *k,* were determined from the observed peaks, from which the lattice

parameters *a, b* and γ can be calculated. Then the third Miller indices of the contact plane *l* and the lattice parameters *c, α* and *β* were calculated in the second step.

References

1. Hamamoto, N., H. Sonoda, M. Sumimoto, K. Hori, and H. Fujimoto, *Theoretical Study on Crystal Polymorphism and Electronic Structure of Lead (Ii) Phthalocyanine Using Model Dimers.* RSC Adv., 2017. **7**: p. 8646-8653.

2. Kumar, T.M. and B. Achar, *Synthesis and Characterization of Lead Phthalocyanine and Its Derivatives.* J. Organomet. Chem., 2006. **691**: p. 331-336.

3. Yoshida, Y., N. Tanigaki, and K. Yase, *Evaluation of Thin Films of Functional Organic Materials by Total Reflection X-Ray Diffraction.* Mol. Cryst. Liq. Cryst. Sci. Technol., Sect. A., 1996. **280**: p. 271-276.

4. Collins, R. and A. Belghachi, *Structural Properties of Lead Phthalocyanine Thin Films.* Mater. Lett., 1989. **8**: p. 349-352.

5. Heilmann, A., M. Müller, C. Hamann, V. Lantto, and H. Torvela, *Gas Sensitivity Measurements on No2 Sensors Based on Lead Phthalocyanine Thin Films.* Sens. Actuators, B, 1991. **4**: p. 511-513.

6. Wruss, E., O.T. Hofmann, D.A. Egger, E. Verwüster, A. Gerlach, F. Schreiber, and E. Zojer, *Adsorption Behavior of Nonplanar Phthalocyanines: Competition of Different Adsorption Conformations.* The Journal of Physical Chemistry C, 2016. **120**: p. 6869-6875.

7. Marom, N., O. Hod, G.E. Scuseria, and L. Kronik, *Electronic Structure of Copper Phthalocyanine: A Comparative Density Functional Theory Study.* The Journal of chemical physics, 2008. **128**: p. 164107.

8. Arillo-Flores, O., M.M. Fadlallah, C. Schuster, U. Eckern, and A. Romero, *Magnetic, Electronic, and Vibrational Properties of Metal and Fluorinated Metal Phthalocyanines.* Phys. Rev. B, 2013. **87**: p. 165115.

9. Sumimoto, M., Y. Kawashima, K. Hori, and H. Fujimoto, *Theoretical Investigation of the Molecular and Electronic Structures and Excitation Spectra of Iron Phthalocyanine and Its Derivatives, Fepc and Fepcl N (L= Py, Cn−; N= 1, 2).* Dalton Transactions, 2009: p. 5737-5746.

10. Koudia, M., M. Abel, C. Maurel, A. Bliek, D. Catalin, M. Mossoyan, J.-C. Mossoyan, and L. Porte, *Influence of Chlorine Substitution on the Self-Assembly of Zinc Phthalocyanine.* The Journal of Physical Chemistry B, 2006. **110**: p. 10058-10062.

11. Järvinen, P.i., S.K. Hämäläinen, M. Ijäs, A. Harju, and P. Liljeroth, *Self-Assembly and Orbital Imaging of Metal Phthalocyanines on a Graphene Model Surface.* J. Phys. Chem. C, 2014. **118**: p. 13320-13325.

12. Scheffler, M., L. Smykalla, D. Baumann, R. Schlegel, T. Hänke, M. Toader, B. Büchner, M. Hietschold, and C. Hess, *Structural Study of Monolayer Cobalt Phthalocyanine Adsorbed on Graphite.* Surf. Sci., 2013. **608**: p. 55-

60.

13. Ma, H.-y., Y.-l. Zhao, M.W. Zaw, J.-f. Jia, R.-q. Zhang, and M.A. Van Hove, *Unusual Self-Assembly of Chloroaluminium Phthalocyanine on Graphite.* Surf. Sci., 2019. **681**: p. 104-110.

14. Huang, Y.L., H. Li, J. Ma, H. Huang, W. Chen, and A.T. Wee, *Scanning Tunneling Microscopy Investigation of Self-Assembled Cupc/F16cupc Binary Superstructures on Graphite.* Langmuir, 2010. **26**: p. 3329-3334.

15. Strohmaier, R., C. Ludwig, J. Petersen, B. Gompf, and W. Eisenmenger, *Scanning Tunneling Microscope Investigations of Lead–Phthalocyanine on Mos2.* J. Vac. Sci. Technol., B: Microelectron. Nanometer Struct. Process., Meas., Phenom., 1996. **14**: p. 1079-1082.

16. Nguyen, T.N., J. Aprojanz, M. Jäger, T.H. Nguyen, and C. Tegenkamp, *Noninvasive Coupling of Pbpc Monolayers to Epitaxial Graphene on Sic (0001).* Surf. Sci., 2019. **686**: p. 45-51.

17. Ukei, K., *Lead Phthalocyanine.* Acta Crystallogr., Sect. B: Struct. Sci., Cryst. Eng. Mater., 1973. **29**: p. 2290-2292.

18. Iyechika, Y., K. Yakushi, I. Ikemoto, and H. Kuroda, *Structure of Lead Phthalocyanine (Triclinic Form).* Acta Crystallogr., Sect. B: Struct. Sci., Cryst. Eng. Mater., 1982. **38**: p. 766-770.

19. Mali, K.S., L. Zöphel, O. Ivasenko, K. Müllen, and S. De Feyter, *Manifestations of Non-Planar Adsorption Geometries of Lead Pyrenocyanine at the Liquid-Solid Interface.* Chem. - Asian J., 2013. **8**: p. 2497-2505.

20. Lackinger, M. and M. Hietschold, *Determining Adsorption Geometry of Individual Tin–Phthalocyanine Molecules on Ag (111)—a Stm Study at Submonolayer Coverage.* Surf. Sci., 2002. **520**: p. L619-L624.

21. Minoia, A., I. Destoop, E. Ghijsens, S. De Feyter, K. Tahara, Y. Tobe, and R. Lazzaroni, *Design of Efficient Sergeant Molecules for Chiral Induction in Nano-Porous Supramolecular Assemblies.* RSC Adv., 2015. **5**: p. 6642-6646.

22. Guo, Z., I. De Cat, B. Van Averbeke, J. Lin, G. Wang, H. Xu, R. Lazzaroni, D. Beljonne, E. Meijer, and A.P. Schenning, *Nucleoside-Assisted Self-Assembly of Oligo (P-Phenylenevinylene) S at Liquid/Solid Interface: Chirality and Nanostructures.* J. Am. Chem. Soc., 2011. **133**: p. 17764-17771.

23. Bonini, M., L. Zalewski, T. Breiner, F. Dötz, M. Kastler, V. Schädler, M. Surin, R. Lazzaroni, and P. Samorì, *Competitive Physisorption among Alkyl-Substituted Π-Conjugated Oligomers at the Solid–Liquid Interface: Towards Prediction of Self-Assembly at Surfaces from a Multicomponent Solution.* Small, 2009. **5**: p. 1521-1526.

24. Orti, E. and J. Bredas, *Electronic Structure of Metal-Free Phthalocyanine: A Valence Effective Hamiltonian Theoretical Study.* The Journal of chemical physics, 1988. **89**: p. 1009-1016.

25. Frisch, M.J., G.W. Trucks, H.B. Schlegel, G.E. Scuseria, M.A. Robb, J.R. Cheeseman, G. Scalmani, V. Barone, G.A. Petersson, H. Nakatsuji, et al., *Gaussian 16 Rev. C.01.* 2016.

26. Zhao, Y. and D.G. Truhlar, *The M06 Suite of Density Functionals for Main Group Thermochemistry, Thermochemical Kinetics, Noncovalent Interactions, Excited States, and Transition Elements: Two New Functionals and Systematic Testing of Four M06-Class Functionals and 12 Other Functionals.* Theor. Chem. Acc., 2008. **120**: p. 215-241.

27. Krishnan, R., J.S. Binkley, R. Seeger, and J.A. Pople, *Self-Consistent Molecular Orbital Methods. Xx. A Basis Set for Correlated Wave Functions.* The Journal of chemical physics, 1980. **72**: p. 650-654.

28. Wadt, W.R. and P.J. Hay, *Ab Initio Effective Core Potentials for Molecular Calculations. Potentials for Main Group Elements Na to Bi.* The Journal of chemical physics, 1985. **82**: p. 284-298.

29. Baran, J.D. and J.A. Larsson, *Inversion of the Shuttlecock Shaped Metal Phthalocyanines Mpc (M= Ge, Sn, Pb)—a Density Functional Study.* Phys. Chem. Chem. Phys., 2010. **12**: p. 6179-6186.

30. Sirtl, T., W. Song, G. Eder, S. Neogi, M. Schmittel, W.M. Heckl, and M. Lackinger, *Solvent-Dependent Stabilization of Metastable Monolayer Polymorphs at the Liquid–Solid Interface.* ACS nano, 2013. **7**: p. 6711-6718.

31. Kashimoto, Y., K. Yonezawa, M. Meissner, M. Gruenewald, T. Ueba, S. Kera, R. Forker, T. Fritz, and H. Yoshida, *The Evolution of Intermolecular Energy Bands of Occupied and Unoccupied Molecular States in Organic Thin Films.* J. Phys. Chem. C, 2018. **122**: p. 12090-12097.

32. Kera, S., H. Fukagawa, T. Kataoka, S. Hosoumi, H. Yamane, and N. Ueno, *Spectroscopic Evidence of Strong Π− Π Interorbital Interaction in a Lead-Phthalocyanine Bilayer Film Attributed to the Dimer Nanostructure.* Phys. Rev. B, 2007. **75**: p. 121305.

33. Yamane, H., H. Honda, H. Fukagawa, M. Ohyama, Y. Hinuma, S. Kera, K. Okudaira, and N. Ueno, *Homo-Band Fine Structure of Oti-and Pb-Phthalocyanine Ultrathin Films: Effects of the Electric Dipole Layer.* J. Electron Spectrosc. Relat. Phenom., 2004. **137**: p. 223-227.

34. Grosse-Kunstleve, R.W., N.K. Sauter, and P.D. Adams, *Numerically Stable Algorithms for the Computation of Reduced Unit Cells.* Acta Crystallogr. Sect. A: Found. Crystallogr., 2004. **60**: p. 1-6.

35. Kainz, M.P., L. Legenstein, V. Holzer, S. Hofer, M. Kaltenegger, R. Resel, and J. Simbrunner, *Gidind: An Automated Indexing Software for Grazing-Incidence X-Ray Diffraction Data.* J. Appl. Crystallogr., 2021. **54**: p. 1256-1267.

36. Jones, A.O., B. Chattopadhyay, Y.H. Geerts, and R. Resel, *Substrate-Induced*

and Thin-Film Phases: Polymorphism of Organic Materials on Surfaces. Adv. Funct. Mater., 2016. **26**: p. 2233-2255.

37.	Soler, J.M., E. Artacho, J.D. Gale, A. García, J. Junquera, P. Ordejón, and D. Sánchez-Portal, *The Siesta Method for Ab Initio Order-N Materials Simulation.* J. Phys.: Condens. Matter, 2002. **14**: p. 2745.

38.	Troullier, N. and J.L. Martins, *Efficient Pseudopotentials for Plane-Wave Calculations.* Phys. Rev. B, 1991. **43**: p. 1993.

39.	Grimme, S., *Semiempirical Gga-Type Density Functional Constructed with a Long-Range Dispersion Correction.* J. Comput. Chem., 2006. **27**: p. 1787-1799.

40.	Horcas, I., R. Fernández, J. Gomez-Rodriguez, J. Colchero, J. Gómez-Herrero, and A. Baro, *Wsxm: A Software for Scanning Probe Microscopy and a Tool for Nanotechnology.* Rev. Sci. Instrum., 2007. **78**: p. 013705.

41.	Schrode, B., S. Pachmajer, M. Dohr, C. Röthel, J. Domke, T. Fritz, R. Resel, and O. Werzer, *Gidvis: A Comprehensive Software Tool for Geometry-Independent Grazing-Incidence X-Ray Diffraction Data Analysis and Pole-Figure Calculations.* J. Appl. Crystallogr., 2019. **52**: p. 683-689.

Chapter 6

Quantifying electron beam damage to Lead Phthalocyanine crystals: Analyzing the sensitivity towards different protective strategies

In chapter 5, we have shown the relevance of using STEM to probe the structure of PbPc crystals. Although two phases of PbPc are successfully determined, the imaging still suffers from the high sensitivity of PbPc crystals to the incoming electrons and the associated beam damage. This is also a common obstacle for the application of (S)TEM in studying organic crystals [1-3], in spite of the atomic-level resolution it can provide. Here, in order to better understand the electron beam damage to organic crystals in TEM and find a way to limit its negative effects, we perform a quantitative study on the electron beam damage to PbPc crystals and compare the performances of several protecting strategies.

6.1. Introduction

The high-resolution imaging capabilities of modern TEMs offer the possibility to directly probe the atomic-scale information from a material and decipher its structural complexity. However, the sensitivity of the material to degradation under the electron beam is a fundamental limitation of electron microscopy [1]. For crystals, electron beam damage corresponds to the gradual disintegration of their periodic structure during their interaction with the incoming electrons. More specifically, electron beam damage is attributed to either elastic or inelastic scattering of electrons by the materials, which then leads to the knock-on and radiolytic process, respectively [4, 5]. Knock-on damage corresponds to the permanent and irreversible displacement of a particular atom from its equilibrium position and is related to the energy of the incident electrons. Inorganic crystals are prone to be damaged in this manner [6]. Inelastic scattering and the associated radiolysis-based damage is predominant for organic crystals [4], such as those studied here.

Radiolysis occurs by secondary free radicals that are generated during the inelastic interaction between the incoming electrons and the material under study [4, 7]. In the case of organic crystals, electrons of individual molecules are excited by the incoming electrons. However, during the subsequent de-excitation process, those molecules may not be able to recover their original electronic state. This facilitates the rupture of chemical bonds as well as the distortion and displacement of the molecules, all of which promote a gradual loss of crystallinity in the presence of the electron beam [4, 8]. Studying this degradation of crystallinity by real-space imaging in a quantitative manner is quite challenging due to the high electron dose (e/Å^2, amount of electrons landing per unit area) that is required to obtain an image with a good signal-to-noise ratio (SNR).

Besides, the necessity to fine tune the microscope parameters (e.g., defocus and sample tilting) prior to the acquisition of the images makes the situation even worse. These steps require a substantial electron dose and the structure can be damaged even before images for further analysis are collected. To overcome these bottlenecks, electron diffraction in reciprocal space is used more frequently to study beam damage in TEM. High-quality diffraction patterns can be collected at relatively short exposure and those measurements can also be performed under a wide range of electron dose rate, with the possibility of using extremely low values i.e., $\sim 10^{-3}$ e/Å^2/s. [8, 9]. More importantly, the beam damage and resulting loss of crystallinity can be quantified by following the fading intensities of the diffraction rings/spots with respect to time or the accumulated electron dose [3, 10-13]. This protocol has been used to assess the beam damage for different types of materials, including proteins [14, 15], organic semiconductors for photovoltaics [16] and polymers [17, 18].

In addition to the quantitative study of the beam damage to PbPc crystals, different protection methods that may help to reduce the beam damage are also evaluated quantitatively in our study. Such evaluations provide better insights on how to minimize the beam damage in practice. One of the known protective strategies to overcome radiolysis is cryogenic cooling [5, 19, 20]. By performing TEM measurements at very low temperatures, the mobility of atoms as well as the free radicals generated during the inelastic interactions is strongly reduced, which prevents the further breakage of chemical bonds and therefore reduces the damage. The positive effects of cryogenic cooling have been reported for biological [21, 22] and organic [23] materials, however, only very limited work were done in a quantitative manner.

Another promising approach to reduce beam damage in TEM is to use graphene either as the substrate [24-27] and/or as a coating on top of the material (often called graphene encapsulation) [28-30]. More specifically, graphene has been suggested as a novel support for the TEM imaging of nano- and bio-particles [25, 27]. Compared with amorphous carbon coating, the background signals associated with graphene are much lower, which can be easily removed by digital post-processing of images (i.e. with Fourier filtering) [24, 31]. However, it needs to be noted that graphene itself also suffers from electron beam damage in TEM, which can be caused by electron-induced etching and/or knock-on displacement [32]. Therefore, to use graphene as a protection layer, delicate control over the beam current and energy of the incoming electrons is required. For instance, it appears from the literature that pristine graphene is almost free from beam damage

when the acceleration voltage of the TEM is below 80kV [33, 34]. The situation for organic crystals is nevertheless opposite, where lowering the acceleration voltage leads to an increase of beam damage [4, 35]. Due to this trade-off between the optimum voltage for the protection of graphene and the protection of organic crystals, it is far from straightforward to employ graphene as a protection layer for organic crystals, which needs to be better understood.

For studying beam damage of PbPc crystals in TEM, time-series of their fading diffraction patterns are collected and the effects of several protecting methods, including graphene as a substrate, graphene encapsulation and cryogenic cooling, on the beam damage are evaluated quantitatively. Taking PbPc as an example, our study enables us to gain deeper insights about the mechanism of damage caused by radiolysis and to further compare the performance of different strategies that can be used to reduce beam damage of organic crystals.

6.2. Diffraction experiments of PbPc crystals

Experimentally, PbPc thin films with constant thickness of ~20nm are prepared by physical vapor deposition (PVD, by Noopur Jain from EMAT). Here, two types of TEM grids are used: the common Au grids and the graphene-coated Au grids. In this manner, the effects of using graphene as the substrate on the beam sensitivity of materials can be examined. After deposition, some graphene-coated Au grids are further encapsulated with another layer of graphene on top in order to study the protection effects of graphene encapsulation. These sample configurations are shown schematically in Figure 6. 1.

Figure 6. 1 Three types of sample configuration used in the experiments

Time-series of diffraction patterns are then collected for these samples at different dose rates: ~11, ~7, ~3 and ~2 e/Å^2/s (Diffraction data collected by Urvi Parekh and Noopur Jain from EMAT, see Appendix 6.1 for more experimental details). With the same set of dose rates, the protection effects of cryogenic cooling are investigated by collecting time-series of diffraction patterns for

PbPc/Graphene/Au samples at the cryogenic temperature (~ -153℃). Figure 6. 2 compares snapshots of diffraction patterns obtained under different experimental conditions. The existence of diffraction rings confirms the polycrystalline nature of the PbPc thin films. In all conditions, the diffraction pattern of PbPc fades out gradually, indicating a gradual loss of crystallinity. Visual inspection already shows some variations in the fading rate, which reflects different beam sensitivity of the samples. However, in order to have a more reliable understanding about the beam damage and the effects of different protection measures (graphene substrate, graphene encapsulation and cryogenic cooling), the degradation of crystallinity is further studied in a quantitative manner.
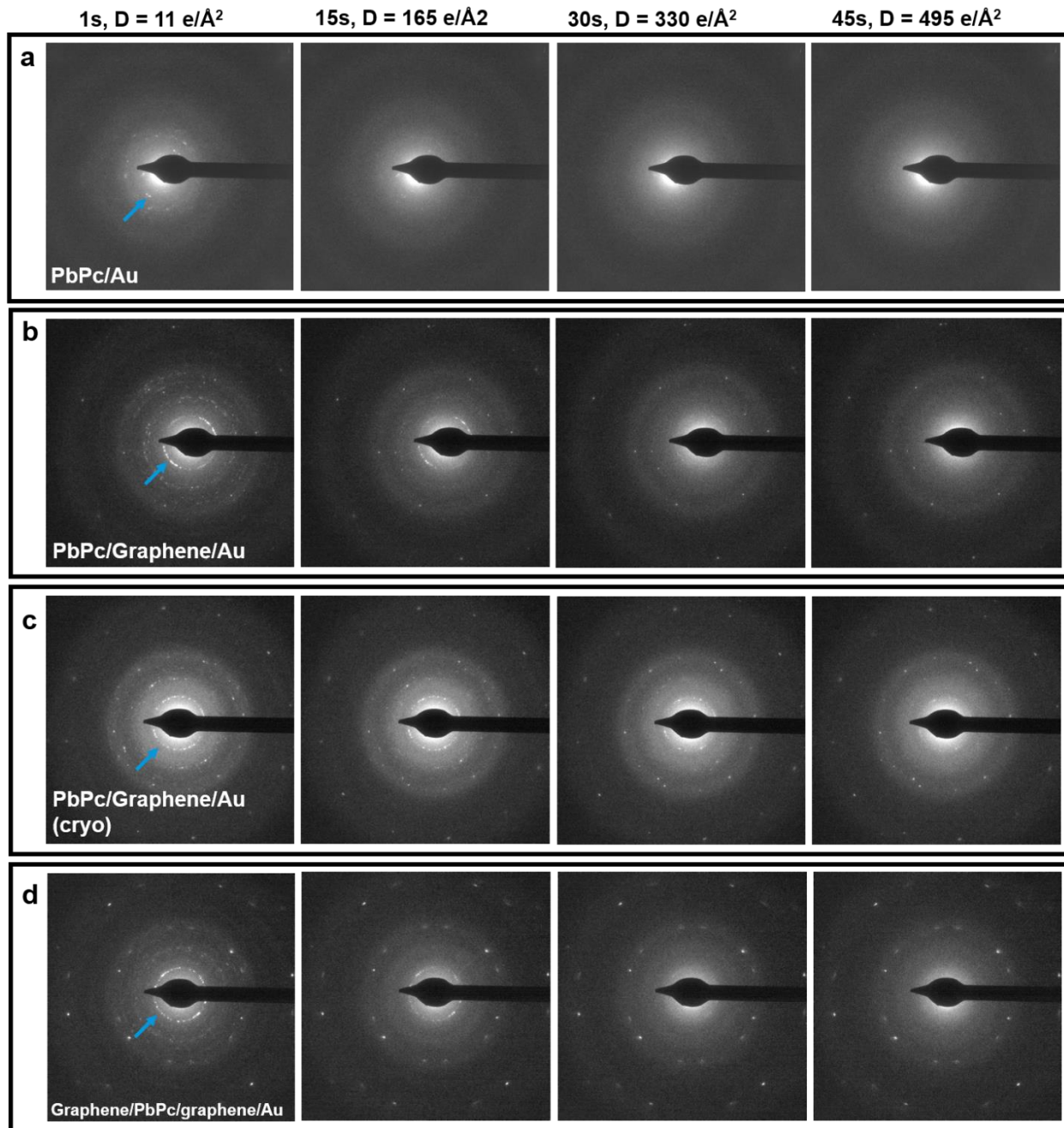
Figure 6. 2 Snapshots showing the degrading diffraction patterns for (a) PbPc/Au, (b) PbPc/graphene/Au, (c) PbPc/graphene/Au at cryogenic temperature and (d) Graphene/PbPc/graphene/Au. The experiments are performed at an acceleration voltage of 200 kV and a dose rate of ~11 e/$Å^2$/s. The time and accumulated dose at each snapshot is labelled at the top. The electron diffraction spots/rings of PbPc that are quantitatively analyzed are highlighted with a blue arrow.

6.3. Quantitative analysis of beam damage and comparison of protection methods

6.3.1. Processing of the diffraction data

In order to have a quantitative description for the beam damage of crystalline PbPc thin film, the intensity of the PbPc diffraction ring is acquired by radially averaging the diffraction pattern. Compared to intensities directly extracted from selected diffraction spots, such a radial averaging process provides a more accurate description for the intensity of the diffraction ring. The obtained-average intensity is then studied as a function of time which enables a quantitative evaluation of the radiation damage of the PbPc crystals The purposed approach is detailed in Figure 6.3.
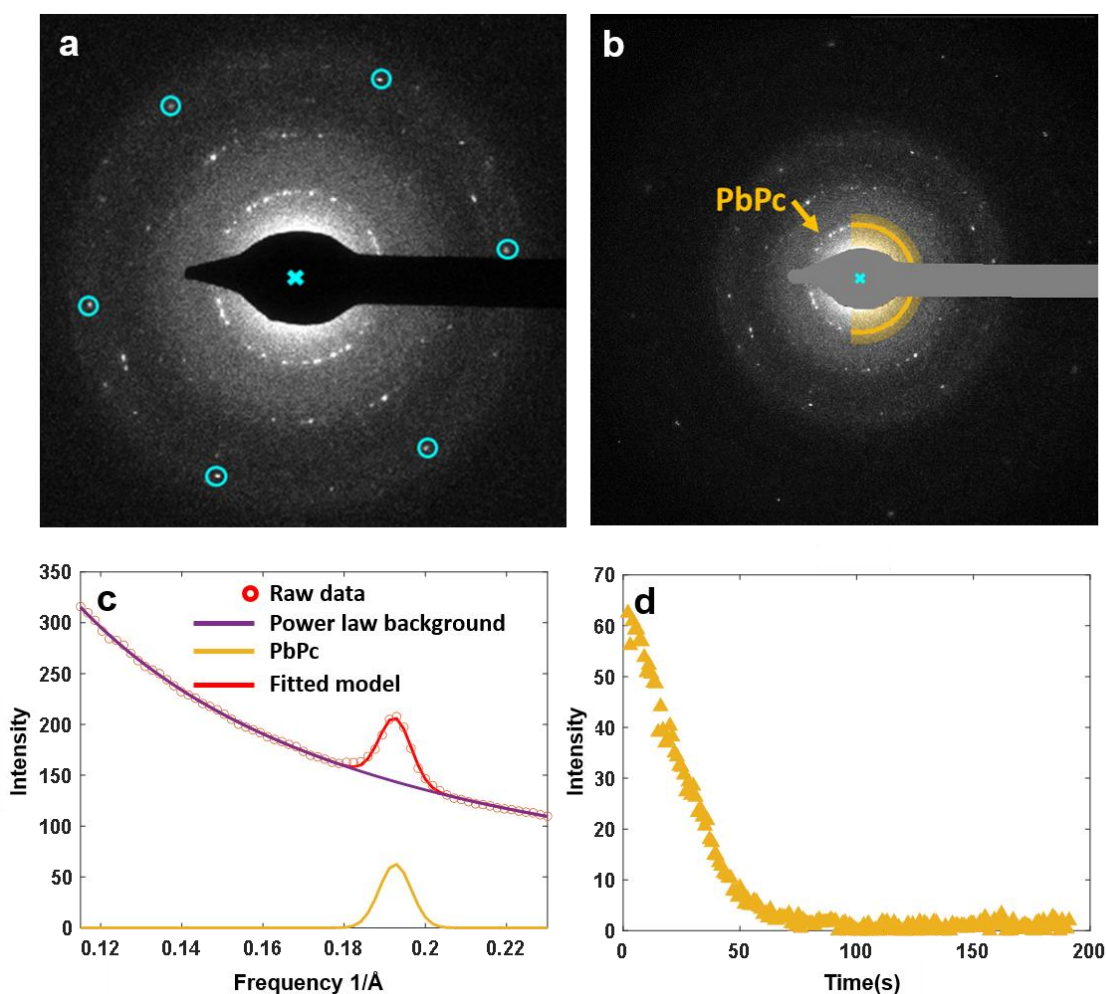
Figure 6. 3 (a) Determination of the center of the diffraction pattern. (b) PbPc diffraction ring to calculate the radial average intensity. Yellow-shaded area shows the range within which radial average intensity is calculated (from 0.12Å⁻¹ to 0.23Å⁻¹) (c) Fitting and decomposition of the radial average intensity and (d) Intensity fading for the diffraction ring of PbPc as a function of time.

Figure 6. 3 (a) is a diffraction pattern from the PbPc/graphene/Au sample. The first step in this procedure is to find the centre of the diffraction pattern and this is accomplished by using the Pets2 software package [36]. Originally, this software was developed for reconstructing the reciprocal lattice of crystals from electron diffraction tomography datasets. In this study, we use Pets2 to determine the centre of diffraction patterns, which is achieved by automatic detection of the Friedel pairs. Such automatic detection is very helpful since, within each diffraction time-series, the beam position varies in each frame. Therefore, it is not feasible to determine the centre of diffraction pattern frame by frame manually. One example is illustrated in Figure 6. 3 (a) where the estimated centre is indicated as a cyan-coloured cross. The black arrow in the middle of the figure is the beam stopper, which is used in all experiments to protect the detector from overexposure and saturation. The accuracy of the centre measurement is demonstrated by the hexagonal diffraction spots of graphene (highlighted by cyan circles), which are distributed symmetrically around the centre.

Next, the beam stopper is manually covered with a mask as the grey region illustrated in Figure 6. 3 (b). The corresponding pixel values are not used in the following calculations, whereas the remaining diffraction pattern is radially averaged using an in-house developed Matlab script. This averaging is performed for a range of frequencies around the diffraction ring of PbPc (highlighted in solid yellow line) as indicated in Figure 6. 3(b). Figure 6. 3(c) shows the calculated radial average intensity where the raw values are represented by the red circles. To quantitatively analyze the intensity decay of the PbPc diffraction ring, a model is fitted to these raw values using a non-linear least squares method which is implemented in Matlab (*lsqnonlin* command). This model consists of two components, including a Gaussian describing the diffraction intensity from the PbPc crystals and a power law describing the background:

$$I = ae^{\frac{-(x-b)^2}{2c^2}} + Dx^{-\gamma} \qquad (Eq. 1)$$

Here, x is the distance to the centre of the diffraction pattern. The intensity of the PbPc signal is described by a, which is the height of the corresponding Gaussian peak; b and c represent the position and width of the gaussian peak, respectively. D and γ describe how the background changes as a function of distance from the centre. The fitted model is represented by the red line in Figure 6. 3 (c), whereas the Gaussian peak for the PbPc crystals and the power law background are shown in yellow and violet, respectively. The excellent quality of fit confirms the validity of

the model to describe the radial average intensity and to extract the contribution from the PbPc crystals.

This radial average intensity profile is calculated for each diffraction pattern of the diffraction time-series. The intensity contribution from the diffraction of the PbPc crystals is then calculated as a function of time t (total recording time of the movie, Figure 6. 3(d)). Next, an exponential decay function is fitted to these measurements:

$$f\_a(t) = A \exp(-R_0 * t) + y_0 \qquad\qquad (\text{Eq. } 2)$$

where A is the initial intensity of the PbPc diffraction ring, $f\_a(t)$ is the fitted intensity of the diffraction ring at a given time t, R_0 is the decay rate and y_0 is an offset term. The explicit determination of the decay rate allows us to quantitatively compare the beam damage rate to PbPc crystals under different experimental conditions. The cumulative dose (e/$\mathring{A}^2$) is calculated by multiplying the dose rate by the duration (t) of the diffraction movie. The critical dose (e/$\mathring{A}^2$) is defined as the cumulative dose at which the intensity of the diffraction ring reduces to 1/e of the initial intensity [5, 19, 37-39], which is calculated by dividing the dose rate (e/$\mathring{A}^2$/s) by the decay rate (1/s) obtained from Eq. 2. All these parameters are used later to quantitatively describe the beam damage behaviors of PbPc crystals in different conditions.

For the PbPc/Au samples, the diffraction pattern does not show clear rings (see Figure 6. 2 (a)). In this case, the intensity of diffraction spots located at the same distance from the centre as the diffraction ring radius is followed directly. The decay rate and critical dose are then calculated in the same way.

6.3.2. Performances of the protection methods

Comparing the decay rate of different sample configurations (PbPc/Au, PbPc/Graphene/Au and Graphene/PbPc/Graphene/Au) under different experimental conditions (room temperature and cryogenic temperature) enables a direct assessment regarding the performance of the applied protection method. The results are shown in Figure 6. 4. Here, all experimental are done at the acceleration voltage of 200 kV.
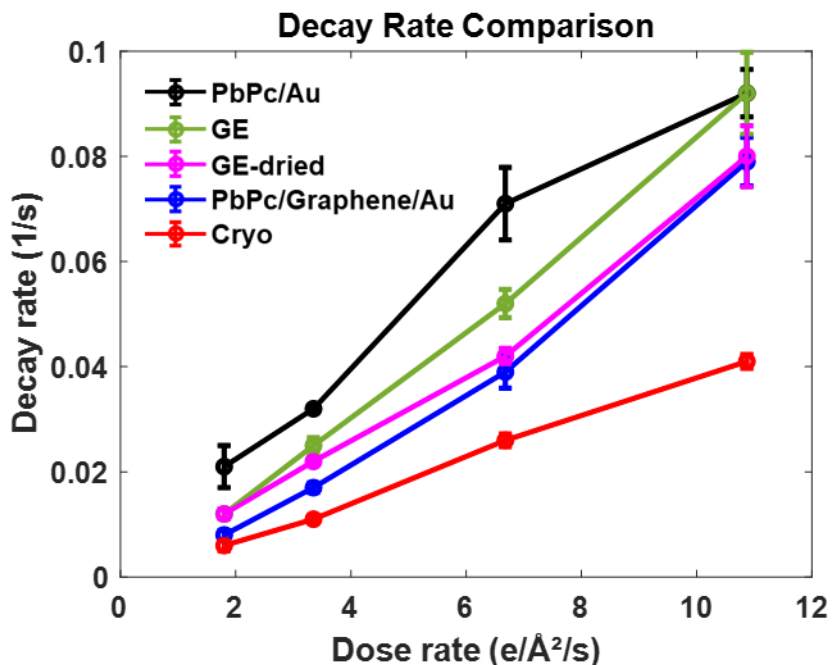
Figure 6. 4 Decay rate (1/s) as a function of the dose rate (e/$\mathring{A}^2$/s) at various conditions at 200 kV

Graphene substrate

The performance of using a graphene substrate to reduce the beam damage is studied first, since graphene has been suggested as the ultimate sample substrate for TEM [40-43]. Experimentally, the graphene substrate is applied by coating a single layer of graphene onto the Au TEM grids via a wet chemical approach (performed by Adrián Pedrazo Tardajos from EMAT). The decay rates (1/s) for PbPc/Au (black line) and PbPc/graphene/Au (blue line) are compared quantitatively in Figure 6. 4. Without the graphene layer on the Au grid, the PbPc crystals undergo beam damage significantly faster. As an example, at the dose rate of 11 e/$\mathring{A}^2$/s, PbPc degrades at a decay rate of 0.092 1/s on the Au grid while only 0.079 1/s on graphene/Au grids, which shows that PbPc is protected by the graphene underneath. The same protective effects are also observed at the other dose rates. In this way, the advantages of using graphene as the TEM substrate for beam-sensitive

153

organic crystals are explicitly proved. One explanation for such protection is that the graphene can rapidly quench the electronic excitations which are induced in the organic crystals by the incoming electrons. The associated damage is therefore suppressed. Following the enhanced beam resistance in PbPc/Graphene/Au samples, the effects of cryogenic cooling are then also studied using this type of sample configuration.

Cryogenic Cooling

The effects of cryogenic cooling are shown directly by comparing the decay rate of PbPc/graphene/Au samples with their diffraction pattern collected at either room (blue line in Figure 6. 4) or cryogenic (red line in Figure 6. 4) temperature. It is clear that cryogenic cooling improves the beam resistance of PbPc crystals considerably, i.e., by a factor of ~2 for all dose rates used in the experiments. At a dose rate of ~11 e/$\mathring{A}^2$/s, the decay rate at room temperature is 0.079 1/s and it is reduced to 0.041 1/s if cryogenic cooling is applied. The protection introduced by cooling the sample is widely known and has been used for a variety of beam-sensitive materials. For PbPc, cryogenic cooling certainly helps to reduce beam damage since the underlying damage mechanism is radiolysis and a lower temperature suppresses the diffusion of free radicals generated during the interaction with the electron beam [5].

Though promising, cryogenic cooling of PbPc samples has drawbacks such as the formation of ice crystals during the TEM measurements, inducing drift of the sample as well as the appearance of extra diffraction spots [44]. It is therefore imperative to understand and develop other methods to reduce beam damage for PbPc and similar organic crystals, where the signal-to-noise ratio in real space imaging is not compromised by the formation of side products, ice in this case.

Graphene encapsulation

We observed that PbPc crystals show an enhanced resistance to beam damage when graphene is used as a substrate. Further exploring this strategy and based on successful attempts with MoS_2 in the literature [28, 45], the PbPc crystals are sandwiched between two layers of graphene using a wet-chemical approach (performed by Adrián Pedrazo Tardajos from EMAT). This process leads to the following configuration: Graphene/PbPc/Graphene/Au and is referred as graphene encapsulation (GE) in the following text. The time-series of the diffraction patterns collected from

the GE samples are processed in the same way as described above. Figure 6. 4 shows that the decay rates for GE samples (green line) is faster than the decay rates for the PbPc/graphene/Au sample. This behavior is in contrast to the expectation that the graphene/sample/graphene configuration would provide enhanced protection to beam damage compared to the sample/graphene configuration [45]. We hypothesize that this unexpected behavior of GE is due to the water molecules that could have remained trapped in the graphene pocket from the encapsulation process. The presence of water molecules could promote the formation of free radicals under the electron beam which could then increase the beam damage. To investigate this hypothesis, GE samples are dried after graphene encapsulation for 48 hours at 100 °C to remove the trapped water/moisture in the graphene pocket, if any. The diffraction experiments are again performed using these dried GE samples (GE-dried) and the decay rates are determined. As shown in Figure 6. 4, the GE-dried samples indeed show improvement in the beam resistance (pink line), confirmed by a lower decay rate. This serves as a clear indication that careful measures need to be taken to remove excess of solvents from the graphene pocket as the solvent molecules are likely to induce extra damage.

Unfortunately, the protection provided by graphene encapsulation with respect to a simple graphene substrate remains negligible even if a prolonged drying process is applied. The decay rates stay close to the non-encapsulated samples (PbPc/Graphene/Au, blue line in Figure 6. 4). A possible reason for this is that the encapsulated graphene layer is prone to knock-on damage at 200 kV where the above-mentioned diffraction experiments are performed. To study the effects of the acceleration voltage on the beam damage and better understand the performance of graphene encapsulation, diffraction experiments are further carried out at 30 kV and 80 kV.

6.3.3. Dependence of beam damage on the acceleration voltage and dose rate

Acceleration voltage – 80 kV and 30 kV

The effects of the acceleration voltage on the decay rate and critical dose (see section 6.3.1 for the calculation of critical dose) are studied using the PbPc/Graphene/Au samples. The results are summarized in Figure 6. 5.
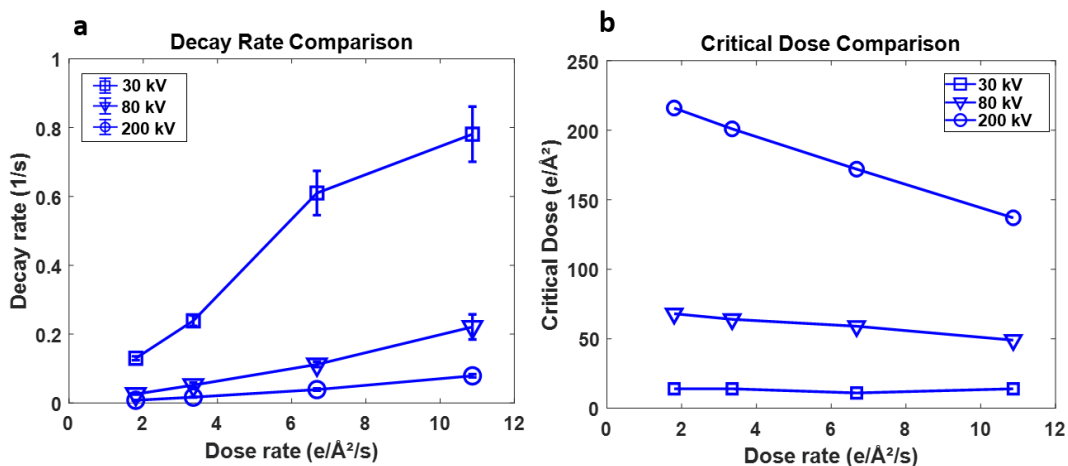
Figure 6. 5 . (a) Decay rate (1/s) and (b) critical dose (e/Å^2) as a function of the dose rate for PbPc/Graphene/Au samples at 30, 80 and 200 kV.

Figure 6. 5 (a) shows that, at 80 kV, samples are damaged at a higher rate compared to that at 200 kV for all dose rates examined, while samples at 30 kV degrade even faster than those at 80 kV. For the same electron dose rate of 1.8 e/Å^2/s, the decay rate at 80 kV is 0.026 1/s, which is significantly higher than the 0.008 1/s value at 200 kV. The situation for samples at 30 kV is worst, reaching a decay rate of 0.130 1/s. In parallel, consistent trends are found when comparing the critical doses at different acceleration voltages. Figure 6. 5 (b) shows clearly that, at each dose rate, the critical dose decreases considerably if the acceleration voltage is reduced from 200 kV to 30 kV, indicating a deteriorating beam resistance of the samples. The dependence of beam damage on the acceleration voltage is explained by the inverse correlation between the radiolysis damage cross-section and the incident energy of the electrons. At lower acceleration voltage, the cross-section for inelastic scattering is larger, which makes the associated radiolysis damage more significant.

Following this, diffraction experiments are also performed for GE-dried samples at 80 kV and 30 kV. Their decay rates are calculated in the same way as described in section 6.3.1. This enables

us to gain a more systematic understanding about the protection performance of the GE. The degradation behavior is then compared to the non-encapsulated samples (PbPc/Graphene/Au). Such comparison is performed at all dose rates and the results are summarized in Figure 6. 6.
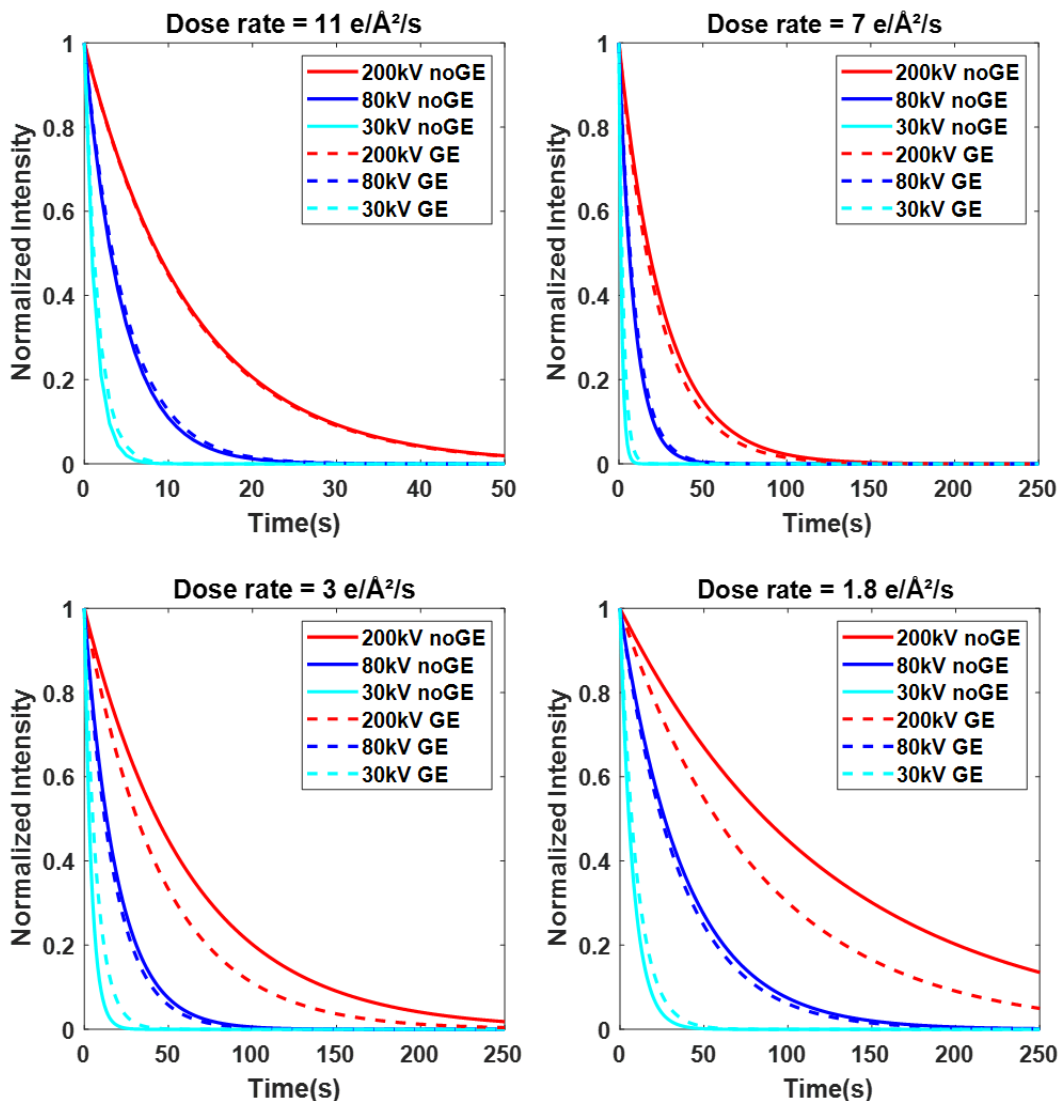
Figure 6. 6 Normalized intensity degradation of the PbPc diffraction ring, showing the effects of GE at different acceleration voltages (200kV, 80kV, 30kV) at dose rates of: (a) ~11, (b) ~7, (c) ~3 and (d) ~1.8 e/Å^2/s. The curves are normalized to the initial intensity value.

Here, a clear trend is followed at each dose rate: GE shows a slightly positive protection effect at 30 kV but shows no effect at 80 kV and a negative effect at 200 kV. This supports our previous observations: the lack of protection from GE at 200 kV is very likely to be caused by the fact the encapsulated graphene already suffers from knock-on damage at this voltage, therefore it cannot provide any protection. The stronger negative effects are most probably due to residual water from

157

the encapsulation process. Though GE protects PbPc crystals at 30 kV, it remains impractical as a protection strategy because PbPc would be damaged very rapidly in this case, as proved by the fastest decay rate and lowest critical dose shown in Figure 6. 5. Hence, a careful consideration regarding the trade-off between the stability of encapsulated graphene and the PbPc crystals is critical for applying GE to protect PbPc from beam damage in TEM. We believe that this should also be considered in the case GE is used in TEM studies of other organic crystals.

Dose-rate

Another interesting observation that can be derived from Figure 6. 5 (b) is that, in addition to the known correlation between beam damage and the accumulated electron dose (e/Å^2), beam damage also depends on the electron dose rate (e/Å^2/s), in other words, on the flux of electrons. At the same acceleration voltage, the beam damage is more pronounced at a higher dose rate, which is demonstrated by the associated lower value of the critical dose. The dependence on the dose rate is more significant at 200 kV as compared to 80 kV and almost no dependence is seen at 30 kV. We believe that the stronger dependence at 200 kV is because the interaction between the higher-energy electrons and the sample is of shorter duration, and an increase in the flux of electrons (dose rate) can accelerate the decay rate by increasing the formation of secondary radicals that contribute to damage caused by radiolysis. In contrast, at 30 kV, the damage is already quite substantial at the lowest dose rate, where the decay rate is comparable to that at the highest dose rate at 200 kV. Therefore, increasing the dose rate at 30 kV does not make extra contributions to the damage. Clearly, the dose rate is also a critical factor to control damage, along with the accumulated dose. One explanation is that the beam damage arises due to sample charging and the resulting development of an electric field within the sample [46, 47]. With an increasing dose rate, the development of the electric field is faster and the damage is enhanced, which can be further boosted by the faster generation of the free radicals.

6.4. Imaging PbPc in real space

As mentioned in the introduction of this chapter, one ultimate goal of using TEM to study organic crystals is to directly probe their atomic structures. Therefore, to better understand the beam damage of PbPc crystals in real space and the effects of different protection methods on imaging, high-resolution TEM imaging is performed on the PbPc/graphene/Au and PbPc/Au samples with an accumulated dose of ~300 e/Å^2 at 200 kV. Figure 6. 7 shows the high-resolution images of: (a) PbPc/graphene/Au at cryogenic temperature, (b) PbPc/Au and (c) PbPc/graphene/Au at room temperature.
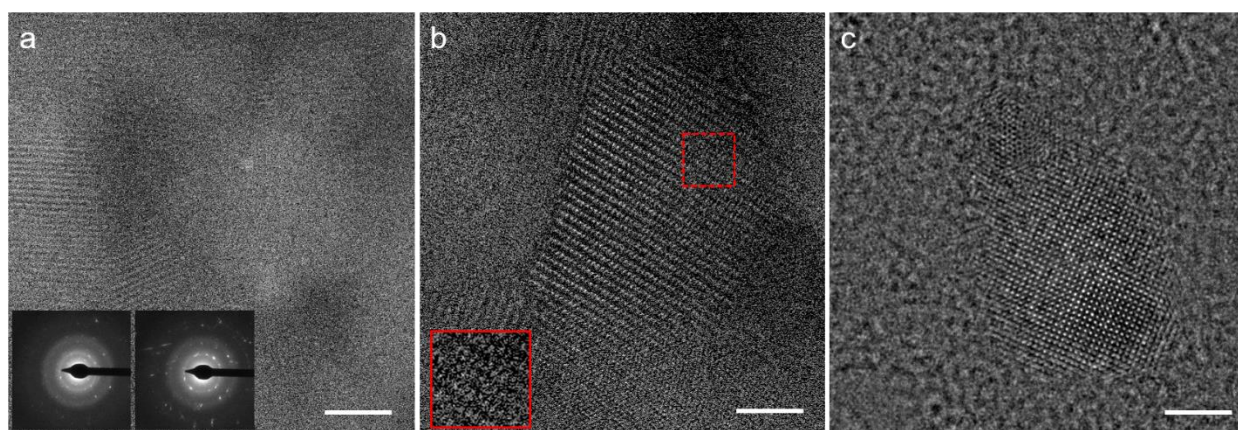
Figure 6. 7 High-resolution TEM images acquired at 200 kV and an accumulated dose of ~300 e/Å^2 for (a) PbPc/graphene/Au at cryogenic temperature, (b) PbPc/Au and (c) PbPc/graphene/Au at room temperature. Scale bar is 2 nm. Inset in panel (b) is a zoomed-in image of an example damaged (red square) region. Images acquired by Noopur Jain from EMAT.

The quantitative analysis on the diffraction data showed that the resistance to beam damage is best when cryogenic cooling is used. However, for imaging purpose, cryogenic cooling is not the optimal option. As it is shown in Figure 6. 7(a), the formation of ice crystals deteriorates the resolution of the image. While, the growth of the ice crystals is indicated by the extra diffraction spots which appear gradually during the time-series of the diffraction (see insets in Figure 6. 7 (a), diffraction pattern at the beginning (left) and ending (right) of a time-series). On Au grids (Figure 6. 7(b)), the resolution is improved where atomic columns can be distinguished, but beam damage of the PbPc crystals is also observed. The inset here shows a zoomed-in image of an example damaged region (red dash squared) where the atomic columns cannot be identified anymore. The best resolution and image quality is obtained from the PbPc/graphene/Au samples at room temperature (Figure 6. 7 (c)). Although, based on the quantitative analysis performed for the time-

series of the diffraction patterns, the graphene support does not provide the best protective effects, using a graphene substrate still appears as the optimal protocol for the real-space imaging of PbPc crystals. Furthremore, this is also interesting in a sense it turns out the best experimental settings determined from diffraction studies cannot always be transferred directly to the real-space imaging, indicating again the delicacy of using TEM to study organic crystals.

6.5. Conclusions

In this chapter, we present a detailed quantitative analysis of the beam damage of PbPc crystals, which is induced by the electron beam used in TEM. Such quantitative analysis enables us to compare the performance of several protection strategies in a straightforward way. Although cryogenic cooling is found to have the best performances in protecting PbPc from radiation damage, an in-depth analysis of the protection resulting from coating the samples with graphene is also performed. We establish that graphene encapsulation cannot be blindly used to protect organic crystals such as PbPc from beam damage, whereas a single layer of graphene at the exit surface provides a better protection. Moreover, it is found that the dose rate is also a critical factor, along with the accumulated dose, that affects the beam damage of PbPc crystals. We believe the approach we employed here to analyze beam damage of PbPc crystals under various experimental conditions can provide a framework for future TEM studies, especially in studying the structure of beam-sensitive materials.

Appendix 6.1 Protocol of the diffraction experiments

A Thermo Fischer Scientific Tecnai microscope, operated at 200 kV, was used to acquire time series of fading diffraction patterns from the PbPc samples deposited on a TEM grid. The different dose rates used for this study were obtained by controlling a combination of the spot size, condenser aperture and beam spread in the TEM mode. The various dose rates that were used are: ~11, ~7, ~3 and ~1.8 e/Å^2/s. The dose rates were determined carefully by measuring the electron counts on the fluorescent screen with uniform illumination. Once the desired dose rate is fixed, the diffraction patterns are collected using a specific camera length of 970 mm and an SAED aperture of 10 micrometer. The integration time for collecting the individual frames was kept constant at 1s. These parameters were kept constant for experiments at a particular dose rate and multiple time-series of fading diffraction patterns were collected. The procedure was repeated to obtain diffraction time-series at other dose rates.

References

1.   Egerton, R., *Radiation Damage to Organic and Inorganic Specimens in the Tem.* Micron, 2019. **119**: p. 72-87.

2.   Treacy, M. and J. Newsam, *Electron Beam Sensitivity of Zeolite L.* Ultramicroscopy, 1987. **23**: p. 411-419.

3.   Kharel, P., B.E. Janicek, S.h. Bae, A.L. Loutris, P.T. Carmichael, and P.Y. Huang, *Atomic-Resolution Imaging of Small Organic Molecules on Graphene.* Nano Lett., 2022. **22**: p. 3628-3635.

4.   Egerton, R., P. Li, and M. Malac, *Radiation Damage in the Tem and Sem.* Micron, 2004. **35**: p. 399-409.

5.   Egerton, R., *Control of Radiation Damage in the Tem.* Ultramicroscopy, 2013. **127**: p. 100-108.

6.   Jiang, N., *Electron Beam Damage in Oxides: A Review.* Rep. Prog. Phys., 2015. **79**: p. 016501.

7.   Hobbs, L., *Transmission Electron Microscopy of Extended Defects in Alkali Halide Crystals.* Surface and defect properties of solids, 1975. **4**.

8.   Henderson, R. and R.M. Glaeser, *Quantitative Analysis of Image Contrast in Electron Micrographs of Beam-Sensitive Crystals.* Ultramicroscopy, 1985. **16**: p. 139-150.

9.   Carlson, D.B., J.E. Evans, and K. Maaz, *Low-Dose Imaging Techniques for Transmission Electron Microscopy.* The transmission electron microscope, 2012. **95**: p. 85-98.

10. Glaeser, R.M., *Limitations to Significant Information in Biological Electron Microscopy as a Result of Radiation Damage.* J. Ultrastruct. Res., 1971. **36**: p. 466-482.

11. Hayashida, M., T. Kawasaki, Y. Kimura, and Y. Takai, *Estimation of Suitable Condition for Observing Copper–Phthalocyanine Crystalline Film by Transmission Electron Microscopy.* Nuclear Instruments and Methods in Physics Research Section B: Beam Interactions with Materials and Atoms, 2006. **248**: p. 273-278.

12. Eggeman, A.S., S. Illig, A. Troisi, H. Sirringhaus, and P.A. Midgley, *Measurement of Molecular Motion in Organic Semiconductors by Thermal Diffuse Electron Scattering.* Nature materials, 2013. **12**: p. 1045-1049.

13. Koshino, M., Y.H. Masunaga, T. Nemoto, H. Kurata, and S. Isoda, *Radiation Damage Analysis of 7, 7, 8, 8,-Tetracyanoquinodimethane (Tcnq) and 2, 3, 5, 6,-Tetrafluoro-7, 7, 8, 8,-Tetracyanoquinodimethane (F4tcnq) by Electron Diffraction and Electron Energy Loss Spectroscopy.* Micron, 2005. **36**: p. 271-279.

14. Baker, L.A., E.A. Smith, S.A. Bueler, and J.L. Rubinstein, *The Resolution*

Dependence of Optimal Exposures in Liquid Nitrogen Temperature Electron Cryomicroscopy of Catalase Crystals. J. Struct. Biol., 2010. **169**: p. 431-437.

15. Bammes, B.E., J. Jakana, M.F. Schmid, and W. Chiu, *Radiation Damage Effects at Four Specimen Temperatures from 4 to 100 K.* J. Struct. Biol., 2010. **169**: p. 331-341.

16. Leijten, Z.J., A.D. Keizer, G. de With, and H. Friedrich, *Quantitative Analysis of Electron Beam Damage in Organic Thin Films.* The Journal of Physical Chemistry C, 2017. **121**: p. 10552-10561.

17. Kuei, B. and E.D. Gomez, *Pushing the Limits of High-Resolution Polymer Microscopy Using Antioxidants.* Nature communications, 2021. **12**: p. 1-7.

18. Kuei, B., C. Bator, and E.D. Gomez, *Imaging 0.36 Nm Lattice Planes in Conjugated Polymers by Minimizing Beam Damage.* Macromolecules, 2020. **53**: p. 8296-8302.

19. Baker, L.A. and J.L. Rubinstein, *Radiation Damage in Electron Cryomicroscopy*, in *Methods Enzymol.* 2010, Elsevier. p. 371-388.

20. Egerton, R., P. Crozier, and P. Rice, *Electron Energy-Loss Spectroscopy and Chemical Change.* Ultramicroscopy, 1987. **23**: p. 305-312.

21. De Carlo, S., C. El-Bez, C. Alvarez-Rua, J. Borge, and J. Dubochet, *Cryo-Negative Staining Reduces Electron-Beam Sensitivity of Vitrified Biological Particles.* J. Struct. Biol., 2002. **138**: p. 216-226.

22. Yu, X., L. Jin, and Z.H. Zhou, *3.88 Å Structure of Cytoplasmic Polyhedrosis Virus by Cryo-Electron Microscopy.* Nature, 2008. **453**: p. 415-419.

23. Fryer, J., C. McConnell, F. Zemlin, and D. Dorset, *Effect of Temperature on Radiation Damage to Aromatic Organic Molecules.* Ultramicroscopy, 1992. **40**: p. 163-169.

24. Lee, Z., K.-J. Jeon, A. Dato, R. Erni, T.J. Richardson, M. Frenklach, and V. Radmilovic, *Direct Imaging of Soft− Hard Interfaces Enabled by Graphene.* Nano Lett., 2009. **9**: p. 3365-3369.

25. Pantelic, R.S., J.C. Meyer, U. Kaiser, and H. Stahlberg, *The Application of Graphene as a Sample Support in Transmission Electron Microscopy.* Solid State Commun., 2012. **152**: p. 1375-1382.

26. Meyer, J.C., C.O. Girit, M. Crommie, and A. Zettl, *Imaging and Dynamics of Light Atoms and Molecules on Graphene.* Nature, 2008. **454**: p. 319-322.

27. Nair, R., P. Blake, J. Blake, R. Zan, S. Anissimova, U. Bangert, A. Golovanov, S. Morozov, A. Geim, and K. Novoselov, *Graphene as a Transparent Conductive Support for Studying Biological Molecules by Transmission Electron Microscopy.* Appl. Phys. Lett., 2010. **97**: p. 153102.

28. Zan, R., Q.M. Ramasse, R. Jalil, T. Georgiou, U. Bangert, and K.S. Novoselov, *Control of Radiation Damage in Mos2 by Graphene Encapsulation.* ACS nano, 2013. **7**: p. 10167-10174.

29. Keskin, S. and N. de Jonge, *Reduced Radiation Damage in Transmission Electron Microscopy of Proteins in Graphene Liquid Cells.* Nano Lett., 2018. **18**: p. 7435-7440.

30. Mohanty, N., M. Fahrenholtz, A. Nagaraja, D. Boyle, and V. Berry, *Impermeable Graphenic Encasement of Bacteria.* Nano Lett., 2011. **11**: p. 1270-1275.

31. Westenfelder, B., J.C. Meyer, J. Biskupek, S. Kurasch, F. Scholz, C.E. Krill III, and U. Kaiser, *Transformations of Carbon Adsorbates on Graphene Substrates under Extreme Heat.* Nano Lett., 2011. **11**: p. 5123-5127.

32. Rummeli, M.H., H.Q. Ta, R.G. Mendes, I.G. Gonzalez-Martinez, L. Zhao, J. Gao, L. Fu, T. Gemming, A. Bachmatiuk, and Z. Liu, *New Frontiers in Electron Beam–Driven Chemistry in and around Graphene.* Adv. Mater., 2019. **31**: p. 1800715.

33. Meyer, J.C., F. Eder, S. Kurasch, V. Skakalova, J. Kotakoski, H.J. Park, S. Roth, A. Chuvilin, S. Eyhusen, and G. Benner, *Accurate Measurement of Electron Beam Induced Displacement Cross Sections for Single-Layer Graphene.* Phys. Rev. Lett., 2012. **108**: p. 196102.

34. Meyer, J.C., C. Kisielowski, R. Erni, M.D. Rossell, M. Crommie, and A. Zettl, *Direct Imaging of Lattice Atoms and Topological Defects in Graphene Membranes.* Nano Lett., 2008. **8**: p. 3582-3586.

35. Stevens, M.R., Q. Chen, U. Weierstall, and J.C. Spence, *Transmission Electron Diffraction at 200 Ev and Damage Thresholds Below the Carbon K Edge.* Microsc. Microanal., 2000. **6**: p. 368-379.

36. Palatinus, L., P. Brázda, M. Jelínek, J. Hrdá, G. Steciuk, and M. Klementová, *Specifics of the Data Processing of Precession Electron Diffraction Tomography Data and Their Implementation in the Program Pets2. 0.* Acta Crystallogr., Sect. B: Struct. Sci., Cryst. Eng. Mater., 2019. **75**: p. 512-522.

37. S'ari, M., J. Cattle, N. Hondow, H. Blade, S. Cosgrove, R. Brydson, and A. Brown. *Analysis of Electron Beam Damage of Crystalline Pharmaceutical Materials by Transmission Electron Microscopy.* in *Journal of Physics: Conference Series.* 2015. IOP Publishing.

38. Hayward, S.B. and R.M. Glaeser, *Radiation Damage of Purple Membrane at Low Temperature.* Ultramicroscopy, 1979. **4**: p. 201-210.

39. Unwin, P.N.T. and R. Henderson, *Molecular Structure Determination by Electron Microscopy of Unstained Crystalline Specimens.* J. Mol. Biol., 1975. **94**: p. 425-440.

40. Kaiser, U., J. Biskupek, J.C. Meyer, J. Leschner, L. Lechner, H. Rose, M. Stöger-Pollach, A.N. Khlobystov, P. Hartel, and H. Mueller, *Transmission Electron Microscopy at 20 Kv for Imaging and Spectroscopy.* Ultramicroscopy, 2011. **111**: p. 1239-1246.

41. Yuk, J.M., J. Park, P. Ercius, K. Kim, D.J. Hellebusch, M.F. Crommie, J.Y. Lee, A. Zettl, and A.P. Alivisatos, *High-Resolution Em of Colloidal Nanocrystal Growth Using Graphene Liquid Cells.* Science, 2012. **336**: p. 61-64.

42. Longchamp, J.-N., T. Latychevskaia, C. Escher, and H.-W. Fink, *Low-Energy Electron Transmission Imaging of Clusters on Free-Standing Graphene.* Appl. Phys. Lett., 2012. **101**: p. 113117.

43. Westenfelder, B., J. Meyer, J. Biskupek, G. Algara-Siller, L. Lechner, J. Kusterer, U. Kaiser, C. Krill, E. Kohn, and F. Scholz, *Graphene-Based Sample Supports for in Situ High-Resolution Tem Electrical Investigations.* J. Phys. D: Appl. Phys., 2011. **44**: p. 055502.

44. Li, X., P. Mooney, S. Zheng, C.R. Booth, M.B. Braunfeld, S. Gubbens, D.A. Agard, and Y. Cheng, *Electron Counting and Beam-Induced Motion Correction Enable near-Atomic-Resolution Single-Particle Cryo-Em.* Nature methods, 2013. **10**: p. 584-590.

45. Algara-Siller, G., S. Kurasch, M. Sedighi, O. Lehtinen, and U. Kaiser, *The Pristine Atomic Structure of Mos2 Monolayer Protected from Electron Radiation Damage by Graphene.* Appl. Phys. Lett., 2013. **103**: p. 203107.

46. Jiang, N., *Damage Mechanisms in Electron Microscopy of Insulating Materials.* J. Phys. D: Appl. Phys., 2013. **46**: p. 305502.

47. Cazaux, J., *Correlations between Ionization Radiation Damage and Charging Effects in Transmission Electron Microscopy.* Ultramicroscopy, 1995. **60**: p. 411-425.

Chapter 7

Conclusions and perspectives

7.1. Conclusions

This dissertation has been devoted to gain a fundamental understanding over the substrate-induced polymorphism of organic molecules. Previous efforts in this field often focused on discovering SIPs of organic molecules in experiments rather than providing insights into the mechanism for the formation of SIPs. The conceptual connection between SIPs and SAMNs (2D crystallization) has been proposed to interpret the origin of SIPs but it was only based on a rather simple structural comparison [1]. With the aim of going beyond the state-of-art, a *bottom-up* approach relying on multi-scale computational chemistry modelling is developed in this thesis, which describes in detail the structure of the initial monolayer assemblies as well as the formation and stability of the multilayer systems that can lead to the formation of SIPs. It needs to be emphasized that throughout this thesis our modelling activities are constantly connected with the experimental studies undertaken by the partners in the 2Dto3D project consortium. Such joint modelling/experimental methodology enables us to explicitly unravel the delicate interplay between the substrate, SAMNs and SIPs, from which the 2D to 3D crystallization of organic molecules is understood in a detailed way.

First (chapter 4), the peculiar nature of the self-assemblies of a molecular semiconductor, TODT-TTF, at the solution/HOPG interface is studied thoroughly by a joint STM/molecular modeling approach. Going beyond traditional studies that focus only on the first adsorbed monolayer, our simulations reveal the molecular-scale conformational changes and self-assembly processes at work in the formation of bilayers (and possibly thicker deposits). In particular, different types of STM molecular footprints are successfully correlated to the versatile adsorption conformations of the TODT-TTF molecules on the substrate and those different conformations are further proved to be the building blocks for the monolayer and bi-layer assembly, respectively. Such complex behavior also illustrates the crucial role of the substrate in the 2D crystallization of organic molecules. This is a clear example to show how molecular modelling associated to STM can provide exquisitely detailed information on 2D assembly and the growth of the subsequent layers.

Next (chapter 5), we move a step further from the bi-layer assemblies to study the possible formation of a SIP in PbPc which is another organic semi-conductor compound. One major, initial aspect is that when PbPc molecules assemble on the substrate, they adopt an organization that does not exist in the known bulk polymorphs. The second important aspect is that the new molecular

organization of PbPc can template the subsequent crystal growth, leading to the formation of a SIP. Such a sequence may represent a typical growth mechanism for the SIPs. Based on the simulations, the first known SIP for PbPc has been predicted; its structure has been confirmed later on by X-ray diffraction and TEM measurements. More generally, we believe that the bottom-up approach we propose here, where the substrate is explicitly involved and the thin film growth is followed layer by layer, shows strong potential for predicting SIPs of organic molecules, beyond the specific case of PbPc. To summarize, our work proposes a new methodology to generate substrate-induced polymorphs for organic (semiconducting) materials using self-assembled monolayers as the template.

In the last part (chapter 6), we focus on radiation damage in TEM for beam-sensitive materials, such as, organic compounds. This is a long-standing bottleneck in the TEM community. Taking PbPc as an example, the radiation damage behavior of organic crystals and the performance of several radiation damage protection strategies are evaluated in a quantitative way. More specifically, two classes of protection methods are compared: either by modifying the specimen configuration (using a graphene substrate or graphene encapsulation) or varying the imaging conditions (using cryogenic cooling). The advantages and disadvantages of each protection strategy are discussed in detail, building a framework for future studies, where the aim is to optimize the high-resolution imaging conditions of beam-sensitive materials, including but not limited to organic crystals.

In conclusion, this work illustrates the vital role of molecular modelling in understanding substrate-induced polymorphism. Molecular modelling can not only provide a detailed, molecular-scale interpretation of the experimental data, but more importantly, it shows great potential to predict, *a priori,* the crystal structures of SIPs. Finally, our work highlights the conceptual connection between SIPs and SAMNs (2D crystallization). Such connection is promising as a design strategy in crystal engineering of organic (semiconducting) materials in general. This is of prime importance for practical applications since many SIPs have shown improved properties compared to their bulk polymorph counterparts.

7.2. Perspectives

Thanks to the joint modelling/experimental methodology developed in this dissertation, a framework based on a bottom-up approach is established to predict the SIPs of organic molecules. In particular, this approach enables us to unravel how the HOPG substrate affects/drives the 2D crystallization and further promotes the formation of a previously-unknown SIP of PbPc. Nevertheless, in order to have a more comprehensive understanding about the role of the substrate during the crystallization, a first perspective of this thesis is to study the crystallization of PbPc on other types of substrate. As an example, the GIXD patterns of PbPc thin films prepared on the silicon dioxide are completely different from the patterns of the thin films that are deposited on the HOPG substrate (see Figure 5.25), even though all these films are prepared in the same conditions. This is a clear indication that the crystallization of PbPc molecules is sensitive to the nature of the substrate. We believe deep insights to explain such different behavior of PbPc molecules can only be acquired with the help of molecular modelling. Following this scheme, the *bottom-up* approach employed in this thesis can be further expanded to study the crystallization of PbPc on functionalized substrates, e.g., graphene layers or oxide surfaces decorated with various chemical groups. A combination of all these investigations will give us a much more integrated view over the general role of the substrate in the substrate-induced polymorphism of organic molecules, providing more inspiration for practical applications in crystal engineering.

Similar to the substrate, another perspective is to also diversify the molecules for which the formation of SIPs is targeted. In the current consortium, we decided to find a molecule that is suitable for versatile characterization techniques (STM, TEM and XRD) as well as molecular modelling. In the context of this requirement, PbPc is a perfect case to develop the *bottom-up* approach we have presented in this thesis. However, we should not limit ourselves to PbPc-like molecules whose only form of intermolecular interaction is π-stacking. A step further is to apply our *bottom-up* approach on molecules with a more complex pattern of intermolecular interactions. Some examples are: pharmaceutical molecules [2, 3] and conjugated oligomers [4, 5] with functional groups that favor the formation of hydrogen bonds. In this way, the applicability and robustness of our approach would be better evaluated. It can be hypothesized that with the increasing complexity of the intermolecular interactions, the approach we have proposed (mimic the crystal growth by building multilayer structures from which potential SIPs structures are

extracted) will be less straightforward and will require more and more efforts. A future perspective related to this is to find a protocol to broadly screen the prediction of SIPs. Crystal Structure Prediction (CSP) calculations have been proved efficient in the prediction of bulk polymorphs. However, as mentioned in section 5.5, they are not applicable for predicting SIPs since the effects of the substrate are not considered. Therefore, it is very appealing for future studies to include substrates in the CSP calculations. In case of physisorption, a first step in that direction would be to incorporate a fictitious Van der Waals potential wall in the CSP calculations, which represents the substrate.

Another aspect to be considered in the future is that more kinetic effects should be included in the modelling. Many SIPs found in experiments have been reported to be the kinetically-driven phase with metastability [6-8]. In other words, the formation of SIPs is sensitive to the experimental parameters that control the kinetic behavior of the molecules. For instance, the deposition rate, substrate temperature and the presence of solvents. Although implementing those parameters in the simulation studies is a challenging endeavor, some molecular dynamics studies have been performed in this area [9-11]. We believe that taking more kinetic factors into consideration can certainly contribute to a better understanding of substrate-induced polymorphism.

Several aspects in the field of electron microscopy deserve further investigation as well. It is already a great experimental achievement that the very beam-sensitive PbPc crystals could be imaged for this study. Another strong expertise at EMAT is to extract quantitative information from the electron microscopy images. It will be worthy to apply those methodologies on the images of PbPc crystals and explore whether different types of atomic columns can be distinguished, even for columns containing light elements. Furthermore, the experience of imaging beam-sensitive materials gained from our study enables such quantitative studies to be performed on different materials that suffer less from the complicated molecular structure and the peculiar zone axis under TEM. One potential candidate is covalent-organic frameworks (COFs) that generally lie parallel to the substrate. Quantitative studies can help us to determine their composition, which has a significant effect on their catalytic properties [12].

In our TEM radiation damage study, the response of PbPc crystals under the electron beam as well as the performances of different protection strategies are identified in a quantitative way. What is still missing is an understanding of the underlying physical mechanism responsible for the damage.

One of the best ways to solve this issue is to simulate the interactions between electrons and materials, which is, however, a challenging and rather new aspect. Up to now, the modelling of radiation damage focuses more on understanding the materials behavior in nuclear-irradiated conditions, where molecular dynamics simulations are used to model the cascade collision induced by the incoming irradiation [13, 14]. This can be correlated to the knock-on damage in the TEM but for the radiolysis damage that dominates in materials such as organic crystals, a better way still needs to be found for the modelling.

References

1. Fu, C., H.-p. Lin, J.M. Macleod, A. Krayev, F. Rosei, and D.F. Perepichka, *Unravelling the Self-Assembly of Hydrogen Bonded Ndi Semiconductors in 2d and 3d.* Chem. Mater., 2016. **28**: p. 951-961.
2. Case, D.H., V.K. Srirambhatla, R. Guo, R.E. Watson, L.S. Price, H. Polyzois, J.K. Cockcroft, A.J. Florence, D.A. Tocher, and S.L. Price, *Successful Computationally Directed Templating of Metastable Pharmaceutical Polymorphs.* Crystal Growth & Design, 2018. **18**: p. 5322-5331.
3. Braun, D.E., A. Rivalta, A. Giunchi, N. Bedoya-Martinez, B. Schrode, E. Venuti, R.G. Della Valle, and O. Werzer, *Surface Induced Phenytoin Polymorph. 1. Full Structure Solution by Combining Grazing Incidence X-Ray Diffraction and Crystal Structure Prediction.* Crystal growth & design, 2019. **19**: p. 6058-6066.
4. Miura, A., P. Jonkheijm, S. De Feyter, A.P. Schenning, E. Meijer, and F.C. De Schryver, *2d Self-Assembly of Oligo (P-Phenylene Vinylene) Derivatives: From Dimers to Chiral Rosettes.* Small, 2005. **1**: p. 131-137.
5. Matmour, R., I. De Cat, S.J. George, W. Adriaens, P. Leclere, P.H. Bomans, N.A. Sommerdijk, J.C. Gielen, P.C. Christianen, and J.T. Heldens, *Oligo (P-Phenylenevinylene)− Peptide Conjugates: Synthesis and Self-Assembly in Solution and at the Solid− Liquid Interface.* J. Am. Chem. Soc., 2008. **130**: p. 14576-14583.
6. Kaltenegger, M., S. Hofer, R. Resel, O. Werzer, H. Riegler, J. Simbrunner, C. Winkler, Y. Geerts, and J. Liu, *Engineering of a Kinetically Driven Phase of Phenoxazine by Surface Crystallisation.* CrystEngComm, 2022.
7. Reischl, D., C. Röthel, P. Christian, E. Roblegg, H.M. Ehmann, I. Salzmann, and O. Werzer, *Surface-Induced Polymorphism as a Tool for Enhanced Dissolution: The Example of Phenytoin.* Crystal Growth & Design, 2015. **15**: p. 4687-4693.
8. Al-Mahboob, A., J.T. Sadowski, Y. Fujikawa, K. Nakajima, and T. Sakurai, *Kinetics-Driven Anisotropic Growth of Pentacene Thin Films.* Phys. Rev. B, 2008. **77**: p. 035426.
9. Muccioli, L., G. D'Avino, and C. Zannoni, *Simulation of Vapor-Phase Deposition and Growth of a Pentacene Thin Film on C60 (001).* Adv. Mater., 2011. **23**: p. 4532-4536.
10. Roscioni, O.M., G. D'avino, L. Muccioli, and C. Zannoni, *Pentacene Crystal Growth on Silica and Layer-Dependent Step-Edge Barrier from Atomistic Simulations.* The Journal of Physical Chemistry Letters, 2018. **9**: p. 6900-6906.
11. Roscioni, O.M., L. Muccioli, R.G. Della Valle, A. Pizzirusso, M. Ricci, and

C. Zannoni, *Predicting the Anchoring of Liquid Crystals at a Solid Surface: 5-Cyanobiphenyl on Cristobalite and Glassy Silica Surfaces of Increasing Roughness.* Langmuir, 2013. **29**: p. 8950-8958.

12.   Liu, W., X. Li, C. Wang, H. Pan, W. Liu, K. Wang, Q. Zeng, R. Wang, and J. Jiang, *A Scalable General Synthetic Approach toward Ultrathin Imine-Linked Two-Dimensional Covalent Organic Framework Nanosheets for Photocatalytic Co2 Reduction.* J. Am. Chem. Soc., 2019. **141**: p. 17431-17440.

13.   Bacon, D., F. Gao, and Y.N. Osetsky, *The Primary Damage State in Fcc, Bcc and Hcp Metals as Seen in Molecular Dynamics Simulations.* J. Nucl. Mater., 2000. **276**: p. 1-12.

14.   Malerba, L., *Molecular Dynamics Simulation of Displacement Cascades in A-Fe: A Critical Review.* J. Nucl. Mater., 2006. **351**: p. 28-38.

Scientific activities during this PhD

Journal Articles

1. **Hao Yansong**, Gangamallaiah Velpula, Martin Kaltenegger, Wolfgang Rao Bodlos, François Vibert, Kunal S. Mali, Steven De Feyter, Roland Resel, Yves Henri Geerts, Sandra Van Aert, David Beljonne, Roberto Lazzaroni. "From 2D to 3D: Bridging Self-Assembled Monolayers to a Substrate-Induced Polymorph in a Molecular Semiconductor." *Chemistry of Materials* 34, no. 5 (2022): 2238-2248.

2. Noopur Jain[#], **Yansong Hao**[#], Urvi Parekh, Martin Kaltenegger, Adrian Pedrajos Tarjados, Roland Resel, Roberto Lazzaroni, Sara Bals and Sandra Van Aert; "Quantifying electron beam damage to Lead Phthalocyanine crystals: Analyzing the sensitivity towards different protective strategies" (Ready for Submission)

3. Catarina L. Delfino[#], **Hao Yansong**[#], Andrea. Minoia, Kunal S. Mali, Steven De Feyter, Yves Henri Geerts, Sandra Van Aert, Roberto Lazzaroni. "Unravelling the nature of peculiar molecular self-assemblies at the solid/liquid interface: A experimental/theoretical study on an alkylated tetrathiafulvalene derivative" (In preparation)

 # Equal contribution to the work.

Presentations

1. Self-assembly monolayer of PbPc: a starting point for substrate induced polymorphism. Oral presentation, ATOM-XV, **2020**, Online

2. From 2D self-assembly to 3D thin film crystal: A joint experimental-modelling study for lead phthalocyanine, a prototypical molecular semiconductor. Oral presentation, Euromat **2021**, Online

3. From 2D to 3D: Bridging self-assembled monolayer to substrate-induced polymorph in a molecular semiconductor. Poster presentation, 2D to 3D international workshop, **2022**, Brussel, Belgium

4. From 2D to 3D: Bridging self-assembled monolayer to substrate-induced polymorph in a molecular semiconductor. Oral presentation, ACS Fall **2022**, Online

5. Quantification of electron beam damage in Lead-Phthalocyanine. Poster presentation, NanoLab day **2022**, Antwerpen, Belgium